Investigations on the Mechanisms of Non-Photochemical Laser-Induced Nucleation and Sonocrystallisation

Clarissa Forbes

Department of Chemical and Process Engineering

University of Strathclyde

A thesis submitted for the degree of

Doctor of Philosophy

2021

Declaration

This thesis is the result of the author's original research. It has been composed by the author and has not been previously submitted for examination which has led to the award of a degree.

Signed:

Date:

Acknowledgements

Thank you to Dr Chris Price and Dr Richard O'Leary for supervision during this project. I am very grateful for Richard's guidance on signal processing as otherwise; this work would not have been possible. I cannot thank Dr Martin Ward enough for directing the laser experiments and for valued discussions on the topics of this thesis. Working with Martin inspired me to be a better scientist.

I must also thank colleagues across CUE for the loan of apparatus and workshop support. Additionally, thank you to Dr Thomas McGlone for the invaluable laboratory support and to Dr Alan Martin for the assistance and access to the X-ray laboratory within the CMAC National Facility. Additionally, thank you to Dr Iain Burns and Prof Jan Sefcik for access to the laser laboratory in CPE, together with Dr Alastair Wark for the assistance and access to the NanoSight in the Centre for Bionanotechnology.

Also, thank you to Dr Lauren Connor and Dr Václav Svoboda for being incredible friends and inspirations throughout my time at CMAC. Lauren, thank you so much for everything and especially for my beautiful guide daughter, Amélie. Finally, to Tony, Ross, Lucinda and Mum, I cannot express how grateful I am to you for everything that you have done for me. Mum, it is you to which I dedicate this thesis.

Abstract

In recent years, a number of authors have steered Non-Photochemical Laser-induced Nucleation (NPLIN) and sonocrystallisation from mystery towards viable and valuable application for improved control over the industrial crystallisation of drug substances. However, the underlying mechanisms of nucleation induction from the phenomena generated by laser irradiation and ultrasonic wave propagation are both still under investigation. So far, a complex picture of bubbles and localised pressure fluctuations at the interplay of clusters and crystals has been provided. This thesis presents detection of bubble fields in order to provide mechanistic insight into NPLIN and sonocrystallisation.

On the underlying mechanisms of the NPLIN effect, doubts have been cast on the initially proposed effects of the optical electric field acting directly upon solute clusters. Recently, it has been proposed that at laser pulse energies below the threshold for optical breakdown of the liquid, impurity particle heating generates transient vapour cavities, the associated phenomena of which provide opportune conditions for nucleation induction. However, there have been a lack of experimental attempts to detect vapour cavities in order to support this mechanism. Chapter 4 provides significant evidence of nucleation induction within an unfocused beamline *via* cavitation generated by particle heating. For the first time, single-pulse (1064 nm, 6ns) laser-induced nucleation of ammonium chloride was captured with high-speed imaging. Observations at 100000 fps allowed for the detection of multiple micron-sized bubbles before the appearance and growth of multiple primary crystal nuclei within the irradiated volume of the solution. Further compelling evidence for the impurity particle-heating mechanism is provided by needle hydrophone measurements, in which the effect of solute concentration alongside solution filtration and iron oxide nanoparticle doping prior to irradiation were investigated. Signal processing allowed for quantification of the broadband noise produced by bubbles that were generated on laser irradiation. Overall, the results demonstrate a direct relationship between absorbing particles, cavitation generation and crystal nucleation, which has powerful implications for discussions behind the mechanism for laser-induced nucleation.

The effects of propagating ultrasound waves through a liquid occur *via* the generation of acoustic cavitation: the growth and collapse of vapour cavities under an applied ultrasound field. This mode of cavitation generation is well established for inducing crystal nucleation and fragmentation. However, few previous sonocrystallisation studies have involved measurement of cavitation activity in the generated sound field. Moreover, the physical properties of a liquid have been reported to significantly affect the cavitation activity, under the same applied ultrasound parameters. Chapter 5 presents a comparison of cavitation activity in typical crystallisation solvents, under a high-power ultrasound field. A setup was established in order to perform needle hydrophone measurements, from which the acoustic pressure and broadband integrated voltage were obtained at increasing drive powers. The broadband noise measurements are discussed in relation to the solvent physical properties.

Previous paracetamol (PCM) sonocrystallisation studies involving the application of high-power ultrasound fields have reported (i) the selective crystallisation of the elusive metastable form II and (ii) higher impurity rejection in the presence of acetanilide and metacetamol, both on comparison with silent conditions. However, the mechanisms behind these observations remain unclear. Chapter 6 provides an investigation of PCM cooling sonocrystallisation, with a focus on the mechanisms for polymorphism and purity effects. It was established that, under the same applied frequency, the selective crystallisation of form II relied upon the application of cavitation energy above a threshold, together with both high supersaturation and rapid growth conditions. Meanwhile, greater impurity purging with cavitation generation was attributed to nucleation induction at significantly lower supersaturation levels, as opposed to cavitation phenomena promoting impurity rejection. Moreover, a morphology change from equant to columnar crystals of PCM form I was observed in the presence of impurities only under an applied cavitation field, which was attributed to the acceleration of surface integration caused by stable cavitation phenomena. This effect has not before been reported and it is expected to influence the development of industrial sonocrystallisation processes for drug substance purification.

Contents

List of Figures

List of Tables

Introduction

1.1. Crystallisation

The pharmaceutical industry brings life-changing scientific innovations to patients through both a lengthy and expensive journey of drug development, clinical evaluation and drug manufacturing. Crystallisation is the predominant separation and purification technique employed in the manufacturing of drug substances (the active ingredients). This unit operation is preceeded by synthesis and followed by isolation, before downstream processing in order to obtain the drug product (the final marketed dosage form).

In the design of industrial crystallisation processes, the ultimate aim is to create products with consistent particle attributes, such as crystal size distribution, shape, purity, and of the most suitable polymorphic form.[1] An overview of the processes that govern industrial crystallisation and the resulting product quality is presented in Fig. 1-1.

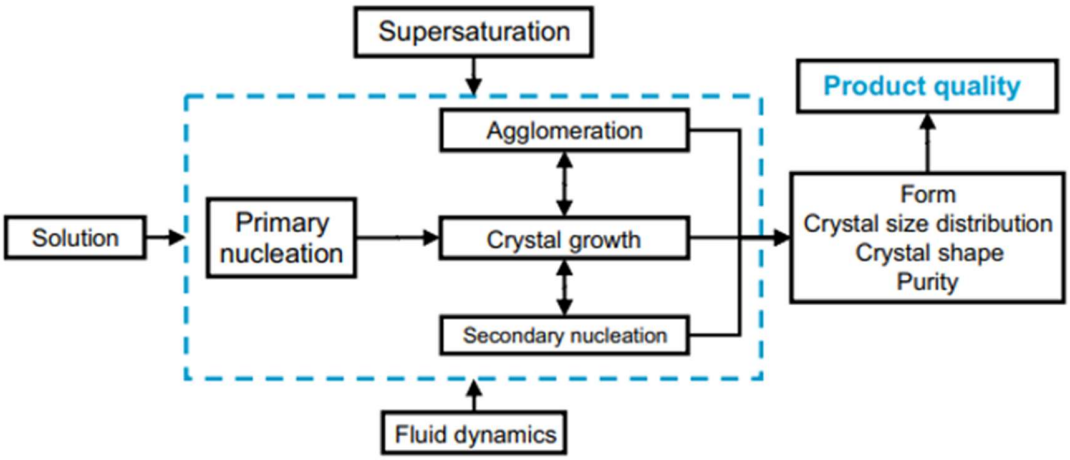

Figure 1-1 Overview of crystallisation processes governing product quality (reproduced from ter Horst et al.[2])

Essentially, crystallisation starts with nucleation, proceeded by growth and individually, these processes can be considered as the transport of building blocks from the bulk of the mother phase to the nucleus. Control over both nucleation and growth is critical, as the resulting product quality not only influences downstream operations, but also the physicochemical properties of the crystalline product such as solubility, dissolution rate and therefore, bioavailability.[3] This section outlines crystallisation in the context of pharmaceutical manufacturing and with reference to paracetamol (PCM); the drug substance of interest for the crystallisation work carried out in this thesis.

1.1.1. Supersaturation

Solubility is the amount of solid that can be dissolved in a solvent at a specific temperature and pressure. The saturation status of a solution is dependent on the concentration of solute, relative to the solubility at a specific temperature and pressure. A solution is saturated when the solute is in thermodynamic equilibrium with the solution. When there is less solid dissolved relative to the solubility, the solution is undersaturated and the solute will remain in solution. When a solution has more solid dissolved relative to the solubility, the solution is supersaturated; a driving force for crystallisation has been established and crystal nucleation can occur.

Supersaturation is usually described as a concentration ratio or relative supersaturation, with respect to the equilibrium saturation concentration. In this thesis, the supersaturation ratio (*S)* is the preferred descriptor, which is expressed as the ratio of solute concentration (c) and the solubility (c^*) at a specific temperature and pressure:

$$S = \frac{c}{c^*} \tag{1-1}$$

A typical solubility diagram with the regions of saturation and supersaturation is provided in Fig. 1-2, where the solubility curve (solid line B–B') describes the thermodynamic limit for the solute to remain in solution, which is well-defined and can precisely be determined.[4] Whereas, the supersolubility curve (dashed line C–C′) represents the

metastable limit and past this line into the labile region, solid will crash out of solution uncontrollably. Accordingly, C–C′ is less well-defined than B–B'.

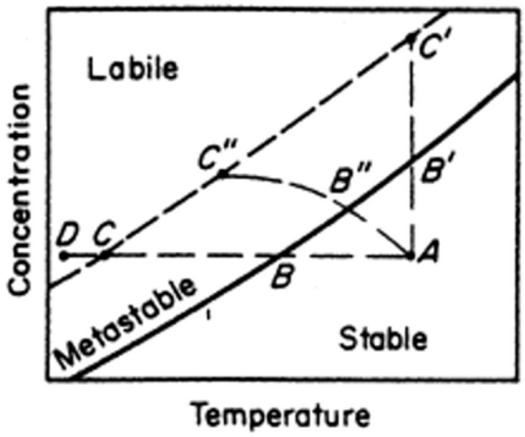

Figure 1-2 Typical diagram of solubility expressed in concentration as function of temperature and the different regions of saturation (reproduced from Mullin[4])

The area between these curves is the metastable zone, in which spontaneous nucleation can take place in a controllable fashion and after a certain induction period. Thus, the metastable zone width (MSZW) is commonly used to determine the crystallisation process operation window.[5] The lines A–C and A–C′ represent two typical routes to achieve supersaturation: cooling a solution of fixed concentration and removal of solvent *via* evaporation to increase solute concentration at fixed temperature, respectively. The line A-C″ represents a combination of these routes. Supersaturation generation can also be achieved via the addition of an anti-solvent: a solvent in which the solute is poorly soluble. A large proportion of commercial drug substances (including PCM), exhibit poor aqueous solubility thus, water is commonly a suitable choice of anti-solvent.[6]

1.1.2. Nucleation Classifications

Nucleation can be classified as primary or secondary, as outlined in Fig. 1-3. Crystals forming directly from the solution phase alone is classed as primary nucleation whereas; crystals forming due to the presence of crystals of the solute is classed as secondary nucleation.

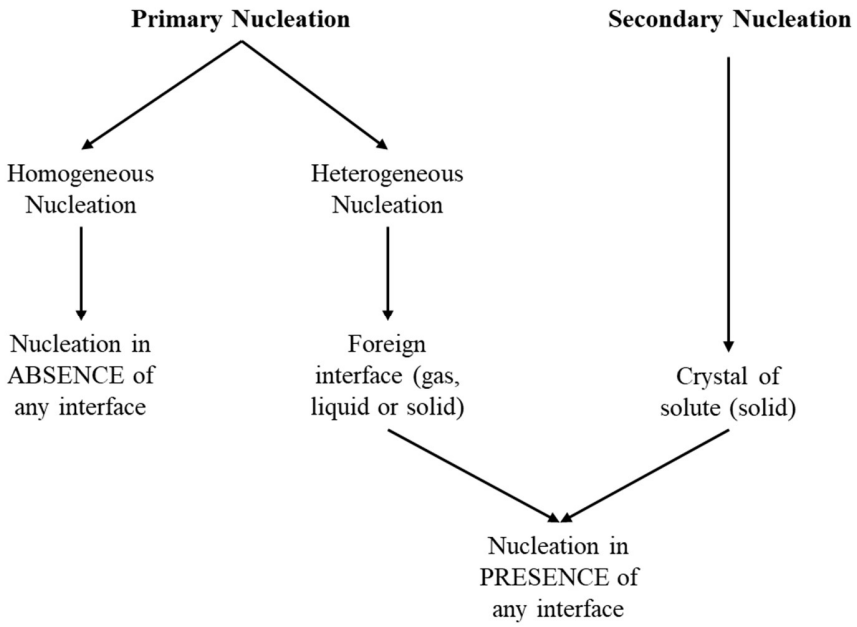

Figure 1-3 Nucleation classifications (adapted from Beckmann[7])

Primary nucleation is further divided into the sub-classes of primary homogeneous and heterogeneous nucleation. Primary nucleation is considered homogeneous when it occurs in the absence of an interface. When nucleation occurs in the presence of a solid (other than crystals of the solute), gas or a third-party liquid, this can be classified as primary heterogeneous nucleation. In the laboratory and especially on an industrial scale, the presence of many different heterogeneous particles or surfaces is impossible to avoid.[7] Thus in practice, heterogeneous nucleation is considered to be more prevalent and in this case, the free energy barrier for nucleation is lowered by the interface provided by foreign particles present.[4] Secondary nucleation occurs when there are already crystals of the solute present (from strategically added seeds or primary nuclei already present in the system). According to Myerson, the presence of crystalline material has a catalytic effect on nucleation and therefore, secondary nucleation can occur at much lower supersaturation levels compared to primary nucleation.[8] Seeding is routinely employed in the industrial crystallisation of drug substances in order to reproducibly yield crystals within a desired size distribution.

Fluid shear causes high-energy collisions of existing crystals with impellers, vessel walls and each other, resulting in the breakage of existing crystals to generate secondary nuclei. This is also considered secondary nucleation, although this has been questioned, since it is a mechanical process that does not involve the formation of a new solid phase.[9] An in-depth discussion on the mechanisms of secondary nucleation is beyond the scope of this thesis. Agrawal and Paterson recently provided a comprehensive review of secondary nucleation in industrial crystallisers.[10]

Importantly, Kadam *et al.* reported that the MSZW is not a fixed quantity and that nucleation probability increases with the volume of the crystalliser.[11] This report involved MSZW measurements as a function of crystalliser volume (1 mL—1 L) for an unseeded PCM-water cooling crystallisation process. At 1 mL volume, MSZW values were reported as a wide distribution (varying ~ 25°C) however, on a 1 L scale, variations in the MSZW were almost absent.[11] It was established that the smallest MSZW measured at 1 mL coincided with the MSZW at 1 L. Therefore, the authors concluded that on a scale one thousand times larger (1 L), there is a higher probability of a single nucleation event occurring, that would lead to nucleation in the entire crystalliser.[11] The larger variation on a smaller scale was attributed to the inherently random nature of the nucleation process, which would not necessarily be detected at a fixed temperature.[11] The nucleation process requires further discussion.

1.1.3. Nucleation Models

The two prominent models used to describe crystal nuclei formation from solution are Classical Nucleation Theory (CNT) and the two-step nucleation model (2SM). CNT is a long-established model used to describe the sequential addition of solute molecules to form a crystalline nucleus, of radius (r) from a supersaturated solution. Although this second phase has a lower free energy (ΔG) than the initial phase, there is a free energy penalty associated with the formation of a new interface in solution. For a spherical nucleus, the free energy of forming the second phase is the sum of a negative volume term (ΔG_v) and a positive surface term (ΔG_s):

$$\Delta G = \Delta G_s + \Delta G_v = 4\pi r^2\gamma - \frac{4}{3}\pi r^3 A \ln S \quad (1\text{-}2)$$

where S is the supersaturation and γ is the interfacial tension of the crystal–solution interface. $A = \frac{\rho RT}{M}$, where ρ is the mass density, R is the gas constant, T is the temperature and M is the molar mass. Fig. 1-4 schematically represents the energetics of CNT, in relation to the size of the forming nucleus. As the nucleus size increases, the total free energy goes through a maximum at a critical radius (r_{crit}). As r further increases, the total free energy decreases as the nucleus grows bigger and growth becomes energetically favourable. At below r_{crit}, re-dissolution will occur.

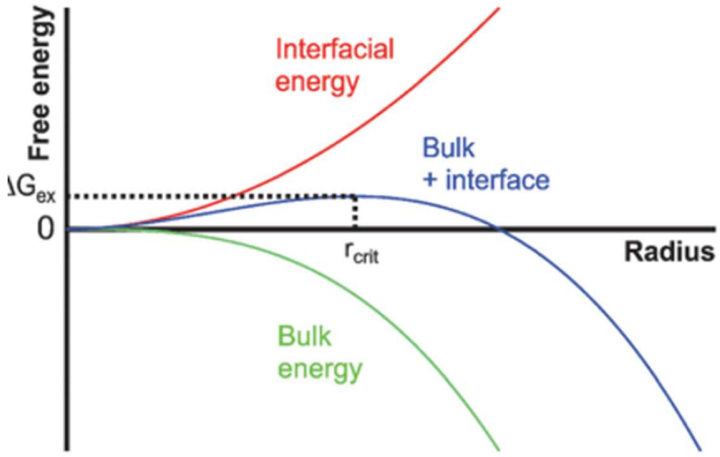

Figure 1-4 Schematic of the size dependence of the energetics of forming a nucleus, according to CNT (reproduced from Gebauer et al.[12])

CNT has successfully been combined with probability distributions of induction time measurements in order to gain insight into nucleation kinetics.[13, 14] Nevertheless, several shortcomings of this model have been identified; including that the surface of the nucleus is modelled as an infinite plane with neglect of the curvature dependence of the surface tension.[15] These assumptions do not hold if the critical nucleus is on the order of a few nm.[16] Furthermore, CNT assumes nuclei to be ordered in structure, which conjectures that the molecular packing within clusters is reflected in the resulting macroscopic crystal form.[17] Overall, the size of a critical nucleus is typically in the range of 10—1000

molecules and the time scale of formation ranges from less than a second to days thus, crystal nucleation is extremely challenging to study experimentally.[16]

Following observations made, primarily in the study of protein crystallization by Galkin *et al*., an alternative mechanism has been proposed in order to account for the nucleation event.[18] Several detailed discussions on the 2SM have since been provided. [17, 19-21] In short, the initial step of the 2SM involves the formation of an amorphous and liquid-like cluster. Crystalline order is developed during the second step, where the cluster achieves a critical size to form a nucleus and survive. The 2SM makes no assumptions regarding the shape of a solute cluster or its internal structure.[17] In 2016, Ito *et al*. reported direct visualisation of the 2SM of a dibenzoylmethane boron complex that displays mechanofluorochromism.[22] From fluorescence emission measurements of an evaporative crystallisation process, the authors detected transitional emission from the amorphous cluster state prior to crystallisation. More recent classical density functional theory calculations, performed by Lutsko *et al.*, support the proposal that metastable and disordered sub-critical clusters play an important role in nucleation.[23, 24] A schematic of both the classical and the two-step nucleation models is provided in Fig. 1-5.

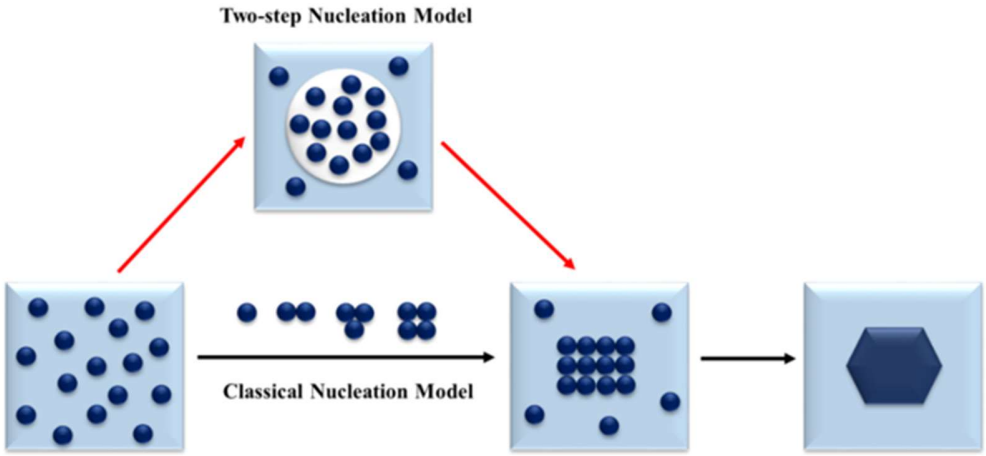

Figure 1-5 Schematic of the classical and the two-step nucleation models (adapted from Chen et al.[16])

A further point to note is the fluid dynamics greatly influence the nucleation process.[25] In 2013, Jawor-Baczynska *et al*. proposed agitation-enhanced cluster aggregation from the mechanical action of a tumbling stirrer bar significantly shortening the time to form observable glycine crystals.[26] Since this mechanical action was also observed to promote coalescence of 250 nm nanodroplets into larger nanodroplets, the latter were assumed to be the prime source for nucleation.[26]

1.1.4. Polymorphism

The majority of organic and inorganic compounds can exist in different solid-state forms.[1] McCrone defined polymorphism in 1965 as "the ability of a compound to crystallise as more than one distinct crystal species".[27] It is important to note that polymorphism refers to the crystal structure, whereas crystal morphology describes the macroscopic shape of a crystal. According to Hilfiker; the same polymorph can easily be crystallised in different morphologies and different polymorphs can also have the same morphology.[1] Therefore, it is imperative to carry out structural characterisation of the crystalline material in order to definitively assign the polymorphic form.

The selection of the most suitable polymorphic form of a drug substance is a critical aspect of industrial crystallisation process development. Different solid-state forms of the same compound will exhibit different physicochemical properties, such as thermal and mechanical stability, solubility, and hygroscopicity. Moreover, discovery of the lowest energy (most stable) polymorph in early development is essential. Unexpected conversion to a previously unknown, lower energy form in the manufacturing phase can cause catastrophic delays to drug supply, as in the case of Ritonavir.[28] This makes the case for efforts in crystal structure prediction in order to evaluate the solid form landscape of a compound, combined with extensive experimental polymorph screening as early as possible in pre-clinical drug development.[29-31]

Ostwald's rule of stages provides a guide to the design of a polymorph screen. This rule states that during a crystallisation process, the system moves to equilibrium from an initial high energy state through minimal changes in free energy, and thus implies that the least

stable polymorph should be the first isolated in any crystallisation process.[32] It should also be noted that phase transformations to lower energy forms can take place before sampling is possible. Fig. 1-6 shows the various crystallisation experiment types that can be employed to favour stable or metastable polymorphs.

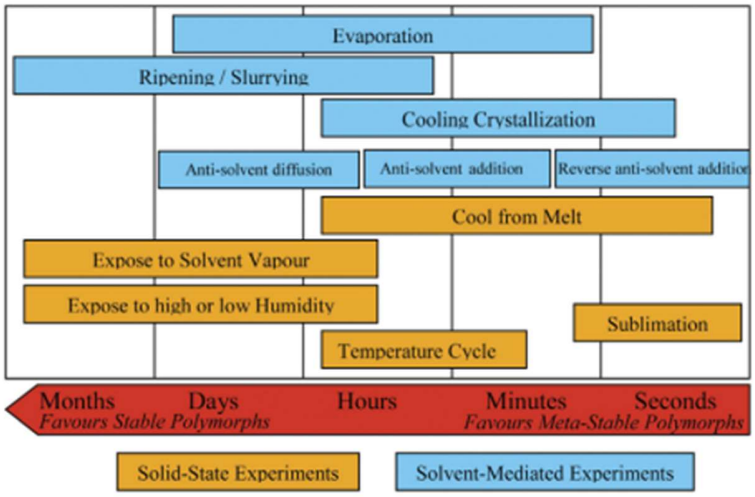

Figure 1-6 Crystallisation experiments that can be employed in the polymorph screening of a drug substance (reproduced from Llinás and Goodman[31])

Yet, many violations of Oswald's rule have been reported.[33, 34] It is generally accepted that the rule is not applicable to every system for instance, in the case of polymorphs nucleating concomitantly.[35] Considerations have also been extended to include studies of potential links between solution chemistry, molecular self-assembly and the appearance of polymorphs.[17, 36, 37] For example, different solvents can be also be employed to modify interfacial energies in such a way to promote the formation of different polymorphs.[2] Black *et al.* recently noted that the experimental observations which support Ostwald's rule have been made on macroscopic observations and that the polymorphic outcome may owe at least as much to the relative crystal growth rates of available structures, as it does to their nucleation.[38]

From an extensive experimental polymorph screen of PCM, Peterson *et al.* demonstrated that solution crystallisation attempts almost invariably led to the isolation of the most

stable polymorph.[39] PCM is the most widely used antipyretic and analgesic worldwide.[40] From solution, two polymorphs of PCM have been long-established: form I, the thermodynamically stable form at ambient conditions and form II, the metastable form at ambient conditions.[41-43] Form I is the commercially manufactured form, with a crystal packing structure that results in poor compactibility, leading to poor tabletting quality.[40] Form II can undergo plastic deformation and therefore, exhibits improved compaction behaviour.[44] However, difficulties in producing form II at scale has limited the viability of form II commercial manufacture.[45] Experimental morphologies of PCM form I and II (from water) are shown in Fig. 1-7, where form I crystals exhibit a relatively equant shape and form II crystals are more needle-like.

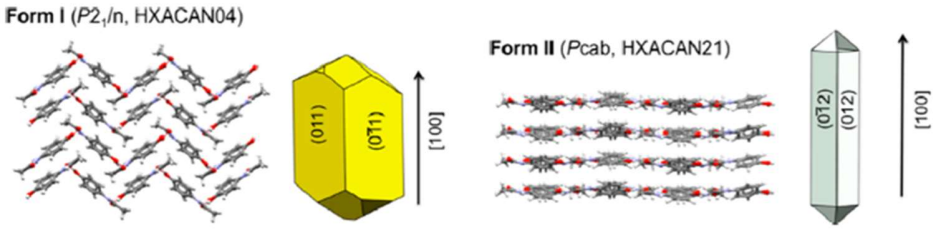

Figure 1-7 Paracetamol form I (monoclinic) and form II (orthorhombic) morphologies and packing views along a-axis for form I and along b-axis for form II (reproduced from Liu et al.[46])

A typical strategy for polymorph control is to seed with the desired form. Though, a recent study from Nicoud *et al.* reported that at temperatures above 0 °C, seeding a crystalliser with crystals of form II was insufficient to induce the crystallisation of form II.[47] The elusive nature of form II has been linked to the rapid competitive crystallisation of form I, since in solution the presence of form I results in the rapid conversion of form II to form I.[43] Barthe and Grover studied the solution-mediated transformation of form II to form I PCM in ethanol:methanol (95:5 v/v) solution, using Focussed Beam Reflectance Measurements (FBRM).[48] The authors reported a rapid transformation over a period of minutes, with an observed complete conversion taking place over *ca.*1 hour.[48] In 2007, Deij *et al.* presented a study on a growth probability method for predicting homogeneous

nucleation rates for three widely-studied polymorphic organic compounds, including PCM.[49] The authors reported that PCM disobeyed Ostwald's rule, *i.e.*, the stable polymorph was formed directly in favour of the metastable polymorph. These findings corroborate that PCM form II has a substantially higher nucleation barrier than form I and as a consequence, will not be formed easily.[49] More recently, Agnew *et al.* demonstrated a multicomponent templating approach to produce 100% PCM form II, with the addition of 10–40% w/w metacetamol (MCM).[50, 51] In 2020, Liu *et al.* further investigated this approach by studying the growth rates of PCM in the presence of MCM, concluding that MCM inhibits the nucleation of PCM form I through various strong non-crystallographic adsorption geometries, whilst not impacting form II.[46] Thus, stable quantities of form II PCM can be produced by the inhbition of form I. Although, the final product purity is another critical aspect of industrial crystallisation process development and the promoted incorporation of an additive or impurity (such as MCM) may not be acceptable for commercial manufacture.

PCM form III has been reported as highly unstable in air and the crystal structure of this polymorph was solved using high quality laboratory X-ray Powder Diffraction (XRPD) data by Perrin *et al.* in 2009.[52] The first air-stable formulations of PCM form III were reported by Telford *et al.* in 2016.[53] Forms I and II are the PCM polymorphs of interest for the solution crystallisation work carried out in this thesis. Whilst under ambient conditions, PCM form II is thermodynamically less stable than form I, form II has a higher density and according to the Le Chatelier principle it should therefore, be more stable at high pressure.[54] In 2005, Espeau *et al.* reported that PCM form II is the thermodynamically preferable phase at high pressure, from the construction of topological pressure-temperature and temperature-volume phase diagrams.[55]

Diamond Anvil Cell (DAC) technology provides a high pressure environment, in which PCM solid-state transitions or crystallisation from solution have been reported, together with the use of X-ray Diffraction (XRD) and/or Raman spectroscopy for structural characterisation.[56-59] In 2002, Boldyreva *et al.* reported that when a powder sample of PCM form I was pressure cycled slightly beyond 4 GPa, a partial transformation of form

I into form II was observed.[56] However, these experiments were described as being kinetically hindered and poorly reproducible.[56] In 2014, Smith *et al.* reported that transitions between a powder sample of form I to II begin at 4.8 GPa, persist until ~6.5 GPa and at ~8.5 GPa, form II was generated. [58] The authors also provided evidence for the existence of forms IV and V at pressures ~8 GPa and ~11 GPa, (persisting until ~21 GPa), respectively.[58] Rather than high pressure solid-state transitions, Oswald *et al.* reported high pressure crystallisation of PCM form II from acetone, dioxane and water solutions by exploiting the (typical) decrease in solute solubility under high pressure.[57] Experiments that were performed in a DAC (~0.4 GPa), yielded single crystals that were all subsequently identified by XRD to be form II.[57]

In 2019, Ward and Oswald reported high pressure PCM crystallisation *via* anti-solvent addition, using water as the anti-solvent and an aqueous solution of methanol as the solvent system.[59] An initial screening of the process was carried out in a DAC (0.8 GPa), where microscopic monitoring was performed to study the process. However, since the dimensions of a typical DAC (~ 200 μm diameter) severely limits the sample volume of study, a Large Volume Press (LVP) was employed for further experiments, in which a maximum pressure of 0.8 GPa was possible. Since the LVP is entirely enclosed, monitoring of the high-pressure nucleation was not possible and structural characterisation was performed following decompression to ambient conditions.[59] An important observation made in this study was solution-mediated transformation of form II (the preferentially nucleated form under high pressure) to form I, during decompression. On lowering the pressure, the solubility increases and thus, crystallised material can re-dissolve (depending on the saturation status of the solution) and at low pressure, form I is more stable and will be preferentially crystallised. A fast isolation procedure (~ 10 minutes) following decompression was performed, which prevented further solution-mediated transformation.[59] From XRPD analysis of recovered powder samples, mixtures of form I and II were reported.[59]

1.1.5. Growth

Crystal growth rates are influenced by process conditions such as the supersaturation, temperature, pressure, mixing conditions and the presence of additives or impurities.[2] A schematic of adsorption sites of growth units on the face of a bulk crystal has been reproduced in Fig. 1-8.

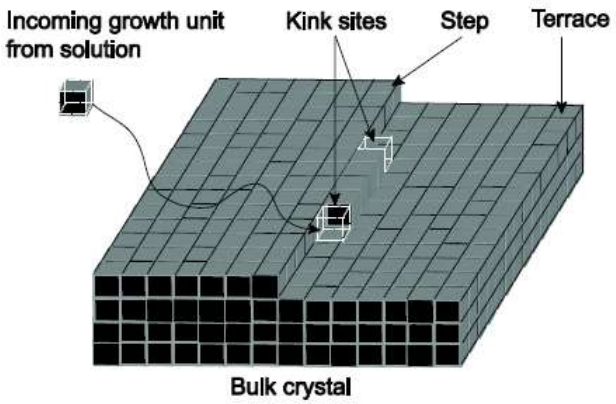

Figure 1-8 Schematic of adsorption sites of growth units at kink, step, and terrace locations on the face of a bulk crystal (reproduced from Lee et al.[60])

Lovette *et al.*[61] summarised the processes that are thought to occur in series, during the growth of a crystal face from solution:

(1) Solute molecules are transported from the bulk solution towards the face by convection and diffusion

(2) Solute molecules and kink sites shed their surrounding solvent molecules (desolvate) and solute molecules are incorporated into kink sites

(3) The latent heat of crystallisation is released and transported to the crystal and solution

The growth rate of a crystal face is limited by the slowest of these processes.[62, 63] The process of solution growth for organic molecular crystals, such as PCM typically involves sequential adsorption at the terrace and then the step, before entering the kink site.[64]

On an industrial scale, crystallisation predominantly remains a molecular-level process.[34] Purification occurs *via* molecular recognition, whereby impurities can be rejected due to the energetically less favourable fit of most impurity molecules into the lattice of the target molecule.[7] The rejection of the impurities requires the replacement of an impurity molecule by a target molecule, the latter being more strongly bound.

Aside from the processes at the interface of a bulk crystal, transport phenomena in the bulk of the mother phase also greatly influence growth and hence the purification process. Crystal growth from solution is limited by mass transfer, which requires a certain concentration gradient (supersaturation).[7] The relative growth rate of the crystal faces determines the final crystal morphology. The main reason that morphologies change with supersaturation is because certain families of faces enter different growth regimes, so increasing the supersaturation can accelerate growth rates and result in morphological changes such as faces growing out, extending aspect ratio *etc.*[65] In the context of purification, fast growth conditions will inevitably lead to a kinetic incorporation of some impurity molecules, since the opportunity for impurity desorption and replacement of target molecules decreases.[66] During growth, mixing significantly affects the mass transfer rate of both the solute target molecules to the growing crystal surface and the impurity molecules away from the crystal surface into the bulk solution.[7] By increasing the mixing intensity, the mass transfer rate increases and the thickness of the interfacial diffusion boundary layer between the growing crystal surface and the bulk solution decreases.[7]

The presence of additives and impurities have been widely reported to influence crystal growth rates and crystal morphologies.[67-70] Impurities are incorporated *via* adsorption into the crystal lattice or onto the crystal surface and also *via* mother liquor inclusion in the crystals.[7] Incorporated impurity molecules may block or inhibit the growth of the face.[66] On the contrary, additives are employed to promote crystal growth rates.[71] PCM structurally similar impurities of interest in this work are acetanilide (ACE) and MCM. The corresponding molecular structures are presented in Fig. 1-9. MCM and PCM are regioisomers, whilst ACE lacks the hydroxyl group positioned para-/meta- relative to the amide group.

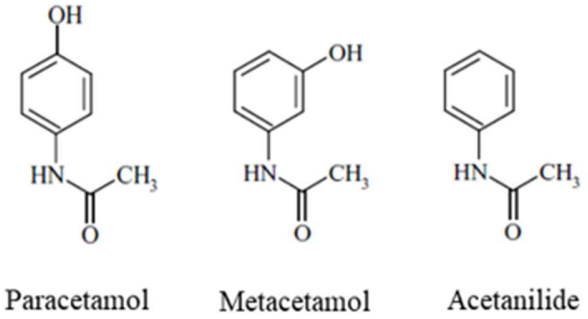

Figure 1-9 Molecular structures of paracetamol, metacetamol and acetanilide

Hendriksen *et al.* studied the effects of structurally similar impurities on the crystallisation of PCM.[72] The authors reported that, to varying degrees both ACE and MCM: (a) block adsorption of PCM molecules (therefore inducing morphological changes), (b) dock onto the surface and become incorporated into the crystal lattice and (c) disrupt the emerging nucleus and thus inhibit the nucleation process. The stronger blocking ability of ACE, compared to MCM was attributed to the lack of hydroxyl groups (proton donor) in ACE to contribute to the existing hydrogen bonding network in PCM, which blocks further addition of PCM molecules.[72] The authors also reported that the aspect ratios of PCM crystals were extended when grown in aqueous solution by a cooling method, with increasing quantities (mol %) of impurity added. This extension was more severe in the case of MCM and by calculation of segregation coefficients, it was determined that uptake levels of MCM were appreciably higher in the grown PCM crystals than in the case of crystals grown in the presence of ACE.[72]

Thompson *et al.* also grew PCM crystals in the presence of ACE and MCM in aqueous solutions by a cooling method.[68] The authors reported that the characteristic morphology of monoclinic PCM crystals was only moderately altered by the presence of ACE, but in the presence of MCM, PCM crystals adopted a more columnar shape (with a higher aspect ratio).[68] Scanning Electron Microscopy images of typical PCM crystals obtained from this study are reproduced in Fig. 1-10.

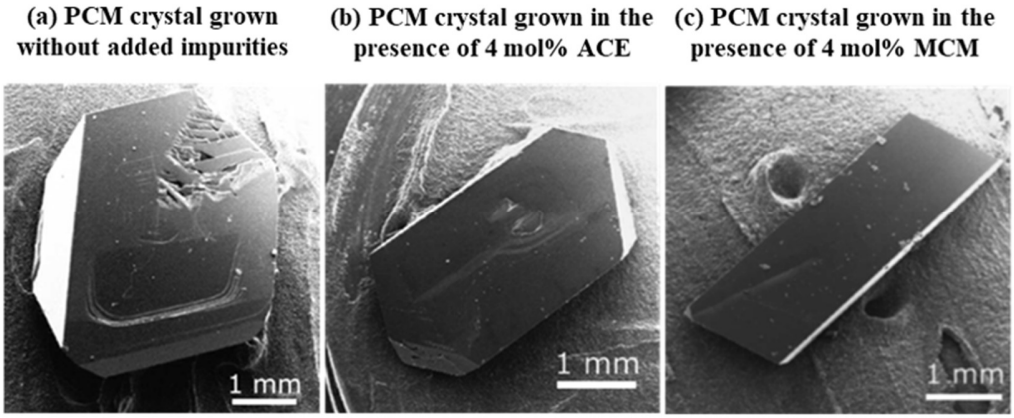

Figure 1-10 Paracetamol crystals grown (a) without added impurities, (b) in the presence of 4 mol% acetanilide and (c) in the presence of 4 mol% metacetamol (reproduced from Thompson et al.[68])

The uptake levels of ACE/MCM in the resulting PCM crystals were not reported, but from the previous study by Hendriksen *et al.*[72] it is expected that the uptake of MCM in PCM crystals grown with this impurity would be higher than in the case of ACE.

In 2020, Urwin *et al.* provided a workflow for the management of impurities during industrial crystallisation process development.[73] Amongst the case studies presented was PCM crystallised in the presence of MCM and ACE. The workflow involved a series of general experiments using standard laboratory instrumentation through which, discrimination between impurity incorporation mechanisms was achievable. The authors determined that adhesion of ACE to the surface of PCM as the incorporation mechanism. Whereas it was reported that MCM is incorporated into PCM during growth through partial miscibility and therefore it was concluded that it will be very difficult to remove MCM through a single cooling crystallisation.

It is important to note that crystal growth is also influenced by the crystallisation solvent, as demonstrated by Saleemi *et al.* in a study of PCM crystallisation in the presence of (1-4 mol %) MCM in both isopropyl alcohol and water.[74] The presence of MCM resulted in a distinct morphological change of pure PCM from the characteristic tabular habit to a columnar habit, which is consistent with aforementioned reports.[68, 72] The average size of

the PCM crystals was reportedly affected by combined solvent and impurity effects.[74] In the presence of 4 mol% MCM, the PCM crystals obtained from water were observed to show a more pronounced morphological change and they were also significantly larger than crystals obtained from isopropyl alcohol.[74] In a study of predicted morphologies of PCM form I in 30 solvents, of various classes, Li and Doherty predicted that lower solvent dispersive energies correspond to PCM crystals with lower aspect ratios grown from hydrogen bond accepting solvents.[75] Higher aspect ratios of PCM crystals corresponded to higher solvent dispersive energies of chlorocarbon, hydrocarbon and water solvents.[75] This is consistent with the more pronounced morphological changes (extended aspect ratio) of PCM crystallised in the presence of MCM in water compared to isopropyl alcohol observed by Saleemi *et al.*[74]

The topic of crystal growth is substantially more mechanistically complex than the current overview has presented. A recent textbook, edited by Roberts, Docherty and Tamura provides a more comprehensive discussion on this topic, along with current research focuses.[76]

1.2. Acoustic Cavitation

Cavitation corresponds to the formation, growth and collapse of bubbles in a liquid, as outlined in Fig. 1-11. The effects of cavitation phenomena can be advantageous or detrimental, depending on the occurrence. Cavitation can cause severe erosion damage of ship propellers and hydraulic machinery, which led to vast research efforts into avoiding these undesired effects in the 1950s.[77-79] Cavitation has been utilised in medical research and recently it has been demonstrated to selectively destroy cancer cells.[80] Furthermore, chemists have used cavitation to drive chemical reactions such as heterogeneous catalysis, where reactivity increases of close to a million fold have been reported.[81] The collapse of a cavity in solution releases a significant amount of energy within a localised volume, which has been identified as being highly valuable for application to chemical process intensification.[82]

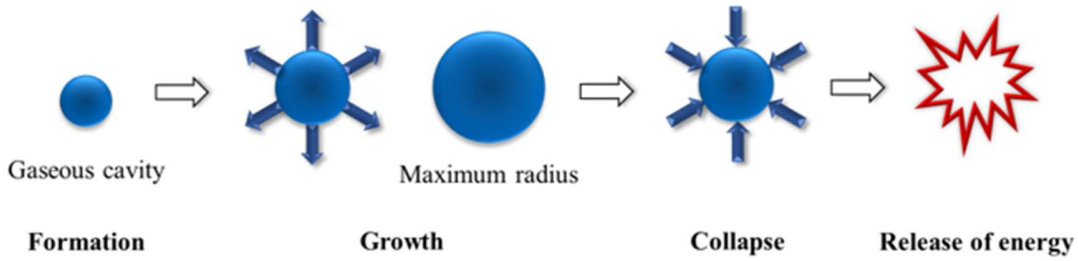

Figure 1-11 Schematic of cavitation phenomena (adapted from Holkar et al.[82])

Principally, cavitation can be generated *via* pressure variation or energy deposition. Lauterborn further classified cavitation into four types[83]:

1. **Hydrodynamic Cavitation**: Produced by pressure variation obtained using the geometry of the system *e.g.* high-speed water flow
2. **Acoustic Cavitation**: Produced by pressure variation when ultrasound is propagated through a liquid.
3. **Optical Cavitation**: Produced by photons of a high intensity laser rupturing a liquid.
4. **Particle Cavitation**: Produced by an elementary particle beam rupturing a liquid.

Acoustic cavitation is the predominant mode of cavitation generation investigated in this thesis, which is outlined herein, culminating with an overview of cavitation detection methods. The topic of optical cavitation will be addressed in Section 2.2.2.

1.2.1. High-Power Ultrasound Field Generation

Sound waves with an oscillating frequency above 20 kHz are defined as ultrasonic.[84] Aside from acoustic cavitation, acoustic streaming is also a consequence of ultrasound being propagated through a liquid. Streaming creates a steady flow, which generates a jet of fluid in the acoustic field.[85] Depending on the application, the frequency region of ultrasound can broadly be divided into two categories: power ultrasound (20 kHz – 5 MHz) and diagnostics (5 MHz – 20 MHz). The diagnostic frequency range is above the frequency limit at which acoustic cavitation is generated.[86] Within power ultrasound, the sub-category of high-power ultrasound (20 kHz – 100 kHz) is where the highest energy intensities from acoustic cavitation are observed, which is most suitable for intensifying chemical processes.[87] These high-energy effects can be explained by bubble size as a function of the resonance frequency (f_r). 1933, Minnaert presented his theory on the resonance frequency of bubbles from the sounds produced by bubbles in water.[88] Equation 1-3 displays an approximation for f_r, which is inversely related to the equilibrium radius (R_0) of a bubble.

$$f_r \approx 3/R_0 \tag{1-3}$$

At low ultrasonic frequencies and therefore longer pressure cycles, bubbles can grow larger, which accordingly leads to larger collapse intensities.[89] On a laboratory scale, high-power ultrasound fields can be generated using equipment designed for high shear mixing, degassing or cleaning, with an ultrasonic horn or bath (generally operated at frequencies between 20-40 kHz). Ultrasound is produced *via* a transducer, which typically comprises of piezoelectric material that converts the high frequency electronic excitation into mechanical vibration, resulting in sound waves propagating into media bounding the piezoelectric element (including any load medium). In order to highlight the difference in

the spatial distribution of maximum acoustic pressure (red) generated in an ultrasonic bath and an ultrasonic horn, qualitatively, simulated acoustic pressure field distributions have been reproduced in Fig. 1-12. Water is the medium in both cases.

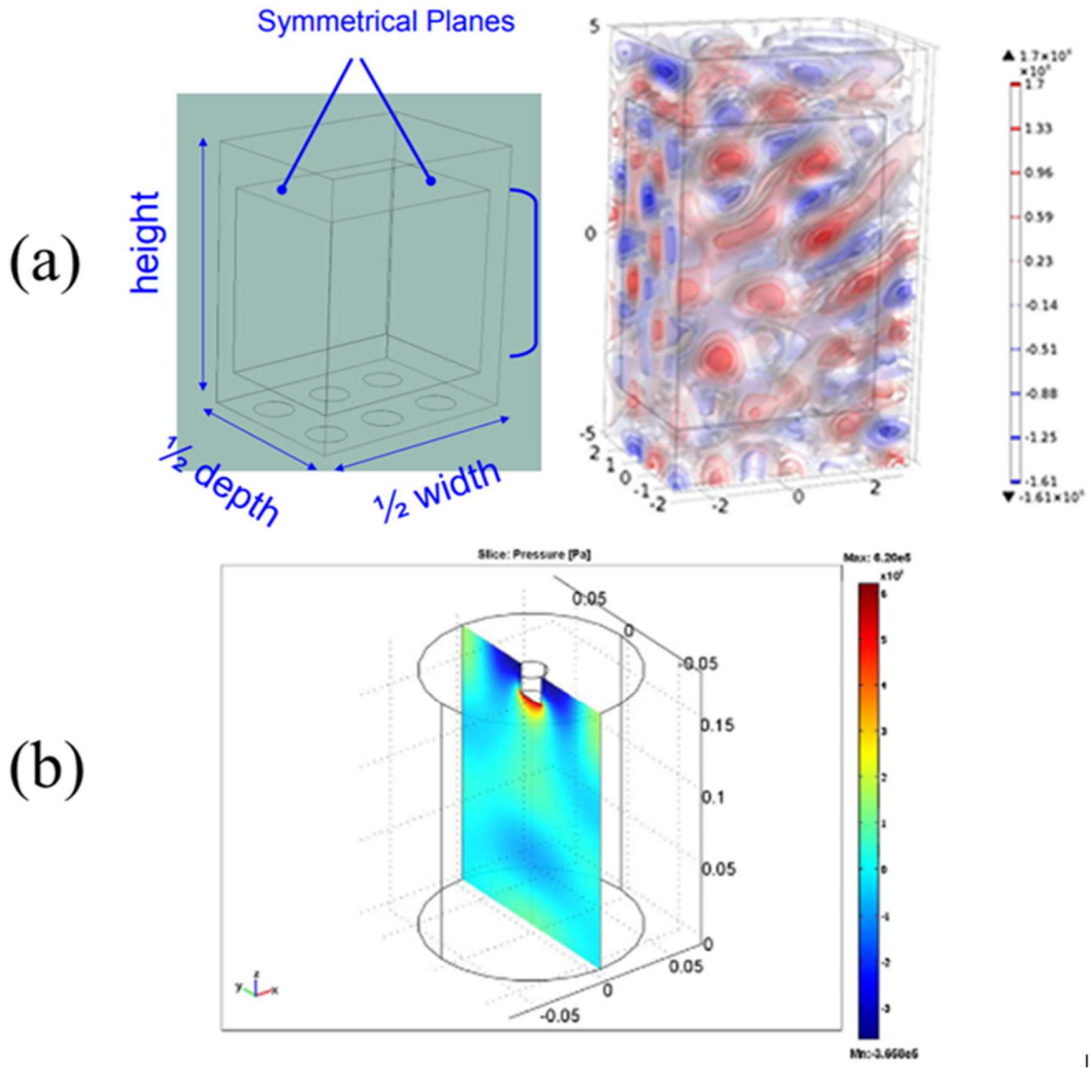

Figure 1-12 Simulated acoustic pressure field distribution in (a) a 40 kHz ultrasonic bath (reproduced from Zhong[90]) and (b) the central plane of a 20 kHz ultrasonic horn immersed into a reactor (reproduced from Sutkar et al.[91])

Ultrasonic horns generate intense bulk fluid shear and heating in addition to cavitation, which is delivered over an active zone localised near the horn tip, as shown in Fig. 1-12

(b).[92, 93] This predominantly generates a spatially decaying travelling wave, with a high density of bubble cloud gathered at the probe tip.[94] The ultrasonic horn is in direct contact with the liquid medium and erosion of the probe tip over long periods of use have been observed.[95] A typical ultrasonic bath comprises a multi-transducer arrangement bonded to the metal walls of the tank and a six-transducer arrangement was simulated in Fig.1.12 (a). A standing wave is generated due to reflections at the bath wall and liquid surface. Although, in reality a mixture of travelling and standing waves are produced, due to considerable sound attenuation and resulting interference from the arrangement of the transducers.[84]An indirect and non-uniform sound field is delivered to the liquid medium.[96]

In a continuously driven sound field, the intensity of ultrasound is attenuated by the molecules of the liquid and due to viscous interactions, a proportion of the mechanical energy of the wave is converted to heat.[97] Attenuation of the sound wave can also arise as result of reflection, refraction, diffraction or scattering of the wave. The intensity (I) of the ultrasound at a distance (d) from the ultrasound source is given by:[97]

$$I = I_0 \exp(-\alpha d) \tag{1-4}$$

Where I_0 is the intensity at the tip of the source and α is the attenuation coefficient, which is obtained from:

$$\alpha = 8\mu\pi^2 f^2 \,/\, 3\rho C^3 \tag{1-5}$$

Where ρ is the liquid density, μ is the liquid viscosity, f is the driving frequency and c is the speed of sound in the liquid, which can be obtained from the Newton-Laplace equation:

$$c = (K/\rho)^{1/2} \tag{1-6}$$

Where K is the elastic bulk modulus of the liquid.

1.2.2. Bubbles under an Applied Ultrasound Field

In 1917, Lord Rayleigh proposed a model to describe the collapse of a spherical cavity.[98] The equations presented are still applicable today, in the context of a freely collapsing

bubble. The Rayleigh collapse time (T_c) of a bubble of maximum radius (R_{max}) is expressed as:[99]

$$T_c \approx 0.915 \cdot R_{max} \sqrt{\rho_0 / P_0} \quad (1\text{-}7)$$

Where ρ_0 is the liquid density and P_0 is the ambient pressure. Plesset expanded upon this work in 1949 to include an acoustical driving term, forming the basis of the Rayleigh-Plesset equation to describe the oscillation of an acoustically driven bubble.[100] Many authors have built upon this over the past century and equation 1-8 is a generalised version:

$$p_g(R,t) = \rho \left\{ R\ddot{R} + \frac{3}{2}\dot{R}^2 \right\} + p_\infty + \frac{2\gamma_\infty}{R} + \left(1 - \frac{\delta_T}{R}\right) + \frac{4\eta_\infty \dot{R}}{R} \left(1 + \frac{\delta_{vis}}{R}\right)^{-1} \quad (1\text{-}8)$$

Where $\dot{R}$and $\ddot{R}$ represent the first and second order time derivatives of the bubble radius, respectively. $p_g(R,t)$ is the pressure in the bubble, p_∞ is the pressure in the liquid at a large distance from the bubble, and ρ is the liquid mass density. The first part of this equation was originally derived by Lord Rayleigh (1917) and Plesset (1949).[98, 100] Then, the surface tension constant of the bubble, γ_∞ was added by Noltingk and Neppiras (1950-51).[101, 102] The coefficient of the viscosity of the bulk liquid, η_∞ was introduced by Poritsky (1952).[103] The first order curvature corrections in the surface tension and viscosity were later added by Dzubiella via the empirical coefficients, δ_T and δ_{vis} (2006-07).[104, 105] Man *et al.* recently noted that whilst the Rayleigh-Plesset equation provides a description of the dynamics of bubbles from a macroscopic point of view, it is unclear whether it is applicable to describe dynamics of microscale or nanoscale bubbles.[106]

The threshold pressure required for acoustic cavitation is considerably below the tensile strength of a given liquid. Under an applied acoustic field, existing gas nuclei present in the liquid are "activated", according to Leighton.[107,108] These bubble nuclei oscillate and can grow during cycles of compression and rarefaction (positive and negative pressure). Bubbles may dissolve if the applied pressure is below the threshold value. At above a threshold pressure, bubbles can expand to reach a critical size, at which they become unstable and undergo inertial collapse, followed by fragmentation and the creation of new

cavitation nuclei. A summary of the potential processes that bubbles can undergo in an acoustic field has been reproduced in Fig. 1-13.

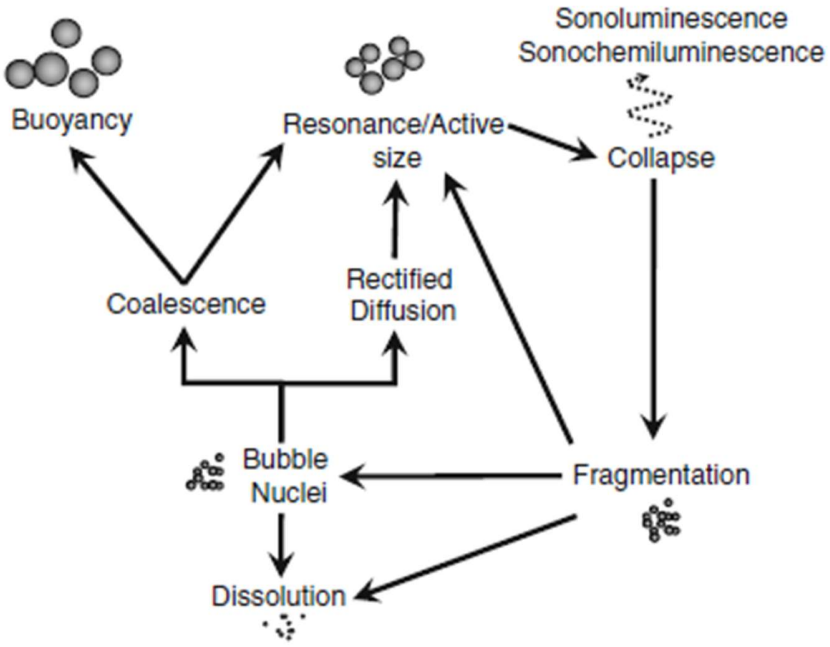

Figure 1-13 Processes associated with bubbles in an acoustic field (reproduced from Lee[109])

Inertial bubble collapse has been reported to simultaneously generate highly localised extremes of temperature and pressure, alongside liquid jets, shockwaves, microstreaming, sonoluminescence and the production of free radicals.[95] Due to rapid bubble collapse, energy is released that does not have time to be transferred to the surroundings and therefore, local "hot spots" are said to be produced.[81, 110] The first proposal of these "hot spots" for application in driving chemical reactions was made by Noltingk and Neppiras, in 1950.[101] Suslick has since reported temperatures of ca. 5000 °C and pressures of ca. 100 MPa and cooling rates above 10^{10} K s^{-1} immediately following bubble implosion.[111] Inertial cavitation is responsible for the formation of large shockwaves, defined as the propagation of a discontinuity in pressure, in a medium.[84] Shockwaves generated from bubble collapse have been reported to have velocities as high as 4000 ms^{-1} and high pressure amplitudes of 10^6 kPa.[112] The generation of flow formed by the oscillations of

microbubbles in a continuously driven pressure field has been termed microstreaming.[113] These oscillations are transferred *via* the boundary layer surrounding the bubble, generating convective motion in the liquid.[114]

Transient and stable cavitation are the two types of inertial cavitation. Transient bubbles are predominantly generated at lower frequencies; these are short lived and typically collapse in less than one acoustic cycle.[115] Stable bubbles, however undergo repetitive inertial collapse.[116] The processes of rectified diffusion and bubble—bubble coalescence have been reported to control bubble growth and hence the cavitation activity.[117] In bubble-bubble coalescence, smaller bubbles coalesce to produce a larger bubble, which takes a much shorter time to reach the resonance size compared to rectified diffusion.[117] Coalescence increases the bubble size, and these larger bubbles can become buoyant when they reach a size above resonance range, above which they are no longer influenced by the acoustic field (as described in Fig. 1-13).[118]

Rectified diffusion refers to the growth of a cavitation bubble due to uneven mass transport across the bubble wall over many cycles of rarefaction and compression. [119] During the rarefaction phase, gases and volatile solvent molecules diffuse into the bubble and material from inside the bubble diffuses out during the compression phase. Crum has also suggested a shell effect, considering a liquid shell next to the bubble wall.[119] As the bubble shrinks, this shell increases in thickness and lowers the gas concentration within the shell, hence decreasing the gas concentration gradient. The shell compresses during bubble expansion, which causes the gas concentration within the shell to become higher than that at the bubble interface. With the shell thickness at a minimum, a steeper concentration gradient increases the mass transfer rate of the gas into the bubble.[117] Furthermore, these gas molecules absorb energy upon collapse and cushion the implosion.[116] Therefore, stable bubble implosion produces lower thermal and mechanical effects. In contrast, transient bubbles expand very rapidly to at least double their initial size. During this short time frame, the dissolved gasses have insufficient time to cross the bubble-liquid interface and do not accumulate inside the bubble.[120] Simulated phenomena associated with stable and transient cavitation has been reproduced in Fig. 1-14.

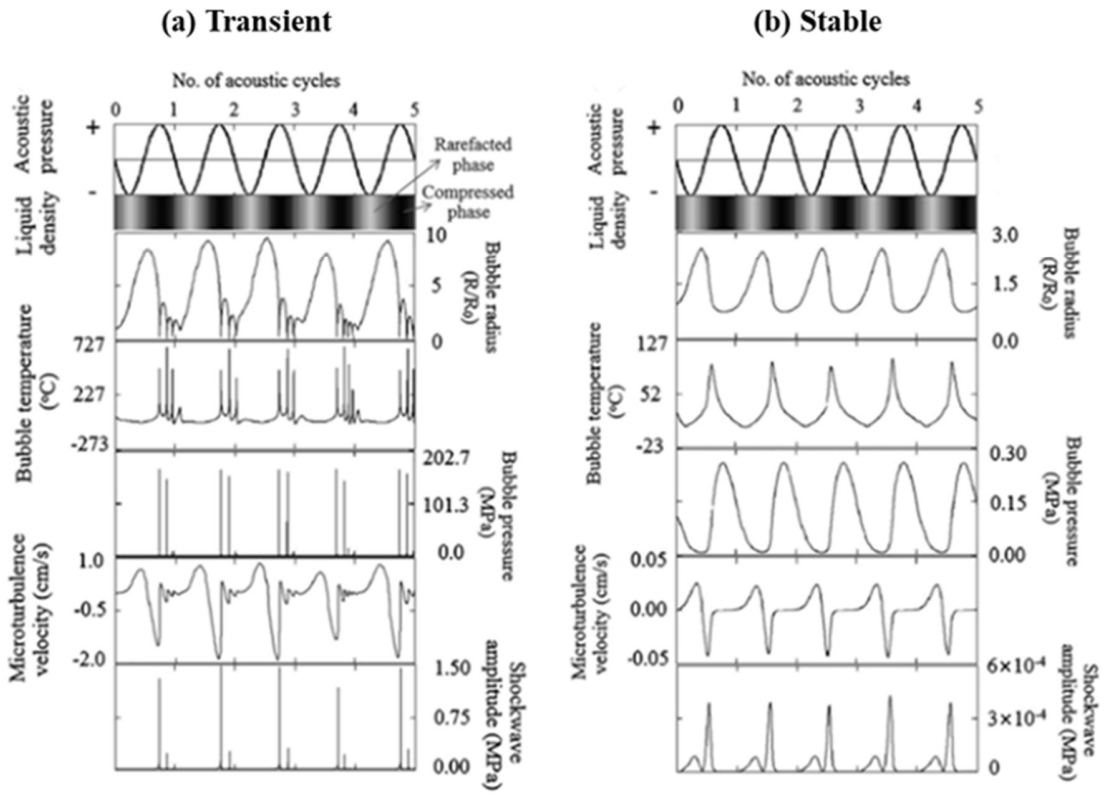

Figure 1-14 Simulated cavitation phenomena for (a) transient and (b) stable cavitation (reproduced from Parkar et al.[121])

The minimum conditions for acoustic cavitation depend on the liquid properties, initial bubble size, acoustic pressure and frequency.[107] These factors are described in expressions such as the Blake threshold and inertial limit, as defined by Flynn[122, 123] and Apfel.[124, 125] These expressions can be used to show that threshold pressures for cavitation generation can be more easily overcome at lower frequency and higher initial bubble size.

Simulated zones of stable cavitation, transient cavitation and bubble dissolution in water and at a driving frequency of 20 kHz, carried out by Horst *et al.*[126] are shown in Fig. 1-15.

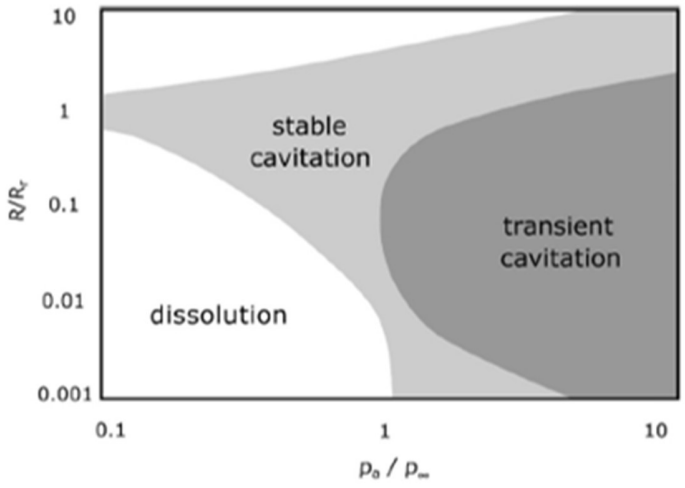

Figure 1-15 Simulated regions of stable cavitation, transient cavitation and dissolving bubbles at 20 kHz as a function of bubble size and acoustic pressure (reproduced from Horst et al.[126]). *The acoustic pressure (P_a) is normalised by the bulk pressure (P_∞) of 1 bar. The bubble radius (R) is normalised by the resonant radius (R_r) of 150μm.*

From the simulated data, it may be concluded that at the same (high-power ultrasound) driving frequency, transient cavitation is dominant at higher driving pressures, but at resonance size ($R \approx R_r$), stable bubbles are predominantly generated.[126] At below the threshold size and pressure, bubbles will dissolve.[126] In the case of high-power ultrasound fields, Ashokkumar *et al.* have reported that there will always be a combination of stable and transient bubbles present, but one type will be more prevalent.[127] Ashokkumar *et al.* further suggested that travelling waves promote bubble shape distortion, resulting in asymmetrical bubbles and thus, more transient behaviour.[116] The authors also proposed that standing waves promote the existence of stable bubbles as they do not create the bubble shape distortion associated with transient cavitation.[116]

In multi-bubble fields, the spatial distribution of bubbles is not homogeneous. Primary Bjerknes forces (acoustic radiation forces generated within the sound field) and secondary Bjerknes forces (attractive and repulsive forces between oscillating bubbles) are often dominant phenomena, which can lead to bubble ensemble structures.[128] It was initially Blake who noted that cavitation bubbles can form streamers in which the microbubbles

appear as long, twisting streams.[129] In this case, primary Bjerknes forces drive the bubbles towards a region of high acoustic pressure in the sound field and they can also form junctions due to attractive secondary Bjerknes forces. Examples of structures, such as a bubble cluster and streamers are shown in Fig. 1-16.

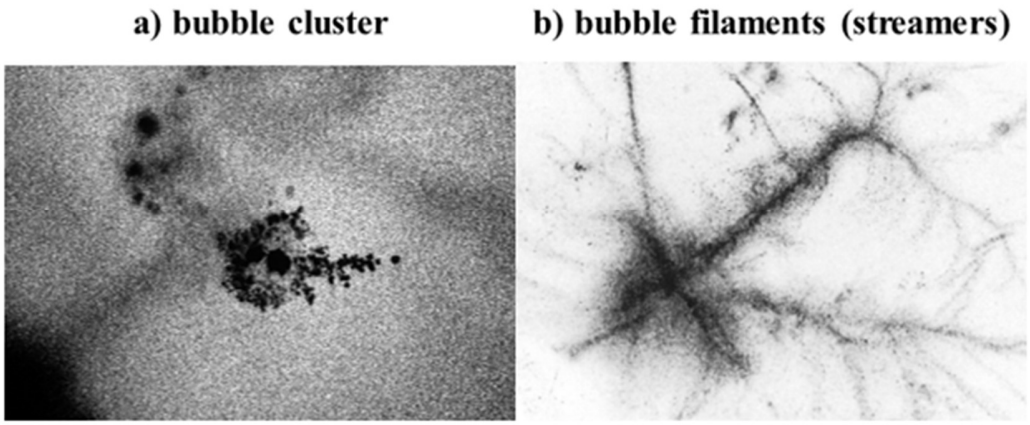

Figure 1-16 Bubble ensemble structures (reproduced from Lauterborn and Mettin[128])

These structures are not static, with coalescence and fragmentation of bubbles repeatedly occurring in an acoustic field.[130] Moreover, Mørch studied the bubble dynamics of clusters and reported that these structures can collapse in such a cooperative manner that they develop cavitation jet velocities and shockwave intensities much in excess of individual bubbles.[131] This concerted collapse starts at the boundary of a bubble cloud and proceeds until collapse of bubbles at the cloud centre occurs. As a result, shockwaves from multiple bubbles converge together and form a single shockwave with a much higher shockwave intensity (several hundreds of kPa) than the collapse of multiple single bubbles.[132] Both primary and secondary Bjerknes forces are influenced by the bubble separation distance, bubble size, driving frequency and acoustic pressure.[133]

A multi-bubble field is a highly complex and dynamic system. The spatial distribution of bubbles is inhomogeneous and temporally changing with the movement, fragmentation, and coalescence of bubbles.[134] The physical phenomena connected with bubble collapse *i.e.* acoustic and light emission, provide opportunities for measurement.

1.2.3. Cavitation Detection

Sonoluminescence (SL) is the light emission phenomenon from collapsing cavitation bubbles.[135] Both Yasui *et al.* and Lauterborn *et al.* have discussed the state of knowledge on the underlying mechanisms of SL, which is beyond the scope of this thesis.[136, 137] In essence, single-bubble sonoluminescence (SBSL) refers to SL from a stable oscillating bubble trapped at the antinode of a standing wave.[138] SBSL was first reported by Gaitan and Crum in 1990 and towards the end of the decade, the pulse width of the light was experimentally determined to range from 40–350 ps.[139-141] SL from a cloud of cavitating bubbles is termed multi-bubble sonoluminescence (MBSL) and the first reports of MBSL were in the mid-1930s.[142, 143] In MBSL, irrespective of standing or travelling waves, transient species formed during the collapse of bubbles emit light, which is proportional to the energy intensity of the collapse.[144] Images of sonoluminescing bubbles have been reproduced in Fig. 1-17.

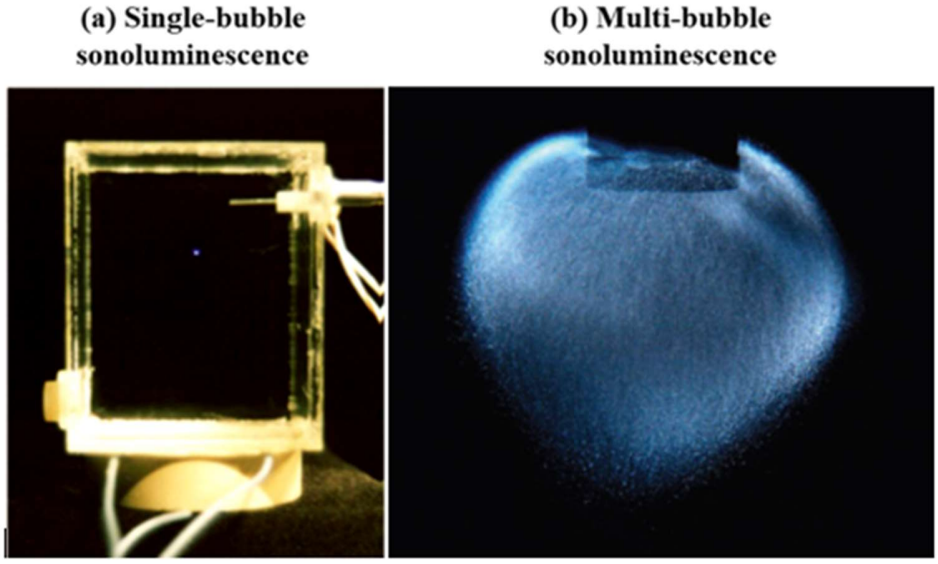

Figure 1-17 Images of sonoluminescing bubbles. *In (a) a long-term exposure photograph of a single sonoluminescing bubble in water, trapped in a standing wave at 25 kHz (reproduced from Geisler[145]). In (b) a true colour photograph of a cloud of sonoluminescing bubbles in xenon gas-saturated sulphuric acid, generated by an ultrasonic horn at 20 kHz (reproduced from Suslick and Flannigan[146])*

Acoustic pressure is the predominant detection technique employed throughout this thesis, which is discussed herein. Hydrophones produce an electrical response to an acoustic field. This instrument is constructed with an active element, usually made from a piezo-polymer such as polyvinylidene fluoride (PVDF). When a hydrophone is placed within an acoustic field, it will produce a voltage signal in response to the surface integral of the acoustic pressure received over its active element. The needle hydrophone tip employed throughout this thesis is shown in Fig. 1-18, which exhibits high sensitivity, a wide bandwidth (100 MHz) and it is suitable for both high and low frequency fields. It was calibrated over the range 20 kHz-20 MHz by the National Physical Laboratory (NPL) in May 2019 (Certificate Reference: 2018100442-3).

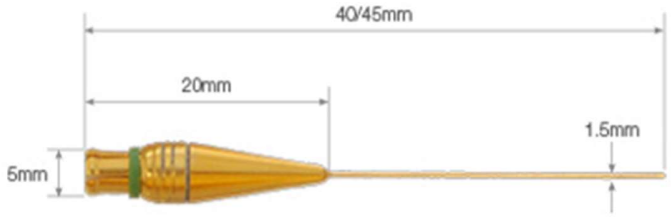

Figure 1-18 Dimensions of the needle hydrophone tip constructed with a 1.0 mm diameter PVDF active element disc (reproduced from Precision Acoustics[147])

Most acoustic measurements require the maximum value of the acoustic pressure field to be located.[147] Acoustic output parameters are obtained from a waveform of acoustic pressure and recommendations for characterisation from this have been published by the International Electrotechnical Commission.[148] The acoustic pressure (P) can be obtained from the raw output voltage of the hydrophone (V) and the sensitivity of the hydrophone as a function of frequency ($M_{(f)}$):

$$P = \frac{V}{M_{(f)}} \tag{1.9}$$

Time-domain signals are not immediately informative however, these waveforms can be decomposed into sum of sine waves of different frequencies *via* Fourier Transform.[149]

Whilst time-domain data describes signal changes over time, frequency-domain data shows how the signal's energy is distributed over a range of frequencies. The Fast Fourier Transform (FFT) is the digital equivalent of a Fourier Transform, which can be executed with the FFT function using the signal processing package in MATLAB®. An example of an acoustic emission spectrum obtained from FFT is provided in Fig. 1-19.

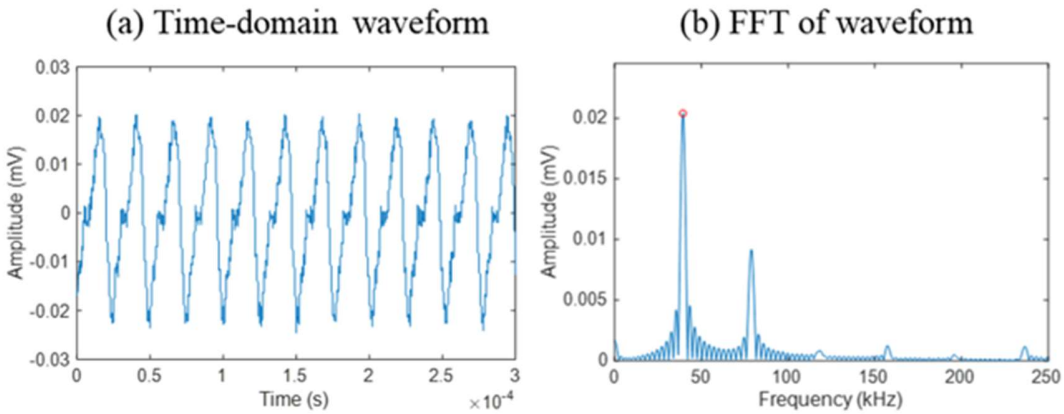

Figure 1-19 Example Fast Fourier Transformation of a time-domain waveform measured in water at 40 kHz, which is marked by the red circle in (b).

Cavitation bubbles act as secondary acoustic sources and the emission spectra contain information about the type of bubble collapse.[150] Since Esche published his seminal work on acoustic emissions from cavitating bubbles in 1952, numerous studies involving acoustic detection of cavitation in water have been reported.[151-156] In order to aid discussion on the typical features of acoustic emission spectra obtained from FFT of hydrophone signals measured in an acoustic cavitation field, an example from Lauterborn and Mettin has been has been reproduced in Fig. 1-20.[128]

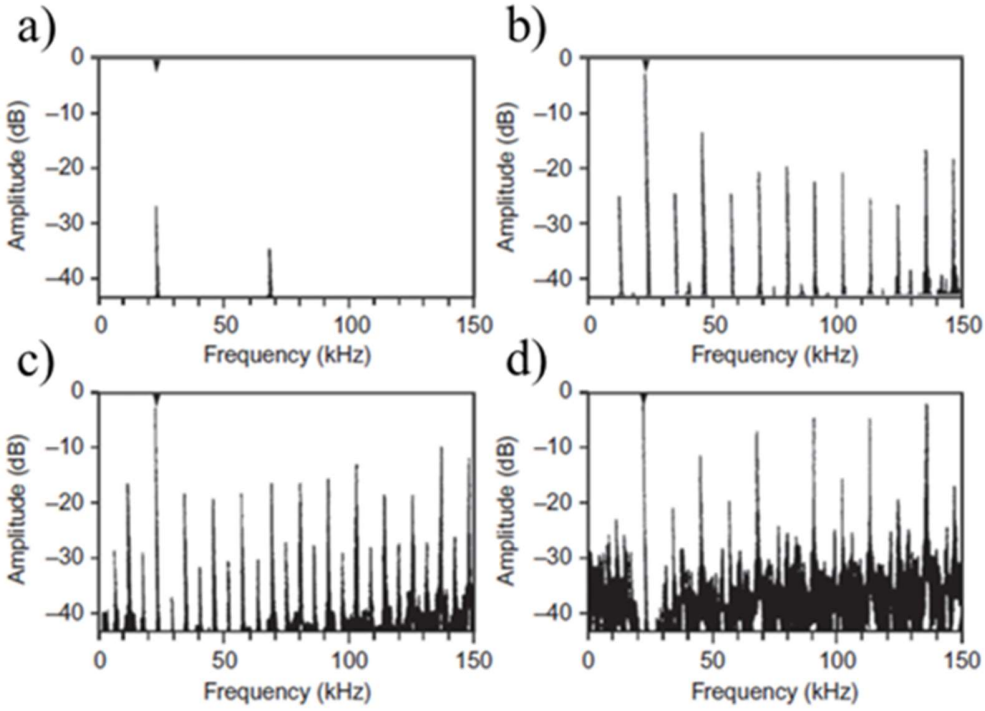

Figure 1-190 Acoustic emission spectra where the drive power (unspecified) at 23 kHz in water is increased from (a) to (d) (reproduced from Lauterborn and Mettin[128]).

The acoustic spectrum displays lines corresponding to:

1. The fundamental frequency (f_0) (marked by the triangle at 23 kHz in all spectra shown in Fig. 1.20), overharmonics (nf_0, where n is an integer) and ultraharmonics (kf_0/n where k is an integer $\neq n$); where pulsating stable bubbles contribute to an increase in f_0, nf_0 and kf_0/n with increasing drive power, together with further contributions from non-linear bubble dynamics
2. Subharmonics (f_0/n, where n is an integer) which arise due to the excitation of bubbles at sub-harmonic resonances and are visible in spectra (b) to (d) in Fig. 1.20
3. Broadband noise between the frequency lines and this is the signature of transient bubble implosion,[157] which is most prevalent in spectrum (d) in Fig. 1.20

According to Hodnett and co-workers from NPL, the broadband noise is proportional to both the number and energy on collapse of transient cavitation bubbles.[158, 159] In order to

separate the broadband noise from spectral lines corresponding to stable cavitation phenomena, the Broadband Integrated Voltage (BIV) is obtained by eliminating all fundamental, overharmonic, subharmonic and ultraharmonic frequencies from the acquired spectrum:

$$\mathrm{BIV} = \int_{fs}^{fe} [V_{\mathrm{S}}(f) - V_{\mathrm{N}}(f)]\, df \tag{1.10}$$

where $V_{\mathrm{S}}(f)$ represents the output voltage received from the hydrophone after these have been removed. $V_{\mathrm{N}}(f)$ represents the output voltage of the background noise. f_{s} represents the integration start frequency and f_{e} corresponds to the stop frequency. In place of eliminating the spectral lines prior to background removal and integration, some authors have focussed on the high frequency zone of the spectrum where no more harmonics appear (>1 MHz).[160-163] Recent work by Grosjean *et al.* and Nguyen *et al.* presented BIV determinations where the spectrum was integrated over the entire frequency range of the acoustic emission spectrum acquired, which is considered to be more rigorous than focussing on the high frequency zone of the spectrum.[164,165]

The work in this thesis involves hydrophone measurements in fields generated by high power ultrasound, as well as laser irradiation. Therefore, it is important to also discuss acoustic emission spectra obtained from the measurement of laser-nucleated bubbles. With regards to the acoustic emission spectrum obtained from hydrophone measurements in a laser-induced cavitation field, only spectral lines corresponding to broadband noise are observed, which can be integrated to give the BIV.

In the development of a reference facility involving both optical and acoustic fields for generating single cavitation bubbles and bubble clouds at NPL, Wang *et al.* compared acoustic emission spectra obtained from hydrophone measurements in water of acoustic cavitation and optical cavitation (selected data has been reproduced in Fig. 1.21).[159]

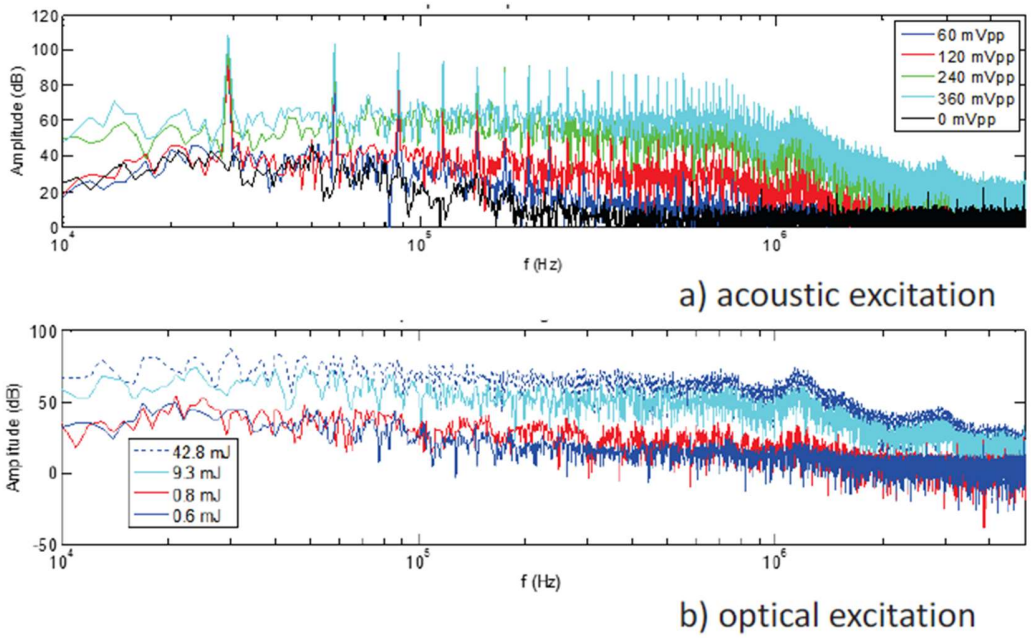

Figure 1-201 Comparison of acoustic emission spectra generated from hydrophone measurements of (a) 29 kHz ultrasound propagation in water (0–360 mV pp) and (b) 532 nm laser irradiation generation (0.6–42.8 mJ) in water (reproduced from Wang et al.[159])

The authors reported the threshold for bubble nucleation by optical excitation at above 1.6 ± 0.2 mJ (15 mm beam diameter) from high-speed imaging observations. The threshold for acoustic cavitation generation was reported as > 100 kPa, which was obtained at amplitudes > 160 mV pp drive (at 29 kHz).

Review: Initiating Crystallisation by Application of Sound and Light

With the global market for pharmaceuticals projected to reach $1.5 trillion by 2023,[166] industry experts have deemed it "essential" for continuous manufacturing to be implemented in order to meet the future demand for sustained access to quality medicines.[167] Continuous production can be described as a process with various steps in flow and it is characterised by the input of raw materials running concurrently with product removal. It has been established that the continuous crystallisation of drug substances can offer advantages such as precise process control, higher efficiency process operation and consistent product quality; compared with less agile batch production.[168-172]

Although continuous crystallisation is beyond the scope of this thesis, it is important to mention, since the potential application of external fields has been identified as particularly advantageous for initiating continuous crystallisation processes.[9] McGinty *et al.* recently noted that nucleation induction at lower supersaturation levels would be highly desirable for delaying the onset of encrustation in the crystalliser, together with the greater product purity associated with lower supersaturation growth conditions.[9] The application of external fields, such as laser irradiation and high-power ultrasound propagation have been demonstrated to induce crystal nucleation within the generated field.[173, 174] External fields provide an opportunity to manipulate process conditions on a local scale and the main benefit of application would be improved control over nucleation and elimination of the requirement for seeding. Other external fields that have been investigated for application in crystallisation include microwaves,[175, 176] electric[177, 178] and magnetic.[179, 180]

The phenomena generated by laser irradiation and ultrasound propagation that lead to nucleation induction, are both still under investigation. This chapter provides an overview of mechanistic proposals from the recent literature.

2.1. Sonocrystallisation

Sonocrystallisation is the application of ultrasound to initiate crystal nucleation and growth processes. Since ultrasonic wavelengths are significantly longer than bond lengths between atoms in a molecule, the crystallisation outcomes from applying ultrasound to the process are not due to interaction of the liquid with the sound waves rather, they are due to acoustic cavitation being generated in the liquid.[181] Therefore, in order to rationalise the outcomes of sonocrystallisation processes, consideration of the phenomena associated with cavitation generation is required, in combination with the applied ultrasound parameters. This section comprises a discussion on ultrasound operating parameters, followed by the mechanisms that have been proposed for nucleation induction, polymorphism effects and crystal growth under an applied ultrasound field.

2.1.1. Ultrasound Operating Parameters

Bubble dynamics and the spatial distribution of bubbles can differ significantly depending on the sound field geometry, even if the operating frequency is the same. It has been suggested that previous reports on the effects of varying ultrasonic frequency on the cavitation activity, could actually have been related to the differences in the sound field geometries.[182] Moreover, conditions such as the material of the vessel wall, power dissipation, both the physical properties and height of the liquid can significantly influence the sound field generated for sonocrystalllisation.[109, 183-185] Therefore, comparisons made across the literature should be interpreted with caution, even if the same solute-solvent system was under investigation. In 1995, Crum provided recommendations from a cavitation physicist's perspective, intended for chemists to utilise cavitation.[183] Incorporating Apfel's golden rules of cavitation,[124] they included;

i. **"Know thy sound field"** as discoveries made cannot be replicated without accurate measurements and careful descriptions of the characteristics of the field.

ii. **"Know thy liquid"** as cavitation bubble dynamics is very dependent on such variables as the dissolved gas concentration (and composition) and liquid vapour pressure.

iii. "**Know thy dirt"** as the source of bubble nucleation is most likely to originate on inhomogeneities that exist within the liquid.

Overall, the majority of sonocrystallisation studies have not actually involved quantification of the cavitation activity. Typically, calorimetric measurements and/or acoustic power have been provided. The main reason for this is likely to be the specialist instrumentation required for quantifying the phenomena associated with bubble collapse (acoustic and light emissions).[186] Several sonochemistry reports have described a levelling off, or even a decrease of cavitation energy when increasing the acoustic power, which was attributed to acoustic shielding effects (denser bubble clouds at higher powers increasing the attenuation of the acoustic wave).[187-189] Therefore, acoustic power measurements can be misleading whereas, cavitation measurements allow quantification of the energy from "active" bubbles contributing to the observed sonocrystallisation outcomes.

Parameter optimisation studies carried out in the last decade have reported that frequencies in the high-power ultrasound category (20-100 kHz) are best for inducing primary nucleation.[190-192] This has been attributed to the generation of transient cavitation, together with the larger size of cavitation bubbles generating higher mechanical energies.[193] In 2014, Jordens *et al.* carried out a systematic investigation on the effect of frequency on the sonocrystallisation of PCM in water within a single reactor geometry, whilst maintaining a constant power dissipation.[190] From the results obtained at 16, 41, 98 and 165 kHz, it was concluded that 41 kHz was optimal for narrowing the MSZW and inducing nucleation, which was attributed to a likely optimal bubble size and population at this frequency.[190]

In 2008, Kordylla *et al.* reported that the solvent properties (such as vapour pressure and surface tension) had no impact on the nucleation and crystallisation behaviour of dodecanedioic acid in acetonitrile, propyl acetate, and ethyl acetate.[194] This study involved frequencies of 40.3, 355.5 and 1046 kHz however, crystallisation results were not explicitly reported or addressed at 40.3 kHz. Comparing the results at 355.5 and 1046 kHz, the greatest reductions in the metastable zone were at 355.5 kHz, which was attributed to

a greater efficiency of power transfer into the solution.[194] However, the same power settings were applied across all frequencies, so the power dissipation inside the reactor was not constant across the frequency range investigated. There are no known studies on the effect of solvent properties on the sonocrystallisation outcomes, under an applied high-power ultrasound field.

In 2003, Price *et al.* reported solute-induced quenching and enhancement of MBSL (previously described in section 1.2.3) for aqueous solutions of two homologous series of methyl esters and ketones at 20 and 515 kHz.[195] The effect of organic solutes on the MBSL emission intensities at 20 kHz (which was delivered *via* an ultrasonic horn) were found to differ significantly from measurements at 515 kHz (which was delivered *via* a plate transducer). The concentration range investigated was up to 200 mM at 20 kHz and 75 mM at 515 kHz. Two factors were identified to explain the observed the observations: (i) the incorporation of solute and decomposition products within the bubble quench MBSL at 515 kHz and (ii) the prevention of coalescence of the bubbles, observed only at lower concentrations of solute (< 50 mM) at 20 kHz, which led to MBSL enhancement. It was concluded that at 515 kHz the predominant effect was stable cavitation, where a bubble undergoes many oscillations during its lifetime. Conversely at 20 kHz, the predominant effect was transient cavitation, where bubbles are short-lived and collapse more violently, producing larger mechanical effects such as the motion of solvent around the bubbles.[195]

Price *et al.* later investigated acoustic emissions from collapsing cavitation bubbles generated using 20 kHz and 515 kHz ultrasonic frequencies in water, with the use of a cavitation meter (incompatible with organic solvents), which was developed by NPL.[150] The results provided a correlation of MBSL measured in water under the same experimental conditions as the previous report, which corroborated the difference in predominant types of cavitation as a function of frequency.[150]

In 2017, Tzanakis *et al*. investigated the cavitation activity and the acoustic emission spectrum measured in water, ethanol, glycerine and molten aluminium.[196] Cavitation detection was performed with a specifically developed cavitometer, in collaboration with NPL. The cavitometer was designed in order to withstand the physical conditions

associated with molten aluminium. The setup involved a 20 kHz ultrasonic horn immersed into a rectangular glass tank. The authors reported that the behaviour of the tested liquids differed significantly, implying that their physical properties dictated the cavitation activity.[196] Cavitation intensities in water and glycerine were reported to be of a similar range and considerably higher than in ethanol. In ethanol, bubbles were observed to be dispersed and oscillating vigorously towards the surface of the liquid. Whereas a continuous bubbly streamer was established in the case of glycerine and a conical bubble structure was reported in the case of water.[196]

In 2018, Lee *et al.* provided the first systematic study of a sonocrystallisation process and the MBSL intensity from transient cavitation, as a function of frequency and calorimetric power.[191] Crystal nucleation was reported to occur at the antinodes of the standing wave and images showing a correlation between MBSL and crystallisation have been reproduced in Fig. 2-1.[191] The results demonstrated that the threshold for crystal size reduction coincided with the power threshold for MBSL activity.

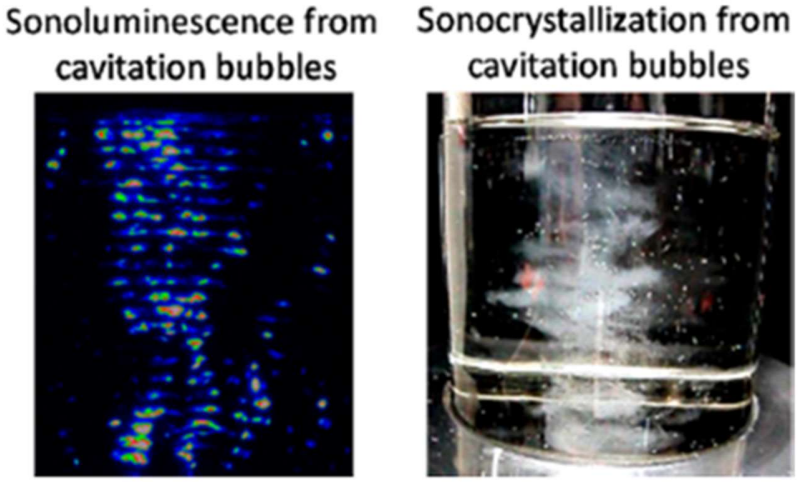

Figure 2-1 Images correlating MBSL emission to sodium chloride crystal crystallisation from water (reproduced from Lee et al.[191])

Currently, there are no known studies linking acoustic emissions from cavitation bubbles to sonocrystallisation outcomes. There is also a requirement for further exploration of

cavitation activity measured in pure organic solvents, in which drug substances are typically crystallised.

2.1.2. Nucleation Induction under an Applied Ultrasound Field

In 1927, the first account of the effect of ultrasound on crystallisation was published by Wood and Loomis, where the authors reported the use of ultrasound to initiate paraffin wax crystallisation.[197] However, almost a century since this report, the underlying mechanisms are still under investigation. Ruecroft provided a comprehensive overview of the developments in the field, alongside the equipment developed for the industrial sonocrystallisation of organic molecules prior to 2005.[198] By this time, it was well established that ultrasound can induce primary nucleation and provide a method of reducing and narrowing the crystal size distribution.[199-204] It was also established that ultrasound can induce secondary nucleation by fragmentation of existing crystals, as demonstrated by Chow *et al.* in an ice sonocrystallisation study.[205]

In 2018, Kiss *et al.* published a roadmap for implementing sonocrystallisation in the pharmaceutical industry, with a timeframe of the application by 2026.[206] A number of key issues were outlined, such as addressing the remaining fundamental questions around the underlying mechanisms, including control of polymorphic form, identifying working process parameters and scale up strategy.[206] In 2019, Jordens *et al.*[193] and Nalesso *et al.*[186] published in-depth discussions on the mechanisms proposed so far for sonocrystallisation. Some of these proposals are discussed herein, alongside additional reports from the recent literature:

Enhanced Heterogeneous Nucleation at the Bubble Surface:

It has been suggested that due to bubble generation in the solution with ultrasound, it is likely that in the majority of cases, primary nucleation will take place heterogeneously.[193] Hem first suggested the bubble surface acting as a nucleation site from sonocrystallisation

studies on hydrocortisone, in 1967.[204] Wohlgemuth *et al.* provided evidence of this hypothesis by demonstrating primary nucleation enhancement in the presence of synthetic air gas bubbles in a supersaturated solution of dodecanedioic acid.[207] Nucleation was enhanced heterogeneously by a lower surface free energy provided at the bubble surface.[207] The same group have recently demonstrated nucleation induction *via* gassing (pure synthetic air) of a continuous crystallisation process with a L-alanine-water model system.[208]

Cavitation bubble collapse can generate extreme temperatures and pressures.[95] As previously discussed, the magnitude of each will depend on the bubble size and cavitation type.[121] Several hypotheses have also been proposed for the effect of bubble implosion phenomena on primary nucleation:

Segregation Theory:

Dodds, Grossier and Louisnard collectively proposed a theory for segregation phenomena taking place between the solute molecules and the solvent under an acoustic field, in 2007.[209-211] In short, this can be described by solute molecules forming clusters that are supersaturated at the wall of an oscillating bubble, which increases the cluster collision probability. During bubble implosion, the inward motion of the liquid is suppressed by the gas compression in the bubble and rapid acceleration of the liquid is created. Thus, clusters that have reached a critical size (and hence density) are expelled from the bubble into the bulk solution. Based on this hypothesis, molecular clusters with different densities will not be accelerated to the same extent. Jordens *et al.*[193] cast doubt on this hypothesis, with a report of nucleation not being induced more quickly with a larger density difference between various solute and solvents (unspecified) investigated.

Solvent Evaporation Theory:

In 1970, Chalmers proposed that rapid heating of the solution surrounding an imploding bubble would result in evaporation of solvent from the bubble surface to the centre of the cavity, increasing the local supersaturation.[212] However, Wohlgemuth *et al.* more recently reported an unaltered degree of supersaturation at the interfacial area for inducing

nucleation and from this, solvent evaporation leading to a supersaturation increase was ruled out.[207]

Ice nucleation from water is achieved *via* supercooling and the generation of acoustic cavitation has been reported to enhance mass transfer and freezing rates through the liquid.[205] Since ice sonocrystallisation studies are single component, they can be considered more simplified on comparison with binary or tertiary systems. In 2016, Cogné *et al.* presented theoretical calculations of the increase in supersaturation for different initial bubble radii and acoustic pressures for the nucleation of ice at 29 kHz.[213, 214] The authors reported that nucleation could be triggered from significantly increased local supersaturation generated during bubble implosion.[213, 214] However, the timescale of this elevated supersaturation was reported as around 1 ns after the collapse, after which the local temperature rapidly returned to ambient conditions.[213] From this, it can be interpreted that there is localised high pressure surrounding the cavity, at ambient temperature.[186]

Nucleation under High Pressure and Shockwave Generation:

In a 2011 sonocrystallisation study by Nalajala and Moholkar, it was reported that shockwaves generated from bubble implosion enhanced the nucleation rate of potassium chloride (KCl) solutions.[215] This was rationalised as the pressure from shockwave propagation accelerating solute molecules with high force, increasing the number of collisions to form clusters which overcome the free energy barrier for nucleation.[216]

In 2017, Liu *et al.* conducted a study in order to compare different methods of nucleation induction of glycine solutions, as a function of supersaturation.[217] The methods employed were laser irradiation, high-power ultrasound and mechanical shock. The similarity of crystallisation outcomes, in terms of the total fraction of samples nucleated from each technique suggested a common mechanism involving localised pressure generation from bubble implosion causing localised supersaturation elevation.[217]

In 1964, Hickling and Plesset theoretically calculated that the liquid pressure near the bubble wall increases to approximately 5 GPa following a violent, transient bubble collapse.[218] On this basis, the authors proposed that high pressure generation is able to

nucleate metastable forms of ice.[218] The aforementioned high pressure crystallisation work by Oswald *et al.* reported high pressure crystallisation of the metastable form of PCM, performed at ~0.4 GPa.[57] Also, solid-state transitions of PCM form I to II have been reported at ~4 GPa.[58] These pressure values are within range of the report by Hickling and Plesset.[218] Therefore, it seems plausible that acoustic cavitation generates highly localised extreme pressures in the proximity of an imploded bubble, which might lead to a decrease in solute solubility and hence a localised region of enhanced supersaturation in the solution.

The generation of acoustic cavitation has been reported to produce crystals with a different polymorphic form compared to silent conditions, for various compounds.[217, 219-224] Discussions on the mechanism behind this have involved an apparent supersaturation dependence, alongside a threshold cavitation energy; this is still under investigation.[217,222,225]

2.1.3. Polymorphism Effects under an Applied Ultrasound Field

On discussing the apparent supersaturation dependence of obtaining metastable forms *via* sonocrystallisation, Jordens *et al.* proposed that at high supersaturation levels, solute clusters have less time to re-orient and rearrange themselves during nucleation so that solution systems are likely to be trapped in a local energy minimum, which could lead to the formation of a less stable polymorphic form.[193] It is yet to be explained why at the same supersaturation level, cavitation generation has been reported to produce a metastable form that was not produced under silent conditions.[223]

In the case of PCM, Mori *et al.* reported a method of selectively crystallising form II, with ultrasound.[223] Highly supersaturated aqueous solutions were prepared by slowly cooling a 32 mg/mL PCM solution to 0°C (corresponding to $S = 4.4$, based on a solubility of 7.21 mg/mL of PCM in water at 0°C from Granberg *et al.*[226]). Sample vials (of 1 mL volume) were held between 0-2°C, either stirred in an incubator or insonated in an ultrasonic

cleaning bath that generated frequencies of 28, 45, and 100 kHz. Periodic insonation was applied (10 s on then 10 s off) to the solutions, up to 800 s and the experiment was stopped when crystallisation was observed. After which, the sample was transferred back to the incubator held at 0°C and following isolation, XRPD analysis was carried out. Reproduced crystallisation probability and assigned polymorphic forms, alongside microscope images of PCM crystals obtained are shown in Fig. 2-2:

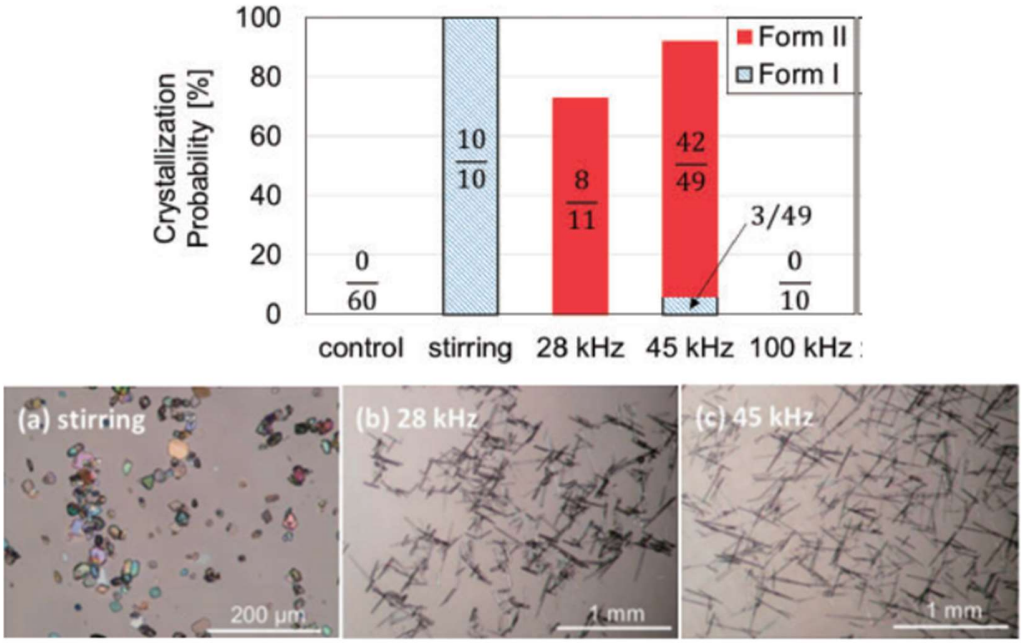

Figure 2-2 The selective crystallisation of form II paracetamol with ultrasound (reproduced from Mori et al.[223]). *Top: Crystallisation probability and assigned form of PCM for unstirred and non-insonated (control) samples, stirred and non-insonated samples and samples insonated at 28, 45 and 100 kHz. Bottom: Microscope images of PCM crystals obtained from (a) stirring (b) insonation at 28 kHz and (c) insonation at 45 kHz. The scale bar is 200 µm in (a) and 1 mm in (b) and (c).*

Control (non-insonated and unstirred) samples were reported to have not spontaneously nucleated within one month. Whereas all stirred samples produced form I PCM. With insonation at 28 kHz, all samples that did nucleate were determined to be form II PCM and at 45 kHz, 93% of samples that crystallised were determined to be form II. At 100 kHz, samples did not crystallise, which was attributed to the less intense mechanical

energies generated at this frequency to induce nucleation.[217] The authors proposed that in the case of selective form II nucleation, no form I was produced, since the presence of form I PCM initiates a rapid conversion to form I.[217] It was also speculated that at 45 kHz, fluctuations of ultrasonic intensity in the bath led to some samples nucleating as mixtures, which eventually transformed to form I, before sampling.[217]

Bhangu *et al.* later reported an anti-solvent PCM sonocrystallisation process which generated mixtures of form I and II.[222] Anti-solvent sonocrystallisation was performed in a glass cell with the ultrasound transducer fixed at the base of the cell, operated at frequencies between 22 and 139 kHz and at calorimetric powers of 3, 6 and 10 W. The anti-solvent (200g water) was firstly placed within the cell (held at 5°C) and ultrasound was turned on as 30g of 30 % wt. PCM in ethanol solution was added to the cell. Solutions were insonated for 180s, before ultrasound was turned off and the samples were filtered and dried prior to analysis. Assignment of polymorphic composition was on the basis of aspect ratios from optical microscope images taken after the isolation procedure. The exact time of sampling was unspecified and since the conversion of form II to form I have been reported to occur over minutes, this may have also affected the accuracy of the polymorphic assignments.[48] Although, it was also observed across all frequencies that the percentage of form II and induction time are inversely related to one another, which correlated with the MBSL intensity measurements.

The authors stated that without ultrasound, only form I was observed (no images of crystals obtained under silent conditions were provided).[222] Therefore, it would be expected that at the same supersaturation and below a threshold cavitation energy, no form II would be obtained. The generation of form II (of varying proportions) in mixtures with form I was reported across all ultrasound parameters investigated. Results of the assigned polymorphic compositions as a function of frequency and power, alongside microscope images of PCM crystals obtained from this study are reproduced in Fig. 2-3.

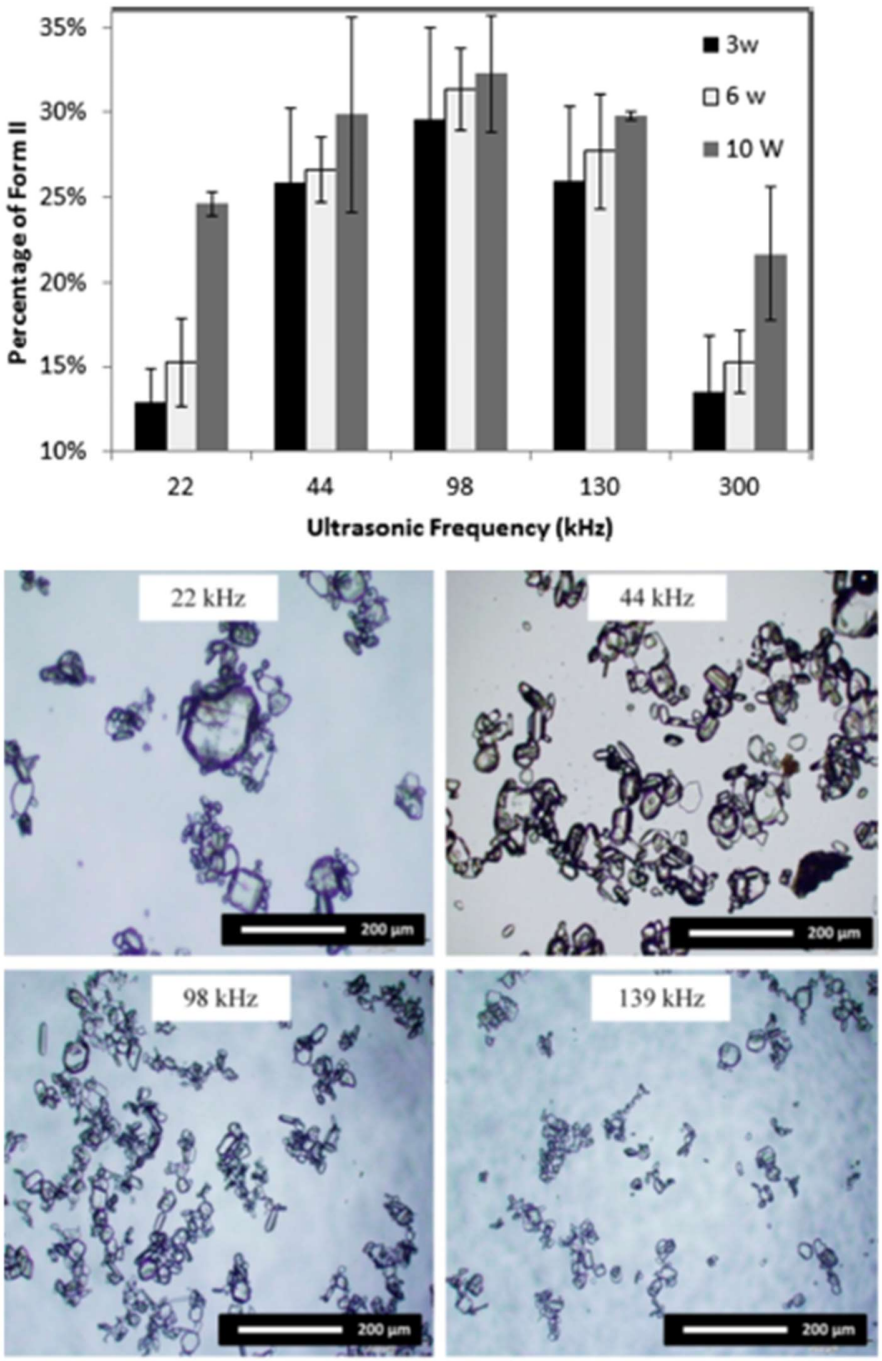

Figure 2-3 Paracetamol anti-solvent sonocrystallisation generating mixtures of form I and II (reproduced from Bhangu et al.[222]). *Top: Assigned percentage of form II as a function of function of frequency at 3, 6 and 10 W calorimetric powers. Bottom: Microscope images of PCM crystals obtained at 22, 44, 98 and 139 kHz at 3W.*

From the results, it was concluded that with an increase in frequency from 22 to 98 kHz, the percentage of the form II increased, whereas with a further increase in frequency, the percentage of form II dropped.[222] It was further speculated that at 98 kHz there is an optimum condition between the population of cavitation bubbles and an appropriate magnitude of shear to promote the intermolecular interaction between molecules at the clustering phase prior to nucleation.[222] Since it is known that PCM form II is the more stable form under high-pressure conditions, nucleation under high pressure seems more plausible to explain these observations. The results from this report appear analogous to the solvent-mediated transformation of form II to form I, observed by Ward and Oswald, on decompression following high pressure anti-solvent crystallisation of PCM form II.[59] On reducing the pressure, the authors reported that the solubility increased and depending on the saturation status of the solution, crystallised form II may have dissolved and recrystallised as form I, the more stable form under ambient conditions.[59] In the study by Bhangu *et al.,* it is presumed that to an unknown extent, solution-mediated transformation to form I took place prior to isolation.[222]

Overall, the mechanism for polymorphic effects under an applied ultrasound field requires further investigation.

2.1.4. Crystal Growth under an Applied Ultrasound Field

The effects of ultrasound on growth need to be considered on the basis of the frequency applied. The fragmentation of existing crystals under high-power ultrasound fields have been attributed to the high-pressure shockwaves generated upon implosion of transient cavitation bubbles.[95, 227] Zeiger and Suslick termed this process sonofragmentation.[228] In a study involving the insonation of an aspirin suspension in dodecane with a 20 kHz ultrasonic probe, the authors established that the primary mechanism for sonofragmentation is *via* particle-shockwave interactions.[228] Optical microscopy images from this work are reproduced in Fig. 2-4.

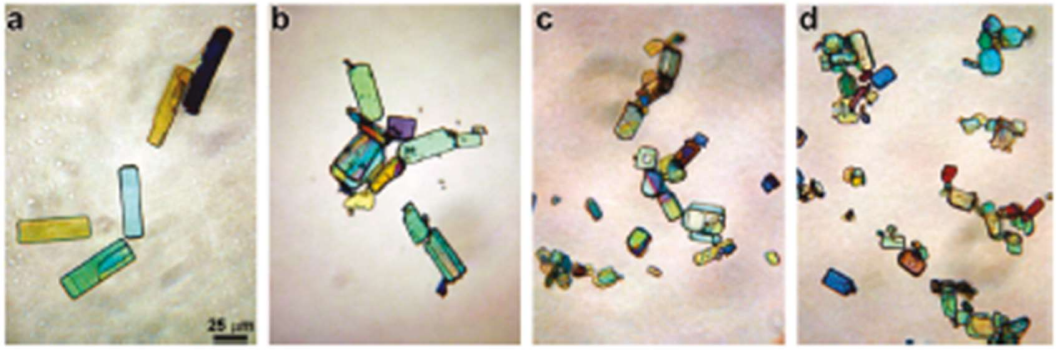

Figure 2-4 Sonofragmentation of aspirin crystals (reproduced from Zeiger and Suslick[228]). *Images were obtained at times (a) before sonication (b) after 1 min of sonication (c) after 3 min of sonication and (d) after 10 min of sonication. Images are of the same magnification level.*

Furthermore, Gielen *et al.* described ultrasound-enhanced secondary nucleation (mechanical division of existing crystals) of PCM *via* sonofragmentation in a study that investigated ultrasound applied only before, and both before and after the induction time.[229] A reduction in the crystal size was only obtained if ultrasound was applied after the induction time. Gielen *et al.* have also demonstrated the deagglomeration of crystals with high-power ultrasound with an unspecified Janssen commercial drug substance.[230]

The propagation of ultrasound through a liquid can generate both acoustic cavitation and acoustic streaming.[85] Streaming enhances bulk mass transfer whereas micromixing, from microbubble oscillations results in a thinning of the hydrodynamic boundary layer around particles in a suspension, enhancing mass transfer rates.[231] Promoted crystal growth has been attributed to micromixing generation.[193] In 2014, Nii *et al.* studied the growth of glycine crystals in an anti-solvent crystallisation process at 1.6 MHz.[232] Under high frequency ultrasound, the incorporation of microcrystals during growth was interpreted as crystal agglomeration and therefore, the promotion of crystal growth.[232] No polymorphic changes from the preferred α-form were reported. These observations are consistent with polymorphic changes *via* the generation of high pressure, produced by transient bubble collapse at low frequencies. Therefore, although this was an anti-solvent

sonocrystallisation procedure that generated high levels of supersaturation, polymorphic changes would not be expected since MHz frequency ultrasound was applied.

There are few reports of crystal growth under the influence of a high-power ultrasound field. Amara *et al.* studied the growth rates of potash alum with ultrasound in a jacketed vessel bonded to a 20 kHz transducer.[233] The authors concluded that the mass growth rate of potash alum was increased under ultrasound compared to that under silent conditions.[233] Jiang examined the sonocrystallisation kinetics of L-glutamic acid and reported that the effects of high-power ultrasound (generated from a 20 kHz horn) on crystal growth are supersaturation dependent. Ultrasound was found to accelerate growth rates at relatively low supersaturations and have no effect on growth at high levels of supersaturation.[225]

As previously discussed in section 1.1.5, crystal growth rates greatly affect impurity uptake levels in impure systems. In 2017, Nguyen *et al.* reported greater impurity rejection from a PCM cooling sonocrystallisation process, in the presence of structurally similar impurities (ACE and MCM).[234] The crystallisation solvent was isoamyl alcohol (IAA) and the crystallisation vessels were placed on top of a magnetic stirrer bath within a 35 kHz ultrasonic bath set at 100% power over the duration of the cooling profile (65-15°C). This study is the only detailed investigation on the effects of impurity incorporation found in the sonocrystallisation literature. The purity enhancement was principally attributed to cavitation phenomena generated during growth.[234] However, this account seems to contradict the aforementioned reports of high-power ultrasound enhancing crystal growth rates.[225, 233] Supersaturation levels were not presented with the results, although it was also suggested that the purity enhancement with ultrasound could be a result of induction at lower supersaturation values.[234] The purity results (determined by High Performance Liquid Chromatography) have been reproduced in Table 2-1, with the addition of the reported nucleation induction temperatures.

Table 2-1 Reproduced results from Nguyen et al.[234] on the purity of paracetamol in the presence of acetanilide and metacetamol, with/without ultrasound (US).

Experimental conditions	Compounds	**Percentage of compounds in product (%)**		**Recorded induction temperature (°C)**	
		With US	**No US**	**With US**	**No US**
PCM with no added impurities	PCM	100	100	41.3	36.0
PCM with 2% ACE	PCM ACE	99.62 0.35	99.15 0.85	43.0	15.5
PCM with 2% MCM	PCM MCM	98.47 1.52	98.12 1.88	36.4	15.0
PCM with 2% MCM and 2% ACE	PCM MCM ACE	98.1 1.19 0.55	97.98 1.44 0.58	34.4	15.0

Under silent conditions, the presence of impurities dramatically inhibited nucleation, leading to induction at high supersaturation ratios (S =2.4 at 15°C, from solubility data of pure PCM in IAA in this report). It is clear that the generation of acoustic cavitation leads to nucleation induction at significantly lower supersaturation ratios (S =1.7 at 34.4°C from solubility data of pure PCM in IAA in this report). The impurity removal trend is inconsistent in the case of ACE and overall, it is difficult to draw comparisons between experiments under silent conditions and with ultrasound applied at one power setting. No significant effects of impurity incorporation on the crystal morphology were reported (with or without ultrasound). This observation contrasts with previous reports of PCM crystallisation (without ultrasound) in the presence of MCM, in which crystals with higher aspect ratios due to MCM incorporation (in water and isopropyl alcohol) were obtained.[68, 72, 74] The proposal of cavitation phenomena enhancing impurity rejection for this system requires further investigation.

2.2. Laser-induced Nucleation

On interaction with matter, light that is neither scattered nor transmitted is absorbed. So far, Laser-induced Nucleation (LIN) has been classified as either photochemical or non-photochemical.[235] In photochemical LIN, the system absorbs light irradiation and subsequently generates reactive intermediate species that act as nucleation centres.[236, 237] Whereas LIN in the absence of photochemical effects defines Non-Photochemical Laser-induced Nucleation (NPLIN). Typical NPLIN studies use ns-pulsed neodymium-doped yttrium aluminium garnet (Nd-YAG) lasers to produce 532 or 1064 nm beams, which are far from any significant absorption bands for the solute-solvent systems employed.[238-240] Furthermore, the laser beam is not focussed tightly in order to avoid optical breakdown of the liquid and therefore the generation of optical cavitation (see section 2.2.2).

It has previously been suggested that the NPLIN effect does not compromise the integrity of the material, which is a key advantage in the context of drug substance manufacturing.[241] The NPLIN effect has also been demonstrated to provide spatiotemporal control over crystal nucleation.[174] Previously reported images of ammonium chloride (NH_4Cl) NPLIN from a single laser pulse suggest that nucleation occurs within the irradiated volume (see Fig. 2-5).

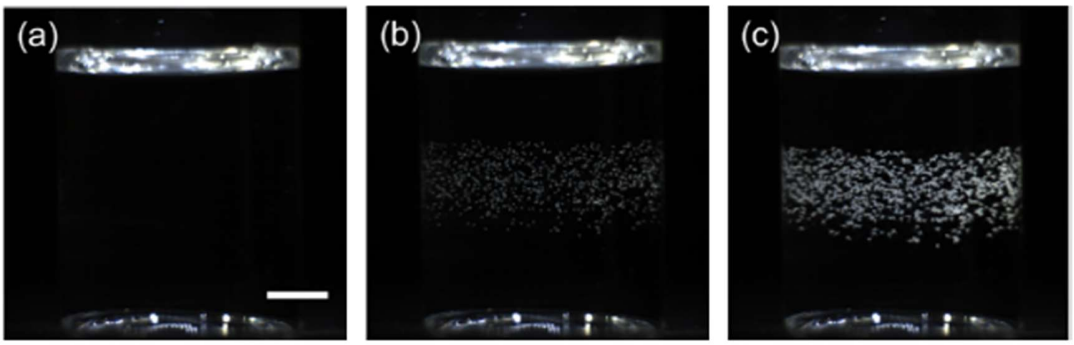

Figure 2-5 Single-pulse NPLIN of ammonium chloride (reproduced from Alexander and Camp.)[235] *Images were obtained at times (a) 0 s, (b) 1 s and (c) 2 s following a single 5 ns, 532 nm laser pulse. The scale bar in (a) represents 0.5 cm.*

In 2019, Alexander and Camp published a comprehensive review of NPLIN, which included a discussion of the mechanisms that have been proposed so far for this remarkable effect.[235] This section firstly outlines these proposals, followed by an imperative distinction from LIN by optical cavitation.

2.2.1. Laser-induced Nucleation in the Absence of Photochemical Effects

In 1996, Garetz *et al.* reported LIN of supersaturated aqueous urea solutions with 1064 nm, unfocused laser pulses of 20 ns duration (up to peak power densities of 250 MW cm^{-2}).[242] A minimum supersaturation and laser power were established in order for the laser-induced nucleation to occur and curiously, the needle-shaped crystals obtained were reported to be approximately aligned with the angle of light polarisation.[242] Importantly, Garetz *et al.* ruled out a photochemical effect, due to both the insignificant absorption of water and the transparency of urea at the incident wavelength.[242] In 2005, the same group established a wavelength independence in the NPLIN of aqueous urea solutions and the authors reported that linearly polarised light was more effective than circularly polarised light to induce nucleation in the aqueous urea system.[238] This observation played a key role in the mechanism proposed by Garetz *et al.* to account for this effect. It was proposed that the laser light acts to orient solute molecules within pre-nucleated clusters along the direction of the electric field of the laser light, similar to the optical Kerr effect (OKE).

Optical Kerr Effect:

The OKE occurs when an applied electric field induces a dipole moment in the liquid.[243] The applied electric field interacts with the induced dipole moment, causing the molecule (or clusters of molecules) to align its most polarisable axis parallel to the electric field, under the action of a weak torque. However, it should be noted that a recent NPLIN report from Liu *et al.* revealed a polarisation independence in the case of urea and no statistically significant correlation between crystal angle and direction of linear polarisation was reported.[244] This report casts serious doubt on the reports by Garetz and co-workers.[238, 242]

NPLIN studies by Garetz and co-workers were extended to supersaturated aqueous solutions of glycine, where different polymorphs of glycine were reportedly obtained by switching between linear and circular polarisation.[245-247] However, several following NPLIN studies by various researchers have reported no significant effect of changing the polarisation state of the laser light on the resulting glycine polymorph obtained.[217, 248, 249] Liu *et al.* recently discussed potential reasons why the polarisation switching of glycine polymorphs has not been observed in later reports.[217] The authors noted that the assignment of polymorphic form was made using second-harmonic generation analysis, of which the α-form of glycine is inactive and this would have led to inaccurate polymorphic assignents.[217] Moreover, in the polarisation switching of glycine polymorphs report, the authors estimated that the OKE would have provided a dipole alignment energy of 10^{-4} k_BT.[245] This has since been deemed insufficient to account for the observed reduction of induction time for crystal nucleation to take place.[250]

In 2009, Alexander and Camp reported that a single, 7 ns pulse of 1064 nm laser light (6.4 mJ pulse^{-1}) can be used to produce a single crystal of KCl.[251] As the solute is symmetrical, it is not possible to induce dipole moment in and there is no preferrable axis for alignment therefore, the OKE mechanism cannot be applied. This led to the proposal of an alternative mechanism of the optical electric field acting on solute clusters, involving the dielectric response of the solution.

Dielectric Polarisation:

The report by Alexander and Camp detailed a quantitative analysis using a theoretical model based on CNT.[251] In short, the dielectric polarisation model postulates that the free energy of a dielectric particle is lowered in the applied electric field, the result of which in the context of nucleation is that the free energy barrier to nucleation is reduced. The consequence of this is that there will exist a fraction of pre-nucleated clusters that are subcritical in size that go on to become supercritical when the electric field is active.[251]

Subsequent work by Ward *et al.* investigated the effect of pulse duration on the NPLIN of supersaturated KCl solutions.[252] At equivalent peak power densities, it was reported that

the same fractions of samples were nucleated as a result of 6 ns and 200 ns 1064 nm laser pulses.[252] From this, the authors concluded that the underlying mechanism of NPLIN is unlikely to be based solely on the diffusion of solute to a sub-critical cluster.[252] In the same year, Knott *et al.* theoretically calculated that ns laser pulses are too short for clusters to assemble purely from monomers.[253] Moreover, theoretical calculations by Agarwal and Peters suggested that thermal fluctuations should overwhelm molecular alignment by the optical electric field.[254] Although, in the 2009 report from Alexander and Camp, the authors had also considered the role of impurity particles behind the NPLIN effect, since the suppression of NPLIN was reported for samples that had been filtered prior to laser irradiation.[251] From the observation of one KCl crystal per laser shot, they suggested that the observed laser-induced nucleation could be caused *via* the interaction of pre-nucleated solute clusters with a rare, intermediate species.[251]

Impurity Particle-Heating Mechanism:

In 2011, Knott *et al.* published work on the use of laser pulses (of wavelengths and intensities typically used in NPLIN studies) to nucleate bubbles in carbonated water samples.[255] The authors defined the threshold pulse energy to generate bubble nucleation at a given supersaturation as the minimum pulse energy that produces at least one bubble from the ten pulses.[255] The authors reported that laser-induced bubble nucleation events become more numerous with increasing laser intensity.[255] Furthermore, the results showed no significant difference in the threshold pulses energy required for samples prepared using ultrapure or municipal tap water.

In 2015, Ward *et al.* provided a study on the LIN of carbon dioxide bubbles in carbonated sugar solutions, reporting that the number of bubbles nucleated was linearly proportional to sucrose concentration.[256] It was also shown that increasing degrees of cleaning and filtering during sample preparation substantially reduced the number of bubbles observed.[256] Additional thermodynamic (Mie scattering) calculations presented with this work determined that the energy absorbed by an irradiated Fe_2O_3 nanoparticle of diameter 200 nm is sufficient to generate a vapour bubble of diameter ~1 μm.[256] On this basis, the authors concluded that the threshold power for NPLIN to be observed could be explained

by a critical threshold temperature, below which vaporisation of solvent around impurities does not occur.[256] Later work on glycine NPLIN by Javid *et al.* corroborated that filtering solutions prior to irradiation suppresses NPLIN.[249]

In 2016, Ward *et al.* explored the role of impurity particles in the NPLIN of supersaturated solutions of aqueous NH_4Cl.[257] Samples were treated by filtration or long-term laser exposure, prior to irradiation (1064 nm, single 5.5 ns pulse). The number of crystals produced by NPLIN was recorded for samples that were untreated (control) and pre-treated, which showed a substantial reduction compared to untreated samples. This reduction was reversed by subsequently doping filtered solutions with iron oxide nanoparticles (Fe_3O_4 NP) in either aqueous or poly(ethylene) glycol (PEG)-stabilised dispersion. Some results from this report have been reproduced in Fig. 2-6.

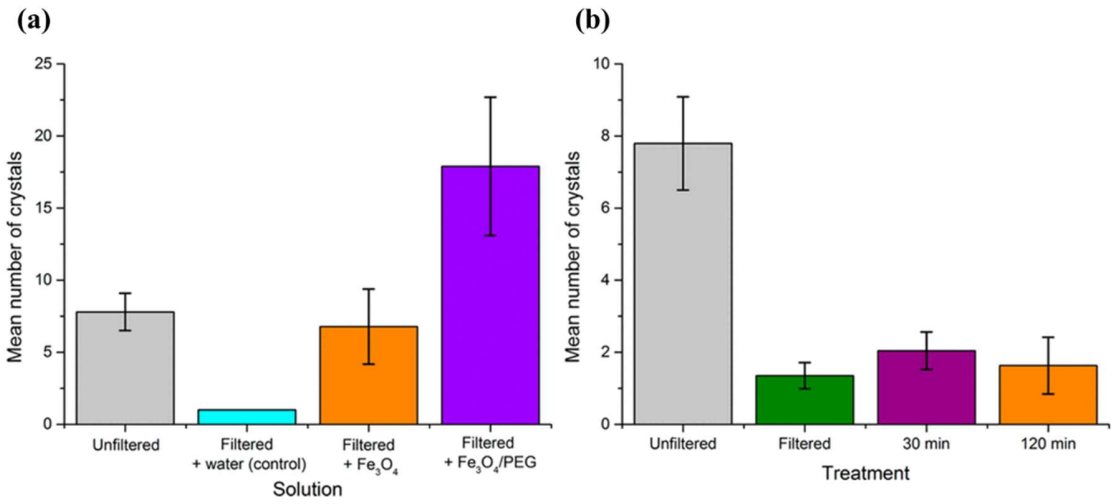

Figure 2-6 The effects of sample pre-treatments on the NPLIN of ammonium chloride (reproduced from Ward et al.[257]). *In (a) filtration decreases the number of crystals nucleated and subsequent nanoparticle doping reverses this; (b) filtration and long-term laser exposure (for 30 and 120 minutes) of unfiltered samples all result in suppression of NPLIN.*

Comparisons made across these results reveal that the average number of crystals produced are very similar for (a) unfiltered samples and filtered samples that were doped with Fe_3O_4 NP (aqueous dispersion) and (b) unfiltered samples that were pre-processed by the laser at 10 pulse s^{-1} for 30 min and 120 min and filtered samples. The surfactant was

thought to have stabilised the dispersion of particles, hindering aggregation and resulting in more nucleation sites.[257] A fascinating aspect of this work was that laser processing was found to reduce the size of trace impurity particles present in NH_4Cl.[257] Inductively Coupled Plasma Mass Spectrometry analysis of filter residues was carried out and from the results, it was inferred that the impurities were iron and phosphate NPs.[257]

Combining these observations with the previous work on carbon dioxide bubble NPLIN, Ward *et al.* proposed a revised mechanism for NPLIN, based on laser heating of impurity particles resulting in the generation of transient vapour cavities, leading to nucleation induction at the new interface, or in a region of increased concentration beyond the new interface.[257] Alexander and Camp further explained that the source of impurity particles may be from the solvent or the reactant (during manufacture e.g. iron oxide particles from mechanical processing with steel components).[235] The proposed mechanism is schematically represented in Fig. 2-7. The events from (b) to (d) are thought to provide opportune conditions for the induction of crystal nuclei (as indicated by question marks).

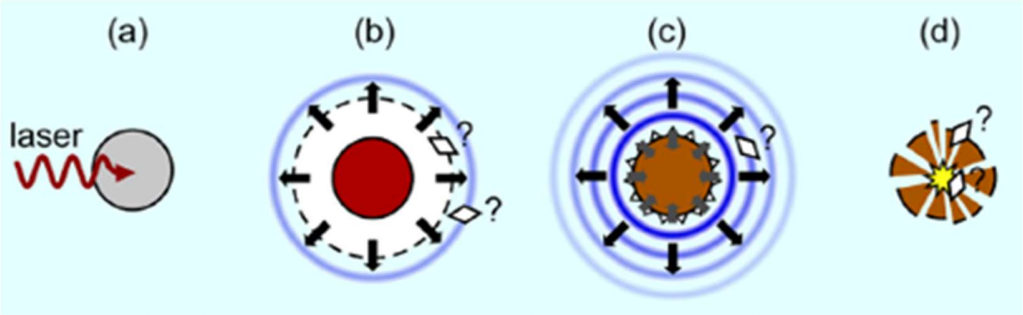

Figure 2-7 Schematic diagram illustrating the proposed role of impurity particle heating in NPLIN (reproduced from Alexander and Camp[235]). *In (a) a nanoparticle absorbs energy from the laser pulse; (b) rapid heating of the particle causes formation of an expanding vapour cavity; (c) collapse of the vapour cavity generates shockwaves and (d) violent collapse of the vapour cavity results in fragmentation of the nanoparticle.*

Numerous authors have established that the pulsed laser irradiation of plasmonic gold NPs can generate superheating and nanobubble formation in water.[258-261] Plasmonic NPs exhibit the unique property of surface plasmon resonance, hence laser excitation (in the

visible to near-infrared spectrum) causes the conduction-band electrons around the surface of the particles to produce collective oscillations (implying heat generation). As a result, plasmonic NPs serve as highly efficient localised heat sources (photothermal agents). According to Lapatko *et al.* generated nanobubbles persist in the liquid and act as thermal isolators that decrease heat dissipation to the bulk liquid and hence increase the temperature of the NP.[262] Furthermore, Plech *et al.* reported that larger particles are heated more effectively, due to lower heat dissipation than in the case of smaller particles.[263] Of relevance to the proposed NPLIN impurity particle heating mechanism, Sindt *et al.* carried out molecular dynamics simulations in a theoretical study of the effects of a rapidly heated NP (of 2 nm diameter) on the structure of a concentrated aqueous salt solution.[264] The simulation revealed the formation of an expanding vapour cavity at the surface of the rapidly heated NP, alongside evidence for solute clustering in the proximal region of solution just outside a collapsed cavity.[264]

A recent KCl NPLIN study by Kacker *et al.* reported PVDF transducer measurements of irradiated samples at laser powers and conditions similar to those in a previous study by Ward *et al*.[239, 240] Firstly, pressure measurements were carried out with the laser passing through the solution and a clear trend showing the increase in amplitude of the waveform was reported with increasing laser intensity.[240] Additional measurements were carried out with a black mask placed on the outside of the glass vial, which blocked the laser light from passing through the solution. Since the recorded pressure signal was higher with the mask and no samples nucleated without laser irradiation, the authors concluded that laser-induced shockwaves can be ruled out for the mechanism behind NPLIN.[240] An example waveform recorded in a KCl aqueous solution has been reproduced in Fig. 2-8.

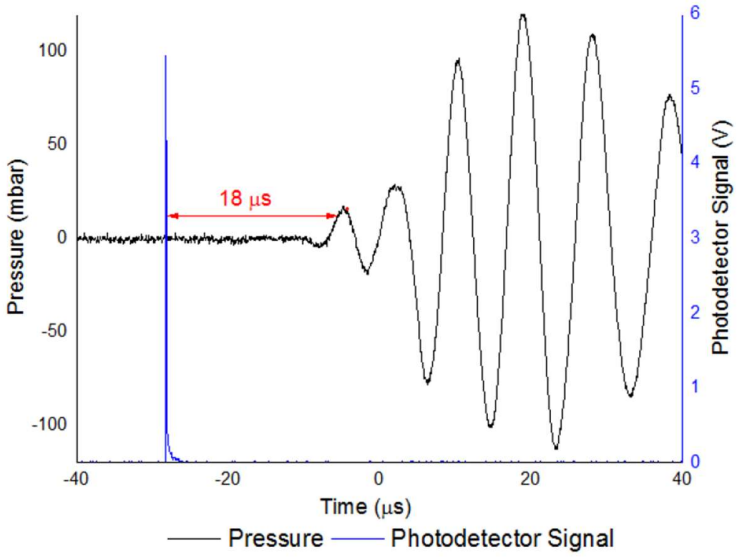

Figure 2-8 An example waveform measured with an acoustic pressure sensor from the single pulse (80 MW cm^{-2}) irradiation of a KCl aqueous solution (reproduced from Kacker et al.[240])

Other than the peak pressure values, no comparison between the waveform recorded with and without the mask was provided. Also, no further signal processing was presented, which could have provided more information on how the energy of the signals (with and without the mask) were distributed over the frequency domain. The authors also noted that filtering samples suppressed nucleation and therefore impurity effects were not ruled out.[240] This is the only available study where acoustic pressure measurements were performed used laser parameters typical of NPLIN studies. Further investigation is required in order to verify if cavitation phenomena can be ruled out as the mechanism behind LIN, at intensities below optical breakdown of the liquid.

Ward *et al.* noted that if the underlying mechanism of NPLIN relies on the presence of impurity particles, then it simply will not work for every system.[257] Mackenzie carried out NPLIN screening experiments (at 44 MW cm^{-2} peak power density) of PCM.[265] Supersaturated solutions of PCM were prepared in various organic solvents and water, up to S = 2.0 (S = 2.7 for 2-propanol and S = 4.4 for acetonitrile) and no LIN was reported since observed crystallising experiments were determined to be spontaneous only.[265]

Moreover, an earlier NPLIN study by Ward *et al.* reported that nucleation of aqueous supersaturated sodium chlorate ($NaClO_3$) solutions, could not be induced with single 7 ns 1064 nm laser pulses (at 140 MW cm^{-2} peak power density).[241] However, in a later NPLIN study it was reported that doping $NaClO_3$ solutions with Fe_3O_4 NP prior to irradiation resulted in nucleation induction.[257] In 2019, Barber *et al.* extended this work, reporting LIN of $NaClO_3$ *via* optical cavitation generation by single, focussed ns pulses (at 87 TW cm^{-2} for 532nm and 68 TW cm^{-2} for 1064 nm).[266] The optical cavitation process requires further discussion.

2.2.2. Distinction from Laser-induced Nucleation by Optical Cavitation

Numerous LIN studies using tightly focussed lasers have been reported in the literature.[266-272] In such cases, bubble nucleation is preceded by plasma formation from optical breakdown, which is considered to be a photochemical process.[235] Optical breakdown can be achieved by focusing a pulsed laser, typically through a microscope objective lens. Plasma is formed by direct ionisation (*via* multiphoton absorption) and avalanche ionisation (*via* inverse bremsstrahlung absorption).[273] Direct ionisation produces seed electrons that accelerate in the laser electric field and transfer their energy to bound electrons in other atoms and molecules via collisions (avalanche ionisation).[274] Significant heating of the focal volume takes place during the laser pulse and if impurity particles are present in the liquid, then thermal emission of free electrons can support the avalanche ionisation by generating the required seed electrons. The plasma heats up by several thousand Kelvin and volume expansion leads to the release of a first shockwave. Following the laser pulse, interaction of the hot plasma with the surrounding liquid generates a cavitation bubble.[275, 276] The plasma is cooled down by electron capture and emission of light. The bubble expands and reaches a maximum radius before collapsing and releasing a second shockwave into the liquid. The laser-induced cavitation process is described schematically in Fig. 2-9.

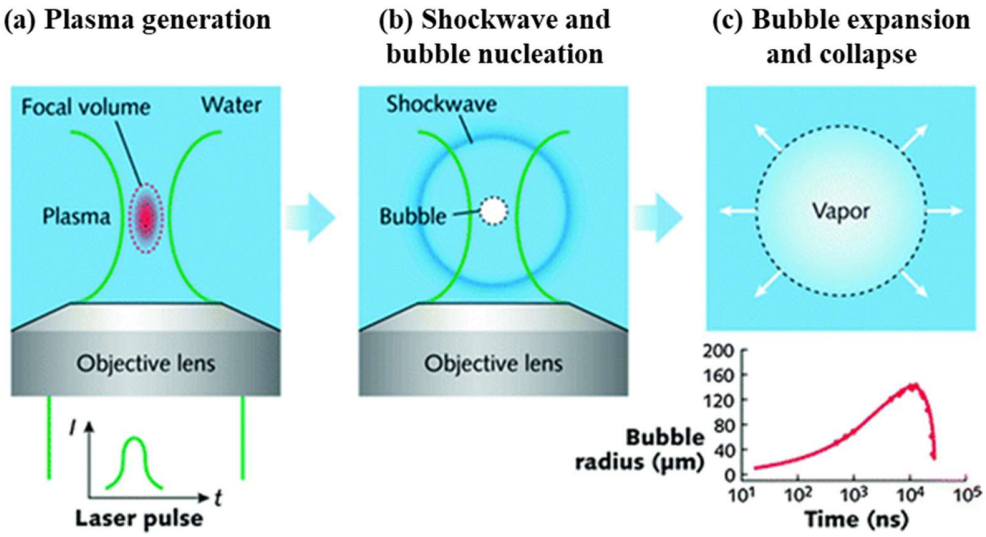

Figure 2-9 Schematic diagram of optical cavitation in water (reproduced from Chiou et al.[277]). *In (a) once the breakdown threshold is reached, enough energy is absorbed in the focal volume and a plasma is generated; (b) subsequently, a shockwave is released, which propagates in the liquid, leaving a vapour bubble and (c) the bubble expands and reaches a maximum radius before collapsing and the launch of a second shockwave.*

The time interval between the bubble maximum expansion and the end of the collapse phase is the Rayleigh collapse time (which is of the order 10-100 μs, as shown in Fig. 2-9). After which, a second bubble forms out of a rebound process and process (c) is repeated until the energy is dissipated by viscosity, dispersed by thermal conduction or radiated by shockwaves.[278, 279] Vogel *et al.* reported an average irradiance threshold for breakdown in distilled water of 76 GW cm-2 (1064 nm, 6 ns pulse duration).[273] The authors also importantly noted that the likelihood of impurities present within the focal volume decreases with decreasing spot size.[273] Therefore, increasing the focal volume increases the likelihood of irradiating impurity particles in the liquid that can produce seed electrons for avalanche ionisation. In addition, shockwave pressures are reportedly higher for ns laser pulses than ps laser pulses (same energy per pulse) and Lauterborn has attributed this to the lower breakdown threshold for ps pulses and thus the energy is deposited in a larger volume than for ns laser pulses.[280] This leads to a higher energy density, temperature increase and thus shockwave pressure for ns laser pulses. In 2019, Sinibaldi *et al.*

demonstrated that the bubble dynamics following breakdown correlates with the plasma shape, which is dictated by the optical electric field.[281]

At present, the underlying mechanisms for nucleation induction from optical cavitation have not been widely discussed and there are no known reports of LIN *via* optical cavitation generation involving acoustic detection. In 2019, computational fluid-flow simulations by Hidman *et al.* provided evidence for the formation of a concentrated fluid region at the periphery of a laser-induced vapour cavity.[282] The aforementioned report from Barber *et al.* provided an estimation for the energy threshold for optical breakdown in the $NaClO_3$ solutions as 70 J cm^{-2}.[266] Despite the large amount of energy dispersed into the solutions from a single laser pulse (460 kJ cm^{-2}), on average only one or two crystals were formed per vial.[266] The authors attributed this observation to very selective and localised primary nucleation events and a low rate of mixing (together with no significant secondary nucleation).[266] It was concluded that the nucleation event was a result of highly localised supersaturation from solute clustering in the proximal region of solution, just outside a collapsed cavity.[266]

This mechanistic proposal aligns with nucleation induction by the impurity particle-heating mechanism from Ward *et al.*, with the key difference being the mode of cavitation generation.[257] NPLIN studies are carried out at intensities below the threshold for optical breakdown of the solution, which rules out optical cavitation generation, but particle heating *via* energy deposition has also been defined as a method of cavitation generation by Lauterborn.[283] Since the threshold pulse energy of laser-induced breakdown for solids is lower than that for liquids or gases, it is possible to induce breakdown of particles suspended in a liquid at pulse energies below the threshold for breakdown of the liquid.[284,285] In this case, the particle absorbs radiation and plasma (of the particle) is formed, which can result in vaporisation of the surrounding liquid and the generation of a cavity. Further investigation is required in order to provide evidence for cavitation generation by impurity particle heating as the mechanism behind the NPLIN effect.

Thesis Overview

Chapter 1 introduced the fundamentals of crystallisation and acoustic cavitation and Chapter 2 provided a literature review of sonocrystallisation and LIN, with a focus on mechanistic proposals from the recent literature. So far, a complex picture of bubbles and localised pressure fluctuations at the interplay of pre-nucleated solute clusters and crystal nuclei has been presented. Given this, it is clear that detection of bubble fields, generated by application of the external fields is required in order to gain further mechanistic insight into NPLIN and sonocrystallisation, experimentally. This chapter provides an outline of the subsequent chapters in this thesis.

Proposals for the underlying mechanism behind NPLIN have stirred active debate since the initial discovery of this effect by Garetz *et al.* in 1996.[242] More recently, doubts have been cast on the initially proposed effects of the optical electric field acting directly upon solute clusters and critically, these proposals do not explain why there is a laser power threshold below which NPLIN does not occur.[256] According to Alexander and Camp, the evidence so far points to the impurity particle-heating mechanism.[235] Nucleation induction from a collapsed cavity generating a localised region of high pressure and elevated supersaturation has been proposed for both LIN by impurity particle-heating and LIN by optical cavitation.[235, 266] Despite a recent report corroborating that filtration prior to laser irradiation suppresses NPLIN, Kacker *et al.* concluded that laser-induced shockwaves were not behind this effect.[240] This conclusion was on the basis of apparent higher peak pressure values recorded with a mask placed outside the vial (blocking the beam), than with the laser passing through the solution.[240]

"Know thy dirt"

Chapter 4 presents an investigation of the NPLIN impurity particle-heating mechanism with needle hydrophone measurements and high-speed imaging performed in single pulse-irradiated aqueous ammonium chloride solutions.

From a review of the sonocystallisation literature, it is clear that the majority of previous studies investigated the use of high-power ultrasound for inducing crystal nucleation and fragmentation. Overall, there have been a limited number of studies investigating the effects of acoustic cavitation on crystal polymorphism and purity, thus these applications are not well understood. Furthermore, few reports involved measurement of cavitation activity in the generated sound field and no studies were found using acoustic detection. The physical properties of a liquid have been reported to significantly affect the cavitation activity, under the same applied ultrasound parameters.[150, 195, 196] More specifically, Tzanakis *et al*. reported significantly higher cavitation intensities measured in water and glycerine, on comparison with ethanol under a 20 kHz ultrasound field (comprising a horn immersed into a rectangular glass tank). There are no known studies on the effect of solvent properties on the sonocrystallisation outcomes under an applied high-power ultrasound field.

"Know thy liquid"

In order to guide further investigation, Chapter 5 presents a comparison of cavitation activity in acetonitrile, butanol, ethanol, isoamyl alcohol, methyl ethyl ketone and water, under a high-power ultrasound field.

Whilst the generation of cavitation bubbles may induce nucleation heterogeneously by providing a lower surface free energy provided at the bubble surface, this does not explain the generation of a metastable form of a solid which is not obtained at the same supersaturation level, without the application of ultrasound. The selective crystallisation of the metastable form of paracetamol is notoriously difficult to obtain in solution.[47] Mori *et al.* reported the selective generation of form II at 28 and 45 kHz and the mechanism behind this remains unclear.[223] Though, the effects of ultrasound on polymorphism do appear to be supersaturation dependent.[193] Furthermore, previously reported greater impurity rejection of paracetamol in the presence of structurally related impurities seems counterintuitive to other accounts of increased crystal growth rates, under a high-power ultrasound field.[225, 234] Nguyen *et al.* compared purity data at one ultrasound setting and silent experiments, in which nucleation induction occurred at significantly higher

supersaturation levels, which made comparison difficult.[234] This report is the only known study on the effect of high-power ultrasound on purity and the mechanistic proposal of cavitation phenomena enhancing impurity rejection requires further investigation.

"Know thy sound field"

Chapter 6 presents an investigation into the effects of cavitation on polymorphism and product purity in the cooling sonocrystallisation of paracetamol with added structurally similar impurities.

An overview of the scope of this research is provided in Fig. 3-1

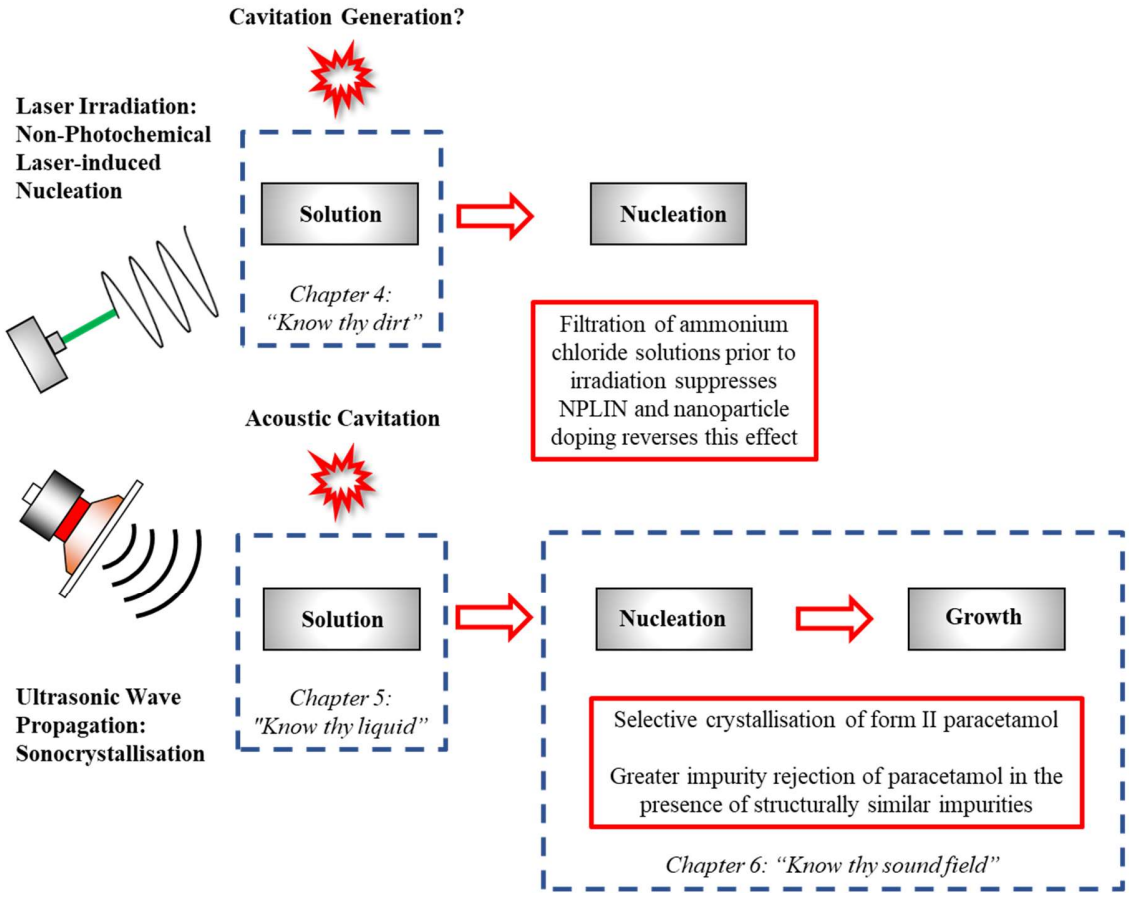

Figure 3-1 Research scope

An Investigation of the Non-Photochemical Laser-induced Nucleation Impurity Particle-Heating Mechanism

"Know thy dirt"

Symbols
Energy density (u)
Peak pulse power (j_{peak})
Rayleigh collapse time (T_c)
Supersaturation ratio (S)

Abbreviations
Ammonium Chloride (NH_4Cl)
Broadband Integrated Voltage (BIV)
Deionised (DI)
Fast Fourier Transform (FFT)
Iron Oxide Nanoparticle (Fe_3O_4 NP)
Laser-induced Nucleation (LIN)
Root Mean Square (RMS)
Ultrapure (UP)

Declaration: Both Martin Ward (MW) and Clarissa Forbes (CF) planned and executed the experimental work presented in this chapter.

4.1. Introduction

At laser pulse energies far below the threshold for optical cavitation generation, the impurity-particle heating mechanism may explain the induction of multiple nuclei within the path of an unfocussed beamline. It has already been established that the pulsed laser irradiation of plasmonic metal nanoparticles in an aqueous dispersion can photothermally generate nanobubbles that persist in the liquid.[262] Of relevance to the impurity particle-heating mechanism, it is not yet clear how the irradiation of nano-sized particles dispersed in a supersaturated solution can lead to crystal nucleation.

A study of cavitation bubble dynamics from laser ablation on a 1 mm thick copper plate in water by Tanabe *et al.* provided relevant prior knowledge.[286] With high-speed imaging (1 000 000 fps), the authors measured the generation of a single bubble from a single laser shot (1064nm, 13ns), both at pulse energies of 50 mJ and 100 mJ. Following formation, each bubble was observed to undergo several repeated expansions and shrinkage with reductions in size exhibited by later bubbles.[286] The bubble lifetime and maximum radius was longer and larger at 100 mJ than for 50 mJ, with the maximum radii at *ca.* 2.2 mm and 1.4 mm, respectively. From equation 1-7, the Rayleigh collapse time of each bubble is approximated ≈ 200 μs and 127 μs at 100 mJ and 50 mJ, respectively. Importantly, the authors noted that when the first bubble collapses, mixing of the gas phase within the bubble and the liquid phase outside the bubble occurs. Following subsequent expansion and shrinkage cycles, small particle-like shadows were observed to form and since some of these objects appeared to merge with each other to form larger bubbles before gradually disappearing, the authors concluded that these particles were likely to be smaller bubbles rather than small copper particles dispersed into the liquid.[286] Reuter *et al.* have described these gas phase entities following bubble collapse as remnant bubbles.[287]

On the mechanism behind LIN, previous computational fluid-flow simulations by Hidman *et al.* provided evidence for the formation of a concentrated fluid region at the periphery of a laser-induced vapour cavity.[282] More recently, the same group theoretically tested and confirmed the plausibility of a high solution supersaturation generated due to solvent

evaporation during the bubble growth period, which triggers the nucleation event.[288] Accordingly, it may be speculated that LIN of multiple primary crystal nuclei within an unfocussed beampath would require the generation of a multi-bubble field.

The laser irradiation setup developed for the work in this Thesis was adapted from a previous study by Javid *et al*.[249] The aqueous ammonium chloride (NH_4Cl) system selected was based upon the aforementioned work by Ward *et al*.[257] Therein, the authors reported an average of 6-10 crystals from the irradiation (1064 nm, 5.5ns, 12 MW cm^{-2}) of unfiltered and undoped samples.[257] The main objective of this work was to investigate the impurity particle-heating mechanism with high-speed imaging and needle hydrophone measurements, in order to gain experimental evidence for LIN *via* laser-induced bubble nucleation.

4.2. Materials and Methods

4.2.1. Solution Preparation and Laser Irradiation

NH_4Cl (ACS reagent, Ph. Eur., ≥99.5%, Lot: STBH2159) and iron (II, III) oxide nanopowder 50-100 nm, 97% trace metals, Lot: MKBT3736V) were obtained from Sigma Aldrich. Aqueous solubility data for NH_4Cl was taken from from Lide.[289] Deionised (DI) water was dispensed *via* an in-house water purification system (Millipore Milli-Q, 1.1 $M\Omega \cdot cm^{-1}$). Aqueous stock solutions of iron oxide nanoparticles (Fe_3O_4 NP) and NH_4Cl were prepared in DI water and particle concentration measurements were performed with the NanoSight LM10 NTA (NanoSight, Amesbury, UK). Ultrapure water (UP, HPLC Grade) was purchased from Alfa Aesar and a further water sample was taken directly from the laboratory tap. The sterile polyethersulfone (PES) syringe filters used were 0.45 μm and 0.8 μm (Millex®, Millipore Express), 0.1 μm, 0.45 μm and 1.2 μm (Acrodisc®, Pall Corporation). Samples were exposed to irradiation by a single-pulse from a Nd:YAG laser (Continuum Surelite II-10) with a wavelength of 1064 nm and a pulse duration of 6 ns. The laser beam was passed through a telescope (constructed in-house with a +300 mm

plano-convex lens and a -150 mm plano-concave lens) before it reached a 1.5 mm circular pinhole (resulting in a spatial profile that was near top-hat). The standard irradiation mode was linear polarized and an incident mean laser power of 310 mW (measured at 10 pulses s^{-1}) was used for all experiments. An average peak pulse power (j_{peak}) of 292 MW cm^{-2} (based on a circular beam, top hat profile) and an energy density (u) of 0.14 J cm^{-2} was calculated (based upon a pulse energy of 3.1 mJ and a spot size of 1.5 mm).

4.2.2. Needle Hydrophone Measurements

A schematic of the needle hydrophone measurement setup is provided in Fig. 4-1.

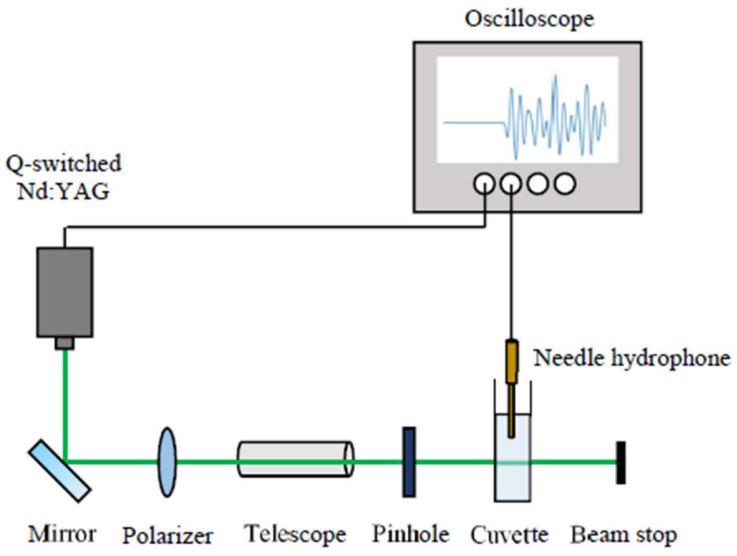

Figure 4-1 Schematic representation of needle hydrophone measurements of single-pulse irradiated samples

Acoustic detection was performed with a NH100 1.00mm PVDF needle hydrophone (Precision Acoustics Ltd., Dorset, UK) which was calibrated by the National Physical Laboratory (Teddington, UK) in 2019 (certificate reference: 2018100442-3). The tip was located using a positioning stage with 0.01mm precision (model: TVP-L, Sauter GmbH,

Wutöschingen, Germany). Signals were collected using an Infiniium Mixed Signal 1 GHz Oscilloscope (model: MSO8104A, Agilent Technologies, Cheadle, UK), which was triggered with each laser pulse. The needle hydrophone measurements were carried out under ambient conditions (room temperature in the range 21.0—21.8 °C). A consistent sample volume of 3000μL was prepared in a macro fluorescence cuvette (model: CV10Q3500F, Thorlabs, Ely, UK) prior to irradiation. The hydrophone tip distance from the laser beam was 10 mm and the time between measurements in the same sample were taken approximately 1 minute apart, allowing for the sample to refresh following a single pulse. Signal processing was performed using MATLAB (Mathworks, Massachusetts, USA). Firstly, the data was treated with a low-pass Kaiser Window filter to remove noise from the time domain data. The Root Mean Square (RMS) of the filtered data was calculated in order to compare the magnitude of each signal. A Fast Fourier Transform (FFT) was also performed, and the output data was integrated to give the Broadband Integrated Voltage (BIV), which is used to quantify the cavitation energy (see section 1.2.3.)

4.2.3. High-Speed Imaging

High-speed imaging was carried out using the Fastcam SA1.1 (model: 675K-M1, Photron, Tokyo, Japan), together with a 5x objective lens (model:8-20-44, OPTEM HR) fixed to a 12x zoom lens (model: 1-50486D, NAVITAR). A 9.87μm depth of field was provided and the frame rate was 100 000 fps, allowing for 10μs observation intervals. Samples were backlit by a LED 24x array arrangement (model:LT-V8-15-24, GSVitec GmbH, Bad Soden-Salmünster, Germany). In order to scale all images, a 1 mm graticule (model: RIL352P Thorlabs, Ely, UK) was imaged and select frames from image sequences were binarised using the default settings in ImageJ (NIH, New York, USA).[290] The field of view was 1120μm by 445μm and the length of one pixel was determined to be 3.6μm, which can be considered as the object size detection limit. In order to count the number of bubbles within a frame of interest, image processing was performed using MATLAB (more specific details together with an example are provided in Appendix A-1).

Experiments were carried out in 10ml screw top clear glass vials (Fischer Sci), placed inside an optical glass cell (model:G-752, Kromatek) that was filled with baby oil (Johnson and Johnson GmbH), which matched the refractive index of the glass. For supersaturated samples, vials containing 6mL (0.441 g/g) NH_4Cl aqueous solution (S=1.2 at 21.1 °C) were initially held at 50°C, to ensure that all solute had dissolved, before being removed to cool slowly to ambient conditions (room temperature from 20.7–21.5 °C). A 0.328 g/g NH_4Cl aqueous solution was used for undersaturated samples (S=0.9 at 21.1 °C) that were irradiated under ambient conditions. Each vial was placed inside the glass cell prior to irradiation with a single pulse. As with the needle hydrophone measurements, the camera recordings were triggered synchronously with a single-pulse.

4.3. Results and Discussion

Initial attempts to record acoustic signals in single-pulse irradiated supersaturated solutions (S= 1.1, 1.2 and 1.3) were unreliable due to the occurrence of spontaneous nucleation. Each solution was dissolved at 50°C in a water bath before removal and the positioning of the hydrophone tip in the centre of the vial. During cooling to room temperature, it was found that heterogeneous nucleation of the NH_4Cl would occur at the hydrophone tip (as shown in Fig. 4-2). Due to the construction and the function of the hydrophone tip, it was not possible to coat or polish the tip in attempt to reduce the propensity for heterogeneous nucleation.

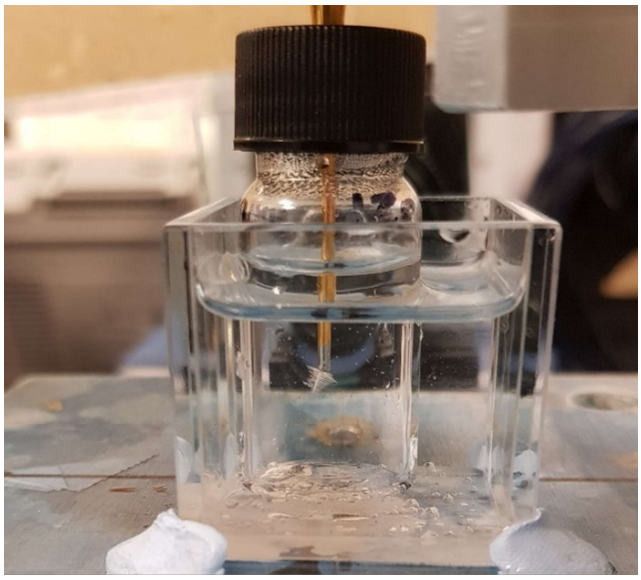

Figure 4-2 Image of the needle hydrophone tip (d=1.5 mm) triggering nucleation in a supersaturated (S=1.2) NH_4Cl solution

From this, it was concluded that simultaneous high-speed imaging and hydrophone measurements of supersaturated samples was not possible. Therefore, the following strategy was conceived:

- Capture single-pulse irradiated undersaturated (S=0.9) and supersaturated (S=1.2) NH_4Cl solutions with high-speed imaging, investigating the effects of Fe_3O_4 NP -doping
- Perform needle hydrophone measurements in single-pulse irradiated undersaturated (S=0.9) NH_4Cl solutions, investigating the effects of Fe_3O_4 NP-doping and solution filtration

A fixed j_{peak} of 292 MW cm^{-2} was used throughout this study, which is significantly higher than the peak power reported in the previous NH_4Cl study by Ward *et al.* (12 MW cm^{-2}).[257] This was selected in order to maximise the likelihood of capturing bubbles and crystals along the beampath with imaging. Yet, this power is still far below the average power threshold for the breakdown of DI water, which was previously reported as 76 GW cm^{-2} (1064 nm, 6 ns pulse duration).[273]

4.3.1. High-Speed Imaging

This section provides a summary of the high-speed imaging observations and reports key frames from the image sequences recorded in (i) an undoped, undersaturated NH_4Cl solution, alongside samples that were doped with Fe_3O_4 NP prior to irradiation, (ii) an undoped, supersaturated NH_4Cl solution (iii) an Fe_3O_4 NP-doped, supersaturated NH_4Cl solution. For all image sequences reported, the laser (single 6 ns pulse) was triggered between the 1395th and 1396th frames. The former was therefore reassigned as frame 0 and taken as the background, with the latter (frame 1) being the first frame in which objects could be detected. The scale bar in all images represents 100 μm.

4.3.1.1. Captures of Laser-induced Bubble Nucleation in Undersaturated NH_4Cl Solutions

The number and size range of bubbles captured following the single pulse irradiation of NH_4Cl solutions (S=0.9) that were doped with increasing volumes of Fe_3O_4 NP solution prior to irradiation, are reported in Table 4-1.

Table 4-1 Bubble counting results from images obtained following the single pulse irradiation of undersaturated NH_4Cl solutions

Volume Fe_3O_4 NP suspension added (μL)	Bubble count	Bubble diameter size range (μm)
0	1	25
20	11	3.6-39
40	16	3.6-45
60	27	3.6-37
80	30	3.6-41
100	51	3.6-52
200	55	3.6-67
300	160	3.6-59

It has already been established that Fe_3O_4 NP are excellent photothermal agents that generate heat on absorption of 1064 nm radiation.[291] From Table 4-1., it is clear that the

number of bubbles generated within the field of view increases with the volume of Fe_3O_4 NP suspension added prior to irradiation. From Nanoparticle Tracking Analysis, the average equivalent particle concentration of the stock Fe_3O_4 NP suspension was determined to be $5.10 \pm 2.12\ 10^8$/mL and the stock NH_4Cl solution was determined to be $1.38 \pm 0.50\ 10^8$/mL. Measurement of an NH_4Cl solution in which 300µL Fe_3O_4 NP suspension had been added provided an average equivalent particle concentration of $1.52 \pm 0.33\ 10^8$/mL. Furthermore, a reduction in the mean particle size was observed for all replicate measurements of the stock NH_4Cl solution (in the range 266-287 nm) following the addition of 300µL Fe_3O_4 NP suspension (in the range 192-240 nm). All NanoSight measurements performed are reported in Appendix A-2.

A mechanism involving NP and /or NP aggregates absorbing light from the laser pulse and rapidly heating up to generate photothermal vaporisation in the surrounding liquid seems plausible to explain the imaging observations of bubbles. As the optical breakdown power threshold of the Fe_3O_4 NP in suspension is unknown, ionisation of the NP and/or NP aggregates present in the irradiated solution can not entirely be ruled out. Both of these mechanisms could potentially explain the generation of multiple cavitation bubbles within the laser beampath. Furthermore, due to the object size detection limit of this setup (3.6µm), the presence of additional nanobubbles cannot be confirmed or ruled out. Following irradiation, bubble nucleation is expected to be initiated at successive time points as the laser beam passes through the solution, leading to each individual bubble reaching its maximum radius at varying time points. It is also expected that the individual bubble size would depend upon the size of the irradiated NP and/or NP aggregate, with more energy being absorbed by larger particles and/or particle aggregates, resulting in the generation of larger bubbles with longer lifetimes.

Select images captured up to 70ms following the single-pulse irradiation of the NH_4Cl solutions (S=0.9) where the solution was (a) undoped, (b) doped with 40µL Fe_3O_4 NP solution and (c) doped with 200µL Fe_3O_4 NP solution prior to irradiation are presented in Fig. 4-3.

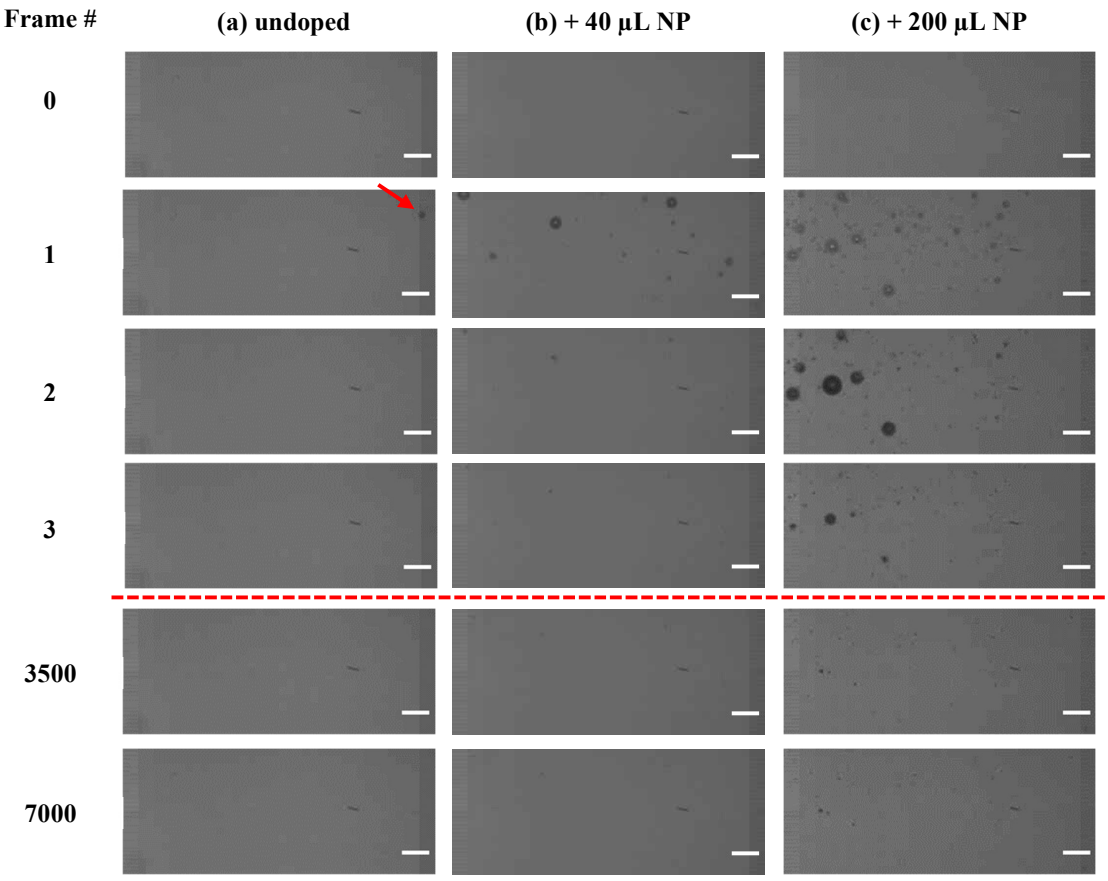

Figure 4-3 Images captured up to 70ms following the single-pulse irradiation of NH_4Cl solutions (S=0.9) where the solution was (a) undoped, (b) doped with 40µL Fe_3O_4 NP and (c) doped with 200µL Fe_3O_4 NP. *The red arrow points to a single 25µm diameter bubble detected in the undoped solution. The largest bubble diameters of 45 and 67µm were detected in doped solutions (b) and (c), respectively.*

The single bubble generated in the undoped solution is visible in frame 1 and no further observations were made in the following frames. Assuming a maximum radius of 12.5µm, a T_c of 1.13µs is calculated from equation 1.7. It is unknown at what stage in the lifetime of this bubble that this image captures, but this approximation confirms that the 10µs observation intervals are insufficient to study the dynamics of this bubble. For doped samples, (b) and (c), multiple bubbles were detected within the field of view following a single pulse. Furthermore, in frame 1 of (b) and (c) light emission can be observed as a

white flash in the centre of particles captured within the frame; the light is of a wavelength < 800nm (below the cut off for the IR optical filter used for stray scatter of 1064 nm laser light in the setup). Based on this, the light emission is presumed to be incandescence from particle heating following laser irradiation however, further investigation would be required to confirm this observation.

Expected observations of a cavitation bubble following formation is growth to a maximum radius, shrinkage to collapse and the bubble expansion and shrinkage repeats until all energy is dissipated and a bubble remnant may remain in the liquid.[278, 279] No shockwaves can clearly be observed following the shrinkage of bubbles in samples (b) and (c), which is attributed to both the temporal and spatial resolution of this setup. From sequence (b), in the case of the largest bubble detected at 45μm bubble in frame 1, a T_c of 2.0 μs was calculated. Whereas, for the largest bubble detected in frame 1 of sequence (c), at 67μm a T_c of 3.0 μs was calculated. Whilst it should be noted that the maximum radii of the bubbles are assumed in these calculations, it is deduced that the collapse of the initial bubbles nucleated would have been outwith the detection limit of this setup and that bubbles/objects seen in following frames may have undergone further expansion and shrinkage cycles following the collapse of the first bubbles. On consideration of the bubble sizes generated under these conditions, it is estimated that imaging shockwave propagation following bubble collapse would require observations at significantly < 1μs intervals (imaging at > 1, 000, 000 fps) and a higher spatial resolution.

Dark particle-like objects were observed at the same locations where the largest bubbles within the field of view were observed prior, even up to 70ms following irradiation in (b) and (c). It is unclear if these objects are (i) bubble remnants (as previously described by Tanabe *et al.*[286]) (ii) debris from the irradiated particles or even (iii) crystal nuclei that eventually re-dissolve.

4.3.1.2. Captures of LIN in Supersaturated NH_4Cl Solutions

In total, six high-speed imaging attempts of LIN were performed in supersaturated NH_4Cl solutions; three were undoped and three were doped with Fe_3O_4 NP prior to irradiation.

The video files of these experiments are attached to this thesis electronically. The undoped samples will be discussed first and a summary of the LIN high-speed imaging attempts are provided in Table 4-2.

Table 4-2 Summary of high-speed imaging observations in undoped supersaturated NH_4Cl Solutions

Experiment	Bubble observations in frame 1	Crystal observations in frame 90 000
Undoped A, *S*=1.2	3 bubbles in the range 14-25µm diameter	10 originated within field of view (+2 outermost crystal that were observed to move into the field of view). The first observable crystal appeared in same location as the 25µm bubble observed prior and further crystal later appeared in the location in which a 20µm bubble was observed in frame 1
Undoped B, *S*=1.2	1 18µm diameter bubble detected	9 originated within field of view. The first observable crystal appeared in the same location as the bubble observed prior
Undoped C, *S*=1.2	0 detected	11 originated within field of view

Key frames from the image sequences recorded in undoped samples B and C are provided in Appendix A-3. In sample C, no bubbles were detected following irradiation and the first observable crystal was detectable from *ca.* 50ms (frame 5000). Interestingly, in samples A and B, the first observable crystal appeared in the same location as the largest (or in the case of B, single) bubble detected prior. The video files of all LIN imaging attempts are attached to this thesis electronically. The final frames of each LIN file (# 138311) are provided in Appendix A-4, in which the growing crystals appear less round and more jagged, which is consistent with the dendritic morphology of NH_4Cl crystals nucleated by laser irradiation.[257] in the case of undoped samples A and C, between 0.9s and 1.38s following irradiation, a further growing crystal was observed to move into the

field of view. Overall, all image sequences clearly showed 9-11 crystals originating and growing within the field of view. Key frames from undoped A are shown in Fig. 4-4 and 4-5. For clarity, binarised images are presented underneath the corresponding frame (obtained from the default binary processing settings in ImageJ and in which the background image was subtracted prior, for the removal of artefacts).

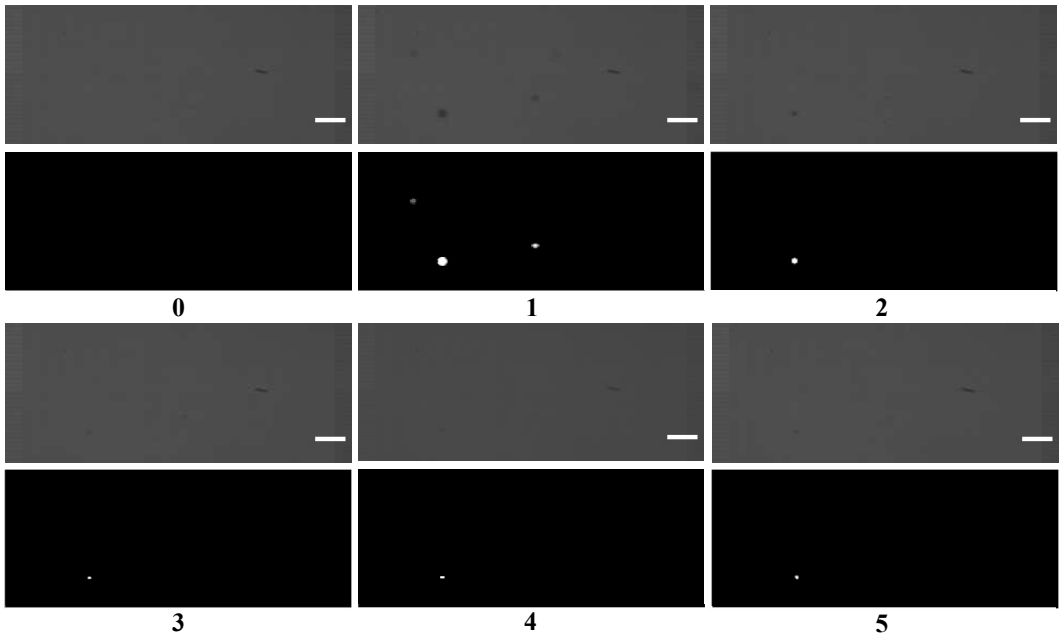

Figure 4-4 Images captured following the single-pulse irradiation of undoped A NH_4Cl solution (S=1.2) *Three bubbles in the range 14-25μm diameter can be observed in frame 1. An unknown object in the position of the largest bubble previously detected is observed to reduce in size and persist in the solution between frames 2-5.*

Following the passage of a single laser pulse through the solution and within the field of view, three bubbles of diameters, three bubbles (size ranging from 14–25 μm) were observed in frame 1. The T_c of a 25 μm bubble was previously approximated to be 1.1μs. Therefore, the object visible in frame 2 may be present from further expansion and shrinkage cycles of the bubble following initial collapse. The unknown object was observed in the frames following, in which no size change was observed to have occurred. Fig. 4-6 shows further images captured in this sequence from 5-900ms. By frame 500

(5ms), the unknown object was still observable in the same location and no obvious size change was observed. It seems likely that this unknown object is a remnant bubble persisting in the liquid, as previously described in the literature.[286, 287] Growth of this object is inferred between frame 500 and 10000 (5-100ms). Due to the imaging resolution, it is not possible to determine the exact frame that the crystal was first observed however, it is clear that there is a growing object that originated in the location where the 25µm bubble in frame 1 was detected prior (circled in red).

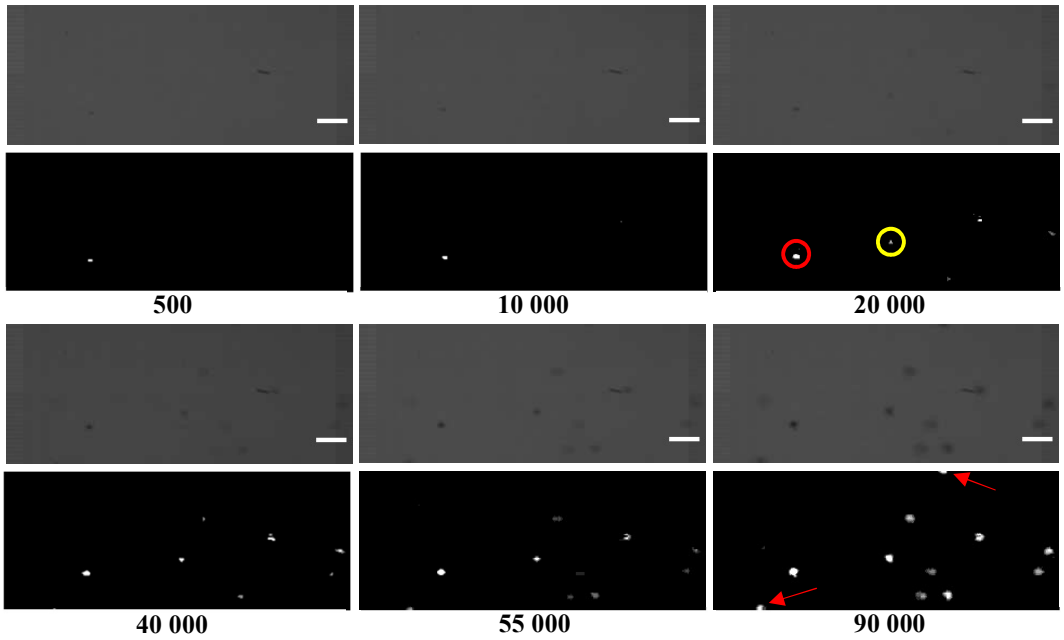

Figure 4-5 Images captured between 5-900ms following the single-pulse irradiation of undoped A NH_4Cl solution (S=1.2). *Growth of the first observable crystal is inferred between frame 500 and 10 000. In frame 20 000, five crystals are observed, two of which (circled in red and yellow) are in the same location as bubbles captured prior. By frame 90 000, twelve crystals can be observed however, the top-most and lower-most crystals (marked by red arrows) did not originate within the frame and were determined to have moved into the field of view.*

Five crystals are observable by frame 20 000 (20ms) and in this frame a crystal originating in the same location as the 20µm bubble detected in frame 1 can be observed (circled in yellow). Reuter *et al.* previously noted that the oscillation and collapse of a single

cavitation in the vicinity of a solid boundary (*i.e.* the walls of a cuvette), induces intense microconvection and vortex formation in the surrounding liquid.[287] A multi-cavitation bubble field within the beampath is expected to be highly turbulent, which may explain why additional crystals (marked by red arrows) are observed to move into the field of view, from above and below. The 14μm bubble in frame 1 seemingly does not lead to a crystal, which either suggests that 100% of cavitation events may not result in nucleation or that the crystal generated has moved out of the field of view, consistent with the generated turbulence and mixing within the beampath. Overall, eight crystals were observed to have originated and grown in locations where bubbles were not detected prior in solution A. Whilst these crystals may have originated from bubbles that were of a size and lifetime out with the temporal resolution of the imaging setup, it may also be plausible that these crystals originated from cavitation events out with the field of view.

Importantly, in both solutions A&B, the first observable crystals were located at the position of the largest bubbles captured in previous frames of the high-speed recording. It is unclear what role, if any, the persisting object (an unidentified, long-lived object noted immediately after bubble shrinkage/collapse) has in nucleation induction. The object may be a persisting bubble remnant that provides a surface for heterogeneous nucleation or it may even be the pre-nucleation event in progress (from which, details cannot be resolved in the current imaging setup). Hidman *et al.* theoretically demonstrated nucleation induced from high solution supersaturation generated from solvent evaporation during bubble growth.[288] It follows that the extent of supersaturation increase would increase with the size of the bubble generated, as more solvent would be vaporised and this proposal aligns with the observation of the first crystal in the position of the largest bubble observed prior.

From the observations of doping undersaturated solutions with absorbing nanoparticles, it is known that cavitation is induced (Section 4.3.1.1.). For supersaturated solutions, this methodology may provide an ideal route to study the relationship between bubble cavitation and crystal nucleation. Fe_3O_4 NP-doped LIN image sequences are summarised in Table 4-3.

Table 4-3 Summary of high-speed imaging observations in NP-doped supersaturated NH_4Cl Solutions

Experiment	Bubble observations in frame 1	Crystal observations in frame 90 000
Doped A (+ 100µL Fe_3O_4 NP), *S*=1.2	2 bubbles were observed in frame 1 (1 bubble was 22µm and the other bubble was very poorly resolved and difficult to size accurately (*ca*. 20µm)	8 originated within field of view. The first crystal appeared and grew in the location of the 22µm bubble observed prior
Doped B (+ 600µL Fe_3O_4 NP), *S*=1.1	50 bubbles in the range 3.6-42µm were observed in frame 1	Nucleation was not observed
Doped C (+ 600µL Fe_3O_4 NP), *S*=1.1	9 bubbles in the range 11-25µm were observed in frame 1	5 originated within field of view. The first observable crystal appeared in same location as the largest bubble observed prior

Firstly, an NH_4Cl solution that was doped with 100µL Fe_3O_4 NP suspension prior to irradiation was imaged and key frames are provided in Appendix A-5. Interestingly, the observable 22µm bubble in frame 1 shrank to 14µm by frame 2 and by frame 3; no object was detected in this position (although it may have been present and non-resolvable). By frame 5000 (50ms) the first crystal was observable in this location, which is consistent with the previous observations made in the undoped samples. In the previous captures of doped undersaturated solutions with absorbing nanoparticles (section 4.3.1.1.), when 100µL Fe_3O_4 NP suspension was added, 51 bubbles were detected. Whereas in doped solution A (*S*=1.2), only 2 bubbles were detected in frame 1. This suggests that an inhomogeneous dispersion of NP is created on addition of the NP suspension though; there may well be regions of high particle density out with the field of view.

Next, an NH_4Cl solution that was doped with 600µL Fe_3O_4 NP was imaged and fifty bubbles were detected in frame 1 (key frames are provided in Appendix A-5). By adding a considerably larger volume of the aqueous NP solution, the absolute concentration of

NH_4Cl was reduced and this sample therefore had a lower *S* of 1.1. It has already been established that decreasing the absolute concentration of the solute decreases the lability of samples to nucleate.[239] Sample B was observed not to nucleate, which can be attributed to the lower *S* of this sample. Furthermore, the large number of bubbles nucleated within the field of view implies a high NP particle density in this region, which would generate considerably higher heat than in sample A, where two bubbles were detected. Therefore, on consideration of the large number of cavitation bubbles generated within the field of view, it seems probable that any primary nuclei generated may have re-dissolved (before reaching a detectable size) if the solution temperature in the beampath was increased substantially. Finally, key frames from the next 600µL Fe_3O_4 NP-doped supersaturated solution (C) imaged are provided in Fig. 4-6 and 4-7.

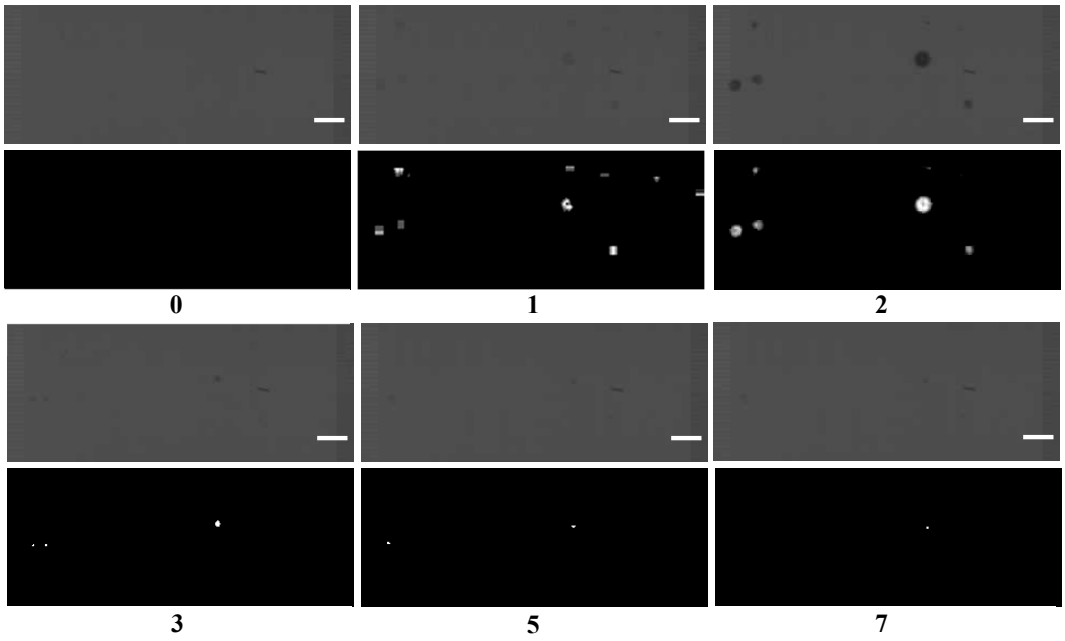

Figure 4-6 Images captured following the single-pulse irradiation of Fe_3O_4 NP -doped NH_4Cl solution C (S=1.1). *Nine bubbles are observed in frame 1 (in the range 11-25 µm). By frame 2, three of the bubbles are not observed within the field of view, three bubbles have shrunk and three bubbles have expanded. By frame 3, the bubbles have shrunk and the object in frame 7 persists in the solution in the same position as the largest bubble (maximum diameter of 50µm in frame 2) observed prior.*

Assuming that the largest bubble was detected at its maximum size (radius = 25 µm), a T_c of 2.3µs is calculated. Therefore, it is speculated that the bubbles observed in frame 3 may have undergone several expansion and shrinkage cycles in the 10µs time difference following frame 2, based on previously reported observations of laser-induced cavitation bubbles.[286] As previously observed in undoped solutions A and B, an unidentified object in the position of the largest bubble detected prior was observed to persist in the solution. Considerably fewer bubbles were detected within the field of view in doped solution C (9 on compassion with 50 in doped solution B) and if the particle density within the beampath was lower then, accordingly fewer bubbles would be generated and it is deduced that this would generate less bulk/macroscopic heating of the supersaturated solution. Fig. 4-7 shows further images captured in this sequence from 5-900ms.

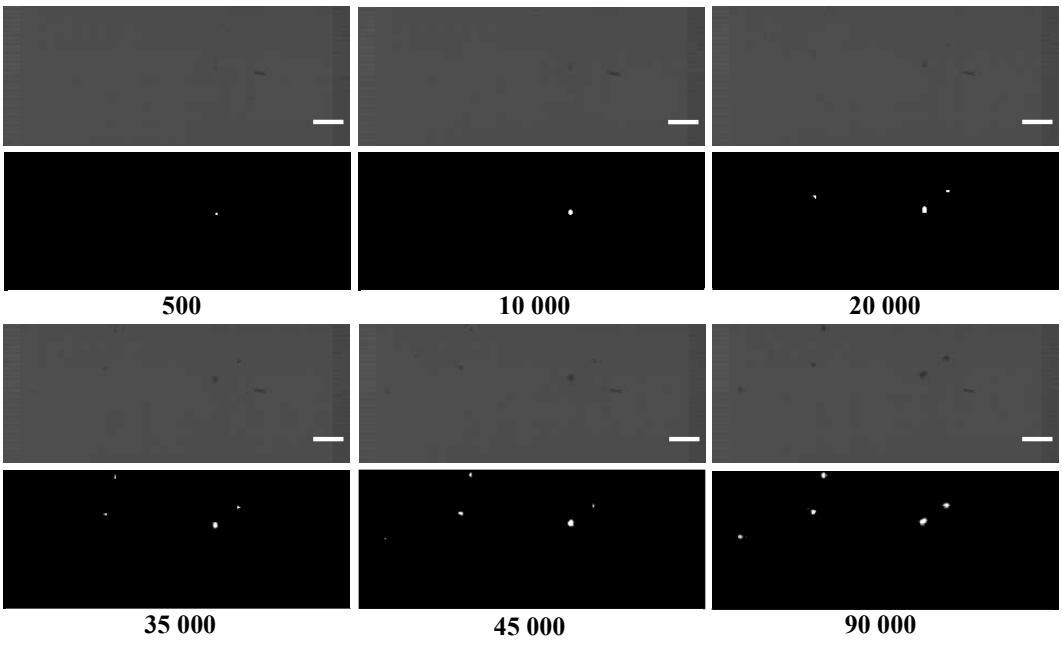

Figure 4-7 Images captured between 5-900ms following the single-pulse irradiation of Fe_3O_4 NP -doped NH_4Cl solution C (S=1.1). *Growth of the crystal is inferred between frame 500 and 10 000, which is in the same location as the largest bubble observed prior. By frame 45 000, five crystals can be observed.*

By frame 45 000 (450ms), five crystals can be observed within the field of view. Aside from the first observable crystal, which originated and grew in the same location as the

persisting object (and the largest bubble observed prior), the remaining four crystals can be observed in the upper half of these frames. This suggests there has been a net upwards drift of particles following the laser pulse, which may be explained by an increase in heat generated within the irradiated volume due to the added Fe_3O_4 NP, which induced an increased convection in the solution.

The dynamics of the multi-bubble cavitation field generated within the beampath are both difficult to visualise and capture, particularly within the constraints of 10μs observation intervals and a 3.6μm object size detection limit. It is highly likely that many sub-micron sized bubbles (nanobubbles) were generated that are far below the object size detection limit. It is thought that the generation of nanobubbles may contribute to the turbulence of the irradiated solution and it is unknown if they play a role in nucleation induction or the location in which generated crystals are observed. Bubble oscillation and collapse events within a confined area are known to cause microconvection and vortex formation in the liquid.[287] This aspect provides a further challenge in capturing bubble and crystal nucleation events.

Out of six imaging attempts, in one case no bubbles at or above the object size detection limit were detected before the appearance and growth of 11 crystals (undoped sample C). Also, in the case of doped sample B, fifty bubbles were detected in frame 1 and no crystals were generated, yet persisting objects in the location of prior bubbles were observable in frame 90 000 (900ms following irradiation). There were four samples in which both bubbles and crystals were detected within the field of view and in every case; the first observable crystal appeared in the same location as the largest bubble observed prior. This observation provides strong evidence that the cavitation event is directly linked to crystal nucleation in LIN. In three of these four solutions, an unknown object (most likely to be a bubble remnant following multiple expansion and shrinkage cycles of the nucleated bubble following the initial collapse) persisted in the solution and it is unknown if this object could have provided a surface for heterogeneous nucleation. Additionally, the theoretical proposal of nucleation induction from high solution supersaturation, generated from solvent evaporation during bubble growth would be extremely challenging to verify

experimentally.[288] However, as the extent of supersaturation increase would increase with the size of the bubble generated (as more solvent would be vaporised), this proposal seemingly aligns with the observation of the first crystal in the position of the largest bubble observed prior. Furthermore, in the undoped solution A, a second crystal was also later observed to originate and grow in the same location as a prior bubble. Overall, the high-speed imaging observations demonstrate a direct relationship between absorbing particles, cavitation generation and crystal nucleation. The induction of multiple primary nuclei by laser-induced particle heating presents an exciting opportunity for future studies of crystal nucleation (which would be expected to involve optimisation of and greater control over solution and optical parameters).

4.3.2. Needle Hydrophone Measurements

Within the unfocussed beampath, the nucleation of multiple bubbles of different sizes and lifetimes resulted in the generation of complex acoustic signals. The signal RMS value of the filtered data allowed the comparison of the magnitude of each signal. Furthermore, the FFT of the signal shows how the energy is distributed over the frequency domain, rather than the time domain. The integration of the signal following FFT provides the BIV, which is used to quantify the cavitation generated on laser irradiation.

Fig. 4-8 shows (a) example needle hydrophone measurements of a single-pulse irradiated DI water sample, a 0.328 g/g NH_4Cl solution (S= 0.9), together with the recorded signal with a beam stop placed in front of this solution (which blocked the passage of the laser through the cuvette). The corresponding FFT output of the waveforms are also provided in (b). The measurements clearly demonstrate that when the laser is allowed to pass through a sample of DI water and an NH_4Cl solution, broadband noise is produced.

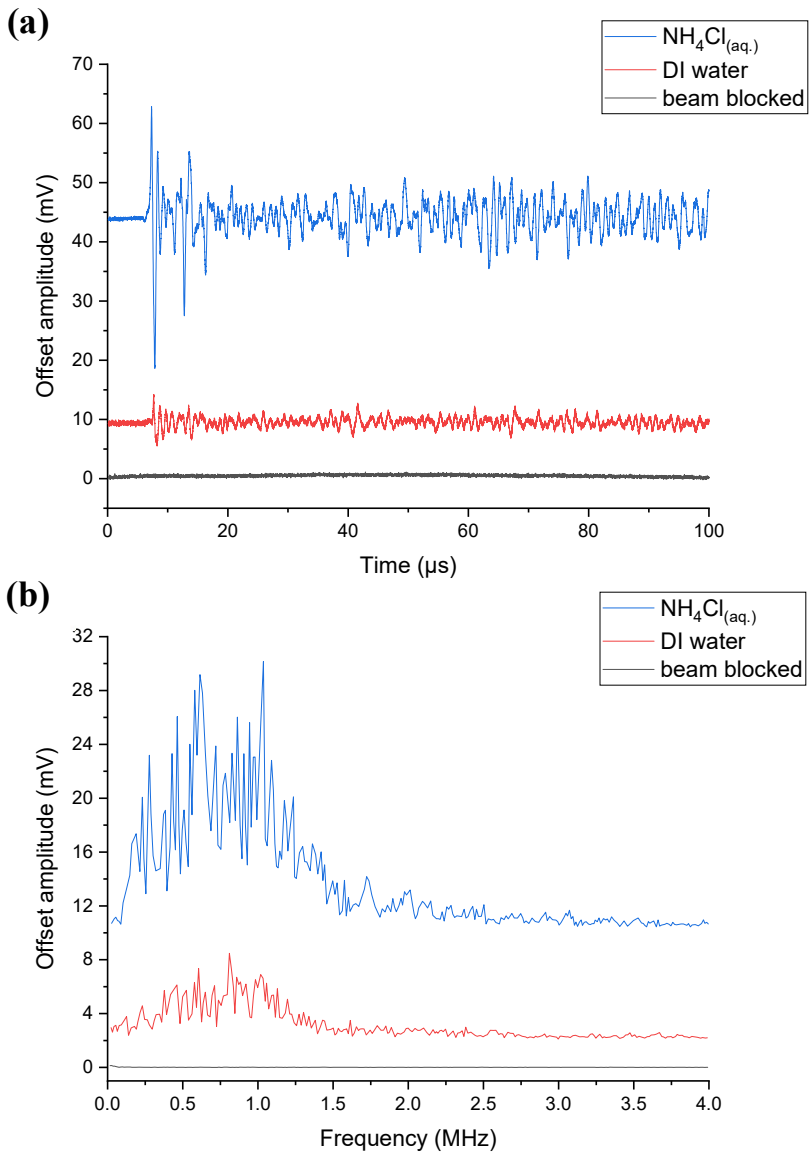

Figure 4-8 In (a) plot of time-domain waveforms recorded in a 0.328 g/g NH_4Cl solution, a DI water sample and with a beam stop placed outside of the solution; (b) Plot showing the corresponding FFT output of the waveforms

From, Nanoparticle Tracking Analysis (Appendix A-2), an equivalent particle concentration of 1.38 ± 0.50 10^8/mL wad determined for the 0.328 g/g NH_4Cl solution prepared in DI water. Furthermore, a DI water sample was measured as a background,

from which an equivalent particle concentration of 0.42 10^8/mL was obtained. Therefore, the particle concentration of the NH_4Cl solution is *ca.* 3.3 times higher than the DI water sample. It is important to highlight the fact that the identity of the impurity particles in both DI water and NH_4Cl are unknown. Though, in the previous NH_4Cl LIN study by Ward *et al,* it was implied that phosphate and iron nanoparticles were present in the solute.[257] However, impurities that are likely generated during the chemical manufacturing process could vary significantly between chemicals, manufacturer and across batches. Comparing the RMS of the waveforms in (a), the signal recorded in the NH_4Cl solution (2.367 mV) and the DI water sample (0.764 mV), the NH_4Cl solution is *ca.* 3.1 times higher, which implies a relationship between the particle population dispersed in the liquid and the recorded acoustic signal.

Spectrograms of the example signals are provided in Fig. 4.9, in which the vertical axis represents the time of the signal and the horizontal axis represents the frequency. This allows for a better visual understanding of the frequency content of the signals. Spectrograms are two-dimensional heat maps which represent the power spectrum of a signal as this signal sweeps through time. In Fig. 4.9, a distribution of frequency components can be observed at each time point. The higher in magnitude the frequency component is, the warmer the colour and vice-versa.

From the high-speed imaging observations reported in an undoped 0.328 g/g NH_4Cl section 4.3.1.1., a maximum bubble radius *ca.* 12.5μm allows for a T_c of this bubble to be approximated as *ca.* 1μs (although, successive expansion and shrinkage cycles following the initial collapse would also be expected to contribute to the broadband noise). From sound velocity (c) measurements performed in aqueous NH_4Cl solutions by Koga, a c of 1697 ms^{-1} was extrapolated for a 0.328 g/g solution at 22°C.[292] This allows a time for the acoustic events generated within the irradiated volume to reach the hydrophone (d=10 mm) to be approximated as 5.9μs. From Fig. 4.9, it is deduced that the energy of the signal recorded in NH_4Cl is mainly concentrated over the frequency range 0.2-1.5 MHz. from 5.6-8.1μs. This observation is consistent with bubbles forming, expanding and undergoing initial collapse within a *ca.* 2.5μs time period following irradiation.

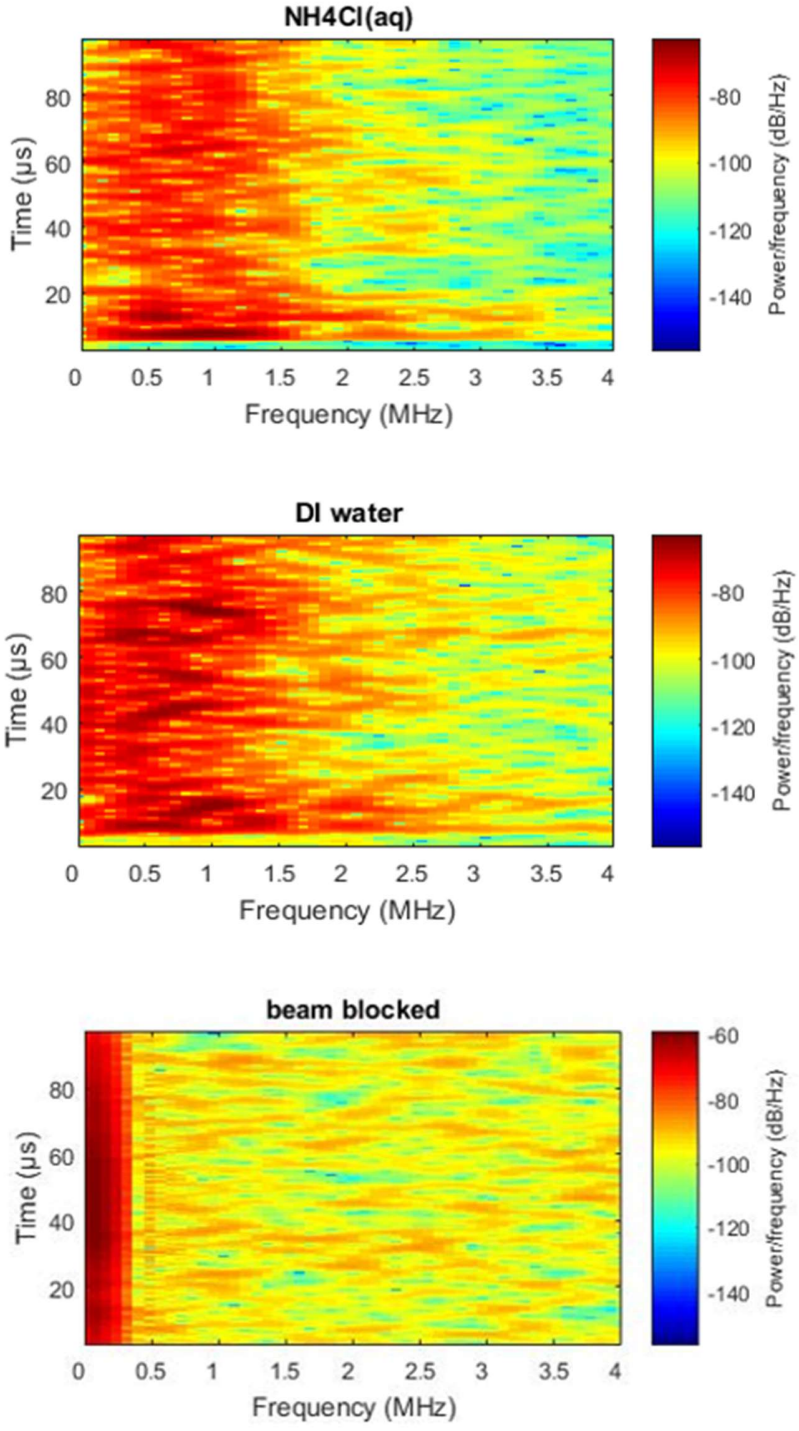

Figure 4-9 Spectrograms of the example signals measured in the 0.328 g/g NH_4Cl solution, a DI water sample and with a beam stop placed outside of the solution

A further region of high signal energy can also be observed in the frequency range 0.3-0.9 MHz, which can possibly be attributed to later bubble shrinkage events, or even the initial collapse of larger bubbles in the time period 11.3-13.8μs following irradiation. In the case of DI water, based on a *c* of 1488 ms^{-1} at 22°C, the time for the acoustic events generated within the irradiated volume to reach the hydrophone can be approximated as 6.7μs.[293] From Fig. 4.9, there are contributions to the frequency range 0.2-1.5 MHz commencing at 6.3μs; however, it is clear that the signal energy is more evenly distributed over the time period succeeding the detection of acoustic events following irradiation. From this, it is deduced that there were fewer and lower energy cavitation events captured in the DI water sample, on comparison with the NH_4Cl solution. Moreover, the signal RMS and BIV values obtained from hydrophone measurements performed in tap, DI and UP water (provided in Appendix A-6) were all of a similar magnitude. The following sections explore the effect of solute concentration, alongside Fe_3O_4 NP doping and filtration of solutions prior to irradiation on the acoustic signals recorded with the needle hydrophone. All of the time domain waveforms recorded in all laser-irradiated samples are provided in Appendix A-6.

4.3.2.1. Effect of Solute Concentration

The 5-shot average RMS values of the acoustic signals recorded in single-pulse irradiated solutions of increasing NH_4Cl concentration are shown in Fig. 4-10. In which, the RMS values have been corrected by subtracting the average RMS measurement in DI water from all samples.

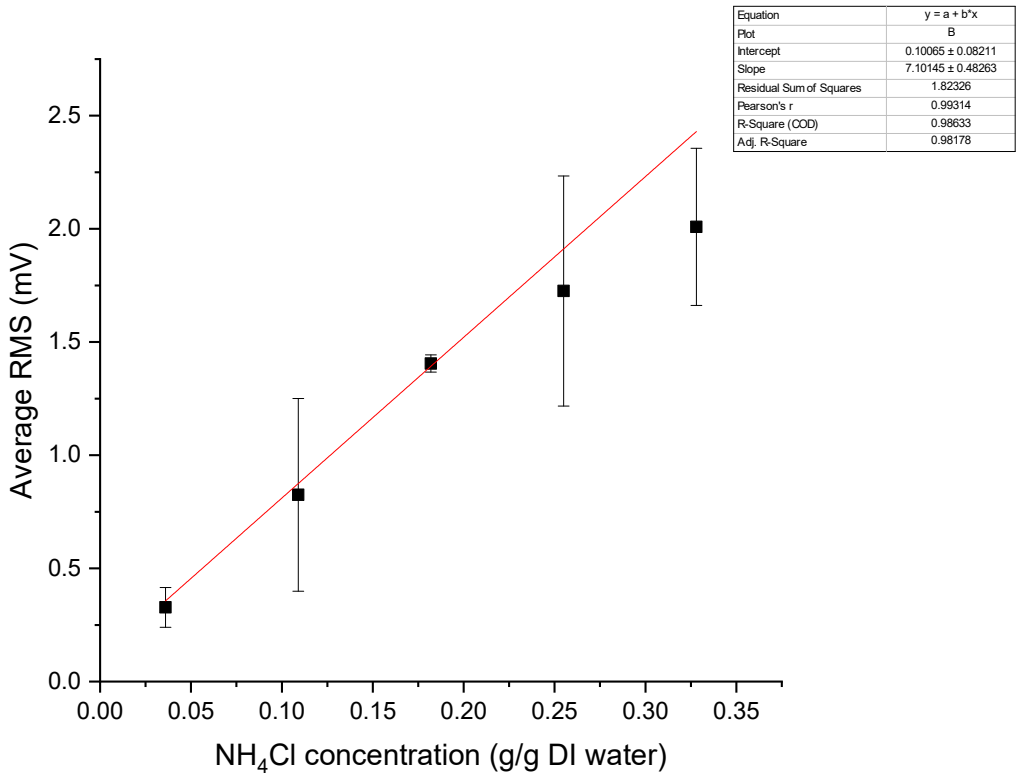

Figure 4-10 Plot showing the corrected 5-shot average RMS values of the signals measured in single-pulse irradiated NH_4Cl solutions as a function of solute concentration

As previously suggested, an increased signal magnitude can be attributed to the higher particle concentration of the solution with increasing amounts of solute added. The data shows a reasonable linear fit that would be expected if the RMS signal was directly dependant on solute concentration. This would be consistent with the presence of impurity particles in the NH_4Cl being responsible for photothermal cavitation and the resulting acoustic signal. Deviation from linearity in Fig. 4-10 can be attributed to the stochastic nature of the experiment. Significant variance was observed in the associated standard deviations from the 5-shot average between several samples and it is unknown how the particle population and size distribution is altered by each laser shot. The 5-shot average results of hydrophone measurements are provided in Table 4-4.

Table 4-4 5-shot average results of needle hydrophone measurements in NH_4Cl aqueous solutions of increasing solute concentration

NH_4Cl concentration (g/g DI water)	RMS (mV)	p-p Aamplitude (mV)	BIV (V Hz)
0.036	1.061 ± 0.088	11.3 ± 1.1	4341 ± 408
0.109	1.559 ± 0.426	20.8 ± 1.2	6940 ± 261
0.182	2.139 ± 0.038	17.2 ± 1.0	6551 ± 554
0.255	2.459 ± 0.508	38.0 ± 0.9	9580 ± 779
0.328	2.743 ± 0.035	45.6 ± 1.0	13004 ± 834

Observations of the signal decreasing following the first shot were originally considered to be due to dirt on the outside of the cuvette, which would presumably be removed after one pulse. However, in some cases (such as the 0.225 g/g solution), the signal RMS decreased following the first and second shot but by the fourth shot, the signal RMS was observed to increase. Overall, the data does demonstrate a trend of a linearly increasing RMS signal with solute concentration that would be consistent with the presence of absorbing impurity particles along with the solute itself.

Laser-induced cavitation is known to induce intense microconvection and vortex formation in the surrounding liquid.[287] Furthermore, in the previous report by Ward *et al*., the results of laser processing suggested that the laser destroys impurity particles.[257] For these reasons, a time between each sample shot of *ca.* 1 minute was allowed for the sample to refresh and for diffusion to refill the beampath to an equivalent particle concentration/distribution following each shot. Increasing the solute concentration of NH_4Cl resulted in the measurements of larger signal RMS values, which correlated with increased BIV values, from which a higher number of and higher energy cavitation events are inferred. Moreover, it is thought that needle hydrophone measurements of single-pulse irradiated solutions, in which the solute concentration is gradually increased, may provide a useful method for indicating whether photoactive impurities are present in the solute and therefore if LIN *via* particle heating is possible.

4.3.2.2. Effect of Solution Filtration and Nanoparticle Doping

Ward *et al.* previously demonstrated that filtering supersaturated NH_4Cl solutions prior to irradiation reduced the probability of LIN and significantly reduced numbers of primary nuclei were generated within the irradiated volume.[257] Dynamic Light Scattering measurements of unfiltered and filtered confirmed that filtration reduced the size distribution of particles present the solution. The authors also reported that this effect could be reversed by subsequently doping the solutions with Fe_3O_4 NP. [257] 5-shot average results of hydrophone measurements in NH_4Cl solutions that had either been filtered or doped prior to irradiation are provided in Table 4-5.

Table 4-5 5-shot average results of needle hydrophone measurements in 0.328 g/g NH4Cl solutions that had been either filtered or NP-doped prior to irradiation

Pre-treatments		RMS (mV)	p-p Amplitude (mV)	BIV (V Hz)
Filter pore size (μm)	Volume Fe_3O_4 NP suspension added (μL)			
unfiltered	-	5.090 ± 1.884	48.7 ± 12.4	23260 ± 7052
5	-	1.711 ± 0.026	26.1 ± 0.4	10712 ± 547
1.2	-	2.065 ± 0.283	28.0 ± 1.4	12330 ± 899
0.8	-	1.758 ± 0.313	26.9 ± 0.2	9838 ± 699
0.45	-	2.088 ± 0.185	28.0 ± 0.9	10736 ± 321
0.1	-	2.336 ± 1.057	30.6 ± 7.7	10336 ± 918
-	undoped	2.465 ± 0.350	31.8 ± 0.3	11977 ± 990
-	30	7.010 ± 0.964	83.4 ± 25.2	38200 ± 12205
-	75	13.589 ± 3.134	157.0 ± 26.9	80533 ± 11777
-	100	20.690 ± 2.746	213.0 ± 41.9	108289 ± 26793
-	150	21.767 ± 1.698	259.8 ± 19.9	104719 ± 22351
-	300	30.252 ± 3.909	418.1 ± 66.9	246413 ± 72877

Firstly, it should be noted that the untreated "unfiltered" and "undoped" samples were replicates that were dispensed from the same stock 0.328g/g NH_4Cl solution. Whilst the average RMS value recorded in the second ("undoped") measurement set was 2.465 ± 0.350 mV, in the first measurement set ("unfiltered") there is a large variance between

measurements with an average RMS value of of 5.090 ± 1.884 mV, in which individual values ranged from 2.773 mV in the fifth shot to 7.146 mV in the second shot. These results suggest that there is a level of inhomegenity in the dispersion of particles, which may be explained by the presence of larger impurity particle aggregates within the irradiated volume of the "unfiltered" solution measurement set in the first four shots. Presumably larger particle aggregates would absorb more energy and vaporise more of the surrounding solvent, producing larger bubbles which collapse with higher energy. The average RMS values of the "unfiltered" and "undoped" measurement sets were combined for comparison in Fig. 4-11., alongside the average RMS values recorded in (a) solutions that were filtered and (b) solutions that were doped with Fe_3O_4 NP.

Filtering solutions prior to irradiation did overall reduce the average RMS values measured on comparison with untreated NH_4Cl solutions. The combined RMS average of the untreated samples was 3.778 ± 1.883 mV, whereas filtering solutions with a 0.1μm pore size resulted in an average RMS of 2.336 ± 1.057 mV and filtering solutions with a 5μm pore size gave an average RMS of 1.711 ± 0.026 mV. These results support the proposal that the highest RMS measurements recorded in the unfiltered solution measurement set may be from large (> 5μm) particles/particle aggregates present in the solution, which are expected to absorb more energy and generate large vapour bubbles.

On consideration of the proposal that LIN occurs via high supersaturation generation due to solvent evaporation occuring during the bubble growth period: it follows that the irradiation of a <100 nm NP in the solution is likely to produce a considerably smaller bubble (vapourising a lower volume of the surrounding solvent), on compasison with a >5 μm particle.[288] It is thought that there will be a critical bubble size (and lifetime) for a cavitation event to lead to nucleation. Hence the nucleation probability is likely to be higher in the case where larger NP/NP aggregates are irradiated and generate larger bubbles with a longer initial growth period, leading to higher supersaturation elevation surrounding the bubbles.

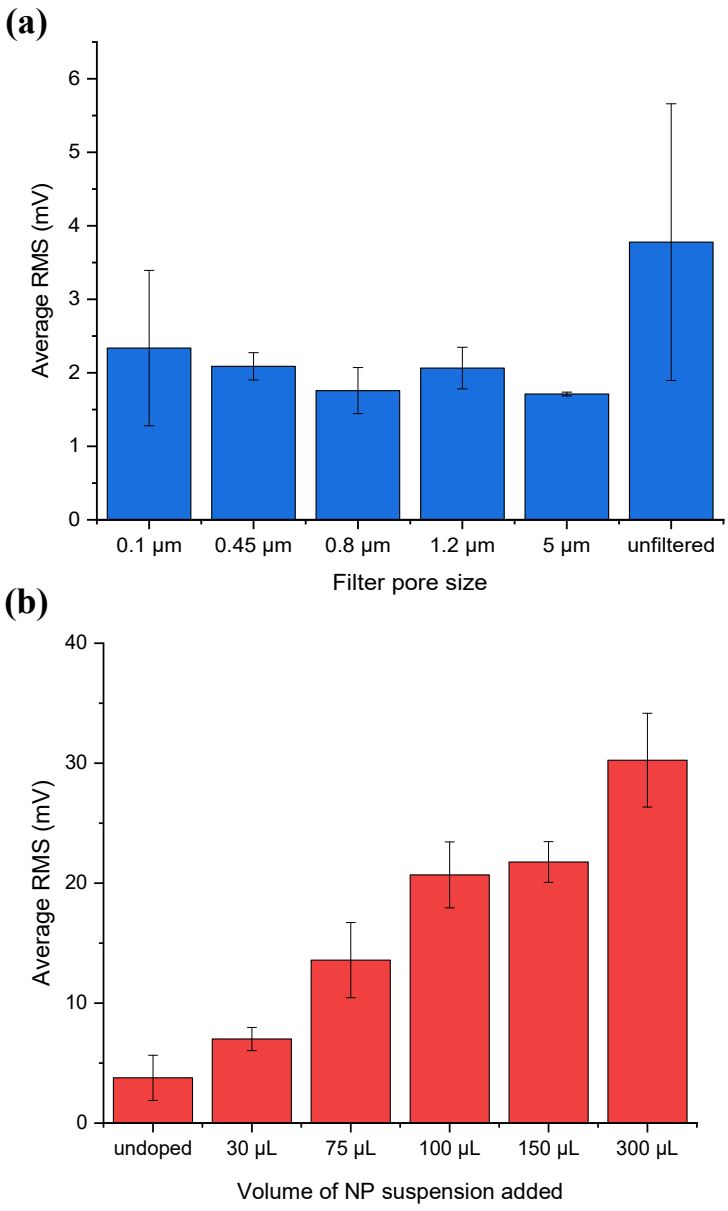

Figure 4-11 Graphs showing (a) the effect of filtration on the average RMS values measured in single-pulse irradiated NH_4Cl solutions and (b) the effect of Fe_3O_4 NP-doping on the average RMS values of the signals measured

Fe_3O_4 NP doping of the NH_4Cl solutions significantly increased the average RMS values measured in the solutions, on comparison with the undoped solution measurements. Combining these results with the high-speed imaging observations in irradiated understaurated NH_4Cl solutions doped with increasing volumes of the Fe_3O_4 NP solution (Section 4.3.1.1.), it follows that adding increasing amounts of absorbing particles resulted in an increased number of cavitation events and larger bubbles with longer lifetimes. The variance between measurements of irradiated samples is attributed to particle aggregation and an inhomogeneous dispersion of absorbing particles/aggregates within the beampath.

For nanoparticles that absorb laser light strongly, it is known that heating can lead to melting and possibly fragmentation.[257] It has previously been reported that light scattering measurements of unfiltered NH_4Cl solutions that underwent long-term laser exposure pulses reduced the particle size distribution (similar in effect to filtration).[257] It has also been suggested that the mechanical energy generated on cavitation bubble collapse causes fragmentation of NP during laser processing.[235] A plot showing the effect of laser processing on the signals recorded in a 100 µL Fe_3O_4 NP-doped NH_4Cl solution is shown in Fig. 4-12.

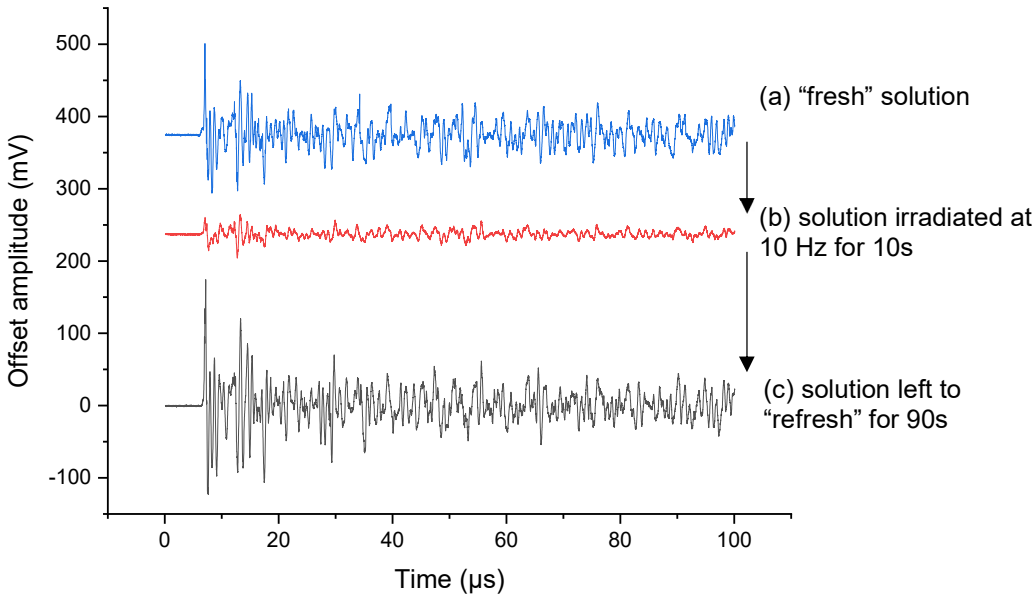

Figure 4-12 Plot showing the effect of laser processing on the signals recorded in a 100 µL Fe_3O_4 NP-doped NH_4Cl solution. *In (a) the solution was irradiated by a single pulse (b) the signal was recorded immediately following irradiation at 10 Hz for 10 s and (c) the signal was recorded after the sample was left to refresh for 90 s.*

The RMS value of (a) was measured as 19.133 mV, and measurement of the solution immediately following 10 Hz irradiation for 10s gave an RMS value of 4.232 mV, which is of a similar magnitude to the undoped and unfiltered NH_4Cl solution measurements. This large reduction in signal magnitude is attributed to the destruction of absorbing particles within the beampath. As the solution mixed by diffusion and more particles moved into the beampath over a 90s period, a further measurement (c) gave an RMS value of 25.778 mV. It is suspected that the absorbing particles/particle aggregates were melted or were fragmented from the mechanical energies generated on cavitation bubble collapse. Overall, the needle hydrophone measurements provide further compelling evidence for the impurity particle-heating mechanism behind NPLIN.

4.4. Conclusions

The role of impurity particles behind the NPLIN effect has been considered since 2009, following observations of filtration suppressing KCl LIN by Alexander and Camp.[251] Since then, some doubts have been cast on proposals of the optical electric field acting directly upon solute clusters.[235] According to Ward *et al*., the impurity particle-heating mechanism can explain why; (a) a threshold laser power is observed for LIN to occur, (b) NPLIN does not work for every system, together with variabilities reported between studies on the same solute-solvent system, and (c) filtration suppresses LIN whilst doping with absorbing NP increases the propensity for LIN.[257] Until now, there has been a lack of experimental attempts to detect vapour cavities in order to support this mechanism. Combining the high-speed imaging observations and needle hydrophone measurements, this work provides compelling evidence for the NPLIN impurity particle-heating mechanism.

High-speed imaging of laser-irradiated NH_4Cl solutions (S=0.9), demonstrated that the number of bubbles generated within the field of view increased with the volume of Fe_3O_4 NP suspension added prior to irradiation. This is attributed to a mechanism involving NP and/or NP aggregates absorbing light from the laser pulse and rapidly heating up to generate photothermal vaporisation in the surrounding liquid, with more energy being absorbed by larger particles and/or particle aggregates, resulting in the generation of larger bubbles with longer lifetimes. Furthermore, what is believed to be incandescence from particle heating was observed prior to bubble growth to a maximum radius. The 10μs observation intervals and spatial resolution of the imaging setup provided a field of view of 1120μm by 445μm and an object size detection limit of 3.6μm. Therefore, a detailed investigation of bubble dynamics was not possible. It is expected that observations at < 1μs intervals (imaging at > 1, 000, 000 fps) and a higher spatial resolution would be required to investigate the cavitation bubble activity in greater detail, but this would also significantly reduce the field of view and reduce the likelihood of capturing bubbles nucleated within the beampath. Interestingly, dark particle-like objects were observed at

the same locations where the largest bubbles within the field of view were observed prior, which are thought to be remnant bubbles that persist in the solution.

Out of six LIN imaging attempts, in one case no bubbles at or above the object size detection limit were detected before the appearance and growth of 11 crystals (undoped sample C). Also, in the case of doped sample B, fifty bubbles were detected in frame 1 and no crystals were generated yet, persisting objects in the location of prior bubbles were observable in frame 900ms following irradiation. Bubble oscillation and collapse events within a confined area are known to cause microconvection and vortex formation in the liquid and this aspect provides a further challenge in capturing bubble and crystal nucleation events. There were four samples in which both bubbles and crystals were detected within the field of view and in every case, the first observable crystal appeared in the same location as the largest bubble observed prior. This observation provides strong evidence that the cavitation event is directly linked to crystal nucleation in LIN and it follows that the extent of supersaturation increase would increase with the size of the bubble generated, as more solvent would have been vaporised. In three of these four solutions, an unknown object (most likely to be a bubble remnant following multiple expansion and shrinkage cycles of the nucleated bubble) persisted in the solution and it is unknown what role, if any, the unidentified, long-lived object noted immediately after bubble shrinkage/collapse may have in nucleation induction. It is thought that there will be a critical bubble size (and lifetime) for a cavitation event to lead to nucleation; therefore, not all cavitation events will lead to nucleation induction. Hence the nucleation probability is likely to be higher in the case where larger impurity particles/particle aggregates are irradiated and generate larger bubbles with a longer initial growth period, leading to higher supersaturation elevation surrounding the bubbles.

Within the unfocussed beampath, the nucleation of multiple bubbles of different sizes and lifetimes resulted in the generation of complex acoustic signals. By investigating the effect of solute concentration on the resulting acoustic signals, a trend of a linearly increasing signal RMS with solute concentration was observed that would be consistent with the presence of absorbing impurity particles along with the solute itself. Therefore, it is

concluded that the impurity particles present in untreated NH_4Cl solutions are responsible for photothermal cavitation and the resulting acoustic signal. Filtering solutions prior to irradiation did overall reduce the average signal RMS values measured on comparison with untreated NH_4Cl solutions. These results support the proposal that the highest RMS measurements recorded in the unfiltered solution measurement set are from large (> 5μm) particles/particle aggregates present in the untreated solution. Fe_3O_4 NP doping of the NH_4Cl solutions significantly increased the average signal RMS values measured in the solutions, on comparison with the undoped solution measurements. It follows that adding increasing amounts of absorbing particles resulted in an increased number of cavitation events and larger bubbles. The variance between measurements of irradiated samples is attributed to particle aggregation and an inhomogeneous dispersion of absorbing particles/particle aggregates within the beampath.

The effect of laser processing was also investigated. Following 10 Hz irradiation, the large reduction in the signal magnitude can be attributed to the destruction of absorbing particles within the beampath. As the solution was left to refresh (mix by diffusion), a further measurement demonstrated that this process allowed for the beampath to be refilled with more particles. Overall, the results demonstrate a direct relationship between absorbing particles, cavitation generation and crystal nucleation and the induction of multiple primary nuclei within an unfocussed beampath, by laser-induced particle heating. This has powerful implications for discussions behind the mechanism for LIN.

A Comparison of Cavitation Activity in Crystallisation Solvents under a High-Power Ultrasound Field

"Know thy liquid"

Symbols
Acoustic pressure (P_a)
Density (ρ)
Dynamic viscosity (μ)
Reynolds number (Re)
Sound velocity (c)
Surface tension (γ)

Abbreviations
Acetonitrile (ACN)
Butanol (BuOH)
Broadband Integrated Voltage (BIV)
Dissolved Oxygen (DO)
Ethanol (EtOH)
Fast Fourier Transform (FFT)
Focused Beam Reflectance Measurement (FBRM)
Isoamyl Alcohol (IAA)
Methyl Ethyl Ketone (MEK)

Declaration: CF planned and carried out all of the experimental work in this chapter. Some results were published in the 2019 IEEE International Ultrasoncs Symposium proceedings.[294]

5.1. Introduction

From a review of the sonocystallisation literature, it was clear that few reports involved measurement of cavitation activity in the generated sound field and the main reason for this is likely to be the specialist instrumentation required for quantifying the phenomena associated with bubble collapse (acoustic and light emissions).[186] As mentioned previously, cavitation measurements allow quantification of the energy from "active" bubbles contributing to the observed sonocrystallisation outcomes. [182] Under an applied ultrasound filed, stable cavitation bubbles undergo many oscillations during their lifetime and grow *via* coalescence or rectified dissusion. Whereas, transient cavitation bubbles bubbles are short-lived and collapse more violently, producing larger mechanical effects.[195] Stable bubbles are mostly observed with plate transducers while transient bubbles are typically observed with ultrasound probes. However, differences in frequency, position of the ultrasound source, reactor design and ultrasound intensity have previosuly been determined to influence the ultrasound field and hence impact the cavitation bubble type. [118]

A continuously driven acoustic cavitation field is highly dynamic and under which, oscillating bubbles are subjected to primary Bjerknes forces (acoustic radiation forces of the applied sound field) and secondary Bjerknes forces (attractive and repulsive forces between oscillating bubbles). According to Crum, cavitation bubble dynamics is highly dependent on variables such as the dissolved gas concentration and liquid vapour pressure.[183] Several authors have reported cavitation measurements in water and other non-aqueous liquids.[97, 150, 196] It has been reported that under the same applied ultrasound field, the physical properties of a liquid dictate the cavitation activity.[196] A high vapour pressure has been reported to result in growing cavitation bubbles filling with liquid vapour.[295] The liquid vapour is thought to cause a cushioning effect, which results in a lower collapse energy.[97] Furthermore, the liquid viscosity influences sound attenuation, with higher liquid viscosities leading to more energy lost to internal friction in the liquid.[87]

Lee noted that a higher concentration of dissolved air in a liquid increases the number of bubble nuclei available for cavitation activity.[130] By performing acoustic emission measurements in tap water and degassed water, Liu *et al.* determined that cavitation bubbles generated in high air content medium have a weaker collapse strength.[296] This was attributed to the diffusion of the air into the bubbles during growth cushioning the collapse. The authors also noted that a higher bubble density results in additional acoustic attenuation due to acoustic scattering and bubble shielding effects.[296] Hatanaka *et al.* explained that this shielding effect arises from bubbles on the outside of a bubble cluster preventing the applied ultrasound from reaching the inner bubbles through impedance mismatch, in a study that reported the quenching of sonoluminecence intensity measurements due to bubble shielding effects .[297]

The solute-solvent system of interest for the later sonocrystalllisation work in this thesis was paracetamol re-crystallised in isoamyl alcohol (IAA), for the further investigation of the effect of cavitation generation on impurity rejection. The frequency of interest was 40 kHz. From this, the following aims were conceived:

- Establish a setup for the measurement of acoustic cavitation in typical crystallisation solvents (including IAA) and water at 40 kHz, exploring the effect of solvent physical properties on the broadband noise produced
- Investigate the effect of degassing the solvents prior to measurement

Furthermore, Focussed Beam Reflectance Measurements (FBRM) have previously proven to be useful for counting bubbles and providing a snapshot of the cavitation activity in continuously driven pressure fields.[298, 299] Since this instrument is readily available to crystallisation scientists, FBRM were also used in conjunction with the needle hydrophone measurements in order to evaluate the use of this instrument for characterising bubble activity under an applied sound field.

There are no known studies on the effect of solvent properties on the sonocrystallisation outcomes, under an applied high-power ultrasound field. Therefore, it was anticipated that the outcomes of this work could guide further sonocrystallisation experiments.

5.2. Materials and Methods

5.2.1. Solvent Preparation

1-butanol (BuOH), ≥ 99.5%, ethanol (EtOH), ≥ 99.8%, IAA (≥ 99.0%, and methyl ethyl ketone (MEK), ≥ 99.5% were purchased from VWR Chemicals. Acetonitrile (ACN),≥ 99.5% and ultrapure water (HPLC Grade) were purchased from Alfa Aesar. Physical property data for the solvents selected is provided in Table 5-1, in which the sound the sound attenuation coefficients were calculated from equation (1.5). The Reynolds number (Re) was calculated using a reference velocity of 0.1 ms^{-1} (which is a typical flow velocity in acoustic flow).[196] The reference length was taken as the diameter of the vessel (70 mm). All other unreferenced data was obtained from Smallwood.[306]

Table 5-1 Solvent physical property data

Property	MEK	ACN	EtOH	BuOH	IAA	Water
Liquid density, ρ at 25°C ($kg\ m^{-3}$)	805	786	789	810	810	997
Surface tension, γ at 20°C (Nm^{-1})	24.6	29.1	22.3	24.6	23.8	72.8
Dynamic viscosity, μ at 25°C (mPa.s)	0.41	0.38	1.08	3.00	4.20	0.89
Vapour pressure at 21°C (mbar)	100.4	94.7	60.9	6.4	3.1	25.3
Sound velocity, c at 25°C (ms^{-1})	1196[300]	1287[301]	1142[302]	1239[303]	1235[304]	1498[305]
Reynolds number (Re)	13744	14479	5114	1890	1350	7842
Sound attenuation coefficient, α at 25°C and 40 kHz (cm^{-1})	12.5	9.6	38.7	82.0	115.9	11.2

The solvents were either used as received or firstly underwent a degassing procedure prior to measurement. More specifically, a Büchner flask containing 500 mL of the solvent was placed into an ultrasonic cleaning bath (model: FB11211 Fisher Sci, 37 kHz, degas mode, 100% power) which was heated at 50°C and under vacuum pump for a duration of 30 minutes. The dissolved oxygen (DO) content of the UP water was monitored with the FiveGo F4 DO meter (Mettler Toledo, OH, USA). A "zero oxygen" solution was prepared with zero oxygen tablets (≥20 — <30% concentration of citric acid, Mettler Toledo) and deionised water (dispensed via Millipore Milli-Q water purification system). A 2-point calibration was performed by measuring the DO concentration in air (8.13 mg/L) and in the "zero oxygen" solution" (0.00 mg/L). Since the electrode housing of the meter is made of acrylonitrile butadiene styrene, it was incompatible with the organic solvents used in this work. Therefore, the only obtainable DO concentration was the "out of the bottle" ultrapure water, which was recorded as 3.30 mg/L. Following the above degassing procedure, a DO concentration of 1.53 mg/L was recorded. The DO content was not found to decrease further following longer durations of sonication (up to 1 hour).

5.2.2. Acoustic Cavitation Measurement Setup

Acoustic detection was performed with a NH100 1.00mm PVDF needle hydrophone (Precision Acoustics Ltd., Dorset, UK) which was calibrated by the National Physical Laboratory (Teddington, UK) in 2019 (certificate reference: 2018100442-3). The tip was located using a positioning stage with 0.01mm precision (model: TVP-L, Sauter GmbH, Wutöschingen, Germany). Time-domain waveforms were recorded with an Agilent Technologies InfinniVision X2024-A digital oscilloscope (Agilent Technologies, South Queensferry, UK). As the hydrophone tip is incompatible with organic solvents, it was protected inside a castor oil-filled latex-rubber sheath (d=5 mm). The vessel was constructed by bonding a 250mL borosilicate glass beaker to a 40 kHz Tonpilz piezoelectric transducer (CeramTec, Hampshire, England) with an epoxy adhesive. The vessel was driven by a 33210A 10 MHz Function Generator (Agilent Technologies, South Queensferry, UK) and a wideband 155LCR power Amplifier (Kalmus Engineering, Rock

Hill, SC). The hydrophone was axially aligned with the Tonpilz transducer and the antinodes of the standing wave were found by moving the hydrophone tip vertically from the bottom of the vessel to the liquid surface (58 mm) in 2 mm increments and finding the height at which the maximum amplitude of the waveform was observed (40 mm). A G400 Focused Beam Reflectance Measurement (FBRM) probe (Mettler Toledo, OH, USA) was also used to detect and count bubbles generated by the acoustic field. The probe was orientated 45° to the surface of the transducer, at the same height in the vessel as the hydrophone tip (40 mm). Measurements were performed under ambient conditions (room temperature: 20.5—21.8°C). Each solvent was subjected to six driving amplitudes in the range 50—800 mV pp (electric power: 0.1—9 W). A schematic of the experimental setup is shown in Fig. 5-1.

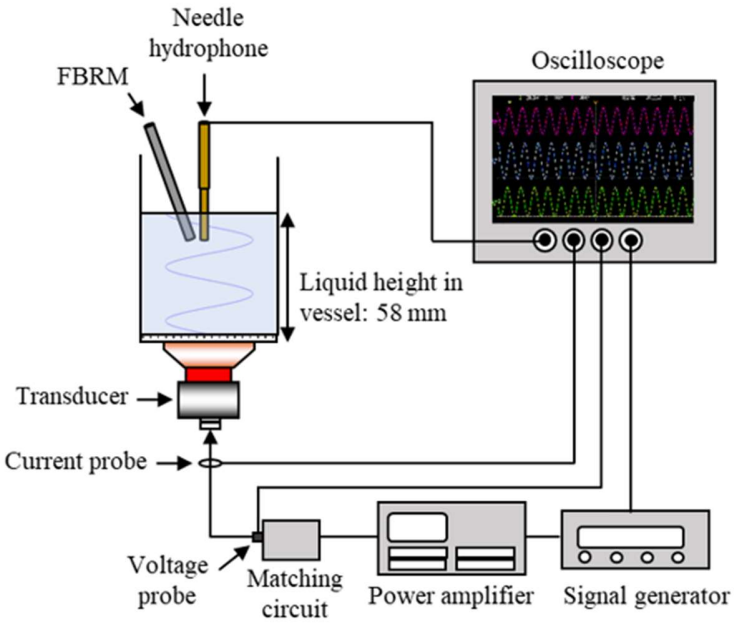

Figure 5-1: Schematic of acoustic cavitation measurement setup

Needle hydrophone measurements were performed in triplicate and signal processing was performed using MATLAB (Mathworks, Massachusetts, USA). A Fast Fourier Transform (FFT) was performed, from which, the acoustic pressure (*Pa*) and Broadand Integrated

Voltage (BIV) were calculated. Each FBRM measurement consisted of acquiring chord length distributions at the various driving amplitudes investigated for 30s of non-insonated (silent conditions), followed by 30s of sonication. The probe was used with iC FBRM V4.3 incorporated in the iControl V5.2 software. Each measurement was collected with a 2 s scan speed and a 2 s sampling interval. Assuming a spherical particle shape, the chord length measurements correlate to particle size and the measurement range 1-1000µm. The average count over a 30s sonication period was calculated by firstly subtracting the average count over the 30s non-insonation period immediately prior. An example FBRM measurement output is provided in Fig. 5-2.

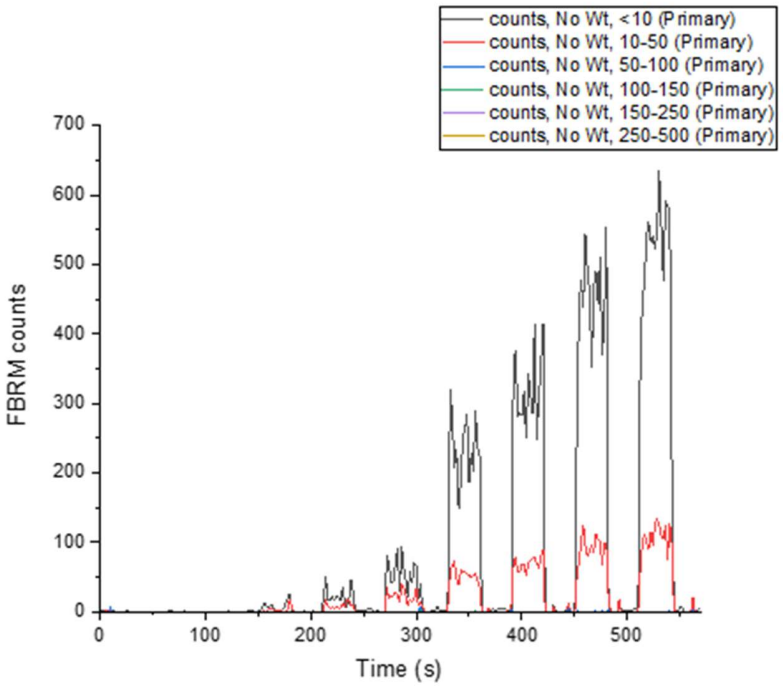

Figure 5-2: Example FBRM measurement output performed in IAA. *Ultrasound was periodically turned on and off for a 30 s duration and each successive measurement with ultrasound on, the p-p driving amplitude was increased from 50-800 mV*

5.3. Results and Discussion

5.3.1. Needle Hydrophone Measurements

The incompatibility of the needle hydrophone tip with non-aqueous solvents was initially a major barrier faced in this work. The hydrophone manufacturer (Precision Acoustics Ltd) recommended the insertion of the hydrophone into a thin water-filled cot prior to measurement, in order to prevent solvent damage and to ensure that the tip experienced the correct acoustic impedance. A further barrier was the cavitation damage sustained to successive hydrophone tips (in the water-filled cot) following long-term exposure to the 40 kHz ultrasound field. Originally, driving amplitudes in the range 20 mV-800 mV pp were investigated in 30 mv pp increments, during which the hydrophone tip was immersed in the vessel with ultrasound on for a total duration of ~ 156 minutes (across all solvent measurements and conditions). Furthermore, the cavitation threshold in water at 43 kHz has been reported as 27.9 kPa, hence it was speculated that at acoustic pressures above this value there could also be interference of measurements in solvents by cavitation generated in the water-filled cot.[165]

In order to (i) protect the tip from damage and (ii) prevent cavitation generation occurring in the liquid-filled cot, castor oil (ρ =0.9624[97]) was selected to fill the cot. Briggs *et al.* provided a cavitation threshold value for castor oil of approximately 405.3 kPa at 25 kHz.[307] Since the cavitation threshold increases with ultrasonic frequency, the threshold value at 40 kHz is expected to be > 405.3 kPa.[165] The risk of cavitation damage to the tip was substantially reduced in the oil-filled cot and the exposure time of the tip was reduced to ~12 minutes. This was achieved by both carrying out larger incremental increases of the driving amplitude and by raising the tip out of the vessel after the hydrophone measurements were recorded and whilst ultrasound was still on for the completion of the FBRM measurements. The tip was visually inspected for signs of damage following each measurement set in each solvent. Fig. 5-3. shows measurements of *Pa* at three driving amplitudes performed in water (i) without a cot, (ii) with a water-filled cot and (iii) with

an oil-filled cot. The average measurements of *Pa* in the oil-filled cot were slightly lower than without a cot or with a water-filled cot, however, on consideration of the error range of the measurements, it was concluded that the measurements were in good agreement within the range of driving amplitudes investigated.

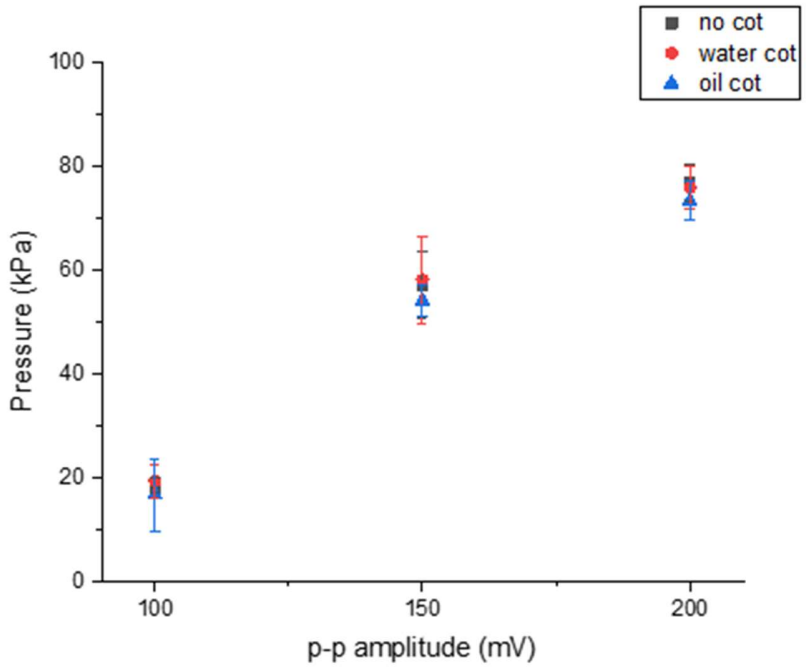

Figure 5-3: Plot of acoustic pressure measurements in water at three driving amplitudes with the needle hydrophone prepared (i) without a cot (ii) in a cot filled with water and (iii) in a cot filled with castor oil

Under the same applied ultrasound parameters, cavitation generation in water was distinctly visibly different from the five organic solvents. In water, no large visible bubbles were observed and the surface of the liquid vibrated vigorously under the application of 350 mV-800mV pp amplitude ultrasound. Whereas, in the case of the organic solvents large visible degassing bubbles were generated from 200mV-800mV pp. This observation is consistent with the previous report by Tzanikis *et al*., who compared cavitation generation in water and ethanol and noted that large bubbles were generated in ethanol that vigorously oscillated towards the free surface, similar to degassing.[196]

According to Lee, it is the coalescence of bubbles that is largely responsible for the large, visible bubbles or degassed bubbles.[109] The moment that ultrasound was turned off, the large bubbles/ clusters of bubbles were observed to dissolve. The generation of large inactive bubbles by coalescence was observed for all organic solvents and it was most severe in the case of IAA (see Fig. 5-4).

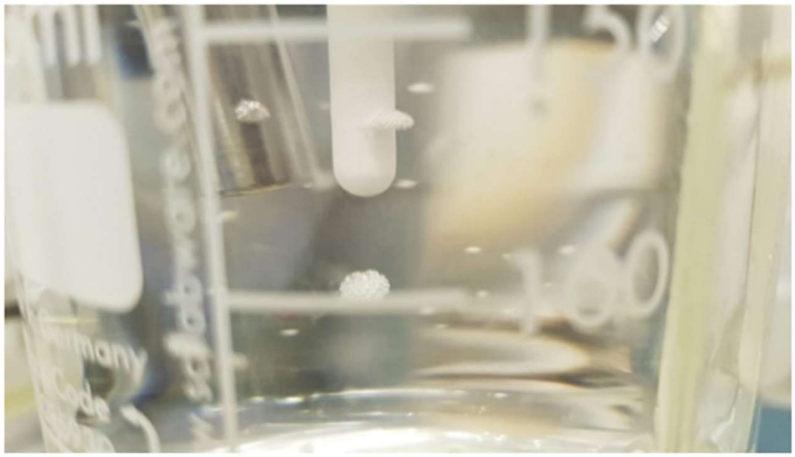

Figure 5-4: Image of acoustic cavitation measurement in IAA. *Visible clusters of inactive bubbles that were significantly larger than the resonant size (75μm at 40 kHz) were observed to form and move to the nodes under the action of primary Bjerknes forces generated in the ultrasound field.*

In the case of high-power ultrasound fields, Ashokkumar *et al.* reported that there will always be a combination of stable and transient bubbles present, but one type will be more prevalent.[127] Within the vessel, a standing wave was generated from the propagation of ultrasound due to reflections at the surface of the liquid. This promoted the generation of predominantly stable cavitation.[116] Though, it has already been established that at the same driving frequency, transient cavitation becomes more dominant as a greater P_a is generated.[126]

The BIV and P_a values obtained from needle hydrophone measurements in each solvent under the same applied ultrasound field are shown in Fig. 5-5. Furthermore, example acoustic emission spectra measured in each solvent are provided in Appendix B-1.

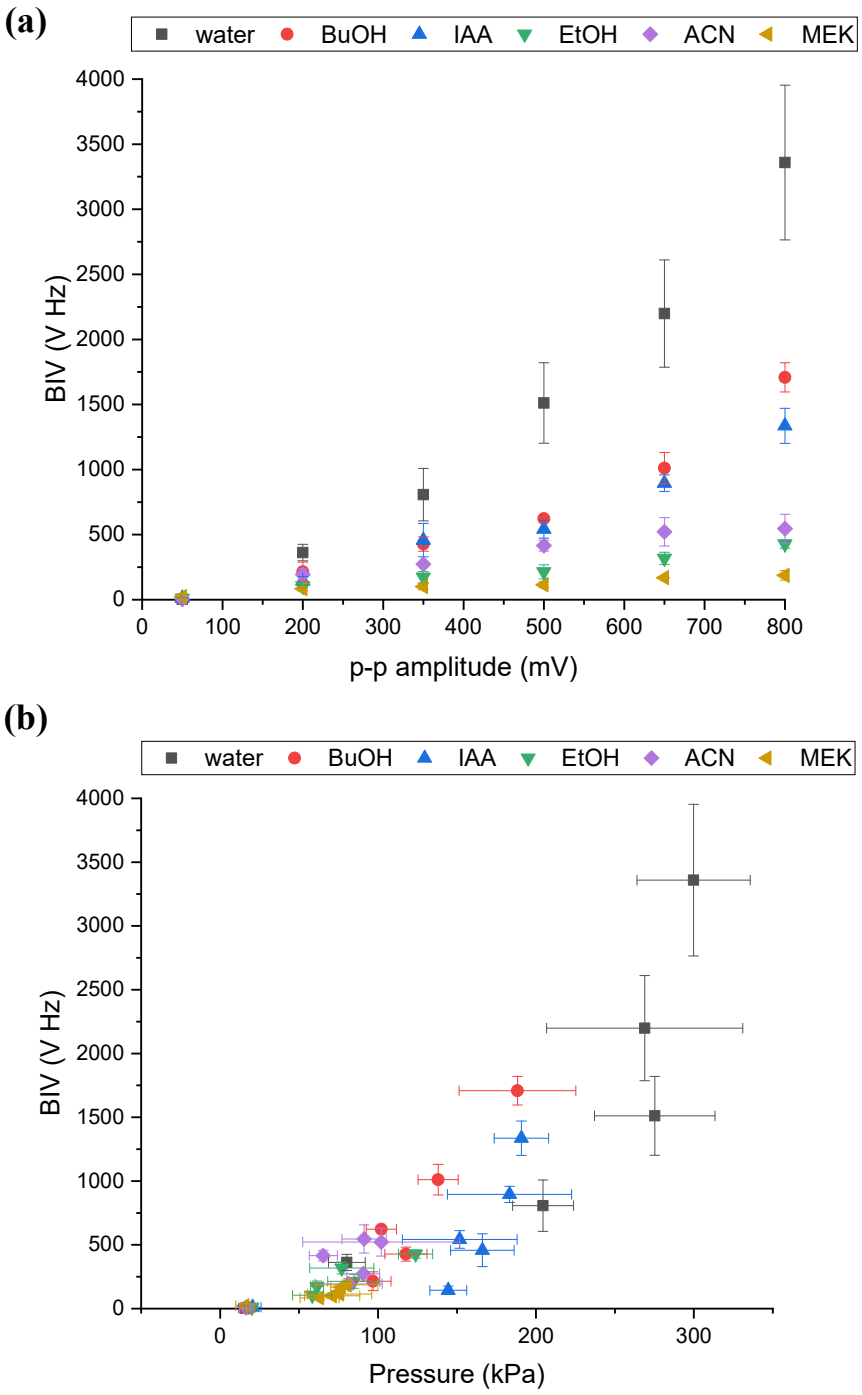

Figure 5-5: Measurements of BIV in six solvents measured under the same applied ultrasound field shown as; (a) a function of p-p amplitude drive and (b) the corresponding measured average P_a

The processes of rectified diffusion and bubble–bubble coalescence control bubble growth and hence the cavitation activity.[117] From Fig. 5-5., it is clear that increasing the driving amplitude resulted in increased BIV and P_a values obtained from hydrophone measurements across each solvent, however marked differences in the magnitude of these values are observed on comparison of all solvents. Strong intermolecular interactions *i.e.* hydrogen bonding in water and alcohols are thought to contribute to this observation. At a driving amplitude of 800mV pp, in order of increasing BIV values obtained were: MEK (187 V Hz) < EtOH (428 V Hz) < ACN (546 V Hz) < BuOH (1336 V Hz) < IAA (1708 V Hz) < water (3360 V Hz). The more volatile a solvent is, the higher the likelihood is that vaporised solvent will enter the bubble during the rarefaction phase of growth by rectified diffusion.[195] The liquid vapour is thought to cause a cushioning effect, which reportedly results in a lower collapse energy.[97] In order of increasing vapour pressure at 21°C (mbar): IAA (3.1) < BuOH (6.4) < water (25.3) < EtOH (60.9) < ACN (94.7) < MEK (100.4). On this basis, the rate of evaporation of water, IAA and BuOH is expected to have been significantly lower than in the case of ACN, MEK and EtOH. Hence, the BIV measurements (indicative of higher energy bubble implosion) are significantly lower in the case of ACN, MEK and EtOH.

The liquid viscosity influences sound attenuation, therefore higher BIV and P_a values observed in water on comparison with IAA and BuOH are attributed to significantly lower energy lost due to internal friction in the case of water (α = 11.2cm^{-1}) compared to IAA (α = 115.9cm^{-1}) and BuOH (α = 82.0 cm^{-1}). Furthermore, across the organic solvents large inactive bubbles were generated, which was not observed in the case of water. From this, it is also speculated that dense clusters of bubbles generated in organic solvents by coalescence may have resulted in additional acoustic attenuation and bubble shielding effects, which could also have contributed to the lower P_a values measured in organic solvents on comparison with water.

5.3.2. Effect of Solvent Degassing

Plots of average BIV measurements under the same applied ultrasound field in untreated solvents and the solvents which had undergone the degassing process are provided in Fig.5-6.

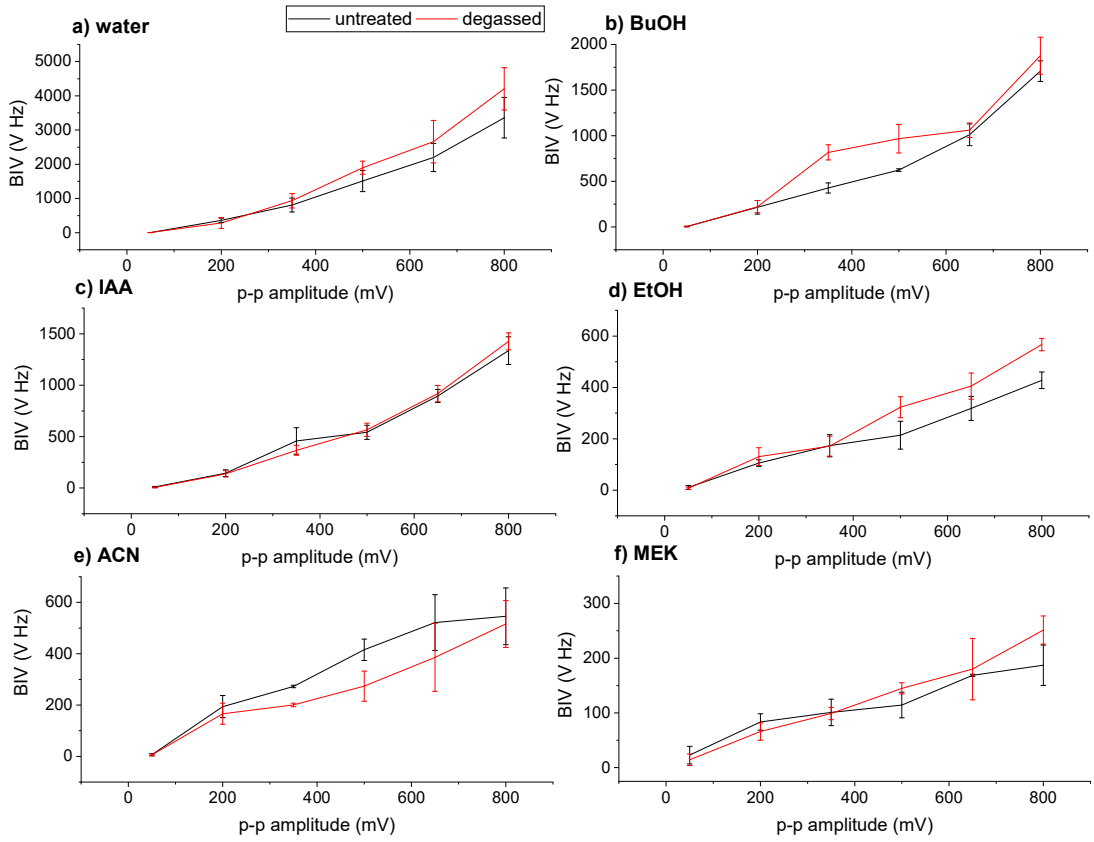

Figure 5-6: Plots of average BIV measurements under the same applied ultrasound field in untreated solvents (black) and degassed solvents (red). *Note the scale difference in the y-axis*

As DO measurements were only possible to in water prior to and following degassing, the effect of degassing on the organic solvents could only partially be evaluated. Nevertheless, in the case of water, BuOH, EtOH and MEK, overall slightly higher average BIV values were measured in the solvent following degassing. This is consistent with the previous

report by Liu *et al.* that reported higher collapse energies for water that had been degassed prior to measurement.[296] In the case of IAA, where very similar BIV values were recorded before and after degassing, it is deduced that the degassing setup and method used may not have been effective or the dissolved gas content of the untreated solvent was already low. In the case of the most volatile solvents (EtOH, MEK and ACN), it is speculated that significant solvent vaporisation occurs during growth and solvent vapour diffusing into bubbles cushions the implosion. Whilst degassing may lower the concentration of dissolved gases that could result in a higher prevalence of cushioned bubble collapse, a lower concentration of dissolved air in a solvent also decreases the number of bubble nuclei available.[130] This effect could partially have masked the effects of degassing on the BIV values obtained, if there were less bubble nuclei available for growth *via* coalescence. Overall, the differences in BIV values obtained before and following the degassing procedure are small.

Plots of average FBRM bubble count measured alongside the needle hydrophone measurements in both untreated and degassed solvents are shown in Fig. 5-7. It should be noted that the FBRM bubble counts are not a direct measurement of cavitation activity and no differentiation between active and inactive bubbles detected in the liquid can be made. Nevertheless, the average bubble count was observed to increase with increasing driving amplitude and this is attributed to a larger population of bubbles generated under the ultrasound field. Moreover, by decreasing the number of available bubble nuclei in the solution by degassing, a decrease in the overall bubble count in degassed samples was anticipated and broadly, this was observed. There is a marked difference in the bubble count in water on comparison with the organic solvents, which agrees with the BIV values obtained from hydrophone measurements.

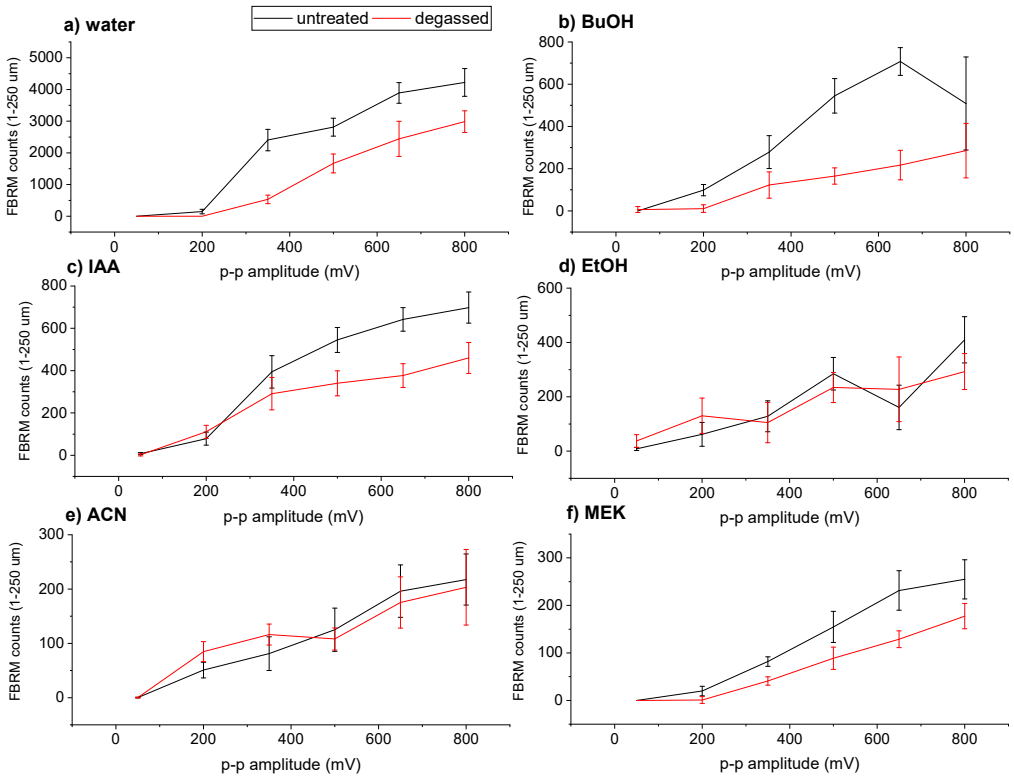

Figure 5-7: Plots of average FBRM bubble count measured under the same applied ultrasound field in untreated solvents (black) and degassed solvents (red). *Note the scale difference in the y-axis*

Whilst the frequency dictates the bubble size, the applied power influences the bubble population.[193] From this, it is also thought the bubble counts may also reflect the mixing conditions within the vessel. Furthermore, in the case of water where the highest cavitation energies were measured, higher shear would have been generated, which is likely to have resulted in more turbulent mixing. Therefore, a greater number of bubbles and bubble fragments following implosion could have been presented to the probe in a single scan, in comparison to less turbulent mixing conditions generated in organic solvents. Moreover since, large bubble clusters were not observed during cavitation generation in water, it is deduced that a larger population of detectable bubbles or bubble fragments from implosion would have been detected. An interesting observation is the bubble count for degassed BuOH and IAA dropped to similar levels to the degassed volatile solvents. It follows that

at similar bubble counts, higher BIV values for IAA and BuOH could be attributed to less-cushioned bubble collapse on comparison with more volatile solvents, in which lower BIV values were obtained.

FBRM measurements have previously been utilised for quantification of micron-sized bubble populations in continuously driven pressure fields.[298, 299] However, it is important to emphasise that the probe detects the chord length rather than the diameter of bubbles and on comparison with the needle hydrophone, it is not a precision instrument. Nevertheless, observed reductions of bubble count in the case of degassed solvents does coincide with a lower number of bubble nuclei available with some removal of dissolved gas present in the solvent. For comparison, a plot of average BIV measurements and average FBRM bubble counts performed at 800 mV pp amplitude drive in untreated and degassed solvents is provided in Fig.5-8.

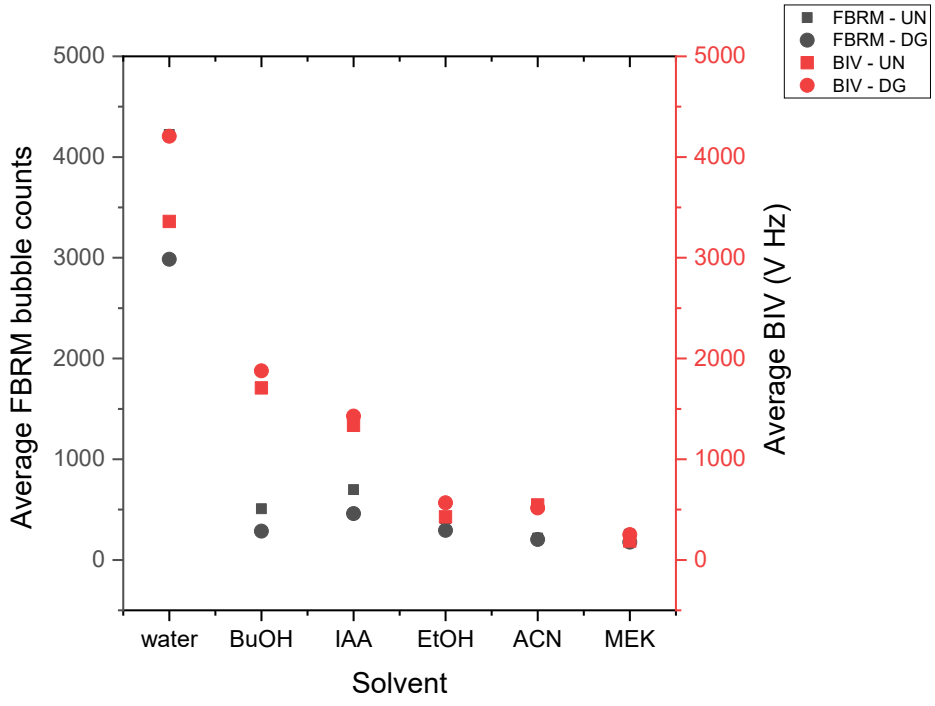

Figure 5-8: Plot of average FBRM bubble counts and average BIV measured in untreated (UN) and degassed (DG) solvents at 800 mv pp amplitude drive.

Overall, the FBRM bubble counting measurements are broadly in agreement with the trends observed with the BIV values across the solvents. However, since the FBRM is incapable of providing temporal measurements of cavitation or distinguishing active bubbles from inactive bubbles, it is less reliable for the quantification of cavitation bubble activity in a sonocrystallisation vessel on comparison with the needle hydrophone.

5.4. Conclusions

A multi-bubble acoustic field is a highly complex and dynamic system. Characterisation by measurement of input electrical power or indirect measurement through calorimetry can be misleading and it also makes linkage of these measurements to the effects of cavitation generation difficult. Measurements of light and acoustic emissions from bubbles allows for the "active" bubbles to be distinguished and measured. In this chapter, a setup for the measurement of acoustic cavitation in water, BuOH, IAA, EtOH, ACN and MEK was established in order to compare cavitation generation across typical crystallisation solvents under the same applied ultrasound parameters. A predominantly stable cavitation field was generated in the vessel and under the same applied ultrasound parameters the following observations were made:

Cavitation generation in water was visibly different from the five organic solvents; in water, no large visible bubbles were observed whereas, in the case of the organic solvents large visible (inactive) bubbles generated by coalescence were observed. From this, it is also speculated that dense clusters of bubbles generated in organic solvents by coalescence may result in additional acoustic attenuation and bubble shielding effects, which may also contribute to the lower P_a and BIV values measured in organic solvents on comparison with water. Significantly lower P_a BIV values were obtained from measurements in the more volatile solvents (EtOH, MEK and ACN) on comparison with IAA, BuOH and water, which is attributed to a higher likelihood of liquid vapour of the solvent entering the bubble during the rarefaction phase of growth by rectified diffusion and cushioning the collapse. Furthermore, lower BIV and P_a values observed in IAA and BuOH on

comparison with water are also attributed to higher energy lost due to internal friction in the higher viscosity solvents.

Degassing the solvents prior to measurement in most cases resulted in higher BIV values, corresponding to a reduction in bubble cushioning effects by the removal of some dissolved gases, but this effect was slight, if at all. This may indicate an ineffective degassing procedure. In general, the FBRM detected increasing bubble counts on increasing the diving amplitude across the solvents. This indicated that it was indeed detecting bubbles generated by the acoustic field, but it is not possible to distinguish between inactive and active bubbles present. The average bubble counts obtained did seem to support the measurements of BIV across the solvents, but alone it is not a reliable method for quantifying bubble activity under an applied ultrasound field.

It is important to note that these observations are exclusive to the reactor geometry, transducer type and frequency used in these experiments. This work serves as the basis for the acoustic cavitation measurement technique and solvent selection for Chapter 6. Alongside IAA, water and ACN were selected as crystallisation solvents as part of the following paracetamol sonocrystallisation study.

An Investigation of Paracetamol Sonocrystallisation: Mechanisms for Polymorphism and Purity Effects

"Know thy sound field"

Symbols
Acoustic pressure (P_a)
Induction temperature (T_{ind})
Supersaturation ratio (S)

Abbreviations
Acetonitrile (ACN)
Acetanilide (ACE)
Broadband Integrated Voltage (BIV)
Differential Scanning Calorimetry (DSC)
Fast Fourier Transform (FFT)
Focused Beam Reflectance Measurement (FBRM)
High Performance Liquid Chromatography (HPLC)
Isoamyl Alcohol (IAA)
Metacetamol (MCM)
Particle Vision and Measurement (PVM)
Paracetamol (PCM)
X-Ray Powder Diffraction (XRPD)

Declaration: CF planned and carried out all the experimental work and all materials characterisation in this chapter.

6.1. Introduction

In the manufacture of drug substances, the crystal size distribution, shape, purity and polymorphic form are critical quality attributes.[2] Most studies in the sonocrystallisation literature have focussed on the application of ultrasound to crystallisation processes for control over the crystal size distribution.[308-315] For the development of industrial sonocrystallisation processes, it is critical that the effects of ultrasound on the crystal product purity, morphology and form are understood; however, there have been a limited number of reports in which these effects were investigated.

In the case of paracetamol (PCM), the metastable polymorph (form II) is notoriously difficult to obtain in solution.[47] Nicoud *et al.* reported that at temperatures above 0 °C, seeding a crystalliser with crystals of form II was insufficient to induce the crystallisation of form II.[47] The elusive nature of form II has been linked to the rapid competitive crystallisation of form I, since in solution the presence of form I results in the rapid conversion of form II to form I.[43] Moreover, Deij *et al.* reported that PCM form II has a substantially higher nucleation barrier than form I and as a consequence, will not be formed easily.[49]

Mori *et al.* reported the selective generation of form II with ultrasound (at both 28 and 45 kHz) and the mechanism behind this remains unclear.[223] These experiments were carried out at 0—2°C, on a 1 mL scale and ultrasound was applied following the generation of a very high supersaturation level (S = 4.4, based on a solubility of 7.21 mg/mL of PCM in water at 0°C from Granberg *et al.*[226]). The authors proposed that the selective crystallisation of form II relied upon no form I being nucleated, since the presence of form I PCM initiates a rapid conversion to form I.[217] At 100 kHz, samples did not crystallise, which was attributed to the less intense mechanical energies generated at this frequency to induce nucleation.[223]

Furthermore, previously reported greater impurity rejection of PCM in the presence of structurally related impurities, acetanilide (ACE) and metacetamol (MCM) seems

counterintuitive to an account of increased crystal growth rates, under a high-power ultrasound field.[225,234] Nguyen *et al.* presented purity data from cooling sonocrystallisation processes at one ultrasound power setting on comparison with the silent experiments, in which nucleation induction occurred at significantly higher supersaturation levels.[234] This report is the only known study on the effect of high-power ultrasound on the crystallisation of a drug substance in the presence of added impurities and the mechanistic proposal of cavitation phenomena enhancing impurity rejection requires further investigation. Overall, the intense mechanical energies generated from cavitation has been linked to both the generation of form II PCM and greater impurity rejection in the presence of structurally similar impurities.[222, 223, 234] From this, it was expected that by varying the cavitation energy generated in PCM sonocrystallisation processes, these effects would be observed to varying extents.

From the above, the following aims were conceived:

- establish a set-up for cooling sonocrystallisation experiments to be carried out in order to further investigate the previously reported (i) selective crystallisation of PCM form II and (ii) greater impurity rejection of PCM in the presence of ACE and MCM
- initially perform scoping experiments (6mL scale) in order to assess the effects of cavitation energy on the purity and form from cooling sonocrystallisation of PCM with 2% mol ACE in (i) isoamyl alcohol (IAA), (ii) water and (iii) acetonitrile (ACN)
- upscale the PCM-IAA system (125mL) in order to assess the effects of cavitation energy on the purity and form from cooling sonocrystallisation of (i) PCM with 2% mol ACE, (ii) PCM with 2% mol MCM and (iii) PCM with 1% mol ACE and 1% mol MCM.

6.2. Materials and Methods

6.2.1. Solution Preparation and Cavitation Generation

PCM (≥ 99.0%,) ACE (≥ 99.0%) and MCM (≥97.0%) were obtained from Sigma-Aldrich. IAA (≥ 99.0%, was purchased from VWR Chemicals and both ACN (,≥ 99.5%) and ultrapure water (HPLC Grade) were purchased from Alfa Aesar. PCM-IAA solubility data was taken from Brown *et al.*[316] Solubility data for PCM-ACN was taken from Granberg *et al.*[226] and PCM-water data was taken from Jiménez *et al.*[317] Urwin reported that the absolute solubility of PCM in IAA is not significantly affected up to 6% mol ACE[318] and up to 10% mol MCM.[319] It is on this basis that the supersaturation ratios in this work (of 2% mol added impurities) are calculated on that of pure PCM in the solvents investigated (IAA, ACN and water).

The sonocrystallisation vessel was constructed by bonding a jacketed 250mL borosilicate glass beaker to a 40 kHz Tonpilz piezoelectric transducer (CeramTec, Hampshire, England) with an epoxy adhesive. The vessel was driven by a 33210A 10 MHz Function Generator (Agilent Technologies, South Queensferry, UK) and a wideband 155LCR power Amplifier (Kalmus Engineering, Rock Hill, SC). The driving amplitude was varied between 100—800 mV pp. The jacket temperature was controlled with a Lauda ECO Gold heating and cooling thermostat (Lauda GmbH, Königshofen, Germany).

6.2.2. Scoping Cooling Sonocrystallisation Experiments

For scoping experiments, 6mL solutions of PCM in IAA, water or ACN were prepared (with and without 2% mol ACE) in 8mL Wheaton clear glass vials (Sigma-Aldrich). As in the previous work by Nguyen *et al*., the solution concentrations were selected based upon an S=1.4 at 40°C.[234] A polytetrafluoroethylene fixture was made in order to hold four vials suspended in water within the jacketed vessel. The solutions were initially dissolved in an oil bath (held at 85°C in the case of water and IAA and 75°C in the case

of ACN) before being transferred to the vessel, which was heated at 75°C. Following a 15-minute hold period, ultrasound was turned on and the solutions were cooled to 10°C at a rate of 0.5°C min^{-1} and held for a further 2 hours at 10°C (similarly to the experimental procedure reported by Nguyen *et al*.) The temperature was monitored by a thermocouple (Omega model: HH800-SW) which was placed into a "blank" vial only containing the crystallisation solvent. The nucleation temperature was determined by visual observation of the solutions becoming cloudy, before turning turbid. At the end of the cooling cycle, ultrasound was turned off and the suspensions were filtered. The cakes were washed twice with 2 mL of the crystallisation solvent, which had been stored at 5°C. Finally, the product was dried overnight at 50°C. A schematic of the setup for scoping experiments is provided in Fig. 6.1.

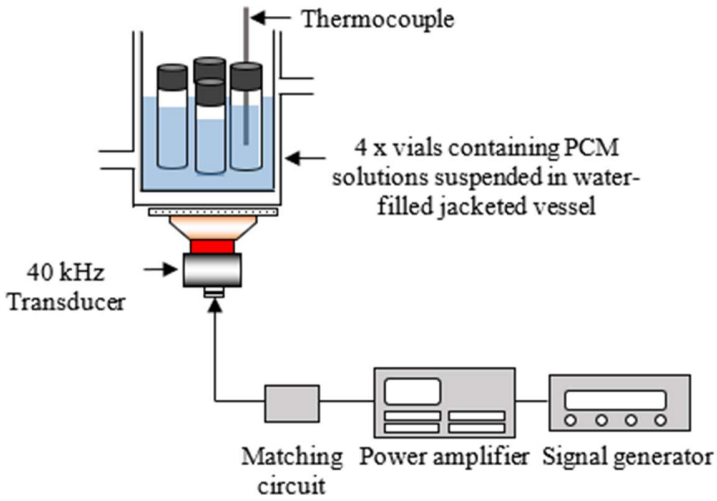

Figure 6-1: Schematic of scoping cooling sonocrystallisation experiments

6.2.3. Upscale Cooling Sonocrystallisation Experiments

For each upscale experiment, 125mL solutions of PCM in IAA were prepared (166 mg/g IAA) either (i) without impurities (ii) with 2% mol ACE (iii) with 2% mol MCM or (iv) with 1% mol ACE and 1% mol MCM. The solution was dispensed directly into the vessel

and a polytetrafluoroethylene fixture was made in order to hold all process monitoring instruments. From the scoping experiments, an increased solute concentration was employed, which required a higher dissolution hold temperature of 95°C before being transferred to the jacketed vessel, which was heated at 85°C. Following a 15-minute hold period, ultrasound was turned on and the solutions were cooled to 10°C at a rate of 0.5°C min^{-1} and held for a further 2 hours at 10°C. All experiments were continuously stirred at a rate of 150 rpm. At the end of the cooling cycle, ultrasound was turned off and the suspensions were filtered. The cakes were washed twice with 50mL of IAA, which had been stored at 5°C. Finally, the product was dried overnight at 50°C. A schematic of the setup for scoping experiments is provided in Fig. 6.2.

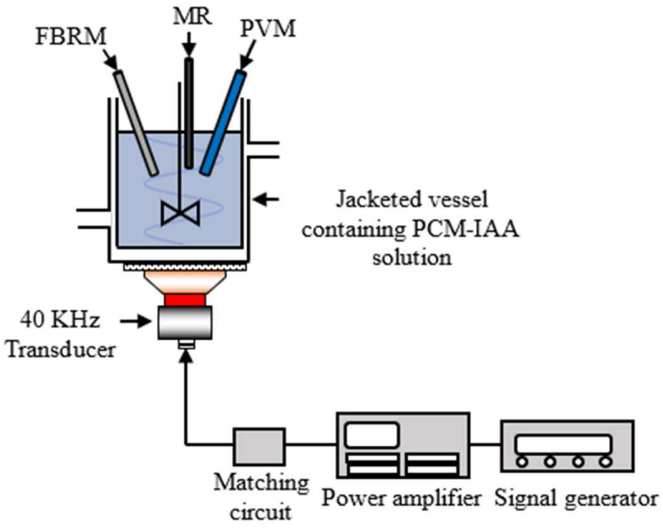

Figure 6-2: Schematic of upscale cooling sonocrystallisation experiments

Process monitoring was performed using a G400 Focused Beam Reflectance Measurement (FBRM) probe and a V819 Particle View Microscope (PVM), both from Mettler Toledo, OH, USA. In select experiments, a Raman Kaiser RXN2 (Kaiser Optical Systems Inc, MI, USA) with the micro Raman (MR) probe was also immersed in order to monitor the polymorphic composition of the sample. The temperature was monitored by a thermocouple (Omega model: HH800-SW). Each FBRM measurement was collected

with a 2 s scan speed and a 2 s sampling interval and the PVM image update rate was 0.1 s. Raman spectra were recorded using iC Raman V4.1 software, also incorporated in the iControl software. Each Raman spectrum was recorded with two scans and a 30 s integration time resulting in one spectrum every 2 min. The laser wavelength of 785 nm was produced by an Invictus diode laser operated at 350 mW at the source, with a CCD detector cooled to −40 °C by a Peltier cooling system. The characteristic Raman bands used to differentiate forms I and II were 1233—1238 (I) and 1218—1219 (II), on the basis of previous work by Agnew *et al*.[51]

6.2.4. Materials Characterisation

X-ray Powder Diffraction (XRPD) data was collected for all samples with a Bruker D8 Advance II diffractometer (GX002103 – Priscilla) using Debye-Scherrer transmission of Cu Kα1 radiation with a wavelength of 1.540596 Å. Patterns were collected between 4 – 35 2θ and were compared to reference patterns located in the Cambridge Crystallographic Data Centre for polymorphic assignment. Optical microscope images were collected for all samples using a Leica DM2700 M Microscope. The product purity of each sample was determined by High Performance Liquid Chromatography (HPLC), using an Agilent 6130 dual source model instrument with a detection wavelength of 243nm and a Poroshell 120 EC-C18 Column operated at 40°C. Solid samples were dissolved in 5 % methanol in water and a mobile phase of 20 % methanol in water was used. For all samples obtained from upscale experiments, Differential Scanning Calorimetry (DSC) measurements were carried out using a Netzsch DSC214 Polyma. Samples were heated at rate of 10 °C min^{-1} to 200°C, held isothermally for 10 minutes, then returned to room temperature at a rate of 10°C min^{-1}.

6.2.5. Needle Hydrophone Measurements

Acoustic detection was performed with a NH100 1.00mm PVDF needle hydrophone (Precision Acoustics Ltd., Dorset, UK) which was calibrated by the National Physical

Laboratory (Teddington, UK) in 2019 (certificate reference: 2018100442-3). The tip was located using a positioning stage with 0.01mm precision (model: TVP-L, Sauter GmbH, Wutöschingen, Germany). Time-domain waveforms were recorded with an Agilent Technologies InfinniVision X2024-A digital oscilloscope (Agilent Technologies, South Queensferry, UK). As the hydrophone tip is incompatible with organic solvents, it was protected inside a castor oil-filled latex-rubber sheath (d=5 mm). For the scoping experiments, the hydrophone was positioned in the centre of the vial whereas, for the upscale experiments, the hydrophone was positioned in the centre of the vessel. The measurements were performed in triplicate, at 20°C ± 1°C solution temperature. Furthermore, (as described previously in Chapter 4) the tip was located at the height in which the maximum amplitude of the waveform was observed. Signal processing was performed using MATLAB (Mathworks, Massachusetts, USA). A Fast Fourier Transform (FFT) was performed, from which the acoustic pressure (*Pa*) and Broadand Integrated Voltage (BIV) were obtained.

6.3. Results and Discussion

6.3.1. Scoping Cooling Sonocrystallisation Experiments

A plot of average P_a and BIV values from needle hydrophone measurements in each solvent within a vial suspended in the water-filled jacketed vessel (from 100-800 mV pp amplitude drive) is provided in Appendix C-1. Since it was not possible to stir the vials, a sub-cavitational driving amplitude was applied (100 mV pp) instead of a silent experiment, which was anticipated to have induced mixing effects *via* acoustic streaming.[120, 199]

6.3.1.1. Paracetamol Sonocrystallisation without Added Impurities

The results of scoping experiments for cooling PCM sonocrystallisation experiments in IAA, water and ACN, without added impurities are shown in Table 6-1. In which, T_{ind} is

the temperature recorded for nucleation induction and from this, the superaturation ratio (*S*) was calculated. An important point to note is that poor mixing was anticipated in the case of the 100 mV pp (no cavitation experiments) and erratic mixing was expected in the experiments where cavitation was generated (350-800 mV pp). These effects are thought to impact the *S* values calculated (based on the T_{ind}), as it only represents the bulk macro-level temperatue measured in the vial and the supersaturation levels in each experiment could have been non-uniform, which was probably most severe in the case of the PCM-IAA system, due to the high viscosity of this solvent. It is also important to note that in the case of PCM, the polymorph formed (I or II) is not determined by the surface energy of the nucleus, but the difference in bulk chemical potential and therefore, solvent effects can be neglected in an investigation of conditions to obtain PCM form I or II.[49] All XRPD patterns for scoping experiments are in Appendix C-2. The corresponding microscope images are provided in Fig. 6-3.

Table 6-1 Polymorphic results of PCM cooling sonocrystallisation experiments without added impurities in IAA, water and ACN

Experiment	p-p Amplitude at 40 kHz (mV)	Average P_a (kPa)	T_{ind}	*S*	Form
104 mg/g PCM-IAA	800	395	10	2.5	II
	650	330	10	2.5	I
	500	347	13	2.4	II
	350	251	10	2.5	II
	100	15	10	2.5	I
35 mg/g PCM-water	800	335	40	1.4	I
	650	323	35	1.7	II
	500	242	30	2.0	I
	350	134	27	2.2	I
	100	8	27	2.2	I
66 mg/g PCM-ACN	800	129	32	1.9	I
	650	141	34	1.7	I
	500	120	29	2.1	I
	350	80	29	2.1	I
	100	14	26	2.5	I

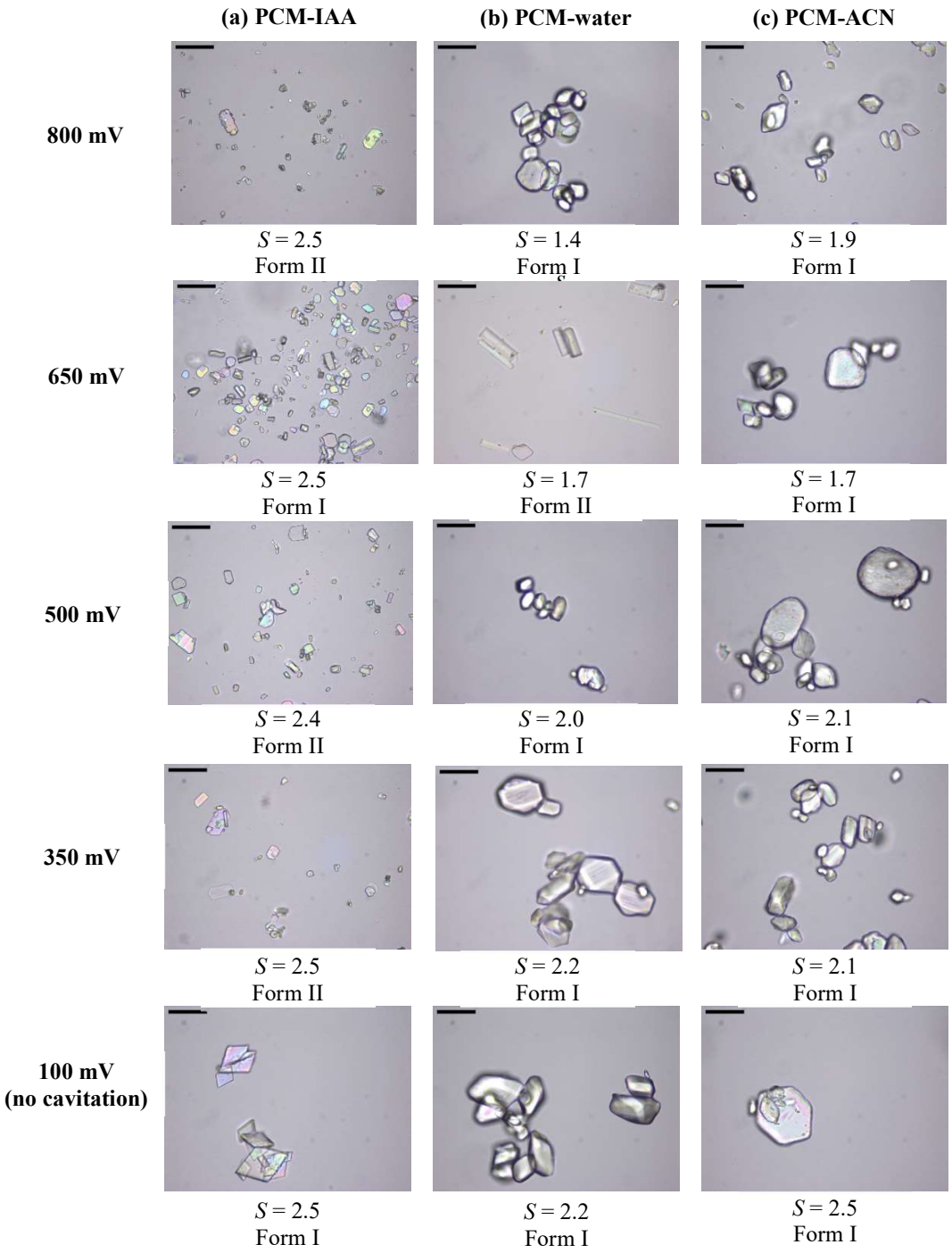

Figure 6-3: Microscope images of PCM sonocrystallisation without added impurities in (a) IAA, (b) water and (c) ACN. *The scale bars represent 50 μm.*

The crystals produced with cavitation generation in IAA are of a fragmented appearance, but it is unlikely that sonofragmentation during growth took place considering that the applied cavitation field was predominantly stable. This is further supported by the appearance of the crystals from water at high cavitation energies. Crystals similar in appearance to those produced from IAA with cavitation generation look like the expected product of a fast anti-solvent addition process, involving the generation of very high and, typically non-uniform supersaturation levels and a rapid crashing out of the product. The crystals obtained are not dissimilar to the images reported in the fast anti-solvent PCM sonocrystallisation study by Bhangu *et al*., that were assigned as mixtures of form I and II (from images).[222]

On comparison with the crystals generated from no cavitation conditions, it is thought that the crystals generated with the application of cavitation followed a different, (more rapid and uncontrolled) growth mechanism, such as birth and spread.[7] Most of the IAA solutions nucleated within the two hour hold period at 10°C, which generated very high supersaturation levels in the solutions and which would have facilitated the rapid growth of the form II obtained in 3/4 solutions where cavitation was applied. In the case where form I was generated (at 650 mV pp), it seems likely that a mixture of form I and II was nucleated in this experiment, which transformed to form I before isolation. It is thought that there will be a cavitation threshold energy above which form II is preferentially nucleated, which would align with the proposal of highly localised, elevated supersaturation levels that promote solute clustering on bubble collapse, leading to different polymorphic outcomes on comparison with silent conditions.[217] Whilst no form II was selectively generated in ACN, in which significantly lower cavitation energies were measured compared to water and IAA, the rapid solution-mediated transformation of PCM II to I cannot entirely be ruled out. In PCM-ACN experiments, cavitation generation did result in nucleation induction at lower *S* levels and no morphological changes were observed, both on comparison with silent conditions. The same observations were made in the PCM-water system, aside from at 650 mV pp, where rod-like form II crystals were

selectively crystallised. Again, rapid solution-mediated transformation cannot be ruled out for the remaining PCM crystals obtained from water with cavitation generation.

6.3.1.2. Paracetamol Sonocrystallisation in the Presence of Acetanilide

It has previously been determined that the impurity incorporation mechanism of ACE is adhesion to the surface of PCM.[73] From the observation of delayed induction times of PCM in the presence of ACE reported by Nguyen *et al.* a second higher concentration was also investigated, with the aim of inducing nucleation in the PCM-IAA system at lower supersaturation levels.[234] An important consideration is the impurity uptake levels at 100 mV (no cavitation) as lower levels of impurity are expected to be purged under the weaker mixing conditions provided in the absence of cavitation generation during growth. The presence of micromixing provided under driving amplitudes 350–800 mV pp is thought to increase the mass transfer rate of impurity molecules away from the crystal surface. Although, it is unknown how uniform micromixing would have been throughout the volume of the vials under the applied cavitation field.

Table 6.2 shows the results from scoping cooling PCM sonocrystallisation experiments in IAA, water and ACN, in the presence of 2% mol ACE. In the experiments where cavitation was generated, if ultrasound in fact enhanced impurity rejection, it was expected that this would be observed to a greater extent at higher cavitation energies. However, this was not observed.

Table 6-2 Polymorphic and purity results of PCM sonocrystallisation in the presence of 2% mol ACE in IAA, water and ACN

Solvent	PCM solution conc. (mg/g)	p-p amplitude at 40 kHz (mV)	Average P_a (kPa)	T_{ind}	S	Form	mol% ACE
IAA	156	800	395	36	2.3	II	0.85
		650	330	36	2.3	II	0.43
		500	347	32	2.5	I	0.28
		350	251	24	2.9	II	1.26
		100	15	18	3.2	I	1.14
	104	800	395	10	2.5	II	1.21
		650	330	10	2.5	II	0.82
		500	347	10	2.5	II	1.31
		350	251	10	2.5	II	1.37
		100	15	10	2.5	I	1.03
Water	53	800	335	50	1.5	I	0.67
		650	323	44	1.8	II	1.07
		500	242	41	2.0	I	0.46
		350	134	41	2.0	I	0.51
		100	8	35	2.5	I	0.79
	35	800	335	34	1.7	I	0.77
		650	323	30	2.0	II	1.46
		500	242	27	2.2	I	0.55
		350	134	27	2.2	I	0.55
		100	8	25	2.4	I	0.87
ACN	98	800	129	41	2.0	I	0.14
		650	141	41	2.0	I	0.11
		500	120	43	1.9	I	0.16
		350	80	39	2.2	I	0.20
		100	14	34	2.6	I	0.32
	66	800	129	32	1.9	I	0.19
		650	141	30	2.0	I	0.18
		500	120	30	2.0	I	0.19
		350	80	28	2.1	I	0.14
		100	14	20	2.8	I	0.39

In order to aid discussion, select microscope images from PCM sonocrystallisation experiments in the presence of 2% mol ACE in (a) IAA (b) water and (c) ACN are given in in Fig. 6-4 (images from every experiment are in Appendix C-3).

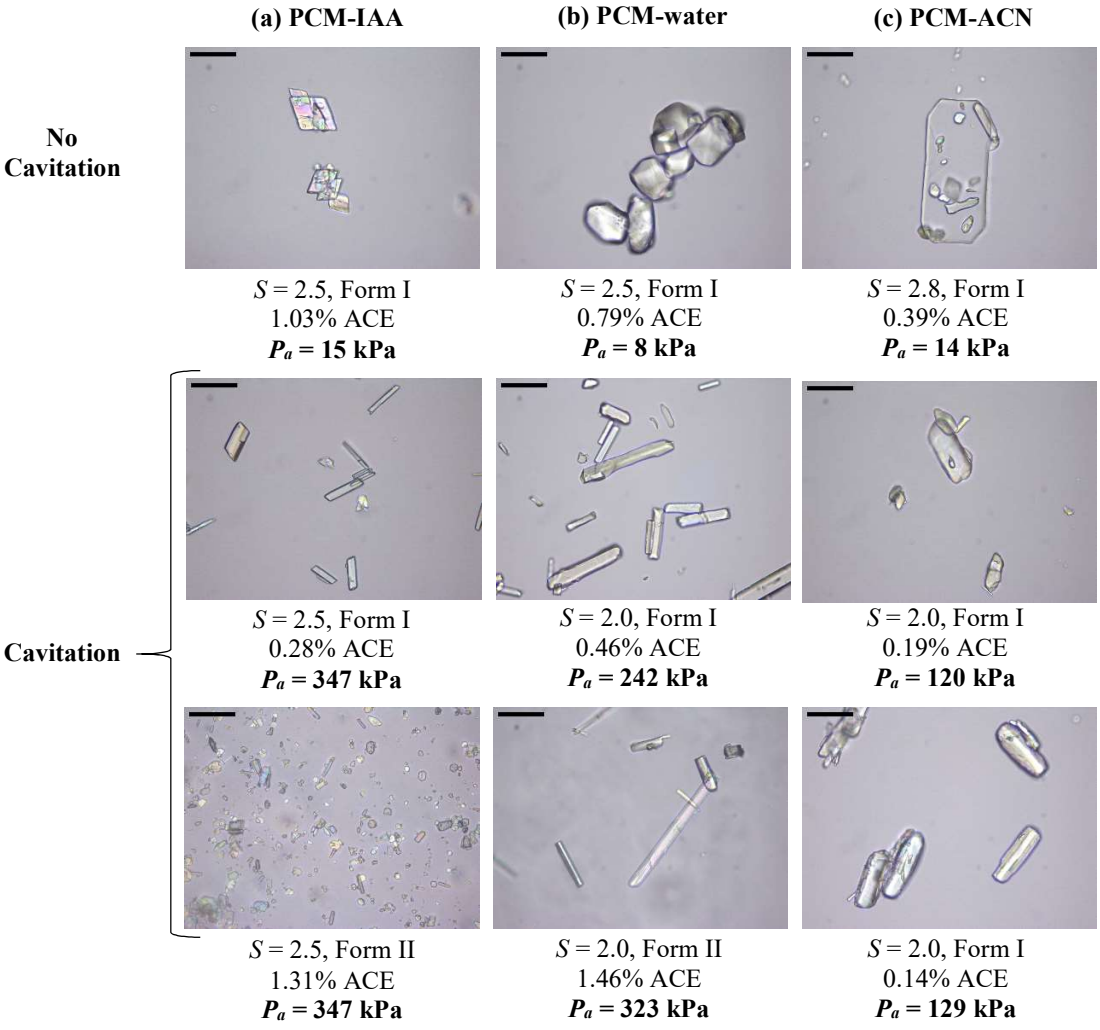

Figure 6-4: Select microscope images from PCM sonocrystallisation experiments in the presence of 2% mol ACE in (a) IAA (b) water and (c) ACN. *The scale bars represent 50 µm.*

From Fig. 6-4, it can be concluded that with no cavitation generated, the experiments at 100 mV pp across all solvents produced crystals of similar PCM form I morphologies observed as in the case where no ACE was added (Fig. 6-3). From Table 6-2, across all solvents and in cases where Form I was obtained, it is generally observed that when cavitation generation induced nucleation at lower *S*, lower amounts of ACE were detected

in the product. This is consistent with the lower supersaturation growth conditions generated. For instance, in the case of 98 mg/g PCM-ACN experiments, at 800 mV pp a *S* of 2.0 was recorded and 0.14 mol% ACE was detected in the product. Whereas at 100 mV pp (no cavitation), a *S* of 2.6 and 0.32 mol% of ACE were measured.

It also generally appears that when form II was selectively crystallised, higher mol % ACE were detected in the product. This indicates rapid growth conditions leading to the incorporation of large amounts of ACE, on comparison with no cavitation (100 mV pp) experiments and experiments in which form I was obtained. For example, in the case of 35 mg/g PCM-water experiments, under no cavitation conditions (100 mV pp) form I was obtained and 0.87 mol% ACE was detected in the product. Whereas, under 650 mV pp, form II was obtained and 1.46 mol% ACE was detected in the product.

The rapid growth conditions are thought to explain why the solution-mediated transformation to form I did not occur before isolation. As observed in the scoping sonocrystallisation experiments without impurities, the selective crystallisation of form II was prevalent in IAA, which resulted in very small (< 20μm) crystals of rough and fragmented appearance, on comparison with the form I crystals obtained at the same bulk supersaturation level, without cavitation generation. In addition, the selective generation of form II was again obtained in water, at both concentrations investigated only at 650 mV pp amplitude drive. No form II was selectively generated in ACN.

Previous PCM crystallisation studies in the presence of ACE and MCM have reported an increase of aspect ratio in the presence of increasing amounts (mol %) of ACE and MCM.[68, 72] The impurity incorporation is known to be face-specific, which results in a final columnar morphology, on comparison with equant crystals obtained without impurities, or with small impurity amounts. Under high supersaturation conditions, growth is limited by the surface integration processes of growth units (including adsorption and incorporation), as opposed to mass transfer from the bulk to the crystal surface. Jiang previously proposed that ultrasound may accelerate surface nucleation and provide more active growth sites for crystal growth, in order to explain enhanced growth rates with the application of ultrasound.[225]

With predominantly stable cavitation generation, the effects of cavitation on growth are more obvious, since predominantly transient cavitation generates sonofragmentation, which enhances secondary nucleation and results in fragmented crystal products of a reduced particle size.[193] From the current study, it seems that cavitation generation can accelerate the surface integration processes of growth, which appears to have resulted in columnar shaped crystals, as opposed to the more equant crystals obtained without cavitation generation (both in the presence of 2 mol% ACE). The results dispute the previously proposed mechanism of cavitation enhancing impurity rejection from the crystal surface.[234] It seems that the lower impurity levels in the crystal product can be attributed to nucleation induction at significantly lower supersaturation levels; it also seems unlikely that impurities are removed during growth by cavitation phenomena, if this accelerates the surface integration processes.

However, it is important to note that the scoping experiments were intended as a guide for upscale experiments involving overhead stirring. The mixing conditions across all scoping experiments were likely to be improper or erratic, resulting in a non-uniform and unknown supersaturation level distribution throughout the vials. This was thought to be most severe in the case of IAA. This effect is further compounded by highly localised supersaturation elevations from bubble collapse that are proposed to lead to form II nucleation.

A plot of polymorphic assignments of PCM form I/II from the scoping experiments in the presence of 2% ACE, as a function of average BIV and *S* is provided in Fig. 6-5. It is thought that the macro *S* levels in Fig. 6-5 cannot entirely be relied upon to represent the nucleation conditions of PCM in each experiment where cavitation was generated. Due to the rapid solution-mediated transformation of form II to form I, it is not possible to define a threshold cavitation energy for form II to be obtained but from the results, it does seem that rapid growth conditions (as indicated by the larger mol % ACE in form II products) is required in order to prevent this transformation.

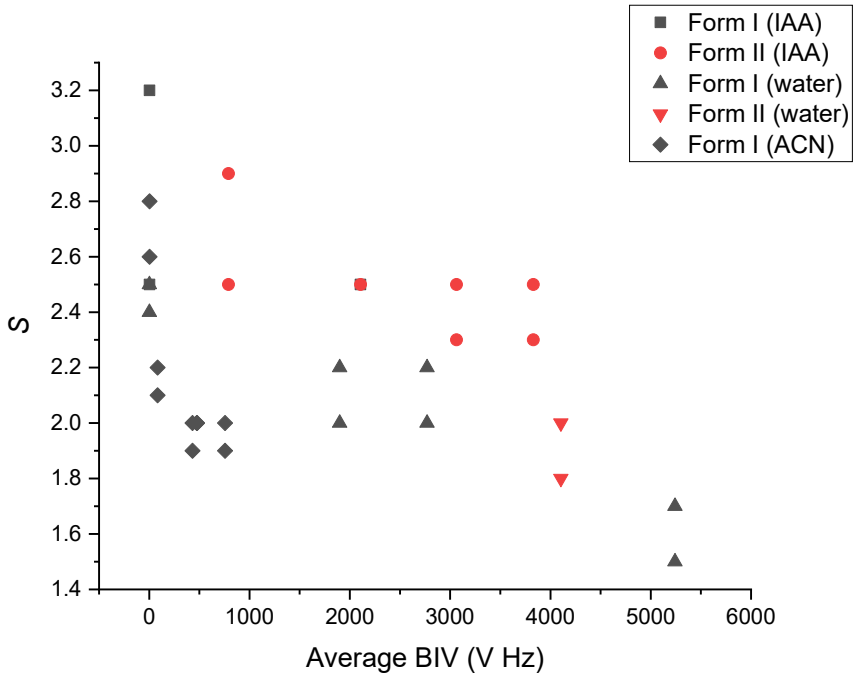

Figure 6-5: Plot of polymorphic assignments of PCM form I (dark grey) and II (red) from scoping experiments with 2% ACE, as a function of average BIV and S.

The system of interest for the upscale experiments is PCM-IAA and the 6mL experiments were designed in order to scope ultrasound parameters and cavitation energies that may lead to the formation of form II. The selective crystallisation of form II appears to be dependent upon very high supersaturation levels, rapid growth conditions and the generation of cavitation energy at above a presumed threshold value (which is undefined from this data). By performing experiments in the presence of 2 mol % ACE, a highly interesting observation was made that has not before been reported; only with cavitation generation was a morphology change from equant to columnar crystals of form I observed, that is consistent with the face-specific inhibition of PCM by ACE adhesion. From this, it is concluded that cavitation generation can accelerate the surface integration processes when applied during growth.

6.3.2. Upscale Cooling Sonocrystallisation Experiments

A plot of average P_a and BIV values from needle hydrophone measurements in the IAA-filled jacketed vessel (from 100-800 mV pp amplitude drive) is provided in Appendix C-4. Overall, the BIV values are significantly lower than those measured in the IAA-filled vials immersed in the vessel (filled with water). This effect is possibly due a lesser disturbance of the standing wave (without the suspension of the glass vials) and as a result, fewer transient cavitation events are expected to be generated within the pressure range measured under cavitation generation (average P_a measured ranged 50-98 kPa). The upscale PCM-IAA cooling sonocrystallisation polymorphism, purity and morphology experimental results are provided in Table 6-3. The measured XRPD patterns and DSC thermograms are in Appendices C-5 and C-6, respectively.

Table 6-3 Upscale PCM-IAA cooling sonocrystallisation polymorphism, purity and morphology experimental results

Experiment	p-p amplitude at 40 kHz (mV)	T_{ind}	S	Form	mol% ACE	mol% MCM	DSC Offset (°C)	Morphology
PCM with 2% ACE	800	68	1.3	I	0.24	-	168.8	Columnar
	650	65	1.4	I	0.36	-	168.7	Columnar
	500	60	1.5	I	0.34	-	168.8	Columnar
	350	58	1.6	I	0.45	-	168.6	Columnar
	100	51	1.8	I	0.52	-	168.3	Equant
PCM with 2% MCM	800	52	1.8	I	-	0.91	168.4	Columnar
	650	55	1.7	I	-	0.96	168.0	Columnar
	500	23	3.1	I	-	1.28	167.6	Equant
	350	18	3.4	I	-	1.41	167.6	Equant
	100	10	4.0	I	-	1.35	167.7	Equant
PCM with 1% ACE and 1% MCM	800	59	1.5	I	0.16	0.37	168.4	Columnar
	650	62	1.5	I	0.18	0.49	168.7	Columnar
	500	55	1.7	I	0.17	0.42	168.6	Columnar
	350	44	1.9	I	0.21	0.50	168.0	Columnar
	100	10	4.0	I	0.36	0.64	168.3	Equant
	800	10	4.0	I	0.56	0.73	167.2	Fines
PCM (pure)	800	70	1.3	I	-	-	169.1	Equant
	100	53	1.7	I	-	-	169.1	Equant

To aid discussion, microscope images of upscale PCM-IAA sonocrystallisation experiments (a) with 1% ACE and 1% MCM and (b) without added impurities are shown in Fig. 6-6 (all remaining upscale images are in Appendix C-7).

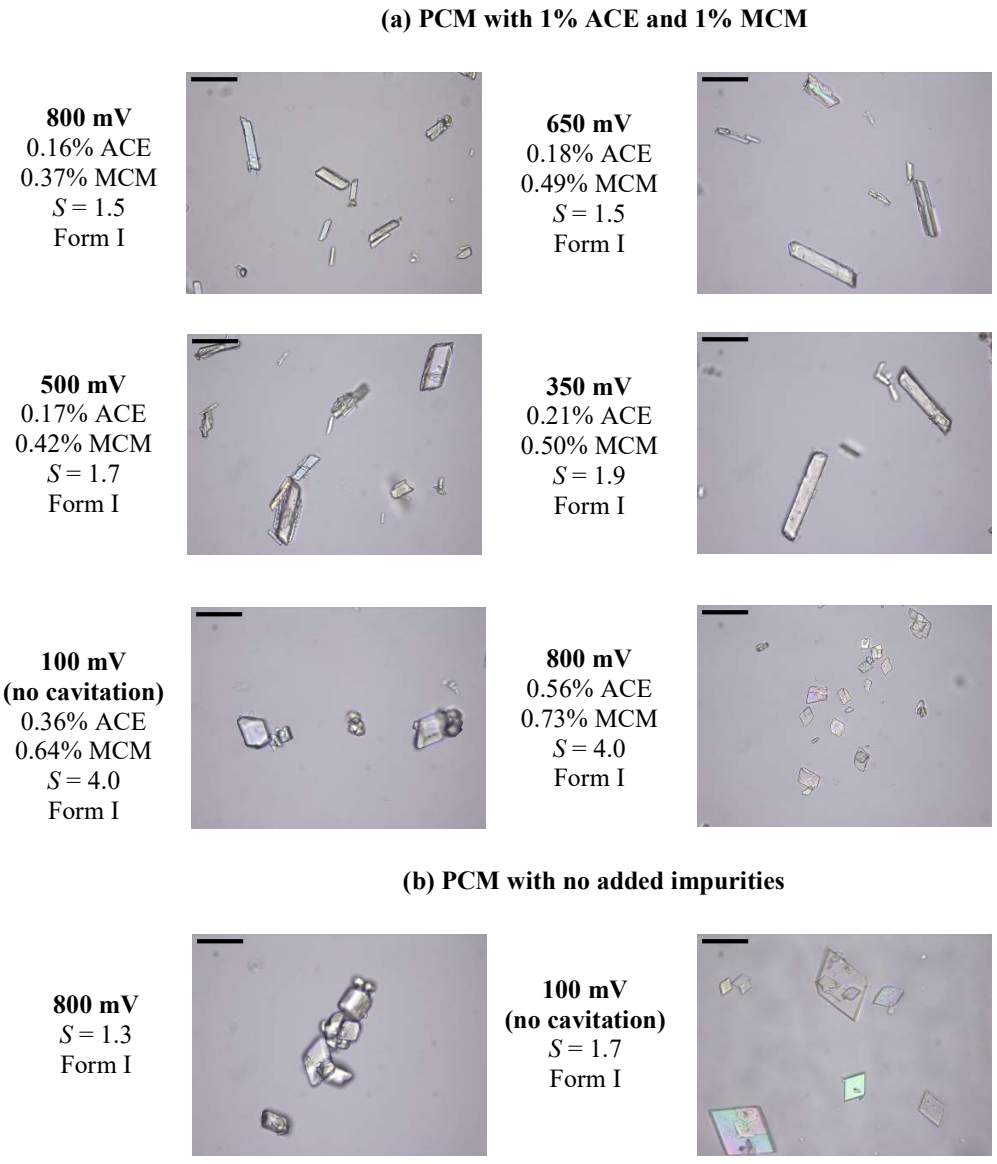

Figure 6-6: Microscope images of upscale PCM-IAA sonocrystallisation experiments (a) with 1% ACE and 1% MCM and (b) without added impurities. *The scale bars represent 50 µm.*

The upscale experiments further verify that lower impurity uptake can be attributed to nucleation induction at lower supersaturation levels, with cavitation generation. In the presence of impurities, it seems that cavitation generation impacted the final morphology through accelerated surface integration, until very high supersaturation levels were generated (S >1.9). It is expected that above this level, growth is not limited by surface integration and a rapid and uncontrolled growth mechanism is followed, which is not expected to be influenced by cavitation phenomena. Otherwise, columnar morphologies were consistently obtained in the presence of impurities, and only with cavitation generation (see Fig. 6-6). On comparison with PCM crystallised under the application of 800 mV pp amplitude without impurities, it is clear that MCM inhibits nucleation, which is consistent with a previous report noting that MCM increases the surface free energy and the size of the critical nucleus; which leads to higher activation energies being required for nucleation and longer induction times.[320] MCM is known to incorporate into PCM during growth through partial miscibility, which makes it very difficult to purge.[73] The DSC results of reduced offset points confirm that a greater proportion of MCM is incorporated into the PCM product compared to ACE. In the case of ACE, the incorporation mechanism into PCM is adhesion to the surface, which is easier to purge.

Plots of S and mol % impurity detected in the product, as a function of average BIV from upscale PCM-IAA sonocrystallisation experiments in the presence of (a) 2% ACE and (b) 2% MCM are provided in Fig. 6-7 in order to illustrate that S and mol % impurity in the product are broadly observed to correlate. From this, it is concluded that cavitation phenomena do not enhance impurity rejection, as at higher cavitation energies a greater extent of impurity removal would be expected. Moreover, if the surface integration of impurities is accelerated with cavitation generation, this would decrease the opportunity for impurity removal. Impurity purging is a critical component in the industrial crystallisation of drug substances and these experiments demonstrate that with cavitation generation, nucleation can be induced at lower supersaturation levels. Although, the extent to which cavitation is applied throughout growth requires further investigation. Aside from impurity purging, there may be slow growing compounds that would benefit from

the application of a stale cavitation field throughout growth, but in the current study, accelerated surface integration in the presence of impurities is an undesired effect.

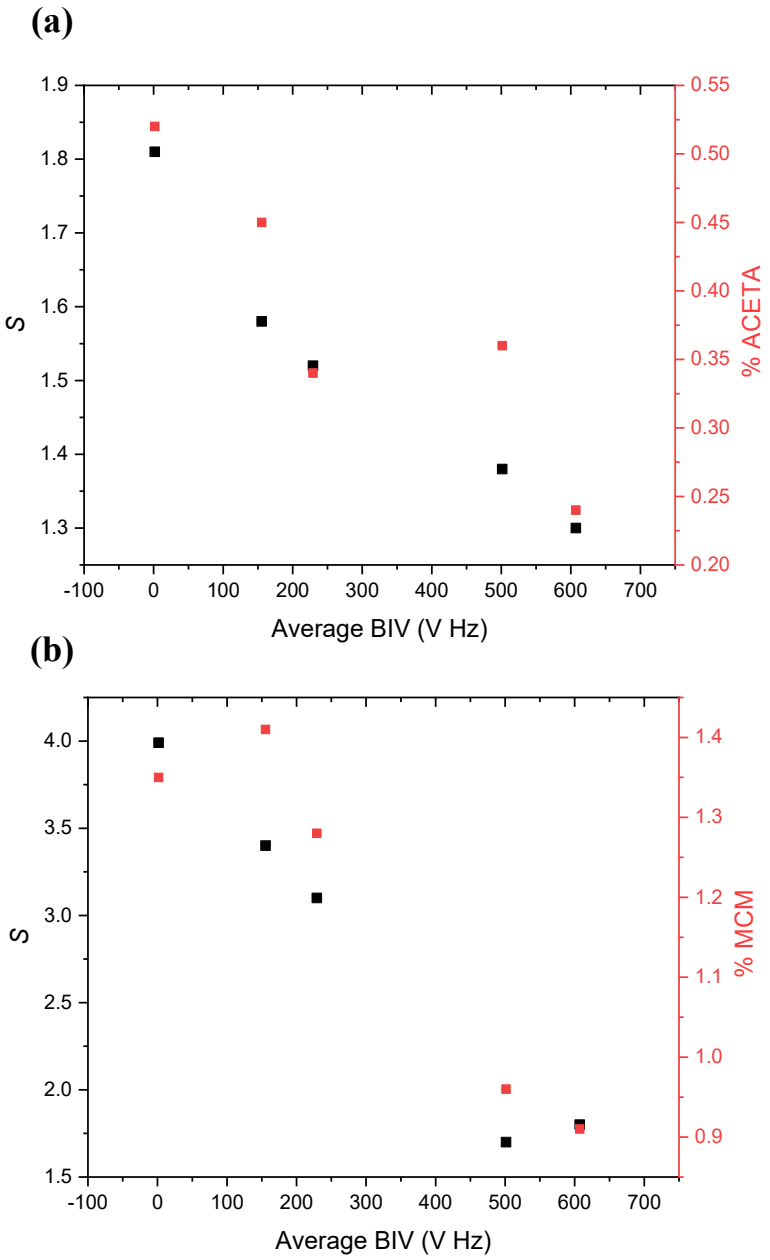

Figure 6-7: Plots of S and mol % impurity detected in the product, as a function of average BIV from upscale PCM-IAA sonocrystallisation experiments in the presence of (a) 2% ACE and (b) 2% MCM

Across all upscale experiments, form I was generated. The MR probe was used for monitoring polymorphic composition at the point of nucleation in the system of all experiments of PCM (pure) and PCM with 1% ACE and 1% MCM. An experiment was additionally performed in order to generate very high *S* and ultrasound was turned on (800 mV pp), at which point nucleation was induced instantly. Plots of measured FBRM particle counts and second derivative Raman spectral intensities for PCM-IAA sonocrystallisation with 1% ACE and 1% MCM at (a) 800 mV driving amplitude applied for the duration of the cooling profile (b) 800 mV driving amplitude applied from 160 min are provided in Fig. 6-8. It should be noted that form I and II of dissolved PCM cannot be distinguished. PVM images obtained from these experiments are also provided in Appendix C-8. Despite the very high supersaturation level (S =4.0) generated in (b), only form I was detected, and this is attributed to the low cavitation energies detected in the IAA-filled vessel (maximum average value = 607± 52 V Hz).

This result is significant because it provides evidence for a minimum cavitation energy being required in order to generate form II. Therefore, at the same applied ultrasound frequency (which dictates the bubble size) a minimum cavitation energy to nucleate a different polymorphic form on comparison with silent conditions implies that the mechanism for nucleation induction is linked to the mechanical energy generated on bubble collapse and not the presence of the bubbles themselves (enhanced heterogeneous nucleation). It is thought that bubble collapse phenomena produces highly localised solute clustering to form a critical nucleus, which is thought to be more probable under high absolute solute concentration/supersaturation conditions. Below this cavitation energy and *S* threshold, it is presumed that the predominant nucleation mechanism is heterogeneous at the bubble surface and if growth is surface-integration limited, the oscillation of these stable bubbles during growth (micromixing) can accelerate the integration of growth units in the vicinity of the growth layer, which may or may not be desired.

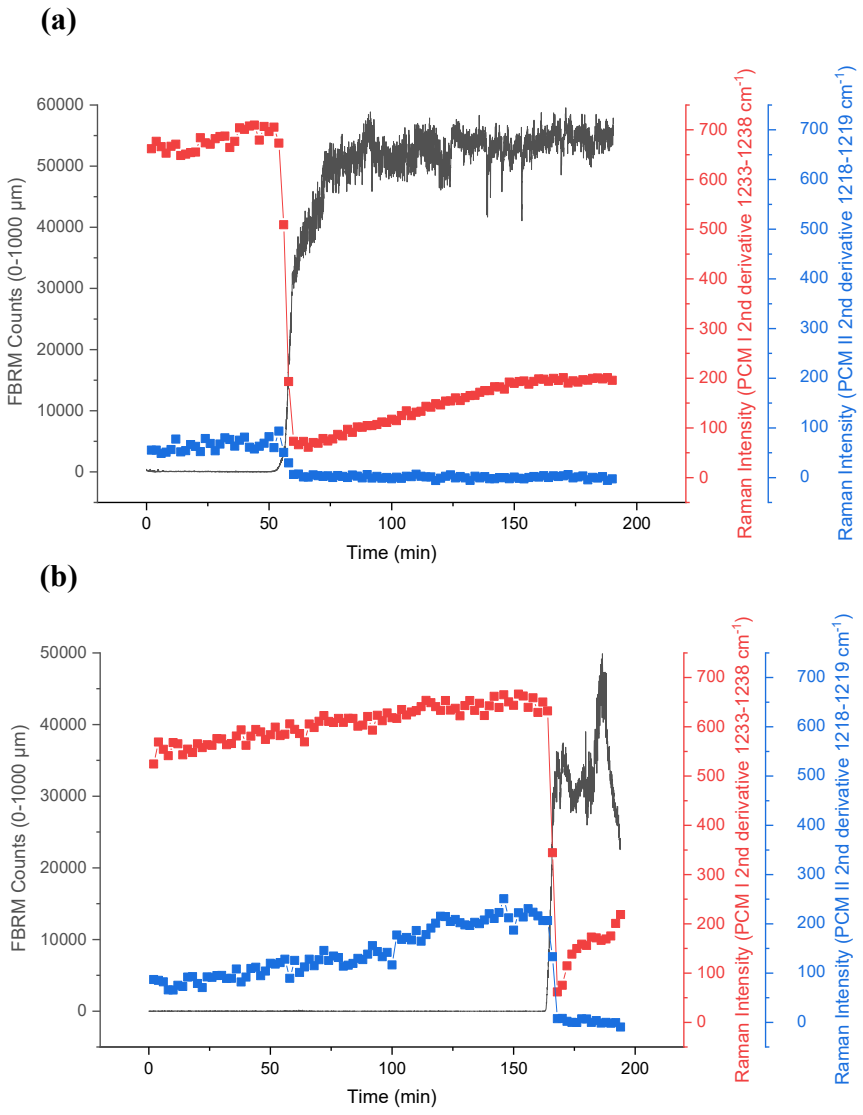

Figure 6-8 Plots of measured FBRM particle counts (grey) and second derivative Raman spectral intensities of PCM form I Raman at 1233-1236 cm^{-1} (red), and PCM form II Raman at 1218-1219 cm^{-1} (blue) for PCM-IAA sonocrystallisation experiments with 1% ACE and 1% MCM at (a) 800 mV driving amplitude applied for the duration of the cooling profile (b) 800 mV driving amplitude applied from 160 min. *Note that in solution (prior to FBRM detecting particle counts) form I and II PCM cannot be distinguished.*

6.4. Conclusions

Previously the intense mechanical energies generated from cavitation were linked to both the generation of form II PCM and greater impurity rejection in the presence of structurally similar impurities.[222, 223, 234] Therefore, it was expected that by varying the cavitation energy generated in PCM sonocrystallisation processes, these effects would be observed to varying extents. A setup was established, in which both 6 mL scoping and 125mL upscale cooling PCM sonocrystallsation experiments were carried out and the cavitation energy was measured with a needle hydrophone.

The selective crystallisation of form II appeared to be dependent upon very high supersaturation levels, rapid growth conditions and the generation of cavitation energy at above a threshold value. Due to the rapid solution-mediated transformation of form II to form I, it was not possible to define a threshold cavitation energy for form II to be selectively obtained from the scoping experiments. Consistent with the report by Mori *et al.,* rapid desupersaturation was thought to prevent this transformation before isolation, in cases where form II was obtained.[223] It is thought that, since erratic mixing conditions were generated in the vials, resulting in non-uniform supersaturation levels and potentially, the macro-level S calculated may not actually have been representative. This effect was thought to be most severe in the case of IAA due to the high viscosity of this solvent-, which may have contributed towards the selective crystallisation of form II being most prevalent in IAA.

The upscale experiments verified that higher impurity purging could be attributed to nucleation induction at lower supersaturation levels with cavitation generation, as opposed to cavitation phenomena enhancing impurity rejection during growth. Sonocrystallisation in the presence of ACE and MCM demonstrated that stable cavitation generation can impact the final morphology through accelerated surface integration, until very high supersaturation levels were generated (S >1.9). It is expected that above this level, growth is not limited by surface integration and a rapid and uncontrolled growth mechanism is followed, which is not expected to be influenced by stable cavitation phenomena.

Otherwise, columnar morphologies were consistently obtained in the presence of impurities, and only with cavitation generation, which is consistent with the face-specific inhibition of PCM by structurally similar impurities. This effect has not before been reported and it is expected to influence the development of industrial sonocrystallisation processes for drug substance purification.

Across all upscale experiments, form I was generated. Raman monitoring of polymorphic composition was performed and even when nucleation was induced at a very high supersaturation level (S =4.0), only form I was detected, which was attributed to the lower cavitation energies detected in the IAA-filled vessel, on comparison with the configuration of IAA and water-filled vials in the scoping experiments. This result is significant because it points to a mechanism for nucleation induction of PCM form II involving cavitation bubble collapse phenomena, as opposed to the presence of the bubbles themselves (enhanced heterogeneous nucleation).

Thesis Summary

The original scope of this project was to improve upon the understanding of a previous sonocrystallisation study that reported greater impurity rejection of PCM in the presence of ACE and MCM, with ultrasound.[234] Nguyen *et al.* principally attributed the purity enhancement to cavitation generation removing impurities at the surface of crystals during growth and the purity results were presented at one ultrasound power setting.[234]

From a review of the sonocystallisation literature, it was clear that few reports involved measurement of cavitation activity in the generated sound field and no studies were found using acoustic detection. The following aims were conceived:

- Establish a set-up for needle hydrophone measurements of typical crystallisation solvents and water to allow a comparison of the cavitation activity under the same applied ultrasound parameters
- Establish a set-up for cooling sonocrystallisation experiments to be carried out in order to further investigate the previously reported (i) selective crystallisation of PCM form II and (ii) greater impurity rejection of PCM in the presence of ACE and MCM; both as a function of cavitation energy

Collaboration with Ward allowed for needle hydrophone measurements and high-speed imaging to be utilised in order to investigate the impurity particle-heating mechanism that had previously been proposed as the mechanism behind the NPLIN effect.[257]

As previously stated, the effects of cavitation phenomena can be advantageous or detrimental, depending on the occurrence. The cavitation damage sustained to several needle hydrophone probe tips from long-term exposure under a 40 kHz sound field led to significant project delays. The severe time constraints for the experimental work in this thesis unfortunately, limited further exploratory work from the results obtained. Nevertheless, by establishing experimental setups in which acoustic detection could be

utilised, outcomes from previous LIN and sonocrystallisation studies were further investigated and the experimental findings are concluded herein.

7.1. Conclusions

7.1.1. Laser-induced Nucleation by Particle Heating

On combination of the high-speed imaging observations and needle hydrophone measurements, Chapter 4 provides compelling evidence for the impurity particle-heating mechanism. Single-pulse (1064nm, 6ns) irradiation at a fixed j_{peak} of 292 MW cm^{-2} was used throughout the study, which is far below the average power threshold for the breakdown of DI water, previously reported as 76 GW cm^{-2} (1064 nm, 6ns).[273]

The imaging setup allowed for 10μs observation intervals and a field of view of 1120μm by 445μm was provided with an object size detection limit of 3.6μm. Irradiated NH_4Cl solutions (S=0.9), demonstrated that the number of bubbles generated within the field of view increased with the volume of Fe_3O_4 NP suspension added prior to irradiation. This is attributed to a mechanism involving NP and/or NP aggregates absorbing light from the laser pulse and rapidly heating up to generate photothermal vaporisation in the surrounding liquid, with more energy being absorbed by larger particles and/or particle aggregates, resulting in the generation of larger bubbles with longer lifetimes. Furthermore, what is believed to have been incandescence from particle heating was observed prior to bubble growth to a maximum radius. Interestingly, dark particle-like objects were observed at the same locations where the largest bubbles within the field of view were observed prior, which are thought to be remnant bubbles that persist in the solution.

Out of six LIN imaging attempts, in one case no bubbles at or above the object size detection limit were detected before the appearance and growth of 11 crystals (undoped sample C). Also, in the case of doped sample B, fifty bubbles were detected in frame 1

and no crystals were generated, yet persisting objects in the location of prior bubbles were observable 900ms following irradiation. Bubble oscillation and collapse events within a confined area are known to cause microconvection and vortex formation in the liquid and this aspect provides a further challenge in capturing bubble and crystallisation events. There were four samples in which both bubbles and crystals were detected within the field of view and in every case; the first observable crystal appeared in the same location as the largest bubble observed prior. These observations provide strong evidence that the cavitation event is directly linked to crystal nucleation in LIN and it follows that the extent of supersaturation increase would increase with the size of the bubble generated, as more solvent would have been vaporised.

In three of these four solutions, an unknown object (most likely to be a bubble remnant following multiple expansion and shrinkage cycles of the nucleated bubble following initial collapse) persisted in the solution and it is unknown what role, if any, the unidentified, long-lived object noted immediately after bubble shrinkage/collapse may have in nucleation induction. It is thought that there will be a critical bubble size (and lifetime) for a cavitation event to lead to nucleation; therefore, not all cavitation events will lead to nucleation induction. Hence the nucleation probability is likely to be higher in the case where larger impurity particles/particle aggregates are irradiated and generate larger bubbles with a longer initial growth period, leading to higher supersaturation elevation surrounding the bubbles.

As the needle hydrophone was found to trigger nucleation in supersaturated solutions, measurements were performed in undersaturated solutions, also at a fixed j_{peak} of 292 MW cm^{-2}. Within the unfocussed beam–path, the nucleation of multiple bubbles of different sizes and lifetimes resulted in the generation of complex acoustic signals. By investigating the effect of solute concentration on the resulting acoustic signals, a trend of a linearly increasing signal RMS with solute concentration was observed that would be consistent with the presence of absorbing impurity particles along with the solute itself. Therefore, it is concluded that the impurity particles present in untreated NH_4Cl solutions are responsible for photothermal cavitation and the resulting acoustic signal. Filtering

solutions prior to irradiation did overall reduce the average signal RMS values measured on comparison with untreated NH_4Cl solutions. These results support the proposal that the highest RMS measurements recorded in the unfiltered solution measurement set are from large (> 5μm) particles/particle aggregates present in the untreated solution. Fe_3O_4 NP doping of the NH_4Cl solutions significantly increased the average signal RMS values measured in the solutions, on comparison with the undoped solution measurements. It follows that adding increasing amounts of absorbing particles resulted in an increased number of cavitation events and larger bubbles. The variance between measurements of irradiated samples is attributed to particle aggregation and an inhomogeneous dispersion of absorbing particles/particle aggregates within the beampath.

The effect of laser processing was also investigated. Following 10 Hz irradiation, the large reduction in the signal magnitude can be attributed to the destruction of absorbing particles within the beampath. As the solution was left to refresh (mix by diffusion), a further measurement demonstrated that this process allowed for the beampath to be refilled with more particles. The hydrophone measurements strongly support the high-speed imaging observations, together with the previous NH_4Cl LIN study by Ward *et al.*, in which the nucleation propensity was suppressed by filtration prior to irradiation, and this was subsequently reversed by doping with Fe_3O_4 NP.[257]

Overall, the results demonstrate a direct relationship between absorbing particles, cavitation generation and crystal nucleation and the induction of multiple primary nuclei within an unfocussed beampath. This has powerful implications for discussions behind the mechanism for LIN.

7.1.2. Sonocrystallisation

Measurement of light or acoustic emission from cavitation bubble collapse are the only methods in which the energy produced from “active” bubbles generated under the ultrasound field can be quantified. Furthermore, it is high cavitation energy that has been

linked to both the generation of form II PCM and greater impurity rejection in the presence of structurally similar impurities.[222, 223, 234]

In Chapter 5, the needle hydrophone measurement technique in organic solvents was established and under the same applied ultrasound parameters, cavitation generation in BuOH, IAA, EtOH, ACN and MEK was compared. in the case of the organic solvents large visible (inactive) bubbles generated by coalescence were observed. From this, it is also speculated that dense clusters of bubbles may result in additional acoustic attenuation and bubble shielding effects, contributing to the lower P_a and BIV values measured in organic solvents on comparison with water. Significantly lower P_a BIV values were obtained from measurements in the more volatile solvents (EtOH, MEK and ACN) on comparison with IAA, BuOH and water, which is attributed to a higher likelihood of liquid vapour of the solvent entering the bubble during the rarefaction phase of growth by rectified diffusion and cushioning the collapse. Furthermore, lower BIV and P_a values observed in IAA and BuOH on comparison with water are also attributed to higher energy lost due to internal friction in the higher viscosity solvents. The effect of degassing was also investigated, which generally did appear to reduce the bubble counts with FBRM measurements and slightly increase the BIV values, from which higher energy collapse is inferred.

From Chapter 6, it may be concluded that the selective crystallisation of form II was dependent upon very high supersaturation levels, rapid growth conditions and the generation of cavitation energy at above a threshold value. Due to the rapid solution-mediated transformation of form II to form I, it was not possible to define a threshold cavitation energy for form II to be selectively obtained from the scoping experiments. Consistent with the report by Mori *et al.,* rapid desupersaturation was thought to prevent this transformation before isolation, in cases where form II was obtained.[223] It is thought that, since erratic mixing conditions were generated in the vials, resulting in non-uniform supersaturation levels and potentially, the macro-level *S* calculated may not actually have been representative. This effect was thought to be most severe in the case of IAA due to

the high viscosity of this solvent-, which may have contributed towards the selective crystallisation of form II being most prevalent in IAA.

The upscale experiments verified that higher impurity purging could be attributed to nucleation induction at lower supersaturation levels with cavitation generation, as opposed to cavitation phenomena enhancing impurity rejection during growth. Sonocrystallisation in the presence of ACE and MCM demonstrated that stable cavitation generation can impact the final morphology through accelerated surface integration, until very high supersaturation levels were generated (S >1.9). It is expected that above this level, growth is not limited by surface integration and a rapid and uncontrolled growth mechanism is followed, which is not expected to be influenced by stable cavitation phenomena. Otherwise, columnar morphologies were consistently obtained in the presence of impurities, and only with cavitation generation, which is consistent with the face-specific inhibition of PCM by structurally similar impurities. This effect has not before been reported and it is expected to influence the development of industrial sonocrystallisation processes for drug substance purification.

Across all upscale experiments, form I was generated. Raman monitoring of polymorphic composition was performed and even when nucleation was induced at a very high supersaturation level (S =4.0), only form I was detected, which was attributed to the lower cavitation energies detected in the IAA-filled vessel, on comparison with the configuration of IAA and water-filled vials in the scoping experiments. This result is significant because it points to a mechanism for nucleation induction of PCM form II involving cavitation bubble collapse phenomena, as opposed to the presence of the bubbles themselves (enhanced heterogeneous nucleation).

7.2. Future Work

7.2.1. Laser-induced Nucleation by Particle Heating

The observed induction of multiple primary nuclei within the irradiated volume in Chapter 4 shows promise for the future study of the relationship between cavitation generation and crystal nucleation with high-speed imaging. The generation of multiple primary nuclei is a clear advantage of LIN by particle heating versus LIN by optical cavitation. However, LIN by optical cavitation generates a less dynamic cavitation field within a tightly focussed volume, which is simpler to study and control. Nevertheless, maintaining the aqueous NH_4Cl system, some fine-tuning and optimisation of the optical parameters and imaging setup would be required in order to gain further insight into LIN by particle heating. Observations at < 1μs intervals (imaging at > 1M fps) and a higher spatial resolution would be required to investigate the cavitation bubble activity in greater detail, including the generation of shockwaves on bubble collapse. However, this would also significantly reduce the field of view and reduce the likelihood of capturing bubbles nucleated within the beampath. A non-invasive method monitoring technique could be investigated in order to quantify the incandescence thought to be produced by heated particles. Since optical breakdown of the particles could not entirely be ruled out in the current LIN study, it is thought that a spectroscopic technique could potentially distinguish incandescence from plasma emission to confirm the exact mechanism of bubble nucleation.

The effects of cavitation generation by laser irradiation on the polymorphic outcome are expected to be aligned with cavitation generation by ultrasound. A previous PCM LIN study using an unfocussed beampath reported that PCM nucleation was not induced by the optical parameters and solution conditions employed.[265] It is therefore proposed that a PCM LIN study using an unfocussed laser and added absorbing nanoparticles is carried out in order to investigate the polymorphic outcome with cavitation generation by particle heating. Whilst metal nanoparticle dopants would not be acceptable in pharmaceutical

manufacturing, they could prove a vital tool for exploratory LIN work when faced with difficult to nucleate compounds or for the study of compounds with elusive solid forms. For the LIN of drug substances, future work could also focus on exploring potential photothermal dopants that are non-metallic and non-cytotoxic. Polypyrrole nanoparticles or chemically conjugated small molecule nanoparticles look to be promising leads.[321, 322]

7.2.2. Sonocrystallisation

The needle hydrophone model employed in this work was found to be susceptible to cavitation damage following long periods of use and it is incompatible with non-aqueous media, which is not well suited for use in monitoring sonorystallisation processes. This does not rule out the possibility of acoustic emission measurement under an applied high power ultrasound field, but it does mean that a highly robust hydrophone like the custom model developed for the work by Tzanakis should be pursued.[196] Alternatively, consideration of a multi-bubble sonoluminescence measurement probe is advised.

Jordens *et al*. reported that the solvent properties are not expected to affect the cavitation activity under a predominantly transient cavitation field, since the bubble lifetime is typically < 1 cycle.[193] Measurements of acoustic emissions by Tzanakis *et al.*, that were performed under a predominantly transient cavitation field (with an ultrasound probe), including water and ethanol are not in agreement with this proposal.[196] The work in Chapter 6 established that there is a minimum cavitation energy to nucleate PCM form II and it was thought that the cavitation energies generated in ACN were below this, which is why form II was not selectively generated in this solvent. However, as it was not possible to entirely rule out potential solution-mediated transformation to form I, this argument is not strong. Therefore, similar upscale experiments could be carried out with another polymorphic compound that satisfies the following criteria: (i) the polymorph formed is not determined by the surface energy of the nucleus, but the difference in bulk chemical potential, (ii) the compound can be recrystallised in water, alcohols, alongside low boiling point esters or ketones, and (iii) a rapid solution-mediated polymorphic

transformation does not occur. This work may also further nail down the mechanism of the selective nucleation of a different polymorph with cavitation generation, on comparison with silent conditions. Seemingly, this may be explained by highly localised elevated supersaturation levels that promote solute on bubble collapse, which is expected to be aligned with the same effects observed with LIN and mechanical shock-induced nucleation.[217] It would be helpful to present a model system in which the cavitation energy is quantified and both the optical and ultrasound parameters and optimised in order to reliably deliver the desired polymorphic outcome. Overall, the effects of cavitation generation on polymorphism should be considered on a case-by-case basis and with consideration of the crystal energy landscape of the system.

The result of cavitation generation inducing nucleation at lower supersaturation levels in the presence of the nucleation inhibiting MCM would be better supported alongside a comparison with experiments in which the upscale PCM sonocrystallisation process was seeded, as this method should also reduce the induction time. It would be useful to compare both methods for effectiveness. Furthermore, the enhanced surface integration of impurities with cavitation has not before been reported and in the case of PCM with ACE and MCM, ideally single crystal growth measurements could be performed under the same applied cavitation field and at the same bulk supersaturation level. This effect would certainly be of interest for compounds that are slow growing. However, in the interest of impurity purging it is thought that applying a stable cavitation field throughout growth could reduce the opportunity for impurity removal or lead to potentially undesired morphological changes. Ultimately, the extent to which a predominantly stable cavitation field is applied during growth requires further investigation. Moreover, there is a clear requirement for equipment to be developed in order to carry out mL-scale sonocrystallisation parameter scoping experiments for new systems under investigation. This extra development work will require greater time and financial investment, which cannot be justified in all cases. However, the true utility of the added energy from an applied cavitation field would likely be realised in the case of more difficult to nucleate systems and/or systems with a complex polymorphic landscape, that are more frequently

faced in the industrial crystallisation process development of drug substances. High-energy cavitation phenomena seemingly yields the potential to provide access to solution conditions for nucleation at localised supersaturation levels, which are difficult to obtain by other means.

References

1. Hilfiker, R.; von Raumer, M., Polymorphism in the Pharmaceutical Industry: Solid Form and Drug Development. Wiley-VCH: 2019.

2. Ter Horst, J. H.; Schmidt, C.; Ulrich, J., Fundamentals of industrial crystallization. In Handbook of Crystal Growth, Elsevier. 2015.

3. Gao, Z.; Rohani, S.; Gong, J.; Wang, J., Recent developments in the crystallization process: toward the pharmaceutical industry. Engineering 2017, 3 (3), 343-353.

4. Mullin, J. W., Crystallization. Elsevier: 2001.

5. Kadam, S. S.; Kulkarni, S. A.; Ribera, R. C.; Stankiewicz, A. I.; ter Horst, J. H.; Kramer, H. J. M., A new view on the metastable zone width during cooling crystallization. Chemical engineering science 2012, 72, 10-19.

6. Lonare, A. A.; Patel, S. R., Antisolvent crystallization of poorly water-soluble drugs. International Journal of Chemical Engineering and Applications 2013, 4 (5), 337.

7. Beckmann, W., Crystallization: Basic concepts and industrial applications. John Wiley & Sons: 2013.

8. Myerson, A., Handbook of industrial crystallization. Butterworth-Heinemann: 2002.

9. McGinty, J.; Yazdanpanah, N.; Price, C.; ter Horst, J. H.; Sefcik, J., Nucleation and Crystal Growth in Continuous Crystallization in The Handbook of Continuous Crystallization. Royal Society of Chemistry: 2020.

10. Agrawal, S. G.; Paterson, A. H. J., Secondary nucleation: mechanisms and models. Chemical Engineering Communications 2015, 202 (5), 698-706.

11. Kadam, S. S.; Kramer, H. J. M.; ter Horst, J. H., Combination of a single primary nucleation event and secondary nucleation in crystallization processes. Crystal Growth & Design 2011, 11 (4), 1271-1277.

12. Gebauer, D.; Kellermeier, M.; Gale, J. D.; Bergström, L.; Cölfen, H., Pre-nucleation clusters as solute precursors in crystallisation. Chemical Society Reviews 2014, 43 (7), 2348-2371.

13. Jiang, S.; ter Horst, J. H., Crystal nucleation rates from probability distributions of induction times. Crystal growth & design 2011, 11 (1), 256-261.

14. Steendam, R. R. E.; Keshavarz, L.; Blijlevens, M. A. R.; de Souza, B.; Croker, D. M.; Frawley, P. J., Effects of scale-up on the mechanism and kinetics of crystal nucleation. Crystal Growth & Design 2018, 18 (9), 5547-5555.

15. Karthika, S.; Radhakrishnan, T. K.; Kalaichelvi, P., A review of classical and nonclassical nucleation theories. Crystal Growth & Design 2016, 16 (11), 6663-6681.

16. Chen, J.; Sarma, B.; Evans, J. M. B.; Myerson, A. S., Pharmaceutical crystallization. Crystal growth & design 2011, 11 (4), 887-895.

17. Davey, R. J.; Schroeder, S. L. M.; ter Horst, J. H., Nucleation of organic crystals—a molecular perspective. Angewandte Chemie International Edition 2013, 52 (8), 2166-2179.

18. Galkin, O.; Chen, K.; Nagel, R. L.; Hirsch, R. E.; Vekilov, P. G., Liquid–liquid separation in solutions of normal and sickle cell hemoglobin. Proceedings of the National Academy of Sciences 2002, 99 (13), 8479-8483.

19. Vekilov, P. G., Two-step mechanism for the nucleation of crystals from solution. Journal of crystal growth 2005, 275 (1-2), 65-76.

20. Erdemir, D.; Lee, A. Y.; Myerson, A. S., Nucleation of crystals from solution: classical and two-step models. Accounts of chemical research 2009, 42 (5), 621-629.

21. Lutsko, J. F., Systematically extending classical nucleation theory. New journal of physics 2018, 20 (10), 103015.

22. Ito, F.; Suzuki, Y.; Fujimori, J.-i.; Sagawa, T.; Hara, M.; Seki, T.; Yasukuni, R.; De La Chapelle, M. L., Direct visualization of the two-step nucleation model by fluorescence color changes during evaporative crystallization from solution. Scientific reports 2016, 6, 22918.

23. Lutsko, J. F., How crystals form: A theory of nucleation pathways. Science advances 2019, 5 (4), eaav7399.

24. Lutsko, J. F.; Lam, J., Classical density functional theory, unconstrained crystallization, and polymorphic behavior. Physical Review E 2018, 98 (1), 012604.

25. Liu, J.; Rasmuson, Å. C., Influence of agitation and fluid shear on primary nucleation in solution. Crystal growth & design 2013, 13 (10), 4385-4394.

26. Jawor-Baczynska, A.; Sefcik, J.; Moore, B. D., 250 nm glycine-rich nanodroplets are formed on dissolution of glycine crystals but are too small to provide productive nucleation sites. Crystal growth & design 2013, 13 (2), 470-478.

27. McCrone, W. C., Polymorphism. Physics and chemistry of the organic solid state 1965, 2, 725-767.

28. Bauer, J.; Spanton, S.; Henry, R.; Quick, J.; Dziki, W.; Porter, W.; Morris, J., Ritonavir: an extraordinary example of conformational polymorphism. Pharmaceutical research 2001, 18 (6), 859-866.

29. Price, S. L., From crystal structure prediction to polymorph prediction: interpreting the crystal energy landscape. Physical Chemistry Chemical Physics 2008, 10 (15), 1996-2009.

30. Price, S. L., Computed crystal energy landscapes for understanding and predicting organic crystal structures and polymorphism. Accounts of chemical research 2009, 42 (1), 117-126.

31. Llinàs, A.; Goodman, J. M., Polymorph control: past, present and future. Drug discovery today 2008, 13 (5-6), 198-210.

32. Ostwald, W., Studien über die Bildung und Umwandlung fester Körper. Zeitschrift für physikalische Chemie 1897, 22 (1), 289-330.

33. Brittain, H. G., Polymorphism in pharmaceutical solids. CRC Press: 2016.

34. Meenan, P., From Molecules to Crystallizers: An Introduction to Crystallization Roger Davey and John Garside. Oxford University Press, New York. 2000. ISBN 0198504896. ACS Publications: 2001.

35. Bernstein, J.; Davey, R. J.; Henck, J. O., Concomitant polymorphs. Angewandte Chemie International Edition 1999, 38 (23), 3440-3461.

36. Du, W.; Cruz-Cabeza, A. J.; Woutersen, S.; Davey, R. J.; Yin, Q., Can the study of self-assembly in solution lead to a good model for the nucleation pathway? The case of tolfenamic acid. Chemical science 2015, 6 (6), 3515-3524.

37. Kulkarni, S. A.; McGarrity, E. S.; Meekes, H.; ter Horst, J. H., Isonicotinamide self-association: the link between solvent and polymorph nucleation. Chemical Communications 2012, 48 (41), 4983-4985.

38. Black, J. F. B.; Cardew, P. T.; Cruz-Cabeza, A. J.; Davey, R. J.; Gilks, S. E.; Sullivan, R. A., Crystal nucleation and growth in a polymorphic system: Ostwald's rule, p-aminobenzoic acid and nucleation transition states. CrystEngComm 2018, 20 (6), 768-776.

39. Peterson, M. L.; Morissette, S. L.; McNulty, C.; Goldsweig, A.; Shaw, P.; LeQuesne, M.; Monagle, J.; Encina, N.; Marchionna, J.; Johnson, A., Iterative high-throughput polymorphism studies on acetaminophen and an experimentally derived structure for form III. Journal of the American Chemical Society 2002, 124 (37), 10958-10959.

40. Beyer, T.; Day, G. M.; Price, S. L., The prediction, morphology, and mechanical properties of the polymorphs of paracetamol. Journal of the American Chemical Society 2001, 123 (21), 5086-5094.

41. Haisa, M.; Kashino, S.; Maeda, H., The orthorhombic form of p-hydroxyacetanilide. Acta Crystallographica Section B: Structural Crystallography and Crystal Chemistry 1974, 30 (10), 2510-2512.

42. Haisa, M.; Kashino, S.; Kawai, R.; Maeda, H., The monoclinic form of p-hydroxyacetanilide. Acta Crystallographica Section B: Structural Crystallography and Crystal Chemistry 1976, 32 (4), 1283-1285.

43. Nichols, G.; Frampton, C. S., Physicochemical characterization of the orthorhombic polymorph of paracetamol crystallized from solution. Journal of pharmaceutical sciences 1998, 87 (6), 684-693.

44. Gharaibeh, S. F.; Iba'a, N., Mechanical energies associated with compaction of form I and form II paracetamol powder. Powder technology 2011, 214 (1), 161-168.

45. Sudha, C.; Nandhini, R.; Srinivasan, K., Polymer-induced selective nucleation of mono or ortho polymorphs of paracetamol through swift cooling of boiled aqueous solution. Crystal growth & design 2014, 14 (2), 705-715.

46. Liu, Y.; Gabriele, B.; Davey, R. J.; Cruz-Cabeza, A. J., Concerning Elusive Crystal Forms: The Case of Paracetamol. Journal of the American Chemical Society 2020.

47. Nicoud, L.; Licordari, F.; Myerson, A. S., Polymorph control in batch seeded crystallizers. A case study with paracetamol. CrystEngComm 2019, 21 (13), 2105-2118.

48. Barthe, S. C.; Grover, M. A.; Rousseau, R. W., Observation of polymorphic change through analysis of FBRM data: transformation of paracetamol from form II to form I. Crystal Growth and Design 2008, 8 (9), 3316-3322.

49. Deij, M. A.; ter Horst, J. H.; Meekes, H.; Jansens, P.; Vlieg, E., Polymorph formation studied by 3D nucleation simulations. Application to a yellow isoxazolone dye, paracetamol, and L-glutamic acid. The Journal of Physical Chemistry B 2007, 111 (7), 1523-1530.

50. Agnew, L. R.; Cruickshank, D. L.; McGlone, T.; Wilson, C. C., Controlled production of the elusive metastable form II of acetaminophen (paracetamol): a fully scalable templating approach in a cooling environment. Chemical Communications 2016, 52 (46), 7368-7371.

51. Agnew, L. R.; McGlone, T.; Wheatcroft, H. P.; Robertson, A.; Parsons, A. R.; Wilson, C. C., Continuous crystallization of paracetamol (acetaminophen) form II: selective access to a metastable solid form. Crystal Growth & Design 2017, 17 (5), 2418-2427.

52. Perrin, M.-A.; Neumann, M. A.; Elmaleh, H.; Zaske, L., Crystal structure determination of the elusive paracetamol Form III. Chemical communications 2009, (22), 3181-3183.

53. Telford, R.; Seaton, C. C.; Clout, A.; Buanz, A.; Gaisford, S.; Williams, G. R.; Prior, T. J.; Okoye, C. H.; Munshi, T.; Scowen, I. J., Stabilisation of metastable polymorphs: the case of paracetamol form III. Chemical communications 2016, 52 (81), 12028-12031.

54. Ledru, J.; Imrie, C. T.; Pulham, C. R.; Céolin, R.; Hutchinson, J. M., High pressure differential scanning calorimetry investigations on the pressure dependence of the melting of paracetamol polymorphs I and II. Journal of pharmaceutical sciences 2007, 96 (10), 2784-2794.

55. Espeau, P.; Céolin, R.; Tamarit, J. L.; Perrin, M. A.; Gauchi, J. P.; Leveiller, F., Polymorphism of paracetamol: Relative stabilities of the monoclinic and orthorhombic phases inferred from topological pressure‐temperature and temperature‐volume phase diagrams. Journal of pharmaceutical sciences 2005, 94 (3), 524-539.

56. Boldyreva, E. V.; Shakhtshneider, T. P.; Ahsbahs, H.; Sowa, H.; Uchtmann, H., Effect of high pressure on the polymorphs of paracetamol. Journal of thermal analysis and calorimetry 2002, 68 (2), 437.

57. Oswald, I. D. H.; Chataigner, I.; Elphick, S.; Fabbiani, F. P. A.; Lennie, A. R.; Maddaluno, J.; Marshall, W. G.; Prior, T. J.; Pulham, C. R.; Smith, R. I., Putting pressure on elusive polymorphs and solvates. CrystEngComm 2009, 11 (2), 359-366.

58. Smith, S. J.; Bishop, M. M.; Montgomery, J. M.; Hamilton, T. P.; Vohra, Y. K., Polymorphism in paracetamol: evidence of additional forms IV and V at high pressure. The Journal of Physical Chemistry A 2014, 118 (31), 6068-6077.

59. Ward, M. R.; Oswald, I. D. H., Antisolvent addition at extreme conditions. CrystEngComm 2019, 21 (30), 4437-4443.

60. Li, J.; Tilbury, C. J.; Kim, S. H.; Doherty, M. F., A design aid for crystal growth engineering. Progress in Materials Science 2016, 82, 1-38.

61. Lovette, M. A.; Browning, A. R.; Griffin, D. W.; Sizemore, J. P.; Snyder, R. C.; Doherty, M. F., Crystal shape engineering. Industrial & engineering chemistry research 2008, 47 (24), 9812-9833.

62. Kuroda, T., Growth of a crystal surface with non-uniformity in supersaturation due to laminar flow of solution along the surface. Journal of crystal growth 1985, 71 (1), 84-94.

63. Wilcox, W. R., Transport phenomena in crystal growth from solution. Progress in crystal growth and characterization of materials 1993, 26, 153-194.

64. Dirksen, J. A.; Ring, T. A., Fundamentals of crystallization: kinetic effects on particle size distributions and morphology. Chemical Engineering Science 1991, 46 (10), 2389-2427.

65. Schmidt, C.; Ulrich, J., Morphology prediction of crystals grown in the presence of impurities and solvents—an evaluation of the state of the art. Journal of crystal growth 2012, 353 (1), 168-173.

66. Schmidt, C.; Jones, M. J.; Ulrich, J., The influence of additives and impurities on crystallization. Crystallization: Basic Concepts and Industrial Applications 2013, 105-127.

67. Sangwal, K., Effects of impurities on crystal growth processes. Progress in Crystal Growth and Characterization of Materials 1996, 32 (1–3), 3-43.

68. Thompson, C.; Davies, M. C.; Roberts, C. J.; Tendler, S. J. B.; Wilkinson, M. J., The effects of additives on the growth and morphology of paracetamol (acetaminophen) crystals. International journal of pharmaceutics 2004, 280 (1-2), 137-150.

69. Scott, C.; Black, S., In-line analysis of impurity effects on crystallisation. Organic process research & development 2005, 9 (6), 890-893.

70. Kubota, N.; Yokota, M.; Mullin, J. W., Supersaturation dependence of crystal growth in solutions in the presence of impurity. Journal of Crystal Growth 1997, 182 (1-2), 86-94.

71. Sangwal, K., Effect of impurities on the processes of crystal growth. Journal of crystal growth 1993, 128 (1-4), 1236-1244.

72. Hendriksen, B. A.; Grant, D. J. W.; Meenan, P.; Green, D. A., Crystallisation of paracetamol (acetaminophen) in the presence of structurally related substances. Journal of crystal growth 1998, 183 (4), 629-640.

73. Urwin, S. J.; Levilain, G.; Marziano, I.; Merritt, J. M.; Houson, I.; Ter Horst, J. H., A Structured Approach to Cope with Impurities During Industrial Crystallization Development. Organic Process Research & Development 2020, 6;24(8):1443-56.

74. Saleemi, A.; Onyemelukwe, II; Nagy, Z., Effects of a structurally related substance on the crystallization of paracetamol. Frontiers of Chemical Science and Engineering 2013, 7 (1), 79-87.

75. Li, J.; Doherty, M. F., Steady state morphologies of paracetamol crystal from different solvents. Crystal Growth & Design 2017, 17 (2), 659-670.

76. Roberts, K. J.; Docherty, R.; Tamura, R., Engineering crystallography: from molecule to crystal to functional form. Springer: 2017.

77. Knapp, R. T., Cavitation mechanics and its relation to the design of hydraulic equipment. Proceedings of the Institution of Mechanical Engineers 1952, 166 (1), 150-163.

78. Knapp, R. T., Recent investigations of the mechanics of cavitation and cavitation damage. Transactions of the ASME 1955, 77, 1045-1054.

79. Plesset, M. S.; Ellis, A. T., On the mechanism of cavitation damage. Transactions of the ASME 1955, 77, 1055-1064.

80. Mittelstein, D. R.; Ye, J.; Schibber, E. F.; Roychoudhury, A.; Martinez, L. T.; Fekrazad, M. H.; Ortiz, M.; Lee, P. P.; Shapiro, M. G.; Gharib, M., Selective ablation of cancer cells with low intensity pulsed ultrasound. Applied Physics Letters 2020, 116 (1), 013701.

81. Suslick, K. S., Sonochemistry. science 1990, 247 (4949), 1439-1445.

82. Holkar, C. R.; Jadhav, A. J.; Pinjari, D. V.; Pandit, A. B., Cavitationally Driven Transformations: A Technique of Process Intensification. Industrial & Engineering Chemistry Research 2019, 58 (15), 5797-5819.

83. Lauterborn, W., Cavitation and coherent optics. In Cavitation and inhomogeneities in underwater acoustics, Springer: 1980; pp 3-12.

84. Yasui, K., Acoustic cavitation and bubble dynamics. Springer: 2018.

85. Wiklund, M.; Green, R.; Ohlin, M., Acoustofluidics 14: Applications of acoustic streaming in microfluidic devices. Lab on a Chip 2012, 12 (14), 2438-2451.

86. Mason, T. J., Sonochemistry. Royal Society of Chemistry United Kingdom: 1990.

87. Gogate, P. R.; Pandit, A. B., Sonochemical reactors: scale up aspects. Ultrasonics Sonochemistry 2004, 11 (3–4), 105-117.

88. Minnaert, M., XVI. On musical air-bubbles and the sounds of running water. The London, Edinburgh, and Dublin Philosophical Magazine and Journal of Science 1933, 16 (104), 235-248.

89. Flint, E. B.; Suslick, K. S., The temperature of cavitation. Science 1991, 253 (5026), 1397-1399.

90. Zhong, L. COMSOL multiphysics simulation of ultrasonic energy in cleaning tanks, 2014. In COMSOL Conference 2014, Boston.

91. Sutkar, V. S.; Gogate, P. R.; Csoka, L., Theoretical prediction of cavitational activity distribution in sonochemical reactors. Chemical Engineering Journal 2010, 158 (2), 290-295.

92. Monnier, H.; Wilhelm, A. M.; Delmas, H., Influence of ultrasound on mixing on the molecular scale for water and viscous liquids. Ultrasonics sonochemistry 1999, 6 (1-2), 67-74.

93. Sutkar, V. S.; Gogate, P. R., Design aspects of sonochemical reactors: Techniques for understanding cavitational activity distribution and effect of operating parameters. Chemical Engineering Journal 2009, 155 (1–2), 26-36.

94. Kadkhodaee, R.; Povey, M. J. W., Ultrasonic inactivation of Bacillus α-amylase. I. Effect of gas content and emitting face of probe. Ultrasonics Sonochemistry 2008, 15 (2), 133-142.

95. Sander, J. R. G.; Zeiger, B. W.; Suslick, K. S., Sonocrystallization and sonofragmentation. Ultrasonics Sonochemistry 2014, 21 (6), 1908-1915.

96. Castillo‐Peinado, L. d. l. S.; Luque de Castro, M. D., The role of ultrasound in pharmaceutical production: sonocrystallization. Journal of Pharmacy and Pharmacology 2016, 68 (10), 1249-1267.

97. Majumdar, S.; Kumar, P. S.; Pandit, A. B., Effect of liquid-phase properties on ultrasound intensity and cavitational activity. Ultrasonics sonochemistry 1998, 5 (3), 113-118.

98. Omfrs, R., On the pressure developed in a liquid during the collapse of a spherical cavity. Philosophical Magazine, Series 1917, 6, 94-98.

99. Neppiras, E. A., Acoustic cavitation. Physics reports 1980, 61 (3), 159-251.

100. Plesset, M. S., The dynamics of cavitation bubbles. Journal of applied mechanics 1949, 16, 277-282.

101. Noltingk, B. E.; Neppiras, E. A., Cavitation produced by ultrasonics. Proceedings of the Physical Society. Section B 1950, 63 (9), 674.

102. Neppiras, E. A.; Noltingk, B. E., Cavitation produced by ultrasonics: theoretical conditions for the onset of cavitation. Proceedings of the Physical Society. Section B 1951, 64 (12), 1032.

103. P. Poritsky, in Proceedings of the 1st US National Congress in Applied Mathematics (ASME, 1952), p. 823.

104. Dzubiella, J.; Swanson, J. M. J.; McCammon, J. A., Coupling hydrophobicity, dispersion, and electrostatics in continuum solvent models. Physical review letters 2006, 96 (8), 087802.

105. Dzubiella, J., Interface dynamics of microscopic cavities in water. The Journal of chemical physics 2007, 126 (19), 194504.

106. Man, V. H.; Li, M. S.; Derreumaux, P.; Nguyen, P. H., Rayleigh-Plesset equation of the bubble stable cavitation in water: A nonequilibrium all-atom molecular dynamics simulation study. The Journal of Chemical Physics 2018, 148 (9), 094505.

107. Leighton, T., The acoustic bubble. Academic press: 2012.

108. Leighton, T. G., The principles of cavitation. Ultrasound in food processing 1998, 12.

109. Lee, J. Y., Importance of sonication and solution conditions on the acoustic cavitation activity In Handbook of Ultrasonics and Sonochemistry. Springer 2016. p137-175.

110. Bang, J. H.; Suslick, K. S., Applications of Ultrasound to the Synthesis of Nanostructured Materials. Advanced Materials 2010, 22 (10), 1039-1059.

111. Suslick, K. S.; McNamara, W. B.; Didenko, Y., Hot spot conditions during multi-bubble cavitation. In Sonochemistry and sonoluminescence, Springer: 1999; pp 191-204.

112. Pecha, R.; Gompf, B., Microimplosions: cavitation collapse and shock wave emission on a nanosecond time scale. Physical review letters 2000, 84 (6), 1328.

113. Chatel, G.; Colmenares, J. C., Sonochemistry: from basic principles to innovative applications. Springer: 2017.

114. Thompson, L. H.; Doraiswamy, L. K., The rate enhancing effect of ultrasound by inducing supersaturation in a solid–liquid system. Chemical Engineering Science 2000, 55 (16), 3085-3090.

115. Laborde, J. L.; Bouyer, C.; Caltagirone, J. P.; Gérard, A., Acoustic bubble cavitation at low frequencies. Ultrasonics 1998, 36 (1-5), 589-594.

116. Ashokkumar, M., The characterization of acoustic cavitation bubbles–an overview. Ultrasonics sonochemistry 2011, 18 (4), 864-872.

117. Ashokkumar, M.; Lee, J.; Kentish, S.; Grieser, F., Bubbles in an acoustic field: An overview. Ultrasonics Sonochemistry 2007, 14 (4), 470-475.

118. Gielen, B.; Jordens, J.; Janssen, J.; Pfeiffer, H.; Wevers, M.; Thomassen, L. C. J.; Braeken, L.; Van Gerven, T., Characterization of stable and transient cavitation bubbles in a milliflow reactor using a multibubble sonoluminescence quenching technique. Ultrasonics sonochemistry 2015, 25, 31-39.

119. Crum, L. A., Acoustic cavitation series: part five rectified diffusion. Ultrasonics 1984, 22 (5), 215-223.

120. Mason, T. J.; Lorimer, J. P., Applied sonochemistry. The uses of power ultrasound in chemistry and processing 2002, 1-48.

121. Parkar, P. A.; Choudhary, H. A.; Moholkar, V. S., Mechanistic and kinetic investigations in ultrasound assisted acid catalyzed biodiesel synthesis. Chemical Engineering Journal 2012, 187, 248-260.

122. Flynn, H. G., Cavitation dynamics. I. A mathematical formulation. The Journal of the Acoustical Society of America 1975, 57 (6), 1379-1396.

123. Flynn, H. G., Cavitation dynamics: II. Free pulsations and models for cavitation bubbles. The Journal of the Acoustical Society of America 1975, 58 (6), 1160-1170.

124. Apfel, R. E., 7. Acoustic cavitation. In Methods in experimental physics, Elsevier: 1981; Vol. 19, pp 355-411.

125. Holland, C. K.; Apfel, R. E., Thresholds for transient cavitation produced by pulsed ultrasound in a controlled nuclei environment. The Journal of the Acoustical Society of America 1990, 88 (5), 2059-2069.

126. Horst, C.; Gogate, P. R.; Pandit, A. B., Ultrasound reactors. Modeling of Process Intensification 2007, 193-277.

127. Ashokkumar, M.; Lee, J.; Iida, Y.; Yasui, K.; Kozuka, T.; Tuziuti, T.; Towata, A., The detection and control of stable and transient acoustic cavitation bubbles. Physical Chemistry Chemical Physics 2009, 11 (43), 10118-10121.

128. Lauterborn, W.; Mettin, R., Acoustic cavitation: bubble dynamics in high-power ultrasonic fields. In Power Ultrasonics, Elsevier: 2015; pp 37-78.

129. Blake Jr, F. G., Bjerknes forces in stationary sound fields. The Journal of the Acoustical Society of America 1949, 21 (5), 551-551.

130. Yasui, K.; Iida, Y.; Tuziuti, T.; Kozuka, T.; Towata, A., Strongly interacting bubbles under an ultrasonic horn. Physical Review E 2008, 77 (1), 016609.

131. Mørch, K. A., On cavity cluster formation in a focused acoustic field. Journal of Fluid Mechanics 1989, 201, 57-76.

132. Luo, J.; Fang, Z.; Smith, R. L.; Qi, X., Fundamentals of acoustic cavitation in sonochemistry. In Production of Biofuels and Chemicals with Ultrasound, Springer: 2015; pp 3-33.

133. Jiao, J.; He, Y.; Kentish, S. E.; Ashokkumar, M.; Manasseh, R.; Lee, J., Experimental and theoretical analysis of secondary Bjerknes forces between two bubbles in a standing wave. Ultrasonics 2015, 58, 35-42.

134. Yasui, K., Unsolved problems in acoustic cavitation. Handbook of ultrasonics and sonochemistry. Springer, Singapore 2016.

135. Suslick, K. S.; Eddingsaas, N. C.; Flannigan, D. J.; Hopkins, S. D.; Xu, H., Extreme conditions during multibubble cavitation: Sonoluminescence as a spectroscopic probe. Ultrasonics sonochemistry 2011, 18 (4), 842-846.

136. Yasui, K.; Tuziuti, T.; Sivakumar, M.; Iida, Y., Sonoluminescence. Applied Spectroscopy Reviews 2004, 39 (3), 399-436.

137. Lauterborn, W.; Kurz, T.; Geisler, R.; Schanz, D.; Lindau, O., Acoustic cavitation, bubble dynamics and sonoluminescence. Ultrasonics Sonochemistry 2007, 14 (4), 484-491.

138. Brenner, M. P.; Hilgenfeldt, S.; Lohse, D., Single-bubble sonoluminescence. Reviews of modern physics 2002, 74 (2), 425.

139. Gaitan, D. F.; Crum, L. A., Sonoluminescence from single bubbles. The Journal of the Acoustical Society of America 1990, 87 (S1), S141-S141.

140. Gompf, B.; Günther, R.; Nick, G.; Pecha, R.; Eisenmenger, W., Resolving sonoluminescence pulse width with time-correlated single photon counting. Physical Review Letters 1997, 79 (7), 1405.

141. Hiller, R. A.; Putterman, S. J.; Weninger, K. R., Time-resolved spectra of sonoluminescence. Physical review letters 1998, 80 (5), 1090.

142. Marinesco, N.; Trillat, J. J., Action of supersonic waves upon the photographic plate. Proc R Acad Sci 1933, 196, 858-860.

143. Frenzel, H.; Schultes, H., Luminescenz im ultraschallbeschickten Wasser. Zeitschrift für Physikalische Chemie 1934, 27 (1), 421-424.

144. Yasui, K.; Unsolved problems in acoustic cavitation. Handbook of Ultrasonics Sonochemistry, Springer, Singapore 2016, 259-292.

145. Geisler, R.; Diploma thesis. Georg-August-University Göttingen 1998.

146. Suslick, K. S.; Flannigan, D. J., Inside a collapsing bubble: sonoluminescence and the conditions during cavitation. Annu. Rev. Phys. Chem. 2008, 59, 659-683.

147. https://www.acoustics.co.uk/. (Accessed June 2018).

148. 62127–3, I., Ultrasonics - Hydrophones - Part 3: Properties of hydrophones for ultrasonic fields up to 40 MHz. International Electrotechnical Commission: Geneva, Switzerland, 2005.

149. Hodnett, M., Measurement techniques in power ultrasonics. In Power Ultrasonics, Elsevier: 2015; pp 195-218.

150. Price, G. J.; Ashokkumar, M.; Hodnett, M.; Zequiri, B.; Grieser, F., Acoustic emission from cavitating solutions: implications for the mechanisms of sonochemical reactions. The journal of physical chemistry B 2005, 109 (38), 17799-17801.

151. Esche, R., Untersuchung der schwingungskavitation in flüssigkeiten. Acta Acustica united with Acustica 1952, 2 (6), 208-218.

152. Neppiras, E. A., Subharmonic and other low ‐ frequency emission from bubbles in sound ‐ irradiated liquids. The Journal of the Acoustical Society of America 1969, 46 (3B), 587-601.

153. Cramer, E.; Lauterborn, W., Acoustic cavitation noise spectra. In Mechanics and Physics of Bubbles in Liquids, Springer: 1982; pp 209-214.

154. Campos-Pozuelo, C.; Granger, C.; Vanhille, C.; Moussatov, A.; Dubus, B., Experimental and theoretical investigation of the mean acoustic pressure in the cavitation field. Ultrasonics sonochemistry 2005, 12 (1-2), 79-84.

155. Liang, Z.; Zhou, G.; Lin, S.; Zhang, Y.; Yang, H., Study of low-frequency ultrasonic cavitation fields based on spectral analysis technique. Ultrasonics 2006, 44 (1), 115-120.

156. Avvaru, B.; Pandit, A. B., Oscillating bubble concentration and its size distribution using acoustic emission spectra. Ultrasonics sonochemistry 2009, 16 (1), 105-115.

157. Yasui, K.; Tuziuti, T.; Lee, J.; Kozuka, T.; Towata, A.; Iida, Y., Numerical simulations of acoustic cavitation noise with the temporal fluctuation in the number of bubbles. Ultrasonics sonochemistry 2010, 17 (2), 460-472.

158. Hodnett, M.; Chow, R.; Zeqiri, B., High-frequency acoustic emissions generated by a 20 kHz sonochemical horn processor detected using a novel broadband acoustic sensor: a preliminary study. Ultrasonics sonochemistry 2004, 11 (6), 441-454.

159. Wang, L.; Memoli, G.; Hodnett, M.; Zeqiri, B. In Dynamic behaviour of laser nucleated bubbles in a focused ultrasound field, 2015; IEEE Xplore: pp 1-4.

160. Hodnett, M.; Choi, M. J.; Zeqiri, B., Towards a reference ultrasonic cavitation vessel. Part 1: Preliminary investigation of the acoustic field distribution in a 25 kHz cylindrical cell. Ultrasonics sonochemistry 2007, 14 (1), 29-40.

161. Hodnett, M.; Zeqiri, B., Toward a reference ultrasonic cavitation vessel: Part 2-Investigating the spatial variation and acoustic pressure threshold of inertial cavitation in a 25 kHz ultrasound field. IEEE transactions on ultrasonics, ferroelectrics, and frequency control 2008, 55 (8).

162. Uchida, T.; Sato, H.; Takeuchi, S.; Kikuchi, T., Investigation of output signal from cavitation sensor by dissolved oxygen level and sonochemical luminescence. Japanese Journal of Applied Physics 2010, 49 (7S), 07HE03.

163. Uchida, T.; Takeuchi, S.; Kikuchi, T., Measurement of amount of generated acoustic cavitation: investigation of spatial distribution of acoustic cavitation generation using broadband integrated voltage. Japanese Journal of Applied Physics 2011, 50 (7S), 07HE01.

164. Grosjean, V.; Julcour, C.; Louisnard, O.; Barthe, L., Axial acoustic field along a solid-liquid fluidized bed under power ultrasound. Ultrasonics sonochemistry 2019, 56, 274-283.

165. Nguyen, T. T.; Asakura, Y.; Koda, S.; Yasuda, K., Dependence of cavitation, chemical effect, and mechanical effect thresholds on ultrasonic frequency. Ultrasonics sonochemistry 2017, 39, 301-306.

166. Aitken, M.; Kleinrock, M.; Simorellis, A.; Nass, D., The global use of medicine in 2019 and outlook to 2023. Parsippany, NJ: IQVIA Institute for Human Data Science: 2019.

167. Badman, C.; Cooney, C. L.; Florence, A.; Konstantinov, K.; Krumme, M.; Mascia, S.; Nasr, M.; Trout, B. L., Why We Need Continuous Pharmaceutical Manufacturing and How to Make It Happen. Journal of pharmaceutical sciences 2019, 30, 1-3.

168. Mascia, S.; Heider, P. L.; Zhang, H.; Lakerveld, R.; Benyahia, B.; Barton, P. I.; Braatz, R. D.; Cooney, C. L.; Evans, J. M. B.; Jamison, T. F., End‐to‐end continuous manufacturing of pharmaceuticals: integrated synthesis, purification, and final dosage formation. Angewandte Chemie International Edition 2013, 52 (47), 12359-12363.

169. Lee, S. L.; O'Connor, T. F.; Yang, X.; Cruz, C. N.; Chatterjee, S.; Madurawe, R. D.; Moore, C. M. V.; Lawrence, X. Y.; Woodcock, J., Modernizing pharmaceutical manufacturing: from batch to continuous production. Journal of Pharmaceutical Innovation 2015, 10 (3), 191-199.

170. Myerson, A. S.; Krumme, M.; Nasr, M.; Thomas, H.; Braatz, R. D., Control systems engineering in continuous pharmaceutical manufacturing. May 20–21, 2014 Continuous Manufacturing Symposium. Journal of pharmaceutical sciences 2015, 104 (3), 832-839.

171. Baxendale, I. R.; Braatz, R. D.; Hodnett, B. K.; Jensen, K. F.; Johnson, M. D.; Sharratt, P.; Sherlock, J. P.; Florence, A. J., Achieving continuous manufacturing: Technologies and approaches for synthesis, workup, and isolation of drug substance. May 20–21, 2014 Continuous Manufacturing Symposium. Journal of pharmaceutical sciences 2015, 104 (3), 781-791.

172. ICH, Guideline Q13: Continuous Manufacturing of Drug Substances and Drug Products. 2018.

173. Wang, J.; Li, F.; Lakerveld, R., Process intensification for pharmaceutical crystallization. Chemical Engineering and Processing-Process Intensification 2018.

174. Duffus, C.; Camp, P. J.; Alexander, A. J., Spatial control of crystal nucleation in agarose gel. Journal of the American Chemical Society 2009, 131 (33), 11676-11677.

175. Gogate, P. R., Intensification of chemical processing applications using ultrasonic and microwave irradiations. Current Opinion in Chemical Engineering 2017, 17, 9-14.

176. Radacsi, N.; ter Horst, J. H.; Stefanidis, G. D., Microwave-assisted evaporative crystallization of niflumic acid for particle size reduction. Crystal growth & design 2013, 13 (10), 4186-4189.

177. Urbanus, J.; Roelands, C. P. M.; Mazurek, J.; Verdoes, D.; ter Horst, J. H., Electrochemically induced co-crystallization for product removal. CrystEngComm 2011, 13 (8), 2817-2819.

178. Urbanus, J.; Bisselink, R. J. M.; Nijkamp, K.; Ter Horst, J. H.; Verdoes, D.; Roelands, C. P. M., Integrated product removal of slightly water-soluble carboxylates from fermentation by electrochemically induced crystallization. Journal of Membrane Science 2010, 363 (1-2), 36-47.

179. Wang, Y.; Babchin, J.; Chernyi, L. T.; Chow, R. S.; Sawatzky, R. P., Rapid onset of calcium carbonate crystallization under the influence of a magnetic field. Water Research 1997, 31 (2), 346-350.

180. Atkinson, M. B. J.; Bwambok, D. K.; Chen, J.; Chopade, P. D.; Thuo, M. M.; Mace, C. R.; Mirica, K. A.; Kumar, A. A.; Myerson, A. S.; Whitesides, G. M., Using magnetic levitation to separate mixtures of crystal polymorphs. Angewandte Chemie 2013, 125 (39), 10398-10401.

181. Suslick, K. S., The chemical effects of ultrasound. Scientific American 1989, 260 (2), 80-87.

182. Mettin, R.; Cairos, C., Bubble dynamics and observations. Handbook of ultrasonics and sonochemistry. Springer, Singapore 2016.

183. Crum, L. A., Comments on the evolving field of sonochemistry by a cavitation physicist. Ultrasonics Sonochemistry 1995, 2 (2), S147-S152.

184. Thangavadivel, K.; Okitsu, K.; Owens, G.; Lesniewski, P. J.; Nishimura, R., Influence of sonochemical reactor diameter and liquid height on methyl orange degradation under 200 kHz indirect sonication. Journal of Environmental Chemical Engineering 2013, 1 (3), 275-280.

185. Wood, R. J.; Lee, J.; Bussemaker, M. J., A parametric review of sonochemistry: Control and augmentation of sonochemical activity in aqueous solutions. Ultrasonics sonochemistry 2017, 38, 351-370.

186. Nalesso, S.; Bussemaker, M. J.; Sear, R. P.; Hodnett, M.; Lee, J., A Review on Possible Mechanisms of Sonocrystallisation in Solution. Ultrasonics sonochemistry 2019.

187. Sivakumar, M.; Gedanken, A., Insights into the sonochemical decomposition of Fe (CO) 5: theoretical and experimental understanding of the role of molar concentration and power density on the reaction yield. Ultrasonics sonochemistry 2004, 11 (6), 373-378.

188. van Iersel, M. M.; Benes, N. E.; Keurentjes, J. T. F., Importance of acoustic shielding in sonochemistry. Ultrasonics sonochemistry 2008, 15 (4), 294-300.

189. Fındık, S.; Gündüz, G.; Gündüz, E., Direct sonication of acetic acid in aqueous solutions. Ultrasonics sonochemistry 2006, 13 (3), 203-207.

190. Jordens, J.; Gielen, B.; Braeken, L.; Van Gerven, T., Determination of the effect of the ultrasonic frequency on the cooling crystallization of paracetamol. Chemical Engineering and Processing: Process Intensification 2014, 84, 38-44.

191. Lee, J.; Yasui, K.; Ashokkumar, M.; Kentish, S. E., Quantification of Cavitation Activity by Sonoluminescence To Study the Sonocrystallization Process under Different Ultrasound Parameters. Crystal Growth & Design 2018, 5108-5115.

192. Sánchez-García, Y. I.; Ashokkumar, M.; Mason, T. J.; Gutiérrez-Méndez, N., Influence of ultrasound frequency and power on lactose nucleation. Journal of Food Engineering 2019, 34-39.

193. Jordens, J.; Gielen, B.; Xiouras, C.; Hussain, M. N.; Stefanidis, G. D.; Thomassen, L. C. J.; Braeken, L.; Van Gerven, T., Sonocrystallisation: observations, theories and guidelines. Chemical Engineering and Processing-Process Intensification 2019, 130-154.

194. Kordylla, A.; Koch, S.; Tumakaka, F.; Schembecker, G., Towards an optimized crystallization with ultrasound: Effect of solvent properties and ultrasonic process parameters. Journal of Crystal Growth 2008, 310 (18), 4177-4184.

195. Price, G. J.; Ashokkumar, M.; Grieser, F., Sonoluminescence quenching of organic compounds in aqueous solution: Frequency effects and implications for sonochemistry. Journal of the American Chemical Society 2004, 126 (9), 2755-2762.

196. Tzanakis, I.; Lebon, G. S. B.; Eskin, D. G.; Pericleous, K. A., Characterizing the cavitation development and acoustic spectrum in various liquids. Ultrasonics sonochemistry 2017, 34, 651-662.

197. Wood, R. W.; Loomis, A. L., XXXVIII. The physical and biological effects of high-frequency sound-waves of great intensity. The London, Edinburgh, and Dublin philosophical magazine and journal of science 1927, 4 (22), 417-436.

198. Ruecroft, G.; Hipkiss, D.; Ly, T.; Maxted, N.; Cains, P. W., Sonocrystallization: The Use of Ultrasound for Improved Industrial Crystallization. Organic Process Research & Development 2005, 9 (6), 923-932.

199. McCausland, L. J.; Cains, P. W.; Martin, P. D., Use the power of sonocrystallization for improved properties. Chemical Engineering Progress 2001, 97 (7), 56.

200. Kim, S.; Wei, C.; Kiang, S., Crystallization Process Development of an Active Pharmaceutical Ingredient and Particle Engineering via the Use of Ultrasonics and Temperature Cycling. Organic Process Research & Development 2003, 7 (6), 997-1001.

201. Dennehy, R. D., Particle Engineering Using Power Ultrasound. Organic Process Research and Development 2003, 7 (6), 1002-1006.

202. Principe, J. R.; Skauen, D. M., Preparation of microcrystalline progesterone using ultrasound. Journal of pharmaceutical sciences 1962, 51 (4), 389-390.

203. Hem, S. L., The effect of ultrasonic vibrations on crystallization processes. Ultrasonics 1967, 5 (4), 202-207.

204. Hem, S. L.; Skauen, D. M.; Beal, H. M., Mechanism of crystallization of hydrocortisone by ultrasonic irradiation. Journal of pharmaceutical sciences 1967, 56 (2), 229-233.

205. Chow, R.; Blindt, R.; Chivers, R.; Povey, M., A study on the primary and secondary nucleation of ice by power ultrasound. Ultrasonics 2005, 43 (4), 227-230.

206. Kiss, A. A.; Geertman, R.; Wierschem, M.; Skiborowski, M.; Gielen, B.; Jordens, J.; John, J. J.; Van Gerven, T., Ultrasound‐assisted emerging technologies for chemical processes. Journal of Chemical Technology & Biotechnology 2018, 93 (5), 1219-1227.

207. Wohlgemuth, K.; Kordylla, A.; Ruether, F.; Schembecker, G., Experimental study of the effect of bubbles on nucleation during batch cooling crystallization. Chemical Engineering Science 2009, 64 (19), 4155-4163.

208. Lührmann, M.-C.; Termühlen, M.; Timmermann, J.; Schembecker, G.; Wohlgemuth, K., Induced nucleation by gassing and its monitoring for the design and operation of an MSMPR cascade. Chemical Engineering Science 2018, 192, 840-849.

209. Grossier, R.; Louisnard, O.; Vargas, Y., Mixture segregation by an inertial cavitation bubble. Ultrasonics sonochemistry 2007, 14 (4), 431-437.

210. Dodds, J.; Espitalier, F.; Louisnard, O.; Grossier, R.; David, R.; Hassoun, M.; Baillon, F.; Gatumel, C.; Lyczko, N., The effect of ultrasound on crystallisation-precipitation processes: Some examples and a new segregation model. Particle and Particle Systems Characterization 2007, 24 (1), 18-28.

211. Louisnard, O.; Gomez, F. J.; Grossier, R., Segregation of a liquid mixture by a radially oscillating bubble. Journal of Fluid mechanics 2007, 577, 385-415.

212. Chalmers, B., Principles of solidification. In Applied solid state physics, Springer: 1970; pp 161-170.

213. Cogné, C.; Labouret, S.; Peczalski, R.; Louisnard, O.; Baillon, F.; Espitalier, F., Theoretical model of ice nucleation induced by acoustic cavitation. Part 1: Pressure and temperature profiles around a single bubble. Ultrasonics sonochemistry 2016, 29, 447-454.

214. Cogné, C.; Labouret, S.; Peczalski, R.; Louisnard, O.; Baillon, F.; Espitalier, F., Theoretical model of ice nucleation induced by inertial acoustic cavitation. Part 2: Number of ice nuclei generated by a single bubble. Ultrasonics sonochemistry 2016, 28, 185-191.

215. Nalajala, V. S.; Moholkar, V. S., Investigations in the physical mechanism of sonocrystallization. Ultrasonics Sonochemistry 2011, 18 (1), 345-355.

216. Bari, A. H.; Chawla, A.; Pandit, A. B., Sono-crystallization kinetics of K2SO4: Estimation of nucleation, growth, breakage and agglomeration kinetics. Ultrasonics sonochemistry 2017, 35, 196-203.

217. Liu, Y.; van den Berg, M. H.; Alexander, A. J., Supersaturation dependence of glycine polymorphism using laser-induced nucleation, sonocrystallization and nucleation by mechanical shock. Physical Chemistry Chemical Physics 2017, 19 (29), 19386-19392.

218. Hickling, R.; Plesset, M. S., Collapse and rebound of a spherical bubble in water. The Physics of Fluids 1964, 7 (1), 7-14.

219. Gracin, S.; Uusi-Penttilä, M.; Rasmuson, Å. C., Influence of Ultrasound on the Nucleation of Polymorphs of p-Aminobenzoic Acid. Crystal Growth & Design 2005, 5 (5), 1787-1794.

220. Hatakka, H.; Alatalo, H.; Louhi ‐ Kultanen, M.; Lassila, I.; Hæggström, E., Closed ‐ loop control of reactive crystallization PART II: polymorphism control of L ‐ glutamic acid by sonocrystallization and seeding. Chemical Engineering & Technology: Industrial Chemistry ‐ Plant Equipment ‐ Process Engineering ‐ Biotechnology 2010, 33 (5), 751-756.

221. Louhi-Kultanen, M.; Karjalainen, M.; Rantanen, J.; Huhtanen, M.; Kallas, J., Crystallization of glycine with ultrasound. International Journal of Pharmaceutics 2006, 320 (1–2), 23-29.

222. Kaur Bhangu, S.; Ashokkumar, M.; Lee, J., Ultrasound Assisted Crystallization of Paracetamol: Crystal Size Distribution and Polymorph Control. Crystal Growth & Design 2016, 16 (4), 1934-1941.

223. Mori, Y.; Maruyama, M.; Takahashi, Y.; Ikeda, K.; Fukukita, S.; Yoshikawa, H. Y.; Okada, S.; Adachi, H.; Sugiyama, S.; Takano, K., Selective crystallization of metastable phase of acetaminophen by ultrasonic irradiation. Applied Physics Express 2015, 8 (6), 065501.

224. Bai, C.; Wang, C.; Zheng, T.; Hu, Q., Growth of β-glycine crystals promoted by standing surface acoustic waves (SSAWs). CrystEngComm 2018, 20 (9), 1245-1251.

225. Jiang, S., An examination of sonocrystallization kinetics of l-glutamic acid. University of Leeds. PhD Thesis. 2012.

226. Granberg, R. A.; Rasmuson, Å. C., Solubility of paracetamol in pure solvents. Journal of Chemical & Engineering Data 1999, 44 (6), 1391-1395.

227. Jordens, J.; Appermont, T.; Gielen, B.; Van Gerven, T.; Braeken, L., Sonofragmentation: Effect of ultrasound frequency and power on particle breakage. Crystal Growth & Design 2016, 16 (11), 6167-6177.

228. Zeiger, B. W.; Suslick, K. S., Sonofragmentation of molecular crystals. Journal of the American Chemical Society 2011, 133 (37), 14530-14533.

229. Gielen, B.; Kusters, P.; Jordens, J.; Thomassen, L. C. J.; Van Gerven, T.; Braeken, L., Energy efficient crystallization of paracetamol using pulsed ultrasound. Chemical Engineering and Processing: Process Intensification 2017, 114, 55-66.

230. Gielen, B.; Jordens, J.; Thomassen, L. C. J.; Braeken, L.; Van Gerven, T., Agglomeration control during ultrasonic crystallization of an active pharmaceutical ingredient. Crystals 2017, 7 (2), 40.

231. Guo, Z.; Zhang, M.; Li, H.; Wang, J.; Kougoulos, E., Effect of ultrasound on anti-solvent crystallization process. Journal of Crystal Growth 2005, 273 (3–4), 555-563.

232. Nii, S.; Takayanagi, S., Growth and size control in anti-solvent crystallization of glycine with high frequency ultrasound. Ultrasonics sonochemistry 2014, 21 (3), 1182-1186.

233. Amara, N.; Ratsimba, B.; Wilhelm, A.; Delmas, H., Growth rate of potash alum crystals: comparison of silent and ultrasonic conditions. Ultrasonics Sonochemistry 2004, 11 (1), 17-21.

234. Nguyen, T. T. H.; Khan, A.; Bruce, L. M.; Forbes, C.; O'Leary, R. L.; Price, C. J., The Effect of Ultrasound on the Crystallisation of Paracetamol in the Presence of Structurally Similar Impurities. Crystals 2017, 7 (10), 294.

235. Alexander, A. J.; Camp, P. J., Non-photochemical laser-induced nucleation. The Journal of chemical physics 2019, 150 (4), 040901.

236. Yoshikawa HY, Murai R, Adachi H, Sugiyama S, Maruyama M, Takahashi Y, Takano K, Matsumura H, Inoue T, Murakami S, Masuhara H. Laser ablation for protein crystal nucleation and seeding. Chemical Society Reviews. 2014;43(7):2147-58.

237. Nakamura, K.; Hosokawa, Y.; Masuhara, H., Anthracene crystallization induced by single-shot femtosecond laser irradiation: Experimental evidence for the important role of bubbles. Crystal growth & design 2007, 7 (5), 885-889.

238. Matic, J.; Sun, X.; Garetz, B. A.; Myerson, A. S., Intensity, wavelength, and polarization dependence of nonphotochemical laser-induced nucleation in supersaturated aqueous urea solutions. Crystal growth & design 2005, 5 (4), 1565-1567.

239. Ward, M. R.; Alexander, A. J., Nonphotochemical Laser-Induced Nucleation of Potassium Halides: Effects of Wavelength and Temperature. Crystal growth & design 2012, 12 (9), 4554-4561.

240. Kacker, R.; Dhingra, S.; Irimia, D.; Ghatkesar, M. K.; Stankiewicz, A.; Kramer, H. J. M.; Eral, H. B., Multiparameter Investigation of Laser-Induced Nucleation of Supersaturated Aqueous KCl Solutions. Crystal Growth & Design 2017, 18 (1), 312-317.

241. Ward, M. R.; Copeland, G. W.; Alexander, A. J., Chiral hide-and-seek: Retention of enantiomorphism in laser-induced nucleation of molten sodium chlorate. The Journal of chemical physics 2011, 135 (11), 114508.

242. Garetz, B. A.; Aber, J. E.; Goddard, N. L.; Young, R. G.; Myerson, A. S., Nonphotochemical, polarization-dependent, laser-induced nucleation in supersaturated aqueous urea solutions. Physical review letters 1996, 77 (16), 3475.

243. Jena, P.; Castleman Jr, A. W., Nanoclusters: a bridge across disciplines. Elsevier: 2010.

244. Liu, Y.; Ward, M. R.; Alexander, A. J., Polarization independence of laser-induced nucleation in supersaturated aqueous urea solutions. Physical Chemistry Chemical Physics 2017, 19 (5), 3464-3467.

245. Zaccaro, J.; Matic, J.; Myerson, A. S.; Garetz, B. A., Nonphotochemical, laser-induced nucleation of supersaturated aqueous glycine produces unexpected γ-polymorph. Crystal Growth & Design 2001, 1 (1), 5-8.

246. Garetz, B. A.; Matic, J.; Myerson, A. S., Polarization switching of crystal structure in the nonphotochemical light-induced nucleation of supersaturated aqueous glycine solutions. Physical review letters 2002, 89 (17), 175501.

247. Sun, X.; Garetz, B. A.; Myerson, A. S., Supersaturation and polarization dependence of polymorph control in the nonphotochemical laser-induced nucleation (NPLIN) of aqueous glycine solutions. Crystal growth & design 2006, 6 (3), 684-689.

248. Clair, B.; Ikni, A.; Li, W.; Scouflaire, P.; Quemener, V.; Spasojević-de Biré, A., A new experimental setup for high-throughput controlled non-photochemical laser-

induced nucleation: application to glycine crystallization. Journal of Applied Crystallography 2014, 47 (4), 1252-1260.

249. Javid, N.; Kendall, T.; Burns, I. S.; Sefcik, J., Filtration suppresses laser-induced nucleation of glycine in aqueous solutions. Crystal Growth & Design 2016, 16 (8), 4196-4202.

250. Knott, B. C.; Doherty, M. F.; Peters, B., A simulation test of the optical Kerr mechanism for laser-induced nucleation. The Journal of chemical physics 2011, 134 (15), 154501.

251. Alexander, A. J.; Camp, P. J., Single pulse, single crystal laser-induced nucleation of potassium chloride. Crystal Growth and Design 2009, 9 (2), 958-963.

252. Ward, M. R.; Ballingall, I.; Costen, M. L.; McKendrick, K. G.; Alexander, A. J., Nanosecond pulse width dependence of nonphotochemical laser-induced nucleation of potassium chloride. Chemical Physics Letters 2009, 481 (1-3), 25-28.

253. Knott, B. C.; Duff, N.; Doherty, M. F.; Peters, B., Estimating diffusivity along a reaction coordinate in the high friction limit: Insights on pulse times in laser-induced nucleation. The Journal of chemical physics 2009, 131 (22), 224112.

254. Agarwal, V.; Peters, B., Solute precipitate nucleation: A review of theory and simulation advances. Advances in Chemical Physics: Volume 155 2014, 97-160.

255. Knott, B. C.; LaRue, J. L.; Wodtke, A. M.; Doherty, M. F.; Peters, B., Communication: Bubbles, crystals, and laser-induced nucleation. AIP: 2011.

256. Ward, M. R.; Jamieson, W. J.; Leckey, C. A.; Alexander, A. J., Laser-induced nucleation of carbon dioxide bubbles. The Journal of chemical physics 2015, 142 (14), 144501.

257. Ward, M. R.; Mackenzie, A. M.; Alexander, A. J., Role of Impurity Nanoparticles in Laser-Induced Nucleation of Ammonium Chloride. Crystal Growth & Design 2016, 16 (12), 6790-6796.

258. Kotaidis, V.; Dahmen, C.; Von Plessen, G.; Springer, F.; Plech, A., Excitation of nanoscale vapor bubbles at the surface of gold nanoparticles in water. The Journal of chemical physics 2006, 124 (18), 184702.

259. Baffou G, Polleux J, Rigneault H, Monneret S. Super-heating and micro-bubble generation around plasmonic nanoparticles under cw illumination. The Journal of Physical Chemistry C. 2014 Mar 6;118(9):4890-8.

260. Siems, A.; Weber, S. A. L.; Boneberg, J.; Plech, A., Thermodynamics of nanosecond nanobubble formation at laser-excited metal nanoparticles. New Journal of Physics 2011, 13 (4), 043018.

261. Pyatenko, A.; Wang, H.; Koshizaki, N.; Tsuji, T., Mechanism of pulse laser interaction with colloidal nanoparticles. Laser & Photonics Reviews 2013, 7 (4), 596-604.

262. Lapotko, D., Optical excitation and detection of vapor bubbles around plasmonic nanoparticles. Optics express 2009, 17 (4), 2538-2556.

263. Plech, A.; Kotaidis, V.; Grésillon, S.; Dahmen, C.; Von Plessen, G., Laser-induced heating and melting of gold nanoparticles studied by time-resolved x-ray scattering. Physical Review B 2004, 70 (19), 195423.

264. Sindt, J. O.; Alexander, A. J.; Camp, P. J., Effects of nanoparticle heating on the structure of a concentrated aqueous salt solution. The Journal of chemical physics 2017, 147 (21), 214506.

265. Mackenzie, A. M., Investigating nucleation control in batch and flow using non-photochemical laser-induced nucleation. PhD Thesis, University of Edinburgh. 2017.

266. Barber, E. R.; Kinney, N. L. H.; Alexander, A. J., Pulsed laser-induced nucleation of sodium chlorate at high energy densities. Crystal Growth & Design 2019, 19 (12), 7106-7111.

267. Soare, A.; Dijkink, R.; Pascual, M. R.; Sun, C.; Cains, P. W.; Lohse, D.; Stankiewicz, A. I.; Kramer, H. J. M., Crystal nucleation by laser-induced cavitation. Crystal growth & design 2011, 11 (6), 2311-2316.

268. Jacob, J. A.; Sorgues, S. b.; Dazzi, A.; Mostafavi, M.; Belloni, J., Homogeneous nucleation-growth dynamics induced by single laser pulse in supersaturated solutions. Crystal growth & design 2012, 12 (12), 5980-5985.

269. Lindinger, B.; Mettin, R.; Chow, R.; Lauterborn, W., Ice crystallization induced by optical breakdown. Physical review letters 2007, 99 (4), 045701.

270. Fischer, A.; Pagni, R. M.; Compton, R. N.; Kondepudi, D., Laser Induced Crystallization. In Science and Technology of Atomic, Molecular, Condensed Matter & Biological Systems, Elsevier: 2010; Vol. 1, pp 343-364.

271. Mirsaleh-Kohan, N.; Fischer, A.; Graves, B.; Bolorizadeh, M.; Kondepudi, D.; Compton, R. N., Laser Shock Wave Induced Crystallization. Crystal Growth & Design 2017, 17 (2), 576-581.

272. Wang, S.; Wang, S.; Jiang, L.; Wang, M.; Wei, Y.; Sun, J.; Zhan, S.; Li, X.; Qu, L., Polymorph-Controlled Crystallization of Acetaminophen through Femtosecond Laser Irradiation. Crystal Growth & Design 2019, 19 (6), 3265-3271.

273. Vogel, A.; Nahen, K.; Theisen, D.; Noack, J., Plasma formation in water by picosecond and nanosecond Nd: YAG laser pulses. I. Optical breakdown at threshold and superthreshold irradiance. IEEE Journal of Selected Topics in Quantum Electronics 1996, 2 (4), 847-860.

274. Bundschuh, T.; Wagner, T. U.; Köster, R., Laser‐induced Breakdown Detection (LIBD) for the Highly Sensitive Quantification of Aquatic Colloids. Part I: Principle of

LIBD and Mathematical Model. Particle & Particle Systems Characterization 2005, 22 (3), 172-180.

275. Sakka, T.; Masai, S.; Fukami, K.; Ogata, Y. H., Spectral profile of atomic emission lines and effects of pulse duration on laser ablation in liquid. Spectrochimica Acta Part B: Atomic Spectroscopy 2009, 64 (10), 981-985.

276. De Giacomo, A.; Dell'Aglio, M.; Santagata, A.; Gaudiuso, R.; De Pascale, O.; Wagener, P.; Messina, G. C.; Compagnini, G.; Barcikowski, S., Cavitation dynamics of laser ablation of bulk and wire-shaped metals in water during nanoparticles production. Physical Chemistry Chemical Physics 2013, 15 (9), 3083-3092.

277. Chiou, P.-Y.; Wu, T.-H.; Park, S.-Y.; Chen, Y. In Pulse laser driven ultrafast micro and nanofluidics system, 2010; International Society for Optics and Photonics: p 77590Z.

278. Magaletti, F.; Marino, L.; Casciola, C. M., Shock wave formation in the collapse of a vapor nanobubble. Physical Review Letters 2015, 114 (6), 064501.

279. Magaletti, F.; Gallo, M.; Marino, L.; Casciola, C. M., Shock-induced collapse of a vapor nanobubble near solid boundaries. International Journal of Multiphase Flow 2016, 84, 34-45.

280. Lauterborn, W.; Vogel, A., Shock wave emission by laser generated bubbles. In Bubble dynamics and shock waves, Springer: 2013; pp 67-103.

281. Sinibaldi, G.; Occhicone, A.; Alves Pereira, F.; Caprini, D.; Marino, L.; Michelotti, F.; Casciola, C. M., Laser induced cavitation: Plasma generation and breakdown shockwave. Physics of Fluids 2019, 31 (10), 103302.

282. Hidman, N.; Sardina, G.; Maggiolo, D.; Ström, H.; Sasic, S., Laser-induced vapour bubble as a means for crystal nucleation in supersaturated solutions—Formulation of a numerical framework. Experimental and Computational Multiphase Flow 2019, 1 (4), 242-254.

283. Lauterborn, W.; Ohl, C.-D., Cavitation bubble dynamics. Ultrasonics sonochemistry 1997, 4 (2), 65-75.

284. Ito, Y.; Ueki, O.; Nakamura, S., Determination of colloidal iron in water by laser-induced breakdown spectroscopy. Analytica chimica acta 1995, 299 (3), 401-405.

285. Kitamori, T.; Yokose, K.; Suzuki, K.; Sawada, T.; Gohshi, Y., Laser breakdown acoustic effect of ultrafine particle in liquids and its application to particle counting. Japanese journal of applied physics 1988, 27 (6A), L983.

286. Tanabe, R.; Nguyen, T. T. P.; Sugiura, T.; Ito, Y., Bubble dynamics in metal nanoparticle formation by laser ablation in liquid studied through high-speed laser stroboscopic videography. Applied Surface Science 2015, 351, 327-331.

287. Reuter, F.; Gonzalez-Avila, S. R.; Mettin, R.; Ohl, C.-D., Flow fields and vortex dynamics of bubbles collapsing near a solid boundary. Physical Review Fluids 2017, 2 (6), 064202.

288. Hidman, N.; Sardina, G.; Maggiolo, D.; Ström, H.; Sasic, S., Numerical Frameworks for Laser-Induced Cavitation: Is Interface Supersaturation a Plausible Primary Nucleation Mechanism? Crystal Growth & Design 2020, 20 (11), 7276-7290.

289. Lide, D. R., CRC Handbook of Chemistry and Physics, volume 90th edition. CRC Handbook of Chemistry and Physics 2009, 2010.

290. Schneider, C. A.; Rasband, W. S.; Eliceiri, K. W., NIH Image to ImageJ: 25 years of image analysis. Nature methods 2012, 9 (7), 671-675.

291. Busquets, M. A.; Fernández, J. M.; Serra, P.; Estelrich, J., Superparamagnetic Nanoparticles with Efficient Near-Infrared Photothermal Effect at the Second Biological Window. Molecules 2020, 25 (22), 5315.

292. Koga, Y., Ultrasonic velocity and absorption studies in aqueous electrolytes. Solution Thermodynamics and Its Application to Aqueous Solutions: A Differential Approach, Amsterdam, Elsevier 2007, 5, 310.

293. Bilaniuk, N.; Wong, G. S. K., Speed of sound in pure water as a function of temperature. The Journal of the Acoustical Society of America 1993, 93 (3), 1609-1612.

294. Forbes, C.; Price, C.; O'Leary, R. In Quantifying Ultrasound for Sono-crystallization, 2019; IEEE: pp 2450-2453.

295. Fuchs, F. J. The Effects of Liquid Properties on Ultrasonic Cleaning.

296. Liu, L.; Yang, Y.; Liu, P.; Tan, W., The influence of air content in water on ultrasonic cavitation field. Ultrasonics Sonochemistry 2014, 21 (2), 566-571.

297. Hatanaka, S.-i.; Yasui, K.; Kozuka, T.; Tuziuti, T.; Mitome, H., Influence of bubble clustering on multibubble sonoluminescence. Ultrasonics 2002, 40 (1-8), 655-660.

298. Li, H.; Afacan, A.; Liu, Q.; Xu, Z., Study interactions between fine particles and micron size bubbles generated by hydrodynamic cavitation. Minerals Engineering 2015, 84, 106-115.

299. John, J. J.; Kuhn, S.; Braeken, L.; Van Gerven, T., Effect of fluid properties on ultrasound assisted liquid-liquid extraction in a microchannel. Ultrasonics sonochemistry 2018, 42, 68-75.

300. Venkatalakshmi, V.; Chowdappa, A.; Venkateswarlu, P.; Reddy, K. S., Volumetric, speed of sound data and viscosity for the binary mixtures of 2-methylaniline with aliphatic ketones and cyclic ketones at different temperatures. Int J Innov Res Sci Eng Tech 2014, 3 (11), 17556-17566.

301. Chauhan, M. S.; Kumar, A.; Chauhan, S., Ultrasonic velocity, viscosity and density studies of binary mixtures. Part 2. 1, 2-Dimethoxyethane and tetrahydrofuran in some dipolar aprotic solvents. Acoustics letters 1998, 21 (11), 228-235.

302. Iglesias, M.; Orge, B.; Piñeiro, M. M.; de Cominges, B. E.; Marino, G.; Tojo, J., Thermodynamic properties of the ternary mixture acetone+ methanol+ ethanol at 298.15 K. Journal of Chemical & Engineering Data 1998, 43 (5), 776-780.

303. Clarke, H. T., CXCI. —The relation between residual affinity and chemical constitution. Part III. Some heterocyclic compounds. Journal of the Chemical Society, Transactions 1912, 101, 1788-1809.

304. SavithaJyostna, T.; Satheesh, B.; Sreenu, D.; Ramesh, G.; Jayanthi Rani, E., The study of thermo-physical properties of binary liquid mixtures of isoamyl alcohol with amines at 298.15–308.15 K. Physics and Chemistry of Liquids 2020, 58 (3), 349-363.

305. Willard, G. W., Temperature coefficient of ultrasonic velocity in solutions. The Journal of the Acoustical Society of America 1947, 19 (1), 235-241.

306. Smallwood, I., Handbook of organic solvent properties. Butterworth-Heinemann: 2012.

307. Briggs, H. B.; Johnson, J. B.; Mason, W. P., Properties of liquids at high sound pressure. The Journal of the Acoustical Society of America 1947, 19 (4), 664-677.

308. Abbas, A.; Srour, M.; Tang, P.; Chiou, H.; Chan, H.-K.; Romagnoli, J. A., Sonocrystallisation of sodium chloride particles for inhalation. Chemical Engineering Science 2007, 62 (9), 2445-2453.

309. Dhumal, R. S.; Biradar, S. V.; Paradkar, A. R.; York, P., Ultrasound assisted engineering of lactose crystals. Pharmaceutical Research 2008, 25 (12), 2835-2844.

310. Narducci, O.; Jones, A. G., Seeding in Situ the Cooling Crystallization of Adipic Acid using Ultrasound. Crystal Growth & Design 2012, 12 (4), 1727-1735.

311. Eder, R. J. P.; Schrank, S.; Besenhard, M. O.; Roblegg, E.; Gruber-Woelfler, H.; Khinast, J. G., Continuous Sonocrystallization of Acetylsalicylic Acid (ASA): Control of Crystal Size. Crystal Growth & Design 2012, 12 (10), 4733-4738.

312. Furuta, M.; Mukai, K.; Cork, D.; Mae, K., Continuous crystallization using a sonicated tubular system for controlling particle size in an API manufacturing process. Chemical Engineering and Processing: Process Intensification 2016, 102, 210-218.

313. Yang, Z.-Y.; Yen, S.-K.; Hu, W.-S.; Huang, Y.-Z.; Yang, T.-M.; Su, C.-S., Sonocrystallization—Case Studies of Salicylamide Particle Size Reduction and Isoniazid Derivative Synthesis and Crystallization. Crystals (2073-4352) 2018, 8 (6).

314. Ramisetty, K. A.; Rasmuson, Å. C., Controlling the Product Crystal Size Distribution by Strategic Application of Ultrasonication. Crystal Growth & Design 2018, 18 (3), 1697-1709.

315. Ramisetty, K. A.; Kumar, K. V.; Rasmuson, Å. C., Advanced size distribution control in batch cooling crystallization using ultrasound. Organic Process Research & Development 2019, 23 (5), 935-944.

316. Brown, C. J.; McGlone, T.; Yerdelen, S.; Srirambhatla, V.; Mabbott, F.; Gurung, R.; Briuglia, M. L.; Ahmed, B.; Polyzois, H.; McGinty, J., Enabling precision manufacturing of active pharmaceutical ingredients: workflow for seeded cooling continuous crystallisations. Molecular Systems Design & Engineering 2018, 3 (3), 518-549.

317. Jiménez, J. A.; Martínez, F., Thermodynamic magnitudes of mixing and solvation of acetaminophen in ethanol+ water cosolvent mixtures. Rev Acad Colomb Cienc 2006, 30 (114), 87-99.

318. Urwin, S. Effect of Acetanilide on the Absolute Solubility of Paracetamol in Isoamyl Alcohol. http://eln.sibs.strath.ac.uk/notebook/experiment/EXP-18-AB6210.

319. Urwin, S. Effect of Metacetamol on the Absolute Solubility of Paracetamol in Isoamyl Alcohol (Repeated). http://eln.sibs.strath.ac.uk/notebook/experiment/EXP-18-AB6213.

320. Prasad, K. V. R.; Ristic, R. I.; Sheen, D. B.; Sherwood, J. N., Crystallization of paracetamol from solution in the presence and absence of impurity. International journal of pharmaceutics 2001, 215 (1-2), 29-44.

321. Chen, M.; Fang, X.; Tang, S.; Zheng, N., Polypyrrole nanoparticles for high-performance in vivo near-infrared photothermal cancer therapy. Chemical communications 2012, 48 (71), 8934-8936.

322. Shao, W.; Wei, Q.; Wang, S.; Li, F.; Wu, J.; Ren, J.; Cao, F.; Liao, H.; Gao, J.; Zhou, M., Molecular engineering of D–A–D conjugated small molecule nanoparticles for high performance NIR-II photothermal therapy. Materials Horizons 2020, 7 (5), 1379-1386.

Appendices

A-1. Image Bubble Counting Procedure

In order to count the bubble number within a frame, the original image was loaded in MATLAB and the contrast was increased. Next, using the adaptthresh function, an adaptive threshold of the inverted image (sensitivity = 0.2) was set, allowing for the number of regions to be counted. An example is provided below. It should be noted that bubbles in close proximity were counted as one region, and there are three cases of this in the example below. The diameter of the maximum bubble was taken as the minor axis of the largest region found, which ensured that the diameter of the largest single bubble was reported. All output files were checked manually for false large regions (comprising multiple bubbles) and therefore, the total bubble count of the example image was taken as 160 in the size range 3.6-59μm.

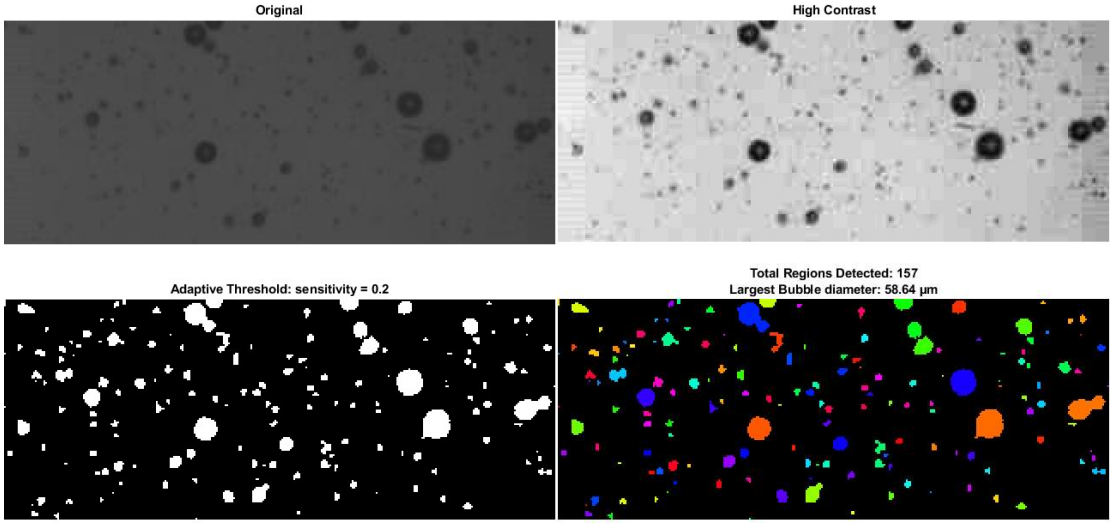

A-2. NanoSight Measurements of Particle Concentration

Sample	Rep.	Mean particle size (nm)	Average # particles/frame	Equivalent particle concentration (10^{8}/mL)
(a) DI water		52 ± 3	2.60	0.42
(b) Stock (undiluted) NP suspension in DI water	1	181 ± 100	38.55	6.21
	2	56 ± 8	39.96	6.44
	3	70 ± 27	16.50	2.66
(c) Stock NH_4Cl solution (0.328 g/g DI water)	1	287 ± 138	12.15	1.96
	2	298 ± 172	6.75	1.09
	3	266 ± 131	6.82	1.10
300 µL NP suspension (b) in 3 mL DI water	1	101 ± 54	12.42	2.00
	2	71 ± 42	4.89	0.79
	3	34 ± 15	10.39	1.68
300 µL NP suspension (b) in 3 mL (c) NH_4Cl solution	1	192 ± 121	10.61	1.71
	2	198 ± 105	10.56	1.70
	3	240 ± 149	7.64	1.14

Note that the DI water measurement was taken as a background and the values obtained were consistent with previous in-house laboratory measurements of DI water samples.

A-3. Additional Undoped Supersaturated LIN Images

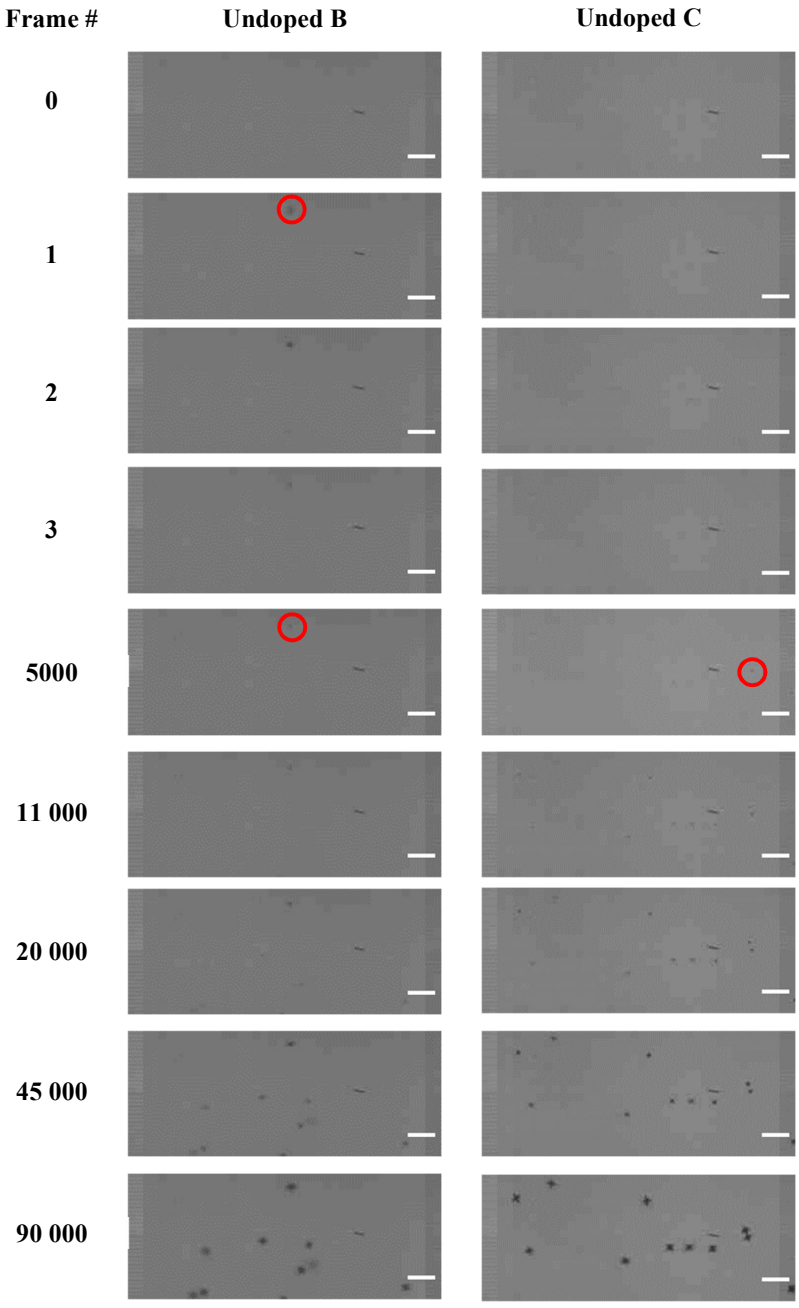

In B, the red circles indicate (i) one bubble detected and (ii) what is inferred as a crystal originating in the same location. In C, the red circle indicates the first observable crystal.

A-4. Final Frames (#138311) of LIN Image Sequences

Undoped A

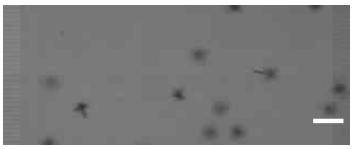

Undoped B

Undoped C

Doped A

Doped B

Doped C

A-5. Additional NP-doped Supersaturated LIN Images

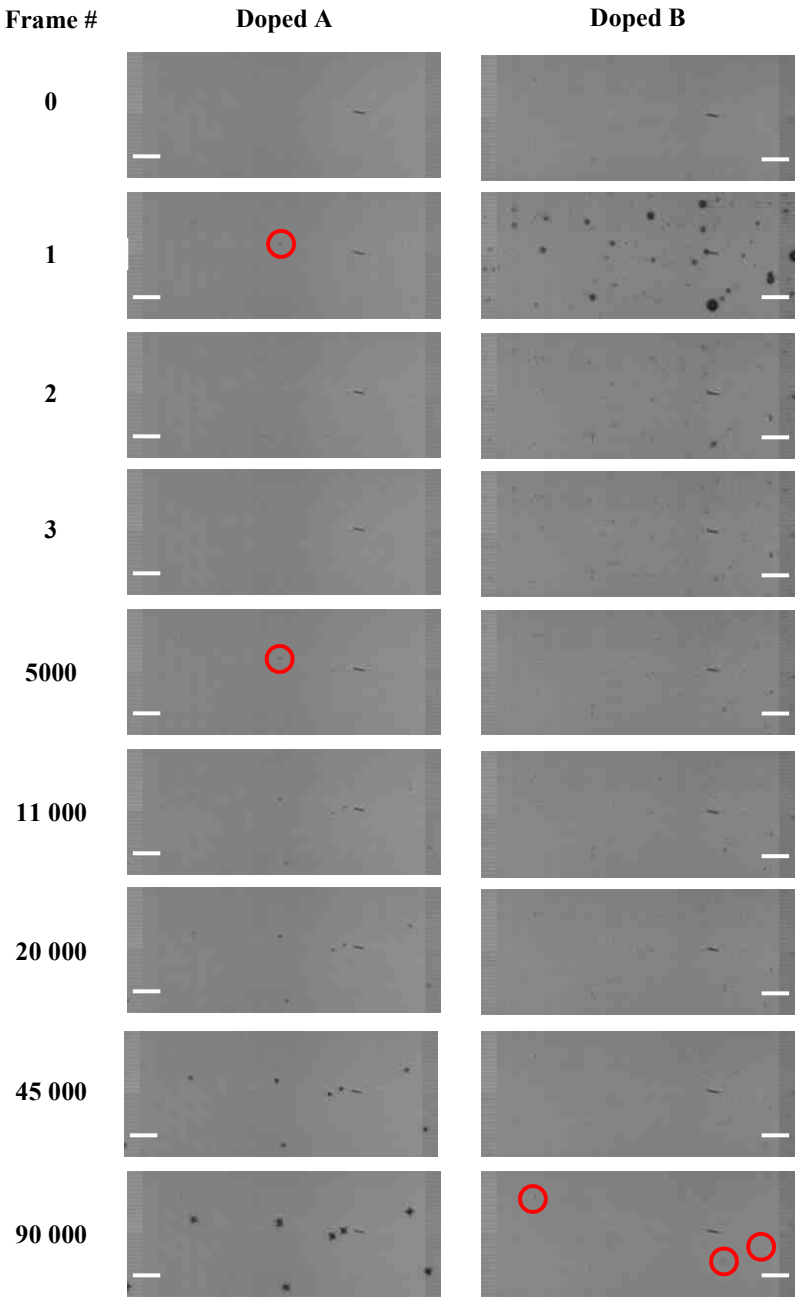

The red circles in A indicate a crystal originating in the same location as a bubble observed prior. Fifty bubbles were counted in B and the sample was not observed to nucleate though, persisting objects are circled in frame 90 000.

A-6. Time-domain Waveforms of all Laser-irradiated Samples

Tap water

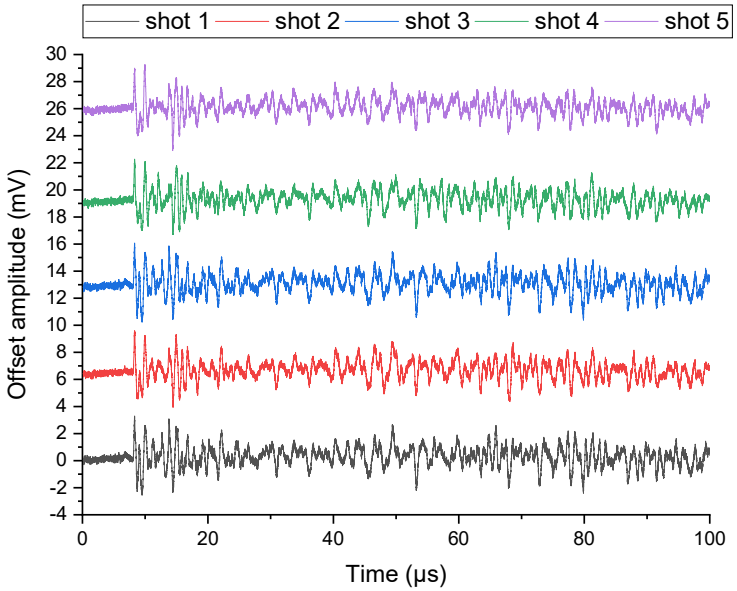

DI water

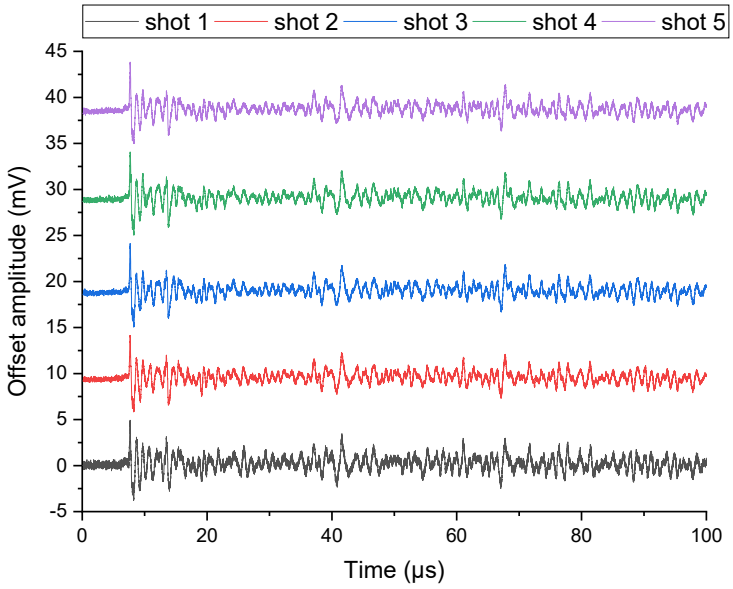

UP water

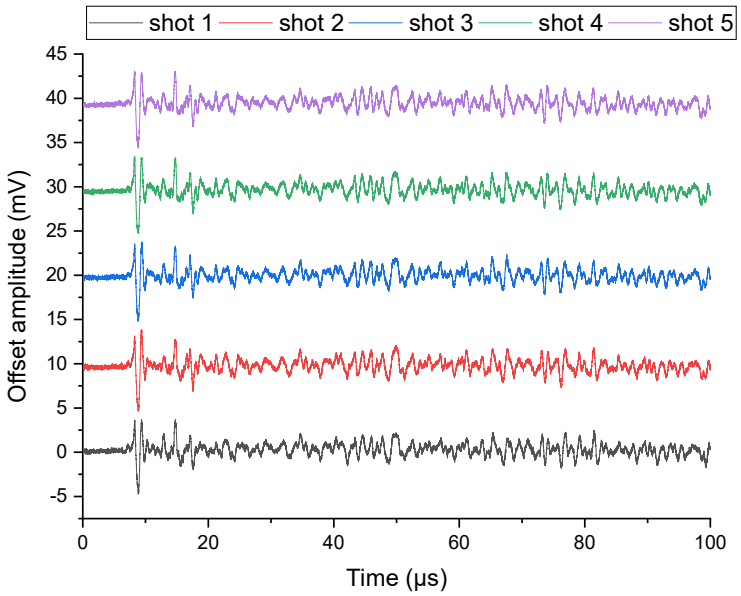

Water sample	Shot	RMS (mV)	p-p Aamplitude (mV)	BIV (V Hz)
Tap	1	0.586	5.6	2886
	2	0.678	5.9	1999
	3	0.758	6.1	1966
	4	0.728	5.7	1974
	5	0.650	6.4	1791
	Average	**0.680 ± 0.067**	**5.9 ± 0.3**	**2123 ± 434**
DI	1	0.764	9.0	4389
	2	0.688	8.5	1633
	3	0.732	9.3	1440
	4	0.737	9.1	1755
	5	0.750	9.0	1392
	Average	**0.734 ± 0.029**	**9.0 ± 0.3**	**2121 ± 1275**
UP	1	0.699	8.6	2143
	2	0.768	9.5	2766
	3	0.648	9.1	1770
	4	0.696	8.9	2576
	5	0.839	8.9	2075
	Average	**0.730 ± 0.074**	**9.0 ± 0.3**	**2265 ± 401**

0.036 g/g NH_4Cl

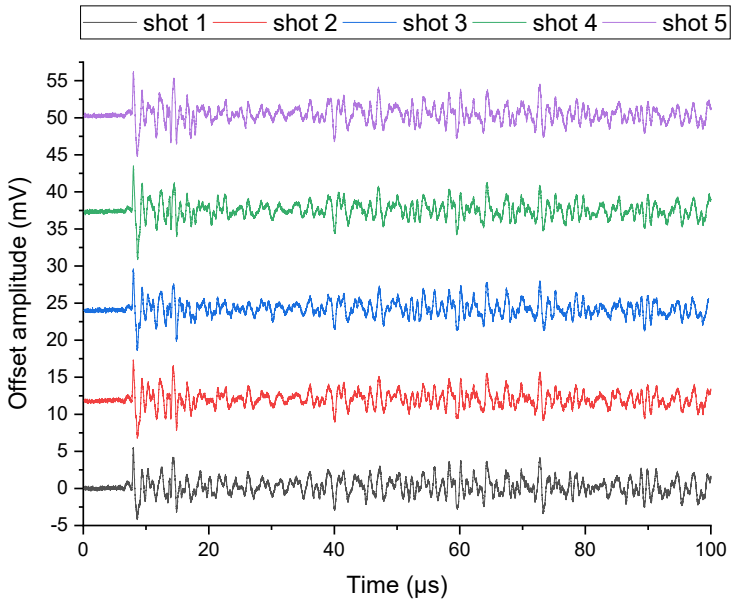

0.109 g/g NH_4Cl

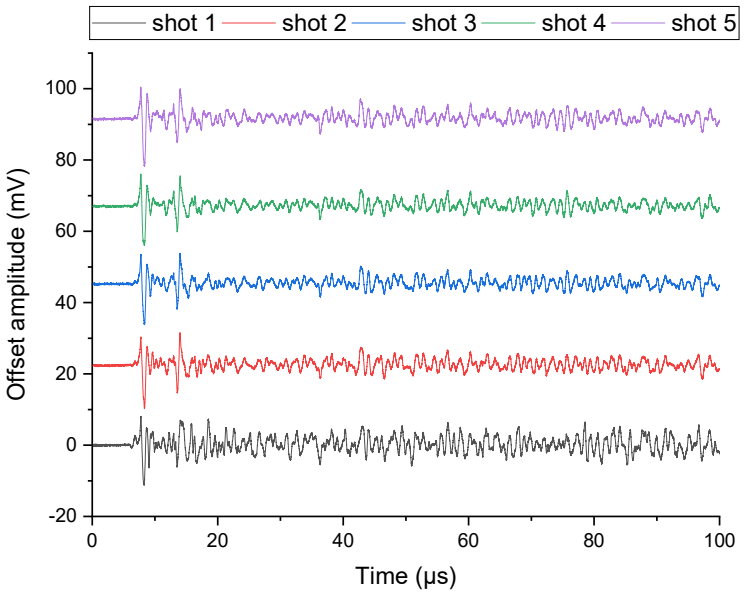

0.182 g/g NH_4Cl

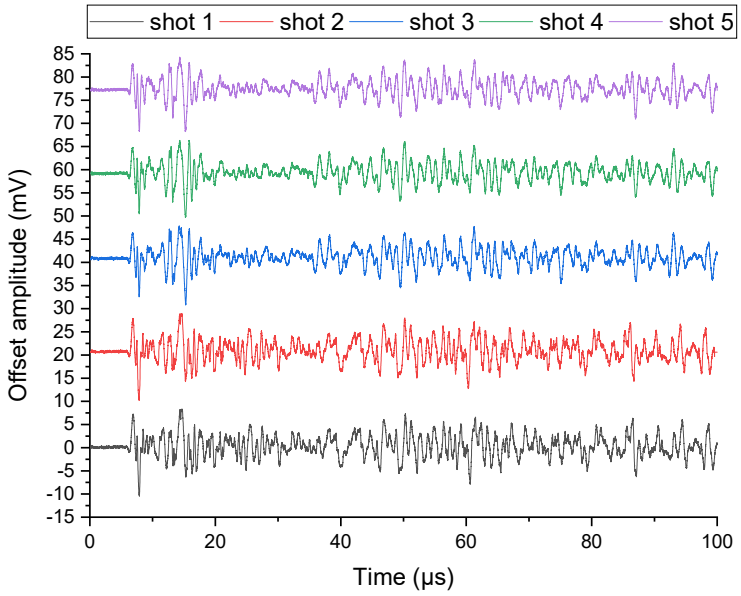

0.255 g/g NH_4Cl

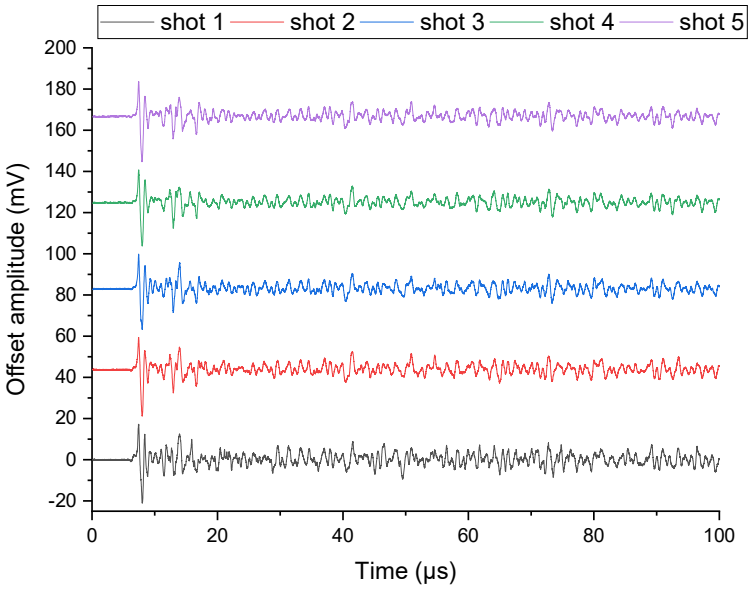

0.328 g/g NH_4Cl

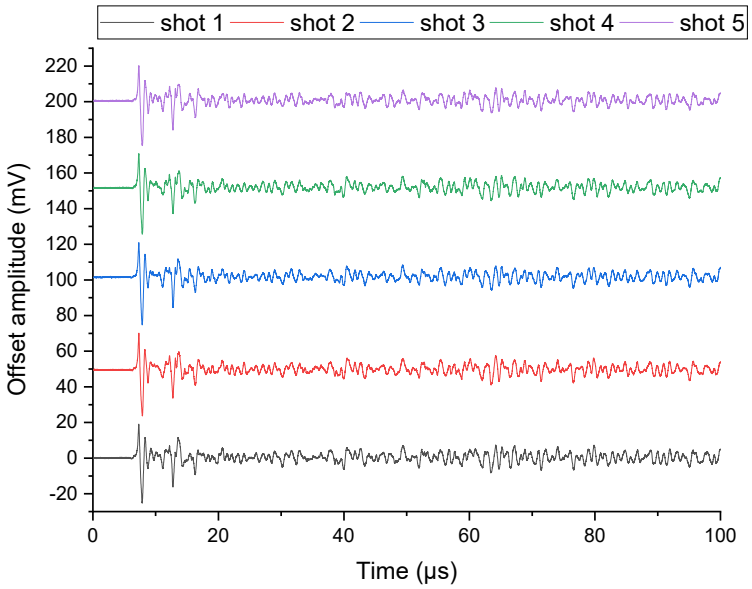

NH_4Cl concentration (g/g DI water)	Shot	RMS (mV)	p-p Aamplitude (mV)	BIV (V Hz)
0.036	1	1.192	9.9	3914
	2	1.055	10.8	4070
	3	1.023	11.3	4355
	4	1.085	12.9	4382
	5	0.953	11.8	4982
	Average	**1.061 ± 0.088**	**11.3 ± 1.1**	**4341 ± 408**
0.109	1	2.310	19.4	6720
	2	1.396	21.6	6927
	3	1.253	20.3	7064
	4	1.399	20.2	6675
	5	1.436	22.5	7312
	Average	**1.559 ± 0.426**	**20.8 ± 1.2**	**6940 ± 261**
0.182	1	2.165	19.0	7502
	2	2.175	16.7	6325
	3	2.089	17.4	6550
	4	2.158	16.9	6117
	5	2.108	16.3	6261
	Average	**2.139 ± 0.038**	**17.2 ± 1.0**	**6551 ± 554**
0.255	1	3.270	38.6	10593
	2	2.550	38.4	9833
	3	1.914	36.9	9586
	4	2.344	37.3	8430
	5	2.219	39.0	9457
	Average	**2.459 ± 0.508**	**38.0 ± 0.9**	**9580 ± 779**
0.328	1	2.367	44.3	13877
	2	3.113	46.7	13198
	3	3.113	46.5	13530
	4	2.573	45.5	12676
	5	2.549	45.0	11741
	Average	**2.743 ± 0.035**	**45.6 ± 1.0**	**13004 ± 834**

Unfiltered 0.328 g/g NH_4Cl

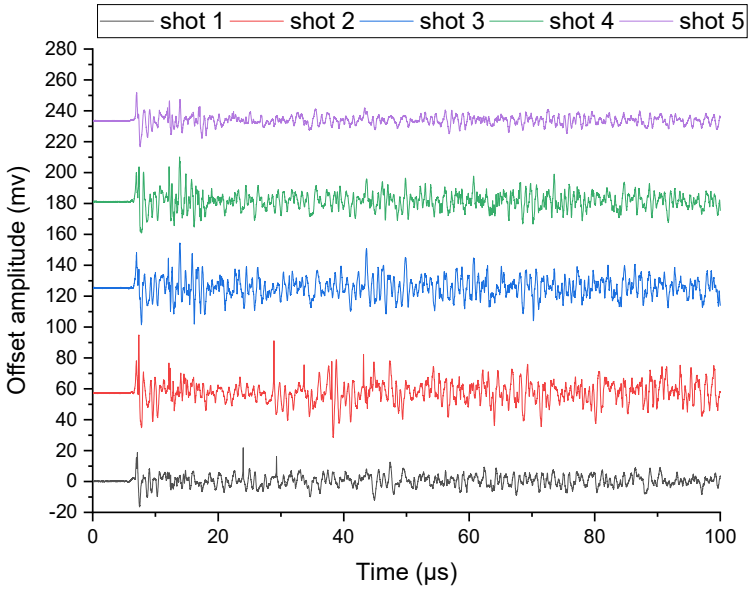

5 μm filtered 0.328 g/g NH_4Cl

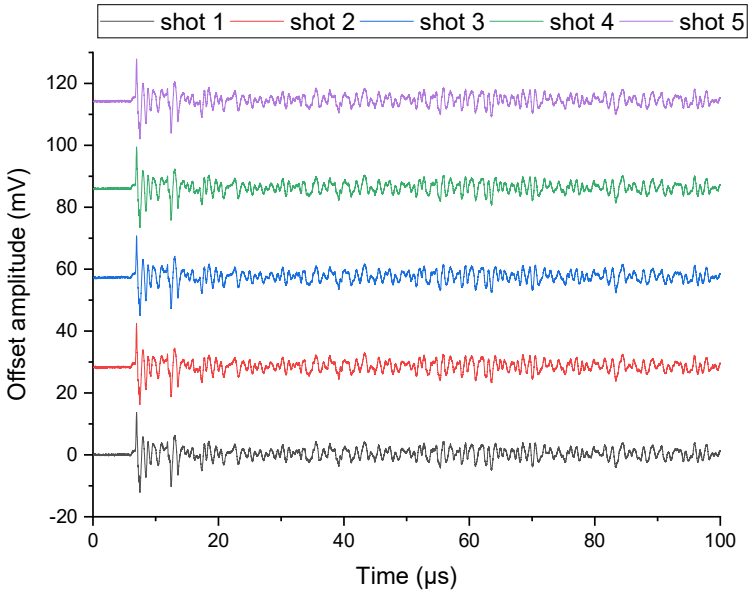

1.2 µm filtered 0.328 g/g NH_4Cl

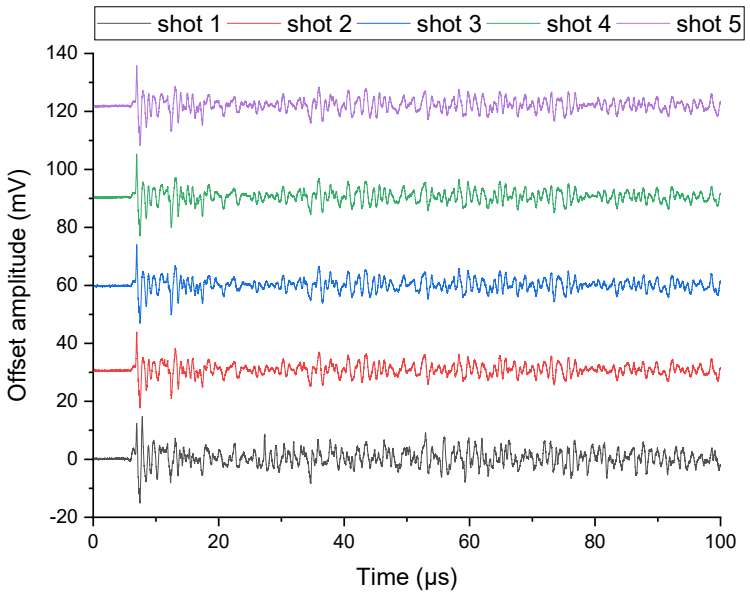

0.8 µm filtered 0.328 g/g NH_4Cl

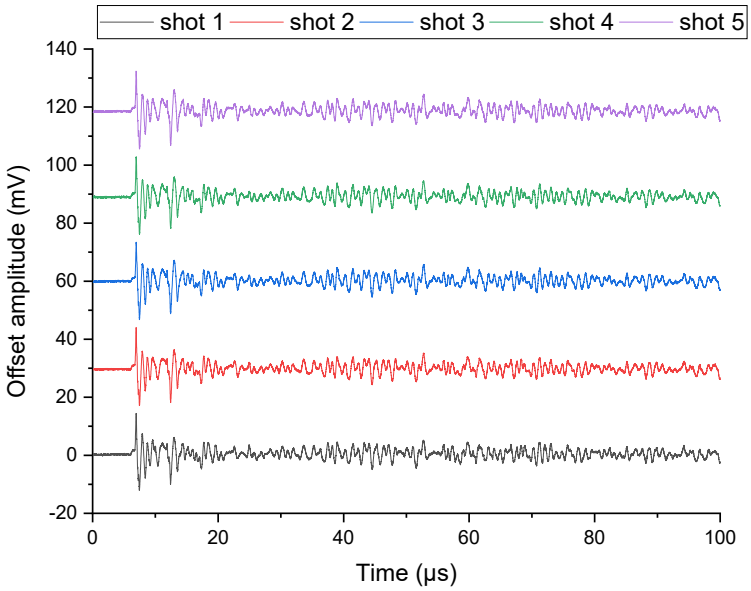

0.45 µm filtered 0.328 g/g NH_4Cl

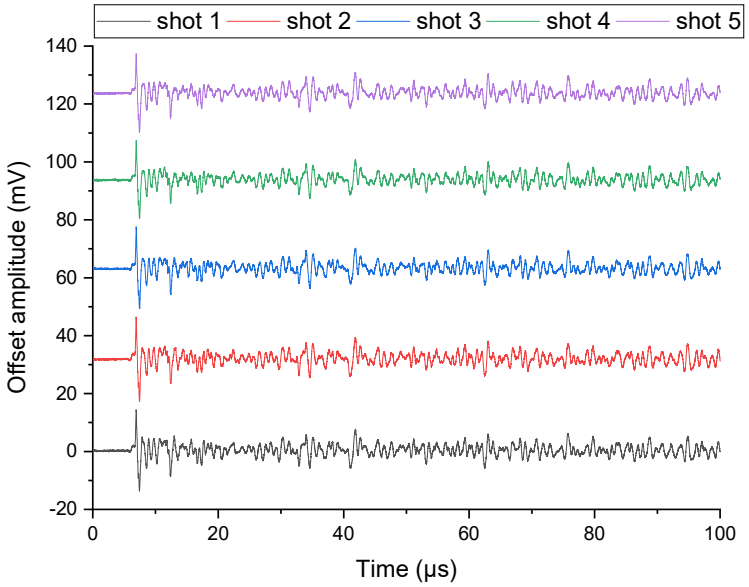

0.1 µm filtered 0.328 g/g NH_4Cl

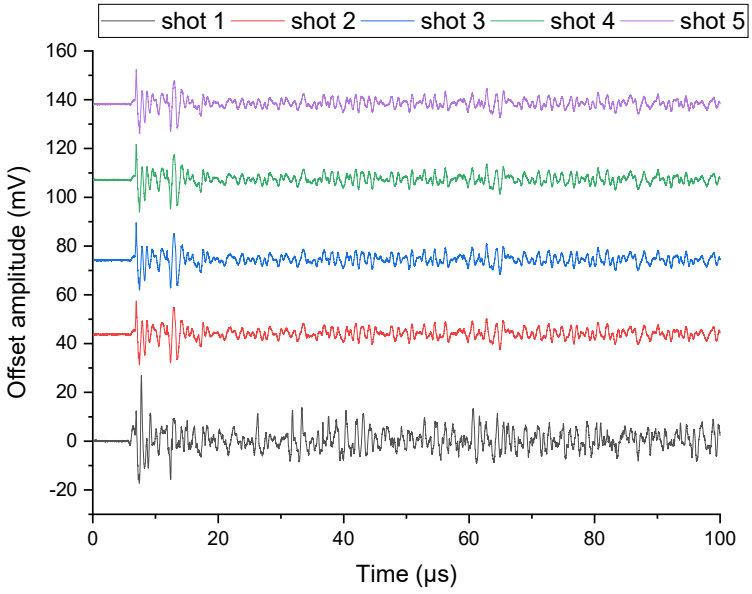

Filter pore size (μm)	Shot	RMS (mV)	p-p Aamplitude (mV)	BIV (V Hz)
unfiltered	1	3.595	38.5	16631
	2	7.146	66.4	33957
	3	6.611	53.4	24863
	4	5.326	49.5	23736
	5	2.773	35.4	17113
	Average	**5.090 ± 1.884**	**48.7 ± 12.4**	**23260 ± 7052**
5	1	1.680	25.6	9883
	2	1.745	26.6	11418
	3	1.711	26.0	10743
	4	1.727	26.3	10811
	5	1.693	26.0	10703
	Average	**1.711 ± 0.026**	**26.0 ± 0.4**	**10712 ± 547**
1.2	1	2.533	30.1	12642
	2	1.969	26.5	10977
	3	1.770	27.5	12743
	4	1.999	28.5	13328
	5	2.054	27.7	11960
	Average	**2.065 ± 0.283**	**28.0 ± 1.4**	**12330 ± 899**
0.8	1	1.274	26.7	10046
	2	2.046	27.1	10698
	3	1.747	26.8	8957
	4	2.026	26.8	10180
	5	1.697	27.0	9311
	Average	**1.758 ± 0.313**	**26.9 ± 0.2**	**9838 ± 699**
0.45	1	2.244	28.3	10563
	2	2.277	29.1	11177
	3	1.842	28.5	10955
	4	2.109	27.1	10391
	5	1.966	27.2	10593
	Average	**2.088 ± 0.185**	**28.1 ± 0.9**	**10736 ± 321**
0.1	1	4.221	44.3	9311
	2	1.948	26.4	9964
	3	1.932	28.0	11748
	4	1.754	27.8	10638
	5	1.825	26.6	10021
	Average	**2.336 ± 1.057**	**30.6 ± 7.7**	**10336 ± 918**

undoped 0.328 g/g NH_4Cl

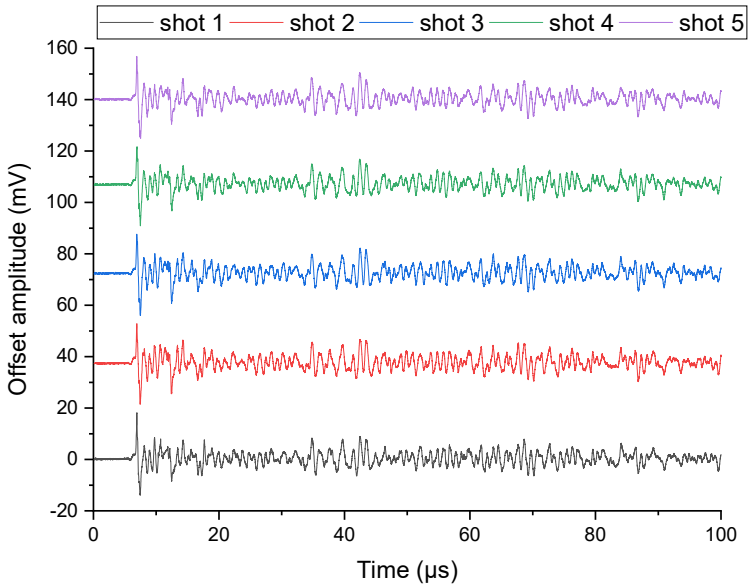

30 μL FeO_3NP-doped 0.328 g/g NH_4Cl

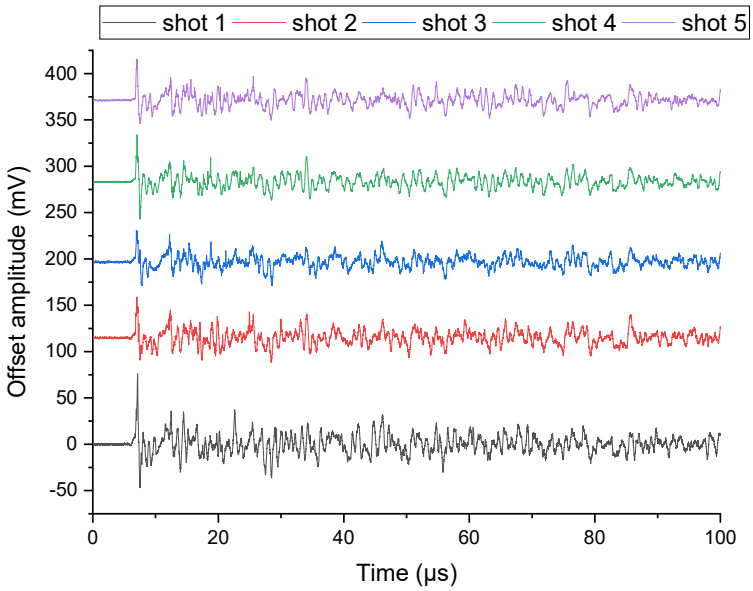

75 µL FeO_3NP-doped 0.328 g/g NH_4Cl

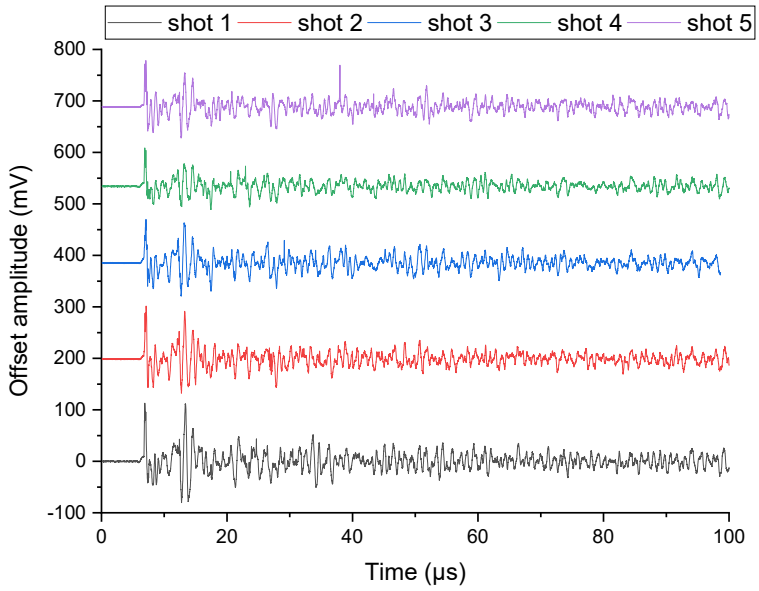

100 µL FeO_3NP-doped 0.328 g/g NH_4Cl

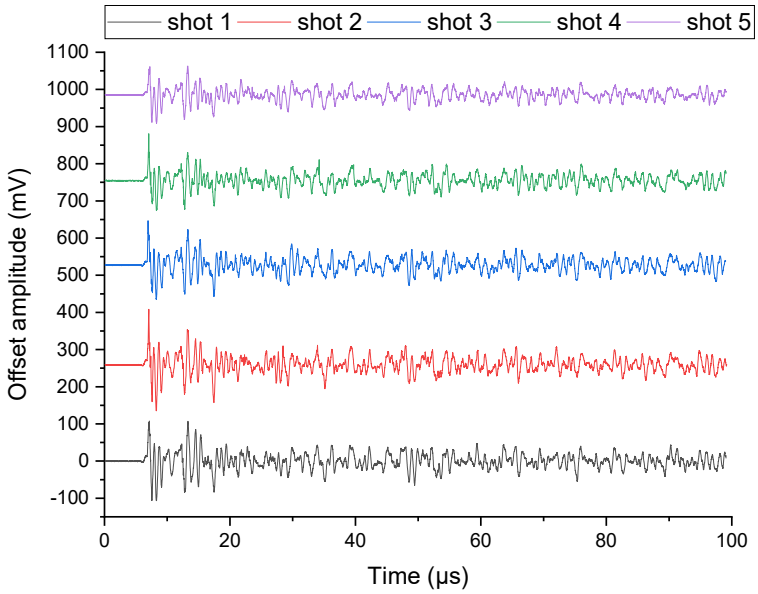

150 µL FeO_3NP-doped 0.328 g/g NH_4Cl

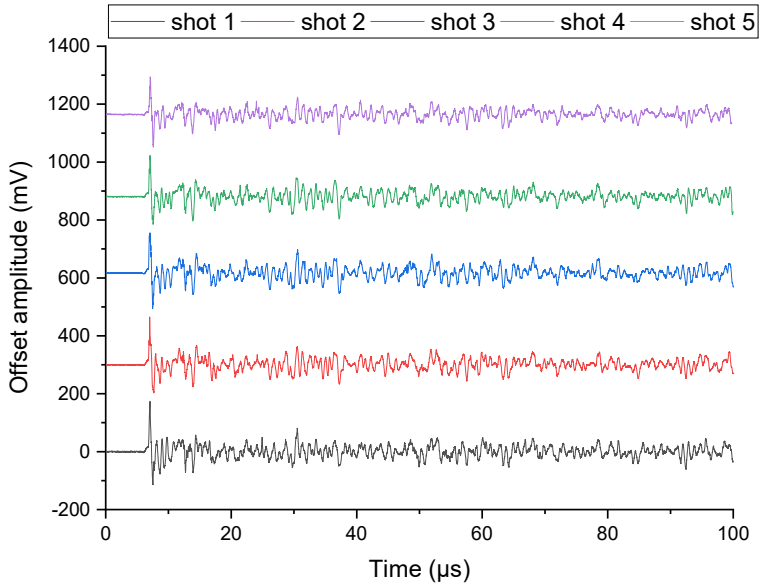

300 µL FeO_3NP-doped 0.328 g/g NH_4Cl

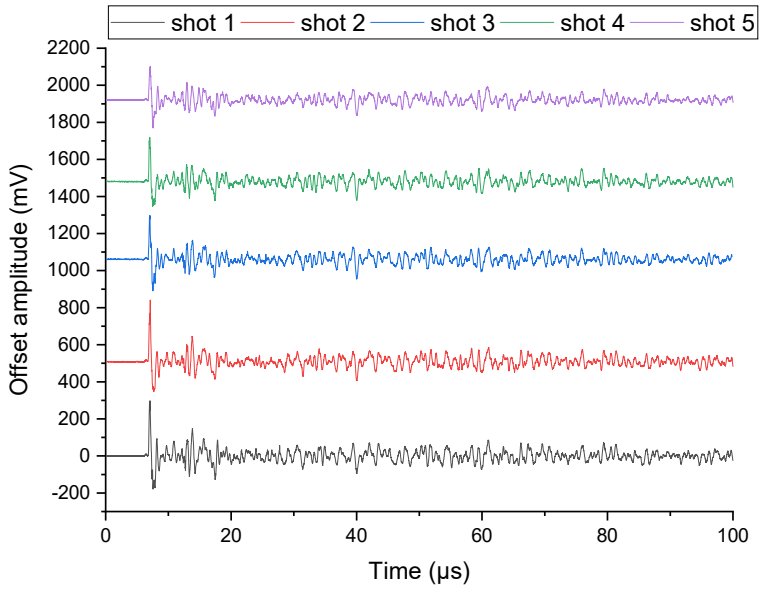

Volume FeO_3 NP suspension added (μL)	Shot	RMS (mV)	p-p Aamplitude (mV)	BIV (V Hz)
undoped	1	2.758	32.4	13656
	2	2.119	31.7	11431
	3	2.534	31.9	11912
	4	2.831	31.0	11783
	5	2.083	32.2	11104
	Average	**2.465 ± 0.350**	**31.8 ± 0.5**	**11977 ± 990**
30	1	7.877	123.6	58536
	2	8.081	71.8	35666
	3	5.750	60.1	25672
	4	6.631	91.7	37146
	5	6.710	69.9	33980
	Average	**7.010 ± 0.964**	**83.4 ± 25.2**	**38200 ± 12205**
75	1	18.210	193.8	78104
	2	15.363	169.7	99995
	3	12.229	149.5	81133
	4	11.417	121.2	69048
	5	10.725	150.9	74383
	Average	**13.589 ± 3.134**	**157.0 ± 26.9**	**80533 ± 11777**
100	1	23.124	215.8	89746
	2	23.044	273.7	148401
	3	21.426	212.2	110643
	4	19.133	207.8	114031
	5	16.724	155.4	78624
	Average	**20.690 ± 2.746**	**213.0 ± 41.9**	**108289 ± 26793**
150	1	22.528	289.1	139915
	2	22.208	265.1	107072
	3	23.326	262.1	79988
	4	21.889	238.7	103795
	5	18.884	244.0	92825
	Average	**21.767 ± 1.698**	**259.8 ± 19.9**	**104719 ± 22351**
300	1	35.342	476.0	286127
	2	32.916	494.5	352121
	3	29.088	409.7	227058
	4	28.547	374.0	205810
	5	25.366	336.4	165948
	Average	**30.252 ± 3.909**	**418.1 ± 66.9**	**246413 ± 72877**

B-1. Example Solvent Acoustic Emission Spectra Measurements

Example FFT outputs of measurements at a driving amplitude of 800 mV (p-p)

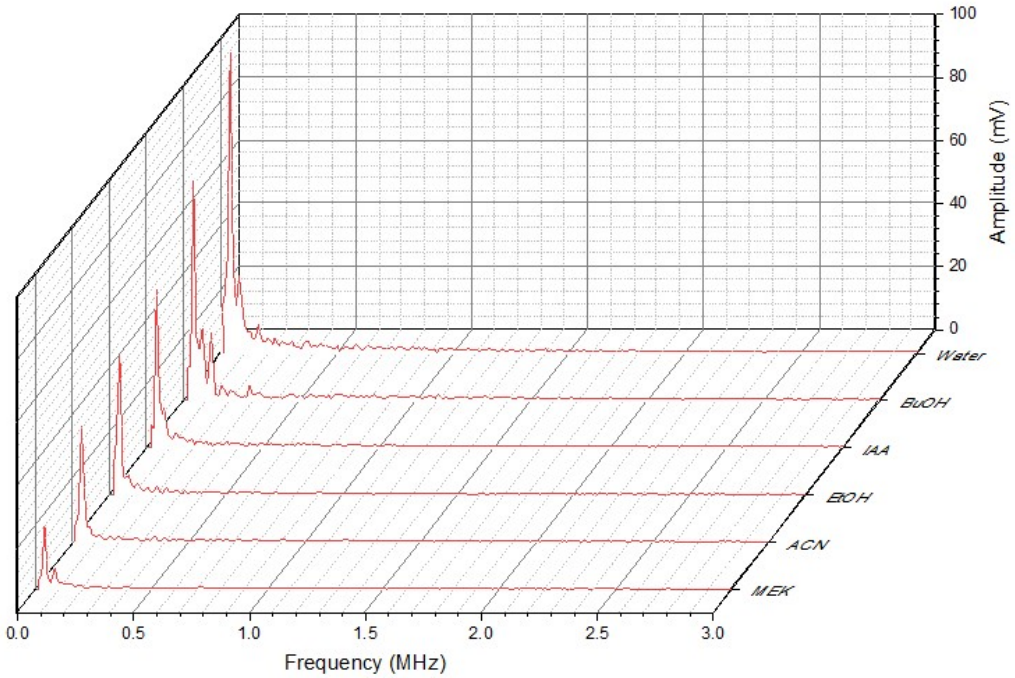

C-1. Scoping Needle Hydrophone Measurements of P_a and BIV

Plot of measurements performed in IAA, water and ACN from 100-800 mV pp amplitude drive at 40 kHz.

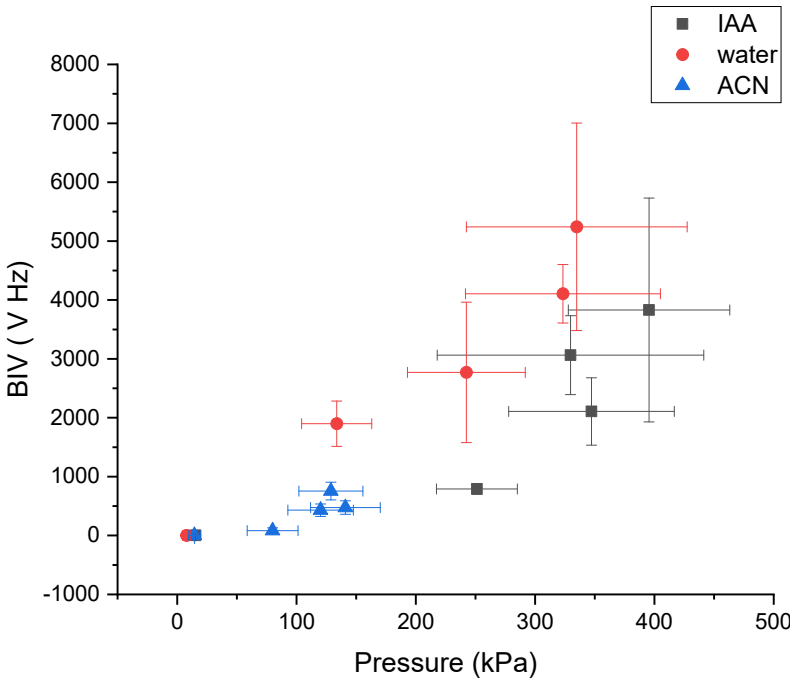

C-2. Scoping XRPD Patterns

PCM-IAA with no added impurities

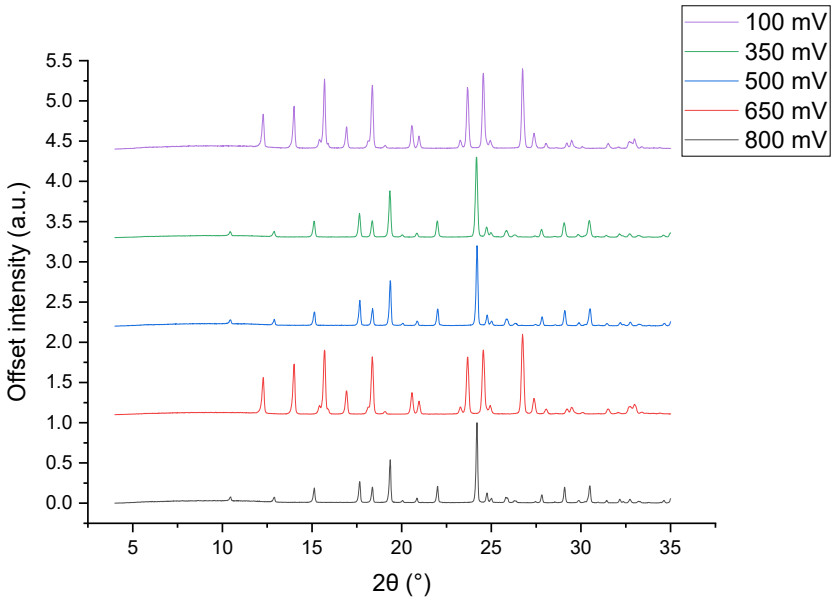

PCM-water with no added impurities

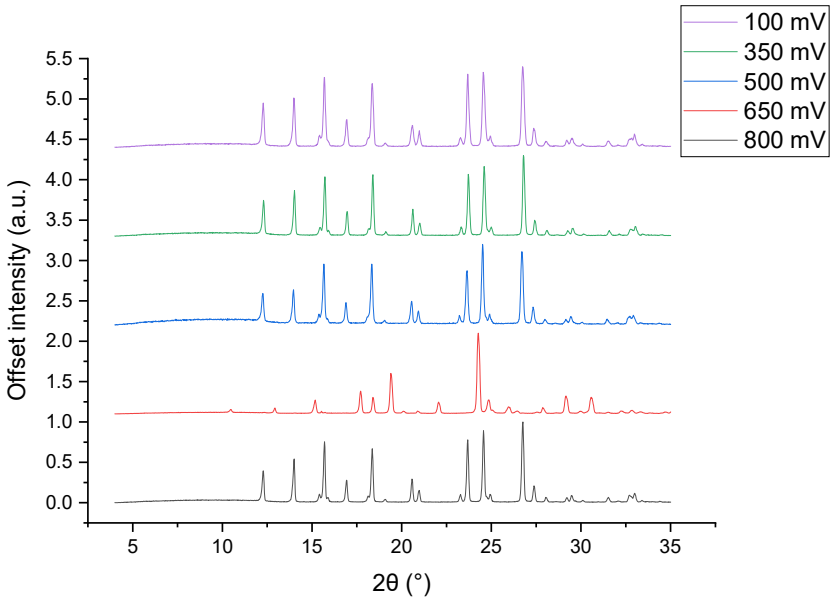

PCM-ACN with no added impurities

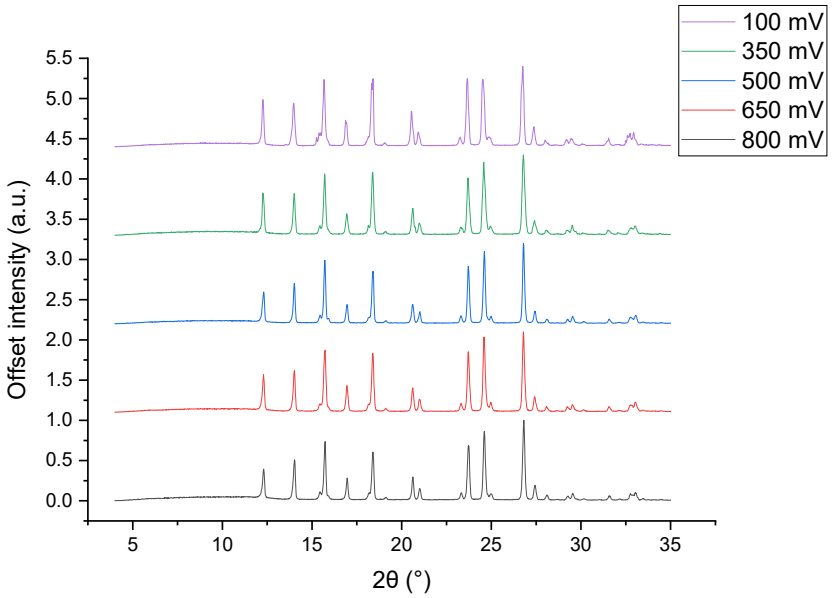

PCM-IAA with 2% ACETA

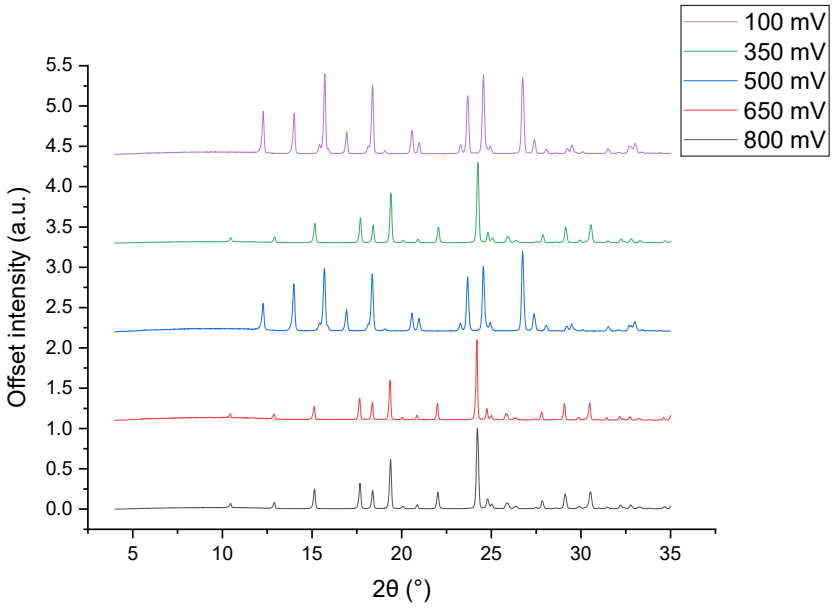

PCM-IAA with 2% ACETA

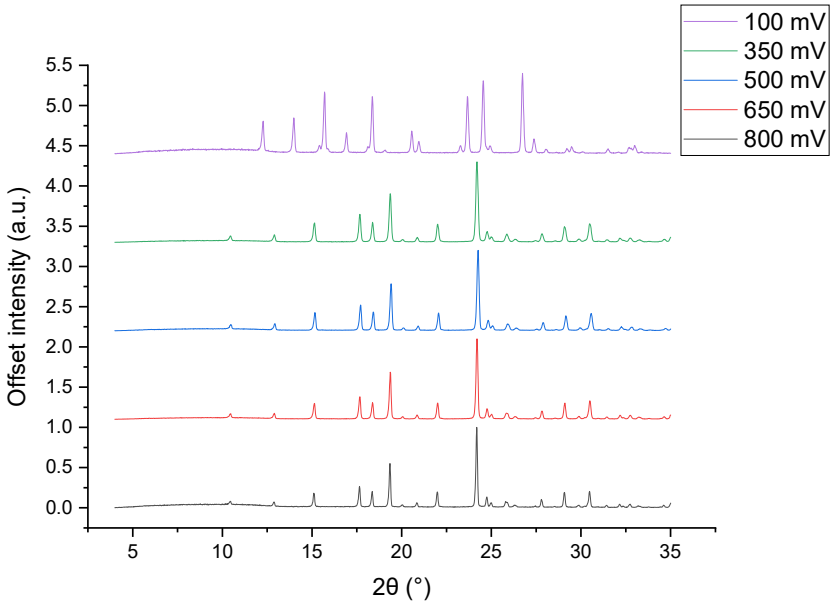

PCM-water with 2% ACETA

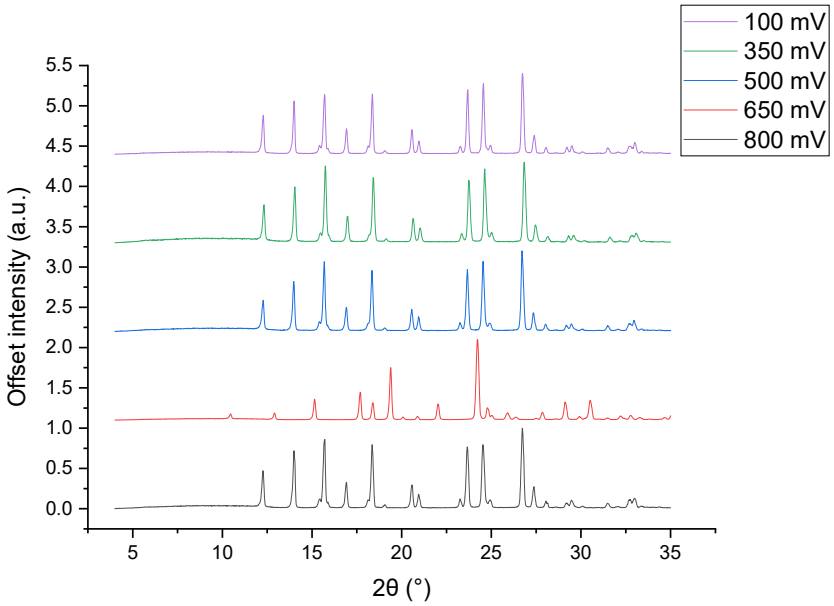

PCM-water with 2% ACETA

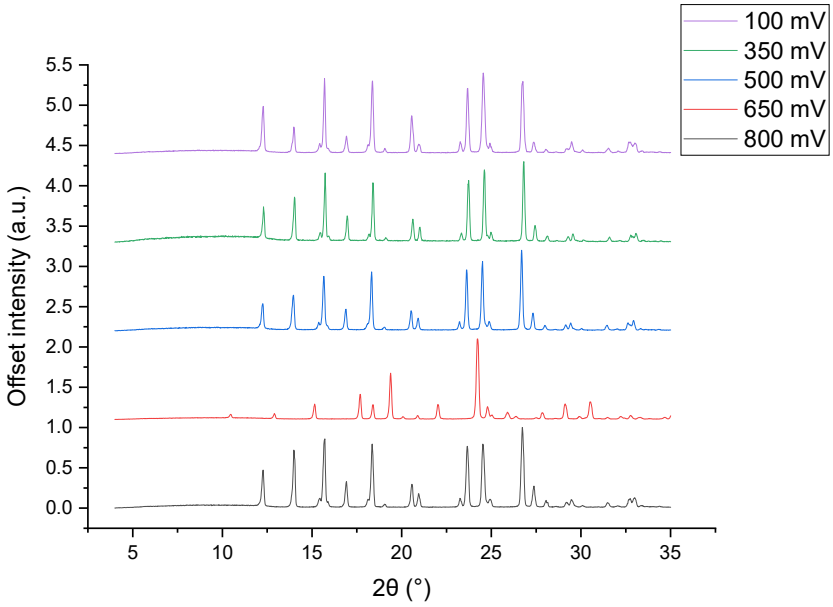

PCM-ACN with 2% ACETA

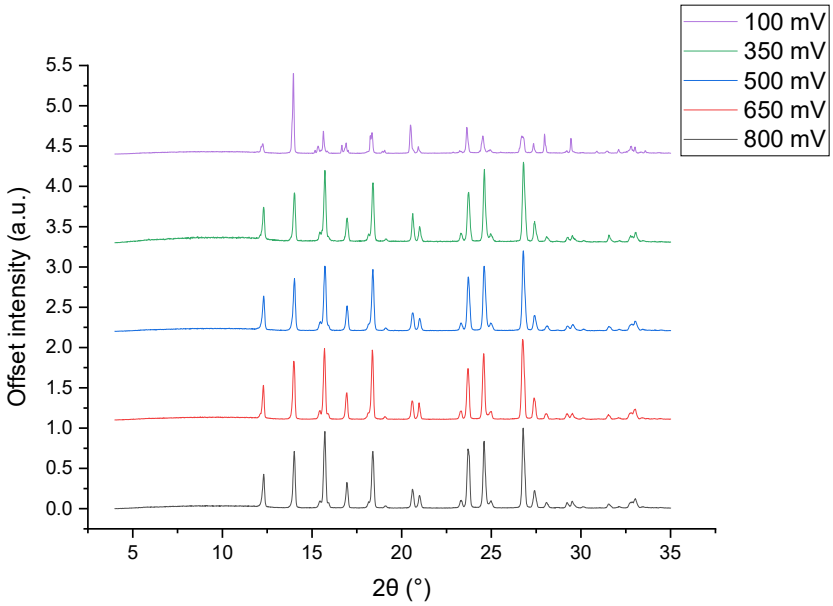

PCM-ACN with 2% ACETA

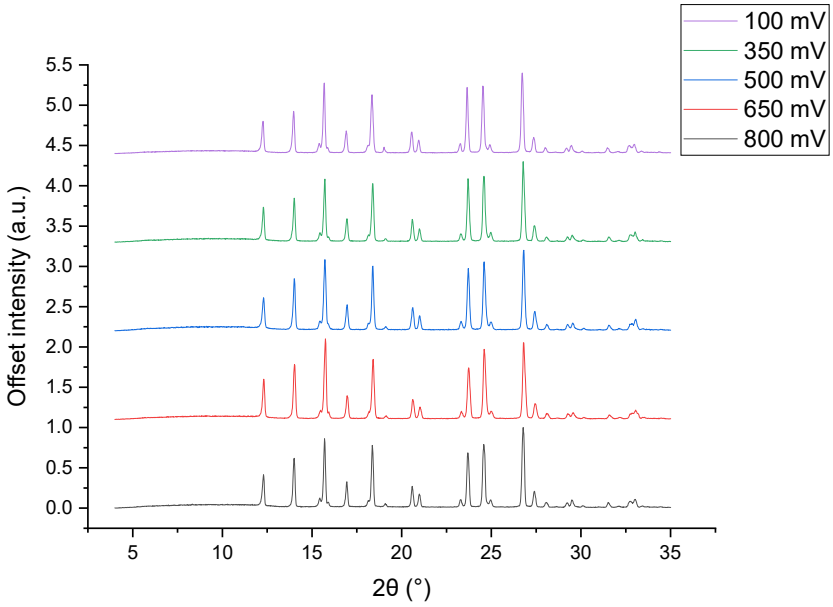

C-3. Additional Scoping Microscope Images

PCM-IAA with 2% ACETA

800 mV	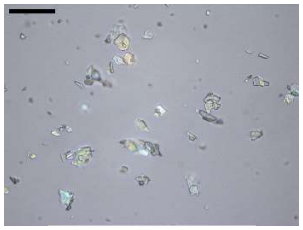	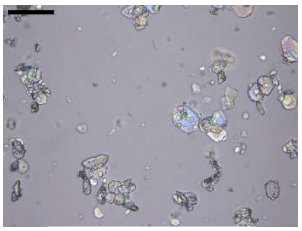
	0.85% ACETA *S* = 2.3 Form II	1.21% ACETA *S* = 2.5 Form II
650 mV	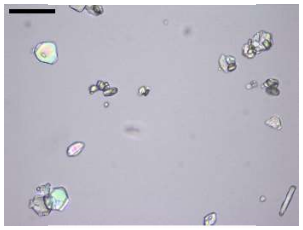	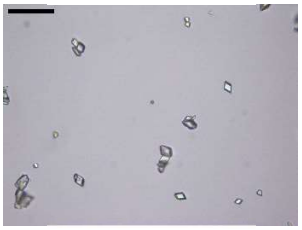
	0.43% ACETA *S* = 2.3 Form II	0.82% ACETA *S* = 2.5 Form II
500 mV	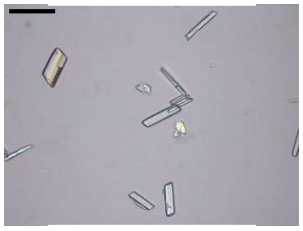	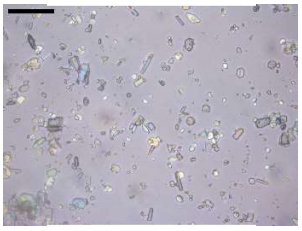
	0.28% ACETA *S* = 2.5 Form I	1.31% ACETA *S* = 2.5 Form II
350 mV		
	1.26% ACETA *S* = 2.9 Form II	1.37% ACETA *S* = 2.5 Form II
100 mV **(no cavitation)**	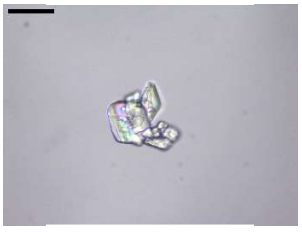	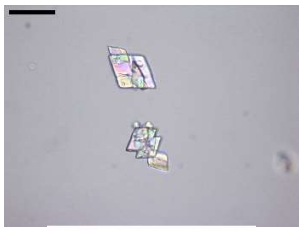
	1.14% ACETA *S* = 3.2 Form I	1.03% ACETA *S* = 2.5 Form I

PCM-water with 2% ACETA

800 mV		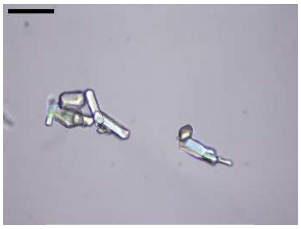
	0.67% ACETA *S* = 1.5 Form I	0.77% ACETA *S* = 1.7 Form I
650 mV	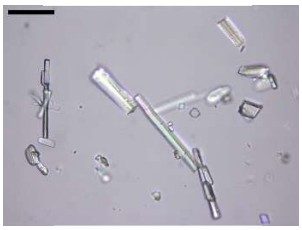	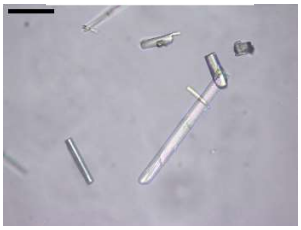
	1.07% ACETA *S* = 1.8 Form II	1.46% ACETA *S* = 2.0 Form II
500 mV	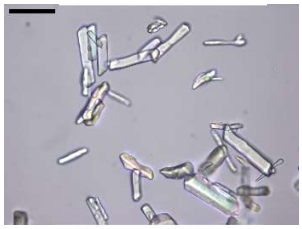	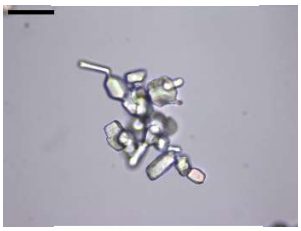
	0.46% ACETA *S* = 2.0 Form I	0.55% ACETA *S* = 2.2 Form I
350 mV	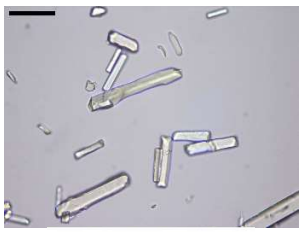	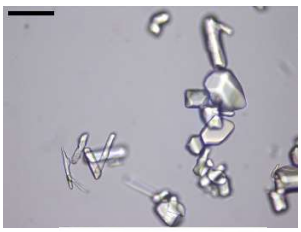
	0.51% ACETA *S* = 2.0 Form I	0.55% ACETA *S* = 2.2 Form I
100 mV **(no cavitation)**	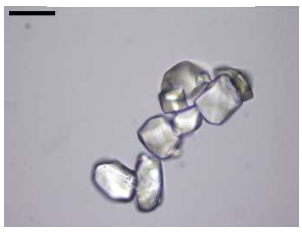	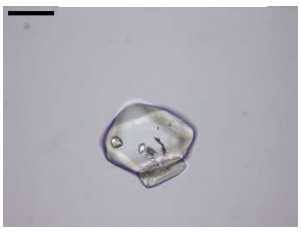
	0.79% ACETA *S* = 2.5 Form I	0.87% ACETA *S* = 2.4 Form I

PCM-ACN with 2% ACETA

800 mV

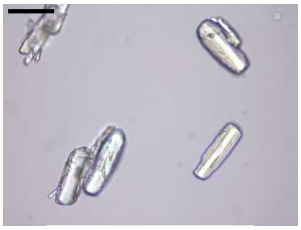

0.14% ACETA
S = 2.0 Form I

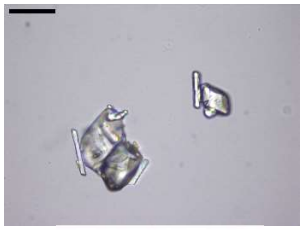

0.19% ACETA
S = 1.9 Form I

650 mV

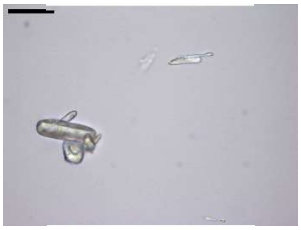

0.11% ACETA
S = 2.0 Form I

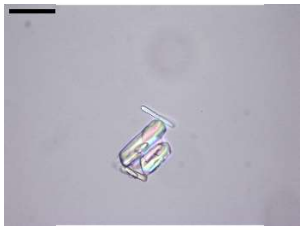

0.18% ACETA
S = 2.0 Form I

500 mV

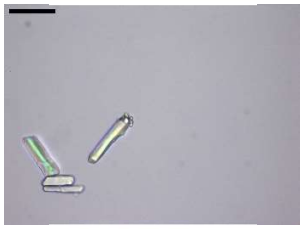

0.16% ACETA
S = 1.9 Form I

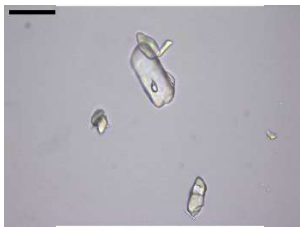

0.19% ACETA
S = 2.0 Form I

350 mV

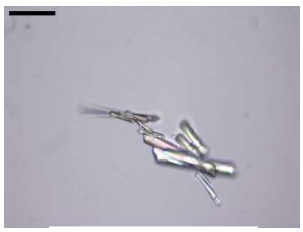

0.20% ACETA
S = 2.2 Form I

0.14% ACETA
S = 2.1 Form I

100 mV
(no cavitation)

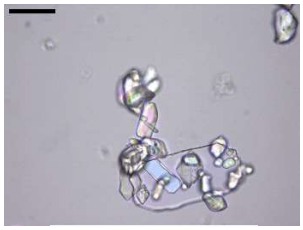

0.32% ACETA
S = 2.6 Form I

0.39% ACETA
S = 2.8 Form I

C-4. Upscale Needle Hydrophone Measurements of P_a and BIV

Plot of measurements performed at 52mm height in the IAA-filled vessel from 100-800 mV pp amplitude drive at 40 kHz.

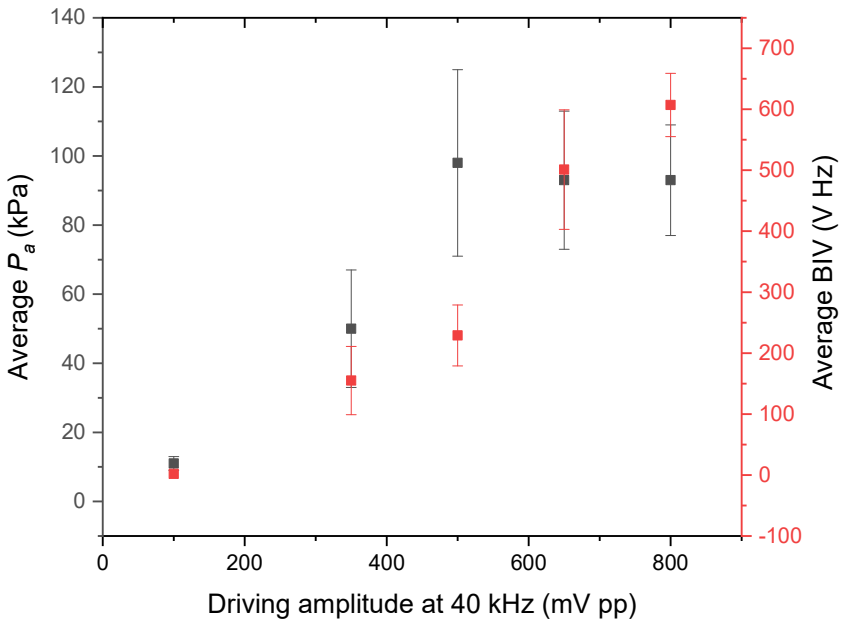

C-5. Upscale XRPD Patterns

PCM-IAA with 2% ACETA

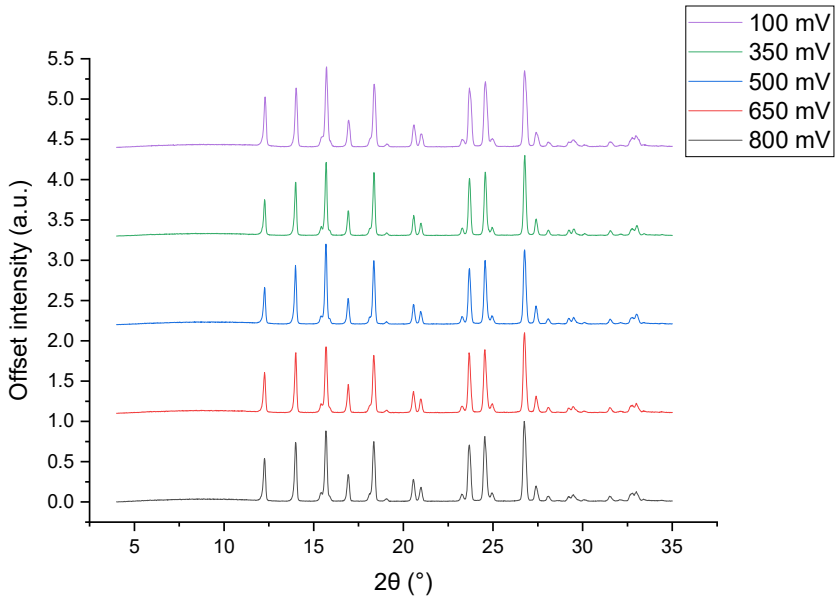

PCM-IAA with 2% MCM

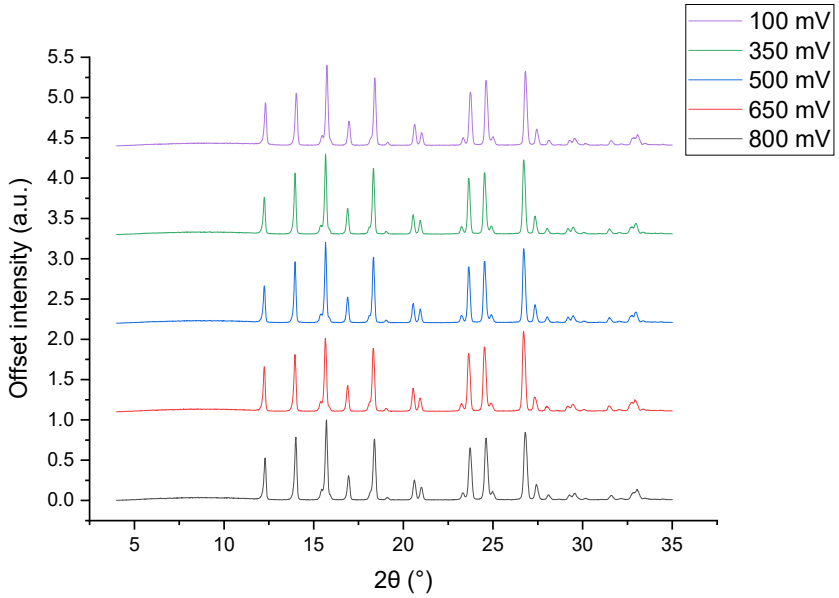

PCM-IAA with 1% ACETA and 1% MCM

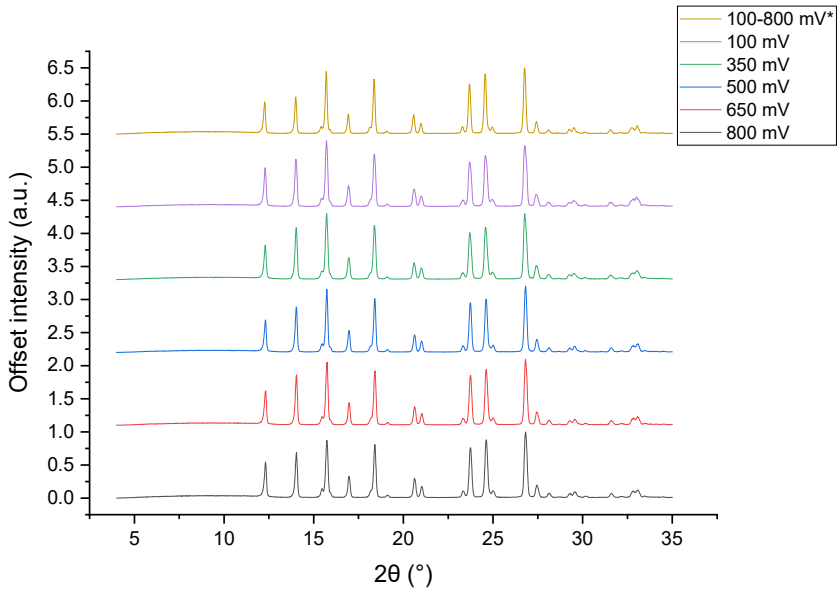

PCM-IAA with no added impurities

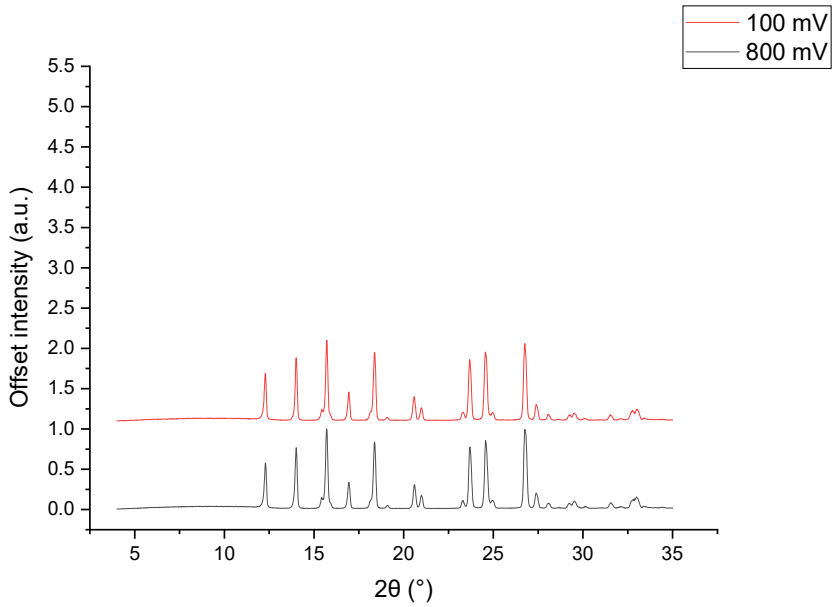

C-6. Upscale DSC Thermograms

Starting materials

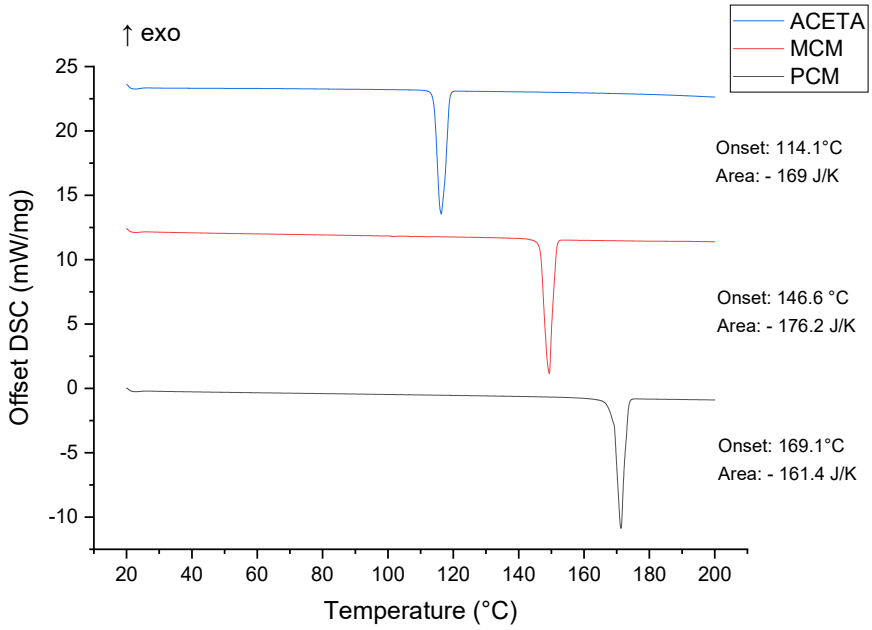

PCM-IAA with 2% ACETA

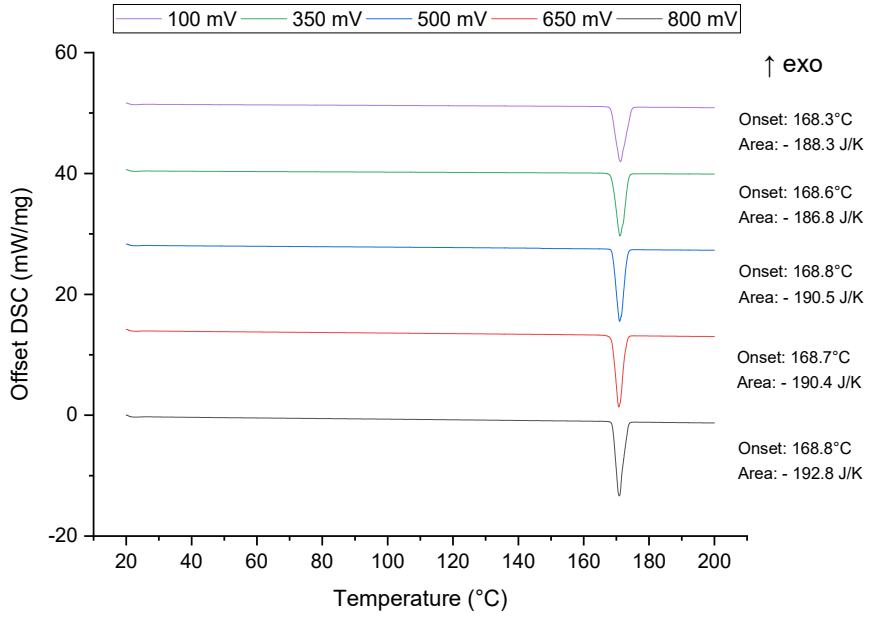

PCM-IAA with 2% MCM

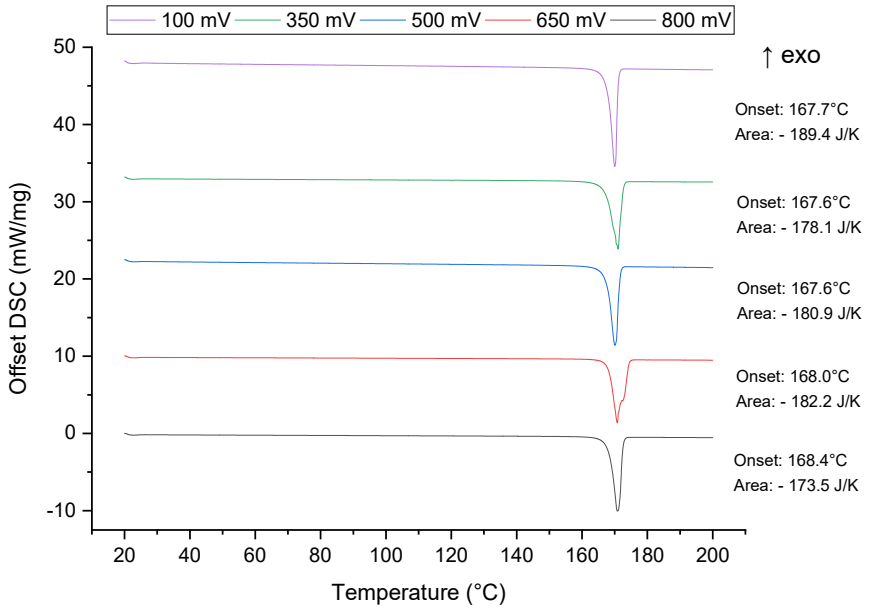

PCM-IAA with 1% ACETA and 1% MCM

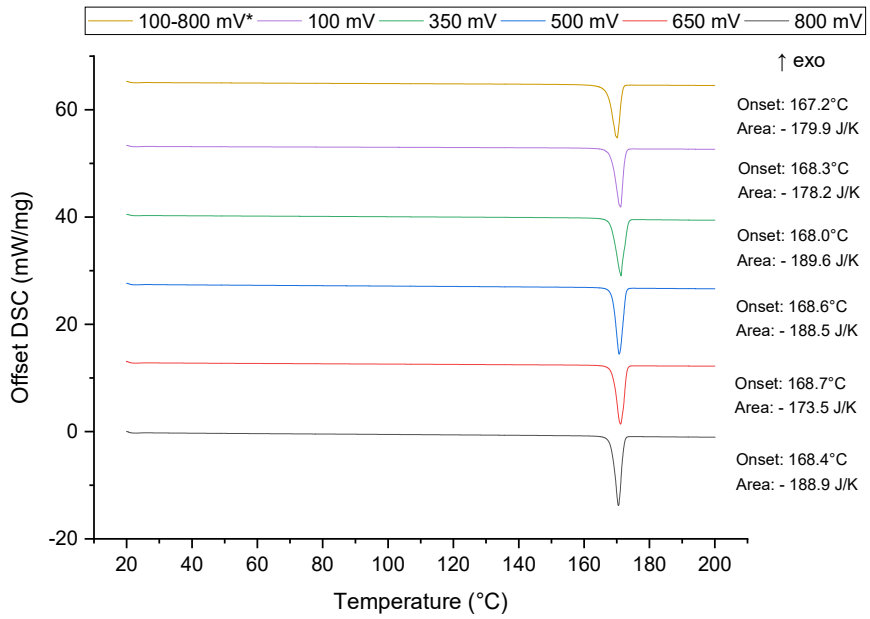

C-7. Additional Upscale Microscope Images

	PCM with 2% ACETA	PCM with 2% MCM
800 mV	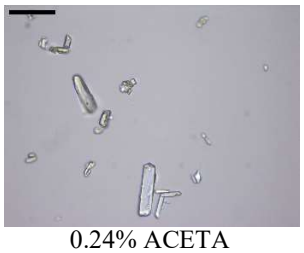 0.24% ACETA *S* = 1.3 Form I	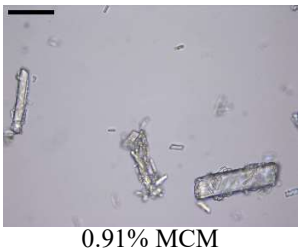 0.91% MCM *S* = 1.8 Form I
650 mV	 0.36% ACETA *S* = 1.4 Form I	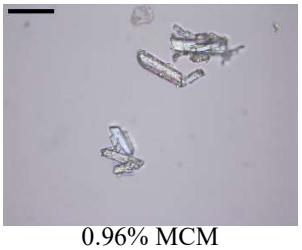 0.96% MCM *S* = 1.7 Form I
500 mV	 0.34% ACETA *S* = 1.5 Form I	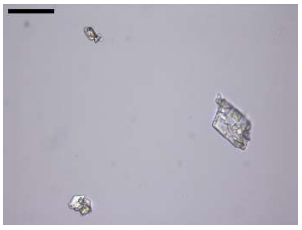 1.28% MCM *S* = 3.1 Form I
350 mV	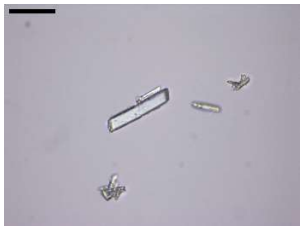 0.45% ACETA *S* = 1.6 Form I	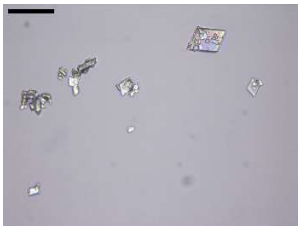 1.41% MCM *S* = 3.4 Form I
100 mV (no cavitation)	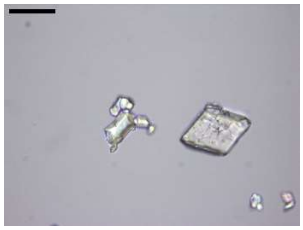 0.52% ACETA *S* = 1.8 Form I	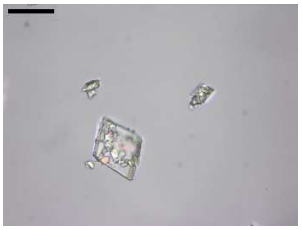 1.35% MCM *S* = 4.0 Form I

C-8. Upscale PVM Images

The scale bar represents 100μm in all images

PCM-IAA with 1% ACETA and 1% MCM

800 mV, *S* =1.5	**800 mV, *S* =4.0**
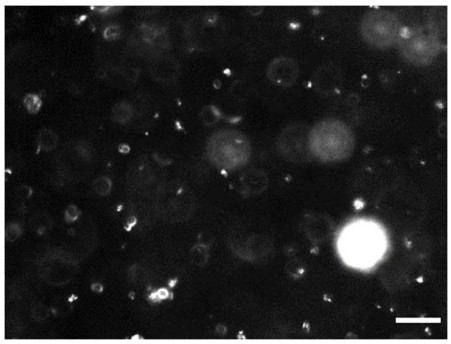	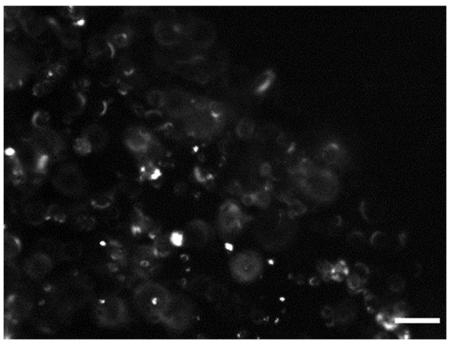
62 min	161 min
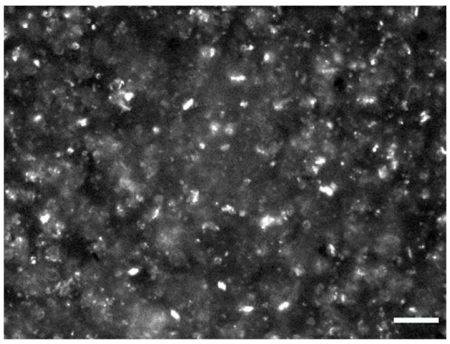	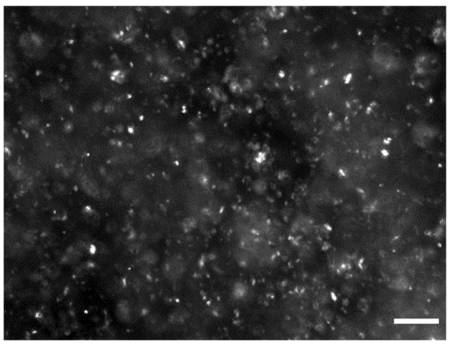
66 min	164 min